Cranfield University

School of Mechanical Engineering
Department of Propulsion, Power, and
Automotive Engineering

Ph.D.

1996

S. J. Brookes

Soot Production and Thermal Radiation from Turbulent Jet Diffusion Flames

Supervisor: Professor J. B. Moss

Submitted 4th October 1996

Abstract

The aim of this study is to advance the present capability for modelling soot production and thermal radiation from turbulent jet diffusion flames. Turbulent methane / air jet diffusion flames at atmospheric and elevated pressure are studied experimentally to provide data for subsequent model development and validation.

Methane is only lightly sooting at atmospheric pressure whereas at elevated pressure the soot yield increases greatly. This allows the creation of an optically thick, highly radiating flame within a laboratory scale rig. Essential flame properties needed for model validation are measured at 1 and 3 atm. These are mean mixture fraction, mean temperature, mean soot volume fraction, and mean and instantaneous spectrally resolved radiation intensity.

These two flames are modelled using the parabolic CFD code GENMIX. The combustion / turbulence interaction is modelled using the conserved scalar / laminar flamelet approach. The chemistry of methane combustion is modelled using a detailed chemistry laminar flame code. The combustion model accommodates the non-adiabatic nature of the flames through the use of multiple flamelets for each scalar. The flamelets are differentiated by the amount of radiative heat loss that is included. Flamelet selection is carried out through the solution of a balance equation for enthalpy, which includes a source term for the radiative heat loss. A new soot model has been developed and calibrated by application to a laminar flame calculation. Within the turbulent flame calculations the soot production is fully coupled to the radiative loss. This is achieved through the use of multiple flamelets for the soot source terms and the inclusion of the radiative loss from the soot (as well as the gases) in the enthalpy source.

Spectral radiative emission from the flames has been modelled using the RADCAL code. Mean flame properties from the GENMIX calculations are used as an input to RADCAL.

Acknowledgements

I would like to take this opportunity to thank Prof. J. B. Moss for supervising this work and using his experience to gently guide the direction of progress.

All my colleagues at Cranfield have helped and contributed to this work in one way or another. However, those particularly worthy of praise are Cecil Stewart, for providing help and experience in the laboratory, and Bernhard Fischer, for helping with all aspects of the work.

The thesis was mainly written after leaving Cranfield, during a period of employment, and my colleagues Graham Hargrave and Glen Sherwood provided the much appreciated encouragement needed to finish this work.

I would also like to thank the sponsors of this work, British Gas plc, for their invaluable financial support and the interest they have shown.

Finally, I would like to thank my parents and Melanie, Yoda, and Obi without whom this would have been impossible.

List of Contents

Contents

Contents

List of Figures

Figures

Nomenclature

The units following each character definition are the defaults, and are used in the text unless otherwise stated.

Latin

a	Gaussian fit constant	*(Dimensionless)*
a	Soot nucleation rate scaling factor	*(s^{-1})*
a	Stoichiometric coefficient	*(Dimensionless)*
a	Constant in Tesner soot model	*(s^{-1})*
a_0	Constant in Tesner soot model	*($kg^{-1}\ s^{-1}$)*
A	Constant in Arrhenius rate expression	*(Varies)*
A	Constant in Magnussen combustion model	*(Dimensionless)*
A_T	Total surface area of soot particles per unit volume	*(m^{-1})*
AFR	Air to fuel mass ratio	*(Dimensionless)*
b	Gaussian fit constant	*(Dimensionless)*
b	Stoichiometric coefficient	*(Dimensionless)*
b	Soot surface growth rate scaling factor	*(Varies with m)*
b	Constant in Tesner soot model	*($m^3\ s^{-1}$)*
B	Blackbody function	*($W\ m^{-2}\ cm$)*
B	Constant in Magnussen combustion model	*(Dimensionless)*
c	Stoichiometric coefficient	*(Dimensionless)*
c_0	Speed of light in a vacuum	*($m\ s^{-1}$)*
C	Function used in the conditional oxidation model	*(Dimensionless)*
C	Constant in Khan soot model	*($s\ m^{-2}$)*
C_{g1}	Used in the source term for $\widetilde{\xi''^2}$	*(Dimensionless)*
C_{g2}	As above	*(Dimensionless)*

Nomenclature

C_P	Specific heat capacity	*(J kg^{-1} K^{-1})*
C_T	Mole fraction	*(Dimensionless)*
C_α	Constant in Moss soot model	*(m^{3}kmolkg^{-2}K$^{-1/2}$s^{-1})*
C_β	Constant in Moss soot model	*(m^3 kmol^{-1} K$^{-1/2}$ s^{-1})*
C_γ	Constant in Moss soot model	*(m^3 K$^{-1/2}$ s^{-1})*
$C_{\epsilon 1}$	Used in the source term for ϵ	*(Dimensionless)*
$C_{\epsilon 2}$	Used in the source term for ϵ	*(Dimensionless)*
C_μ	Used in the definition of μ_T	*(Dimensionless)*
d	Stoichiometric coefficient	*(Dimensionless)*
$\overline{1/d}$	Mean strong line parameter	*(cm)*
d_B	Burner nozzle diameter	*(m)*
d_P	Soot particle diameter	*(m)*
d_S	Diameter of sphere / thermocouple bead	*(m)*
D	Diffusion coefficient	*(m^2 s^{-1})*
D_M	Normalised distribution of soot mass concentration	*(Dimensionless)*
D_N	Normalised distribution of soot particle number density	*(Dimensionless)*
e	$\ln e = 1$	*(Dimensionless)*
e	Stoichiometric coefficient	*(Dimensionless)*
E	Total emissive power	*(W m^{-2})*
E	Energy	*(J)*
E_a	Activation energy	*(J kmol^{-1})*
f	Stoichiometric coefficient	*(Dimensionless)*
f	Constant in Tesner soot model	*(s^{-1})*
f_V	Soot volume fraction	*(Dimensionless)*
g	Stoichiometric coefficient	*(Dimensionless)*
g	Constant in Tesner soot model	*(s^{-1})*
g	Gravitational acceleration	*(m s^{-2})*
$\vec{g}$	Gravitational acceleration vector	*(m s^{-2})*
g_0	Constant in Tesner soot model	*(m^3 s^{-1})*
h	Chemical enthalpy	*(J kg^{-1})*
h	Heat transfer coefficient	*(W m^{-2} K^{-1})*
h	Planck's constant	*(J s)*
Δh_f°	Heat of formation at reference temperature	*(J kg^{-1})*

Nomenclature

i	$\sqrt{-1}$	*(Dimensionless)*
I	Intensity	*($W\ m^{-2}\ sr^{-1}$)*
I_0	Initial intensity	*($W\ m^{-2}\ sr^{-1}$)*
$I_{\lambda,b}$	Planck distribution function	*($W\ m^{-2}\ sr^{-1}\ \mu m^{-1}$)*
k	Boltzmann's constant	*($J\ K^{-1}$)*
k	Imaginary component of complex refractive index	*(Dimensionless)*
k	Thermal conductivity	*($W\ m^{-1}\ K^{-1}$)*
k	Kinetic energy of turbulence	*($J\ kg^{-1}$)*
k	Constant used in the conditional oxidation model	*(Dimensionless)*
k	Reaction rate constant	*(Varies)*
k	Surface specific production rate of f_v	*($m\ s^{-1}$)*
l	Soot model constant	*(Dimensionless)*
l	Path length	*(m)*
L	Distance along a ray / Path length	*(m)*
L	Flame length	*(m)*
L_e	Dissipation length scale	*(m)*
m	Soot model constant	*(Dimensionless)*
m	Complex refractive index	*(Dimensionless)*
$\vec{m}$	Mass flux vector	*($kg\ m^{-2}\ s^{-1}$)*
m_P	Mass of individual soot particle	*(kg)*
M	Measurement	*(Dimensionless)*
M	Molar mass	*($kg\ kmol^{-1}$)*
M	Soot mass density	*($kg\ m^{-3}$)*
M_P	Molar mass of incipient soot particle	*($kg\ kmol^{-1}$)*
n	Soot model constant	*(Dimensionless)*
n	Real component of complex refractive index	*(Dimensionless)*
n	Soot nuclei concentration	*(m^{-3})*
N	Soot particle number density	*(m^{-3})*
N_A	Avogadro's number	*($kmol^{-1}$)*
Nu	Nusselt number	*(Dimensionless)*
P	Pressure	*(Pa)*
P	Probability	*(Dimensionless)*
P_0	Constant used in the conditional oxidation model	*(Dimensionless)*

Nomenclature

Pr	Prandtl number	*(Dimensionless)*
$\vec{q}$	Heat flux vector	*($J\,m^{-2}\,s^{-1}$)*
$\dot{Q}$	Volumetric energy source	*($J\,s^{-1}\,m^{-3}$)*
r	Radial coordinate	*(m)*
r	Radius	*(m)*
r_o	Mitchell's burner diameter	*(m)*
R	Mitchell's confining tube radius	*(m)*
R	Universal gas constant	*($J\,K^{-1}\,kmol^{-1}$)*
R	Flame radius	*(m)*
Re	Reynolds number	*(Dimensionless)*
S_ϕ	Volumetric source of ϕ	*(Varies with ϕ)*
$S_{\phi,Therma.}$	Thermophoretic source of ϕ	*(Varies with ϕ)*
$\overline{S/d}$	Mean line strength to spacing parameter	*(cm^{-1})*
t	Time	*(s)*
T	Temperature	*(K)*
T_α	Constant in Moss soot model	*(K)*
T_γ	Constant in Moss soot model	*(K)*
u	Axial velocity component	*($m\,s^{-1}$)*
$\vec{u}$	Velocity vector	*($m\,s^{-1}$)*
U	Density path length	*(m)*
v	Cross stream or radial velocity component	*($m\,s^{-1}$)*
$v_{Thermo.}$	Thermophoretic velocity	*($m\,s^{-1}$)*
V	Volume	*(m^3)*
w	Circumferential velocity component	*($m\,s^{-1}$)*
x	Axial coordinate	*(m)*
x	Shortest distance from flame centre to laser beam	*(m)*
X	Mole fraction	*(Dimensionless)*
X	Optical depth	*(Dimensionless)*
X_R	Heat loss fraction	*(Dimensionless)*
y	Cross stream coordinate	*(m)*
Y	Mass fraction	*(Dimensionless)*

Nomenclature

Greek

α	Size parameter	*(Dimensionless)*
α	Soot nucleation function	*($m^{-3}\ s^{-1}$)*
α	Used in the definition of the Beta-function	*(Dimensionless)*
α_T	Molar ratio	*(Dimensionless)*
β	Used in the definition of the Beta-function	*(Dimensionless)*
β	Soot coagulation function	*($m^3\ kg^{-1/6}\ s^{-1}$)*
β	Shvab-Zeldovich coupling parameter	*(Varies)*
γ	Soot surface growth function	*(Varies with n)*
γ_L	Line half-width	*(cm^{-1})*
δ	Delta function	*(Not Applicable)*
ϵ	Emissivity	*(Dimensionless)*
ϵ	Dissipation rate of turbulence kinetic energy	*($J\ kg^{-1}\ s^{-1}$)*
ζ	Used in viscosity definition	*($m^2\ N^{-1}\ s^{-1}$)*
θ	Circumferential coordinate	*(m)*
κ	Absorption / extinction coefficient	*(m^{-1})*
λ	Mean free path	*(m)*
λ	Wavelength	*(m)*
λ	Thermal conductivity	*($W\ m^{-1}\ K^{-1}$)*
μ	Dynamic viscosity	*($N\ s\ m^{-2}$)*
ν	Frequency	*(s^{-2})*
ξ	Mixture fraction	*(Dimensionless)*
π	$\cos\pi = -1$	*(Dimensionless)*
ρ	Density	*($kg\ m^{-3}$)*
σ	Molecular diameter	*(m)*
σ	Prandtl / Schmidt number	*(Dimensionless)*
σ	Stefan - Boltzmann constant	*($W\ m^{-2}\ K^{-4}$)*
τ	Transmittivity	*(Dimensionless)*
τ	Deviatoric stress tensor	*($kg\ m^{-1}\ s^{-2}$)*
ϕ	General transported variable	*(Varies)*
ϕ	Stoichiometric mass ratio of oxidant to fuel	*(Dimensionless)*
ϕ_{ij}	Used in mixture viscosity definition	*(Dimensionless)*

Nomenclature

ϕ_M	Soot mass fraction	*(Dimensionless)*
ϕ_N	Number of soot particles per unit mass of gas	*(kmol kg^{-1})*
Φ	Equivalence ratio	*(Dimensionless)*
χ	Scalar dissipation rate	*(s^{-1})*
ω	Soot oxidation rate	*(kg m^{-2} s^{-1})*
ω	Wavenumber	*(cm^{-1})*
ω'	Soot oxidation function	*($kg^{1/3}$ s^{-1})*
Ω_v	Collision integral	*(Dimensionless)*

Subscripts

Abs.	Absorption
Air	Air
Avg.	Average
b	Blackbody
c	Critical property
C	Atomic carbon
CG	Curtis-Godson average
C_2H_2	Ethyne
CH_4	Methane
CO_2	Carbon dioxide
Ext.	Extinction
F	Flame
Fuel	Fuel
Gas	Surrounding gas
h	Enthalpy
H	Atomic hydrogen
H	Homogeneous
HC	Hydrocarbon
H_2O	Water (vapour)
i	Chemical species *i*
j	Chemical species *j*
m / Mix.	Property of gas mixture
M	Soot mass density
N	Soot number density
N	Nozzle
O	Atomic oxygen
OH	Hydroxyl radical
Oxidant	Oxidant
r	Reduced property
S	At the surface of
S	Surroundings

Nomenclature

Soot	Soot
T	Total
T	Turbulent
Thermo.	Thermocouple
Wall	Solid flame confining boundary
Win.	Window
λ	At wavelength λ
ϕ	General transported variable
ω	At wavenumber ω
∞	At infinity

Acronyms and Abbreviations

A	Air
A	Aromatic compounds
CFD	Computational fluid dynamics
F	Fuel
GCMS	Gas chromatography-mass spectrometry
LIF	Laser induced fluorescence
MIN	Minimum
O	Oxidant
P	Reaction Products
PAH	Poly-aromatic hydrocarbon
PDF	Probability distribution function
S	Soot
X	Aliphatic compounds

Chapter 1 - Introduction

Turbulent diffusion flames may be found in many different situations, ranging from the flames resulting from accidental fuel releases from pipelines and process vessels to those employed in furnaces, gas turbines and diesel engines.

Two of the principal hazards from an accidental fire are from the thermal radiation, which is mainly emitted from soot particles within the flame, and from the liberated smoke, which consists of product gases, carbon particulates and condensed hydrocarbon droplets. Thermal radiation is a major factor in determining the rate of fire spread and in causing damage to surrounding structures. More direct danger comes from the effect of this radiation on personnel, measurements suggest that a heat flux of 4 kW m^{-2} will cause first degree burns in less than one minute. Soot emitted from flames in the smoke presents two hazards. First, soot compromises visibility which may adversely affect survivability by hiding escape routes. Secondly, soot itself is injurious to health - if inhaled. This is because soot particles may be drawn deep into the lungs, due to their small (less than 1 μm) size.

In the design of practical devices consideration must be made both to the level of particulate carbon emitted, and to the heat transferred to the flame's surroundings. Particulate carbon represents combustion inefficiency and may be legislated against. The World Health Organisation is now stating that no level of particulate carbon may be termed safe. Heat transferred to the surroundings of the flame may have a detrimental effect on the life of the device, eg. gas turbine combustor liners, or may affect the efficiency of the device, eg. furnaces.

Computational models for prediction of flame behaviour have obvious advantages over bespoke experimental studies. However, while the calculation of general turbulent flame structure is now well within the capabilities of computational fluid dynamics (CFD) the additional problems of soot production and flame radiation are not adequately resolved for entirely confident prediction.

1 - Introduction

In a turbulent diffusion flame the fuel and oxidant are not initially mixed, but are brought into contact by the processes of turbulent mixing and molecular diffusion. Large quantities of soot may be produced within diffusion flames; the soot forming as a result of fuel pyrolysis in the high temperature, fuel rich regions. The processes of soot formation and oxidation are highly temperature dependent and soot is usually the dominant radiating species in hydrocarbon fuelled flames. Therefore, an intimate coupling exists between soot production and radiative heat transfer from the flame. However, despite this coupling it has been customary to decouple these effects, either by prescribing the degree of heat loss, determining the soot properties from non-coupled balance equations or by prescribing the soot concentration and post-processing the computation of the radiative flux. This work attempts to develop a more comprehensive solution of the soot and radiation from a jet diffusion flame by coupling the processes of radiative heat loss, from the gaseous species and the soot, with the rate of soot production.

Methane has been selected as the fuel for this study which, due to the central position it occupies (as natural gas) in the energy field, satisfies concerns in relation to both utilisation and to transmission and storage. Additionally, methane is a convenient fuel as the chemistry of its combustion is well known. There have been few studies, however, on the sooting properties of methane and no soot measurements in turbulent methane flames. This is due to the difficulty in measuring the low levels of soot found in laboratory scale, atmospheric, turbulent methane flames. At a large scale, methane fires would soot heavily; mainly due to the increased time scales under high temperature, fuel rich conditions. However, measurements at such scales - in both pool fires and jet flames - focus on global properties and provide limited information for model development. This work seeks to emulate a larger scale methane flame in the laboratory by running the flame at elevated pressure. At 3 atm the peak soot concentration is increased by approximately a factor of 10 (see the appendix) and the heat loss from the flame is approximately doubled, when compared to a flame of the same fuel mass flow running at atmospheric pressure.

The work detailed in this thesis, therefore, covers four main areas.

Chapter 3 describes the experimental study of methane fuelled turbulent jet diffusion flames, at atmospheric and elevated pressure. This was conducted to establish property maps for subsequent model development and validation. Measurements of mean mixture fraction, mean temperature, mean soot volume fraction, and mean and instantaneous

spectrally resolved, path integrated radiation intensity are presented. Mean mixture fraction measurements were made by gas sampling, using a quartz probe, with the gas sample being passed to a mass spectrometer for analysis. Mean temperature measurements were taken with a Pt / Pt-Rh fine wire thermocouple. These temperatures were corrected for the radiative loss from the thermocouple bead. Mean soot volume fractions were determined by laser absorption tomography. For the radiation intensity measurements a Rees Instruments scanning monochromator was used operating in the range 600 - 5000 nm.

In chapter 4 the soot model to be employed in the turbulent flame calculations is developed. Soot formation chemistry is known to be complex, and the exact sequences of chemical reactions leading to soot remain uncertain. It is, however, now generally agreed that there are two distinct steps in soot formation. The first of these steps is the nucleation of an incipient particle. In the second stage this particle undergoes growth by heterogeneous reactions at its surface. Soot particles may also coagulate and agglomerate and then ultimately oxidise. Soot models for use in engineering applications seek to capture these processes without attempting to include the detailed chemistry of the process. Two quite distinct models have been developed for use with methane - Syed (1990) and Lindstedt (1991). However, these give comparatively poor predictions when compared with the turbulent flame experimental data reported here and this has necessitated the development of a new soot model giving good results at the pressures of interest. Soot model development was carried out by performing detailed laminar flame simulations using the parabolic CFD code GENMIX, Spalding (1977). The conserved scalar approach is used for chemical source term closure. However, in this case scalars are not functions of mixture fraction only but of mixture fraction and enthalpy. An enthalpy transport equation is solved which incorporates a radiative loss source term, including contributions from the main radiating gases and the soot. This couples the soot production rate to the heat loss from the flame. The results of the simulations are compared with previous experimental work on laminar methane flames.

Chapter 5 describes the modelling of the 1 and 3 atm turbulent methane jet flames. The soot model developed in chapter 4 is applied to a scalar field prediction obtained from GENMIX. The flamelet combustion model is used. However, in order to accommodate the non-adiabatic nature of the flames the model employs multiple flamelets, varying in their degree of radiative heat loss. The most appropriate flamelet at a particular location in the flame is chosen on the basis of the local radiative heat loss. This radiative loss is

determined from the mean enthalpy calculated from an enthalpy balance equation, which includes a radiative loss source term similar to that in the laminar flame. In laminar flames the regions of soot growth and soot burnout are reasonably well segregated in physical space. However, in turbulent flames this is not the case and any particular spatial location may see both soot growth and soot oxidation in sequence. The important factor in determining the rate of soot oxidation is the co-existence of soot and oxidising species. The assumption used for this co-existence has a very large effect on the soot production in turbulent flames and in this chapter four oxidation strategies are explored. The scalar fields given by GENMIX are compared with the experimental data detailed in the appendix.

Radiation predictions employing the mean scalar fields obtained from GENMIX are described in chapter 6. The radiative properties model RADCAL, Grosshandler (1979), is used in detailed line of sight calculations. These predictions are compared with the data presented in the appendix.

Of the remaining two chapters, chapter 2 reviews the salient literature on past laminar and turbulent methane flame experiments, laminar and turbulent flame modelling, soot formation and radiation modelling. Chapter 7 concludes the thesis by summarising the work, identifying the important conclusions and making some recommendations for further study.

determined from the mean enthalpy calculated from an enthalpy balance equation, which includes a radiative loss source term similar to that in the laminar flame. In laminar flames the regions of soot growth and soot burnout are reasonably well segregated in physical space. However, in turbulent flames this is not the case and any particular spatial location may see both soot growth and soot oxidation in sequence. The important factor in determining the rate of soot oxidation is the co-existence of soot and oxidising species. The assumption used for this co-existence has a very large effect on the soot production in turbulent flames and in this chapter four oxidation strategies are explored. The scalar fields given by GENMIX are compared with the experimental data detailed in the appendix.

Radiation predictions employing the mean scalar fields obtained from GENMIX are described in chapter 6. The radiative properties model RADCAL, Grosshandler (1979), is used in detailed line of sight calculations. These predictions are compared with the data presented in the appendix.

Of the remaining two chapters, chapter 2 reviews the salient literature on past laminar and turbulent methane flame experiments, laminar and turbulent flame modelling, soot formation and radiation modelling. Chapter 7 concludes the thesis by summarising the work, identifying the important conclusions and making some recommendations for further study.

Chapter 2 - Soot and Radiation from Diffusion Flames

2.1 Introduction

The aim of this study is to develop models, of the physical and chemical processes occurring in turbulent jet diffusion flames, for inclusion in computational fluid dynamics (CFD) calculations. Ultimately these CFD calculations will be used for the prediction of flame radiative emission. This work concentrates on the hydrocarbon methane as a fuel source, although the methodology developed is equally applicable to all hydrocarbon fuels. The primary source of flame radiation in most hydrocarbon fuelled flames is soot, but for methane flames the soot radiation is nearly balanced by that from the main gaseous radiators: methane, carbon dioxide and water.

The sequence of chemical reactions leading to soot formation is very complex and these reaction pathways remain uncertain. However, regardless of the exact detail the complexity of the postulated reaction schemes generally precludes their use in turbulent flame calculations. Therefore, simplified models of soot formation are required that capture enough of the actual physical processes to allow their use over a large range of flame conditions. Such models have been developed and are semi-empirical and usually fuel specific. The more advanced models are 'calibrated' by their application to laminar flame calculations with comparisons made to experimental sooting data.

Flame radiation is an extremely complex phenomena. The radiative energy loss from a flame may be evaluated by calculating a complex integral over all paths that pass through the flame and over all wavelengths of flame emission. For turbulent flames this is complicated by the interaction of the emission / absorption of radiation with the turbulent fluctuations. Soot particles emit continuum radiation but gaseous species only radiate at certain wavelengths according to changes in the internal energy levels of the gas molecules. Joint transitions in the vibrational and rotational energy levels for the

gas molecules gives rise to bands of radiative emission. The form of each band changes with the temperature and the pressure of the gas. Models have been developed that describe the location and strength of these gaseous emission bands, but the complexity of these models renders them impractical for inclusion in a CFD flame calculation. Simplifications may be introduced, such as ignoring the self absorption of radiation in the flame and introducing wavelength integrated emission coefficients, which allow radiative heat loss to be explicitly included in a CFD calculation of a flame. Detailed spectrally resolved calculations of the flame radiative emission may be evaluated as a post-process.

Experimental data for methane turbulent jet diffusion flames is needed for model validation. However, the database detailing the properties of such flames is small when compared with flames fuelled by other hydrocarbons - eg. ethene and ethyne. Also soot properties, vitally important for soot model validation, have not previously been measured. This database is reviewed in section 2.3 but the omission of soot measurements in these studies makes an experimental investigation of turbulent methane diffusion flames a necessary component of this work.

The approach to flame modelling adopted in this study follows a progression from the modelling of laminar methane diffusion flames, for soot model development, through to the modelling of the turbulent methane diffusion flames investigated experimentally. The experimental database on laminar methane diffusion flames is quite extensive. Therefore, the literature is consulted to provide a suitable laminar flame for the soot model development.

The subsequent sections of this chapter provide the necessary background to each component of the work by reviewing the experimental databases available on laminar and turbulent methane diffusion flames, laminar flame modelling and turbulent flame modelling, the chemistry of soot formation and soot models, and radiation modelling.

2.2 Experimental Studies of Laminar Methane Diffusion Flames

One of the most extensively studied laminar methane flames is the Mitchell et al. (1980a) flame. This is an axisymmetric flame consisting of an inner circular fuel jet with an outer annulus through which air co-flows. A perforated brass disc serves as the burner plate. The burner assembly is shielded from disturbances by a Pyrex tube of inner radius 25.4 mm. The radius of the fuel jet is 6.35 mm and the radius of the annulus is 25.4 mm. Mitchell et al. (1980a) report measurements of temperature, major species concentrations and axial velocity from this flame. The temperature measurements were performed using a fine wire thermocouple which was corrected for radiative heat loss from the junction bead and conduction along the support wires. Laser Doppler velocimetry was used to take the axial velocity measurements. Mitchell et al. (1980a) report radial profile measurements at three heights above the burner exit plane: 12, 24, and 50 mm. Mitchell et al. (1980b) extend this dataset by reporting measurements of nitrogen oxide, cyanide and amine concentrations at 12, 18, 24, and 50 mm above the burner exit plane.

This flame has been further studied by Prado et al. (1984), Garo et al. (1986), and Garo et al. (1990). A replica of the Mitchell et al. (1980a) burner is used in these studies. Prado et al. (1984) report measurements of poly-aromatic hydrocarbon (PAH) concentrations, measured using gas chromatography-mass spectrometry (GCMS). Corresponding measurements of the intensity from laser induced fluorescence of the PAH are measured and these are correlated with the concentrations measured by GCMS. Measurements of the scattered intensity at 514.5 nm from soot particles are also reported. Garo et al. (1986) conducted a study of the formation and destruction of soot particles in the Mitchell et al. (1980a) laminar flame. A laser light scattering / extinction technique was used to determine local soot volume fractions, soot particle number densities, and soot particle diameters. Two steps in the formation stage of the soot particles were determined. Firstly soot particles nucleate, these particles then simultaneously coagulate / aggregate and undergo growth by addition of gaseous species to their surface. For the destruction phase three steps were observed. Firstly, the mean particle diameter increases while the number density decreases. This may be due to a decrease in the surface growth reaction rate (and / or an increase in the oxidation reaction rate) while the particles are still agglomerating. Alternatively, this may be explained by the disappearance of the smallest soot particles,

pushing the mean diameter to higher values. The second step consists of a decrease in the mean diameter but an increase in the particle number density. This behaviour has been associated with the break up of the soot particle aggregates. The last step shows a decrease in both the mean particle diameter and the particle number density. Soot volume fraction measurements were made by laser extinction with subsequent Abel inversion of the extinction profiles to obtain the radial profiles of soot volume fraction. Radial and axial profiles of soot volume fraction are reported. It is noted that absorption by PAH, especially low in the flame, will contribute to the extinction of the laser beam. No particulates were detected on the centreline by probe sampling below a height of 38 mm above the burner exit plane. This PAH absorption of the laser beam creates an uncertainty in the measured value of the soot volume fraction. This uncertainty is expected to be greatest on the centreline, where the PAH concentration will be high and the additional uncertainty created by the Abel inversion will be at its maximum. The soot burnout rate was estimated, and a maximal value of approximately 10^{-3} g cm^{-2} s^{-1} was obtained. This value compares well with the Puri et al. (1994) expression used later in this work (see sub-section 4.3.4). Garo et al. (1990) attempted to elucidate the respective roles of oxidant species in the oxidation of soot particles. The experimentally determined surface specific oxidation rate along the symmetric axis of the flame was compared with the expression given by Nagle and Strickland-Constable (1962) for the oxidation of carbon by molecular oxygen. The experimentally observed oxidation rate is over two orders of magnitude greater than that given by Nagle and Strickland-Constable (1962). This leads to the conclusion that the OH radical has a dominant role in the oxidation of soot. Laser induced fluorescence (LIF) measurements of the OH concentrations were made at several heights above the burner's exit. These concentrations were compared with those calculated using a partial equilibrium assumption. The agreement is to within an order of magnitude.

Syed (1990) conducted a study of a methane / air laminar diffusion flame burning on a Wolfhard-Parker three slot burner. The planar configuration of this flame admits considerable simplification in the experimental techniques and interpretation required. The central fuel slot is 6 mm wide by 47 mm long, on each side of this slot is an air slot 9 mm wide by 47 mm long. This burner assembly is surrounded by a secondary air duct, which has dimensions of 90 mm by 90 mm. Syed (1990) reports measurements of mixture fraction, temperature, and soot volume fraction at several heights along traverses across the

flame's width, perpendicular to major axis of the slots. The mixture fraction was measured by quartz micro-probe sampling, with the gas sample being passed to a calibrated mass spectrometer for analysis. A fine wire thermocouple was used for the measurement of temperature. The soot volume fraction was measured with a laser extinction technique. However, in contrast to the study of Garo et al. (1986) no tomographic inversion of the extinction data was necessary.

Smyth et al. (1985) present a very comprehensive set of measurements performed on a methane / air diffusion flame burning on a Wolfhard-Parker type three slot burner. The study included measurements of temperature; vertical and horizontal components of velocity; absolúte concentrations of methane, oxygen, nitrogen, carbon dioxide, water, hydrogen, acetylene, butadiene, and toluene; as well as relative concentrations of OH. In addition laser induced ionization was used to determine the region where the inception of particulate soot occurs. The earliest soot particles are detected at the high temperature side of a region that is rich in aromatic and other unsaturated hydrocarbons. The major species (CH_4, O_2, H_2, CO_2, and H_2O) are found to correlate well with the local equivalence ratio. However, intermediate species and the soot particles are not found to correlate with the local equivalence ratio. Norton et al. (1993) complement this dataset by presenting concentrations of five major radicals in the same flame. These radicals being OH, H, O, CH_3, and CH.

In terms of the species investigated the Smyth et al. (1985) / Norton et al. (1993) study undoubtedly represents the most complete investigation of a laminar methane diffusion flame. However, the Mitchell et al. (1980a) and the Syed (1990) laminar methane flames are more complete in terms of the spatial mapping of the flame properties. Hence, these flames are selected as the basis for the laminar flame modelling presented in chapter 4.

2.3 Experimental Studies of Turbulent Methane Diffusion Flames

Successful model development needs experimental data for validation purposes. However, experimental studies are expensive and time consuming. Therefore, there are obvious advantages to using existing flame databases or only augmenting existing databases to provide measurements not previously recorded. Turbulent jet methane (or natural gas) flames have been studied although the database available is not extensive when compared to that of higher hydrocarbons.

Hassan et al. (1980), Moneib (1980), and El-Banhawy et al. (1983) present data for natural gas fuelled, open, turbulent jet diffusion flames. The vertically mounted burner was circular with an exit diameter of 7.74 mm. Surrounding this was an annulus through which hydrogen flowed to stabilise the flame at the burner's rim. Mean and fluctuating temperature, mean concentrations of O_2, CO, and CO_2, mean and fluctuating axial velocities, and unburned hydrocarbon concentrations are reported at Reynolds numbers of 15 000 and 30 000.

In a series of papers Jeng et al. (1982), Jeng and Faeth (1984), and Jeng et al. (1984) present a very comprehensive dataset for natural gas fuelled, open, turbulent jet diffusion flames. The flames were injected upwards, vertically, from a water cooled burner with an exit diameter of 5 mm. A screened enclosure was used to reduce disturbances from draughts. The flames were attached at the nozzle exit by a small co-flow of hydrogen (less than 2 % of the fuel mass flow). Three flames were investigated with Reynolds numbers of 2 920, 5 850, and 11 700. In Jeng et al. (1982) mean temperatures, measured with fine wire thermocouples, and mean and fluctuating velocity measurements, measured using laser Doppler anemometry, are reported. Jeng and Faeth (1984) extend this dataset by reporting measurements of mean species concentrations and turbulence quantities. Mean concentrations of CH_4, N_2, O_2, CO_2, H_2O, CO, and H_2 are presented. Radial variation of the Reynolds stresses are also reported, together with the radial variation of the three fluctuating velocity components. Mean, spectrally resolved, radiation intensity measurements are described by Jeng et al. (1984). The radiation intensity was measured for radial paths through the flame axis. The wavelength range of the measurements was from 1.5 to 5.5 μm. A notable feature of this dataset is that the flames are reported as being

essentially non-luminous and indeed the spectra illustrated in Jeng et al. (1984) show no contribution from continuum radiation. This is in contrast to the spectra recorded in this study, from (at 1 atm) a very similar flame - cf. chapter 6 or appendix.

Despite its advantages, from a modelling perspective, of an idealised geometry and easily defined boundary conditions, the jet flame is not the only configuration to have been investigated experimentally. Crauford (1984), for example, presents data obtained from a buoyant methane fire. The burner used for this study consisted of a 25 cm diameter porous plate. Crauford (1984) reports spatially and temporally resolved velocity and temperature. Later, Charnley (1986) reports measurements, of instantaneous integrated intensity and spectrally resolved mean intensity along lines of sight, performed on the same fire.

The clear omission from all of these studies is the lack of soot measurements. Soot measurement in atmospheric turbulent methane flames presents a particular problem because of the low sooting propensity of methane. However, soot measurements are vitally important for the development of sooting models suitable for use in turbulent flame calculations. Hence, soot measurements form an important part of this investigation. The flame soot levels may be increased by raising the flame pressure. Unfortunately, the relatively large physical size of the burners used in the studies above precludes the extension of any existing database, because of the confining dimensions of the high pressure flame rig.

2.4 Modelling Laminar Flames

This section does not deal with the conservation equations needed to describe the vector and scalar fields of a flame. These are covered in section 4.2. The subject of molecular transport of species and energy is also not included. Section 4.2 and sub-section 4.3.2 briefly discuss this subject, but the reader is referred to Reid et al. (1977) for a complete description. This section instead concentrates on describing the different representations of laminar flame chemistry that may be employed.

The first quantitative description of a diffusion flame was provided by Burke and Schumann (1928). Burke and Schumann (1928) considered axi-symmetric, co-flowing laminar flames. A number of assumptions were made to ease the calculation, these were

i) At the level of the burner exit plane the velocities of the fuel and air are constant and equal.
ii) The velocity of the fuel and air up the duct, in the flame region, is the same as the velocity at the port.
iii) The product of the density and the mass diffusion coefficient is a constant.
iv) Diffusion in the axial direction is negligible compared to that in the radial.
v) The radial velocity component is zero. Hence, mixing is by diffusion only.
vi) The reaction rate is infinitely fast and therefore reaction takes place at the infinitesimally thin stoichiometric plane only.

The reaction scheme was very simple and is shown in the following equation

$$\phi O + F \rightarrow (1 + \phi) P \tag{2.1}$$

where O represents the oxidant, F the fuel, P the products of combustion, and ϕ is the stoichiometric mass ratio of oxidant to fuel. Under the conditions above, a partial differential equation describing the mass fraction distribution may be derived

$$\frac{u}{D}\frac{\partial \beta}{\partial x} - \frac{1}{r}\frac{\partial}{\partial r}\left(r \frac{\partial \beta}{\partial r} \right) = 0 \tag{2.2}$$

where the Shvab-Zeldovich coupling parameter $\beta = Y_O - \phi Y_F$, Y_i is the mass fraction of

i, u is the axial velocity, D the diffusion coefficient, and x and r the axial and radial coordinates respectively. This partial differential equation may be solved analytically, subject to the boundary conditions of

$$\beta = -\phi [Y_F]_{x=0} \qquad \text{at } x = 0,\ 0 \le r \le r_B$$

$$\beta = [Y_O]_{x=0} \qquad \text{at } x = 0,\ r_B < r \le r_S \qquad (2.3 - 5)$$

$$\frac{\partial \beta}{\partial r} = 0 \qquad \text{at } r = 0 \text{ and } r = r_S,\ x > 0$$

where r_B is the radius of the fuel jet and r_S is the external radius of the air annulus. The location of the $\beta = 0$ contour defines the position of the reaction plane - the 'flame-sheet'. Despite the large number of assumptions, Burke and Schumann (1928) achieved results in good agreement with experiment in terms of the flame shapes and heights.

The Shvab-Zeldovich coupling parameter β is a conserved scalar, that is a variable which is unchanged by chemical reactions. The variable β may be normalised such that it takes a value of zero in the air stream and unity in the fuel stream

$$\xi = \frac{\beta - \beta_A}{\beta_F - \beta_A} \qquad (2.6)$$

where the subscripts A and F denote the values of β in the air and fuel streams respectively. This normalised variable is the mixture fraction, which is also a conserved scalar. At the reaction plane the mass fractions of both the oxidant and the fuel drop to zero. Hence, the mass fractions of the fuel and oxidant outside this reaction plane may be written in terms of the mixture fraction as

in the fuel rich region

$$Y_F = \xi \frac{\beta_A - \beta_F}{\phi} - \frac{\beta_A}{\phi} \text{ and } Y_O = 0 \qquad (2.7)$$

and in the fuel lean region

$$Y_O = \beta_A - \xi(\beta_F - \beta_A) \text{ and } Y_F = 0 \qquad (2.8)$$

Mitchell et al. (1980a) used the Burke and Schumann flame-sheet concept to model an axi-symmetric, co-flowing laminar methane / air flame. However, the Burke and Schumann (1928) model was extended to include buoyancy and variable thermodynamic and transport properties. A numerical solution method was used to solve transport equations for axial and radial momentum, species mass fractions, and energy. Very good agreement with experiment was achieved for the temperature and the mass fractions of the major species, these species being CH_4, O_2, CO_2, H_2O, and N_2. The simple global reaction scheme does not allow for the prediction of the minor species or the reaction intermediates.

Bilger (1976) showed that for any diffusion flame the instantaneous thermo-chemical state of the mixture may be described by functions of a single conserved scalar (such as the mixture fraction), under the assumptions of infinite reaction rate, equal diffusion coefficients for all the species, unity Lewis number, and adiabatic conditions. Bilger (1977) showed that experimental data for real diffusion flame properties also appeared to be unique functions of a conserved scalar, within the limits of experimental accuracy. This may be exploited within the context of a laminar flame calculation. The transport equations for species and enthalpy may be replaced by a single equation for the conserved scalar. This technique admits the effects of finite rate reaction kinetics, as these effects will be embodied in the state relationships (the relationships between the dependent scalars and the conserved scalar). However, the state relationships are not unique for a given fuel / oxidant combination but are also a function of the hydrodynamic strain rate. However, for most laminar flame configurations the influence of strain is negligible and measurements of scalar properties made in one flame will certainly be applicable for the calculation of another flame of similar geometry. Syed (1990) used this technique to model a planar laminar flame of methane / air. Experimentally derived relationships between the chemistry dependent scalars and the mixture fraction were employed. Syed (1990) only reports temperature comparisons, between the modelled flame and experimental data, and the agreement shown is excellent. State relationships may also be determined from laminar flame codes. Such codes tend to simplify the fluid dynamics but incorporate detailed chemical reaction schemes - cf. Warnatz (1981).

More generality may be gained by the introduction of reduced chemical mechanisms. Such reduced mechanisms model the full reaction scheme by a limited number of finite rate reactions. Jones and Lindstedt (1988) present a reduced scheme for hydrocarbon combustion. The mechanism consists of four reaction steps

$$C_nH_{2n+2} + \frac{n}{2}O_2 \rightarrow nCO + (n+1)H_2$$

$$C_nH_{2n+2} + nH_2O \rightarrow nCO + (2n+1)H_2 \qquad (2.9\text{-}12)$$

$$H_2 + \frac{1}{2}O_2 \rightleftharpoons H_2O$$

$$CO + H_2O \rightleftharpoons CO_2 + H_2$$

and may be used for alkane hydrocarbons up to butane. Jones and Lindstedt (1988) modelled the Mitchell et al. (1980a) flame using this scheme. Transport equations were solved numerically for the mass fractions of the species involved, the enthalpy, and the axial velocity, as well as the equation of continuity. Radiative loss from the flame was ignored. Comparisons with radial experimental data are presented at the 50 mm axial station. Excellent agreement is obtained for the species profiles of CO_2, CO, H_2, and O_2. The peak H_2O level is slightly under-predicted. The radial profiles of axial velocity and temperature are also presented at this axial station. Again, these profiles show excellent agreement with the experimental data. Reduced chemical mechanisms do not, however, provide information about minor flame species or intermediates.

Smooke et al. (1989) also present a model of the Mitchell et al. (1980a) flame. A detailed reaction scheme was employed consisting of fifteen species, involved in forty-two reactions. Detailed transport coefficients were also used. The fully elliptic problem was formulated, by considering axial as well as radial diffusion. Mitchell et al. (1980a) present experimental radial profiles of the major species and temperature at heights of 12, 24, and 50 mm above the exit plane of the burner. Smooke et al. (1989) compare their model predictions with experiment at the 12 and 24 mm axial stations. Experimental temperature profiles are reasonably well produced, although at 24 mm the temperature peak lies outside the radius of the experimental peak by approximately 1.5 mm. The methane mole fractions

are poorly reproduced at both heights, with an over-prediction on the centreline by a factor of 2 at the 12 mm height and an over-prediction by a factor of 3 at the 24 mm height. These over-predictions of parent fuel concentration probably result not from the chemistry model used but from the choice of boundary conditions at the burner inlet. At this position the mole fraction of fuel in the fuel stream is assigned a value of unity as is the air in the air stream. This does not take into account any back-diffusion into the burner itself, particularly of air into the lower velocity fuel stream which would tend to lower the initial centreline fuel concentration in this plane.

None of the models presented above has included flame radiation explicitly. A certain degree of radiative loss is implicitly included in the laminar flame modelling of Syed (1990) by the use of experimentally derived state relationships. Kaplan et al. (1994) present a time-dependent model of an ethylene / air diffusion flame. The flame chemistry is represented by a single step, finite rate reaction. The effect of radiative energy transport appears explicitly in the energy equation as the divergence of the radiative heat flux. The flame is not considered as optically thin and the radiative transfer equation is solved using the discrete-ordinate approximation. Radiation from carbon dioxide, water, and soot is considered. The soot concentration is determined from the two parameter model of Moss et al. (1988). The laminar flame experimentally investigated by Gore and Faeth (1986) is used as the basis to benchmark the flame model. Unfortunately, detailed comparisons of the flame structure are not presented. Calculated flame data as a function of the equivalence ratio is reported. This compares well with the experimental data of Gore and Faeth (1986).

Some soot formation models incorporate minor species and / or chemical intermediates into their expressions for soot nucleation, growth, or oxidation - see section 2.6.2. Of the approaches discussed above, only the 'flamelet' model or the use of a detailed chemical simulation would provide such information.

2.5 Modelling Turbulent Flames

Section 2.4 illustrated the problems associated with modelling combustion chemistry in a laminar flow situation. In turbulent flows these problems are compounded by the turbulence. The instantaneous balance equation for the fuel species may be written as

$$\frac{\partial(Y_F \rho)}{\partial t} + \nabla\cdot(Y_F \rho \vec{u} - \rho D \nabla Y_F) = S_F \qquad (2.13)$$

where S_F represents the volumetric production rate of the fuel species. For the sake of simplicity the reaction between the fuel and the oxidant is assumed to take the form

$$\phi O + F \xrightarrow{k} (1 + \phi) P \qquad (2.14)$$

where the rate constant (k) is assumed to take the Arrhenius form

$$k = A\, e^{-\frac{E_a}{RT}} \qquad (2.15)$$

where A is a constant and E_a is the activation energy for the reaction. Hence, the volumetric production rate of the fuel species may be written as

$$S_F = -k \rho^2 Y_F Y_O \qquad (2.16)$$

Time-dependent calculations of the turbulent reacting flowfield may be performed. Kaplan et al. (1994) report time-dependent calculations for an unsteady ethylene / air jet flame. The chemical reaction is represented by a single global reaction similar to that above. The time-dependent solution of the species transport equations allows the chemical source terms to be represented exactly. The flame modelled by Kaplan et al. (1994) is an axi-symmetric (two dimensional) jet flame. Despite this simple geometry, the calculation for this flame takes 7 hours of CPU time on a Cray Y-MP.

Clearly, for situations of practical interest, where the geometry is more complex than that of the idealised jet flame, time-dependent calculations are not feasible. However, most flows in practice show behaviour that is either statistically stationary or varies over a time

period that is long compared to the time scales of the turbulent fluctuations. Hence, balance equations of the mean variables may be formulated which describe these systems. The removal of the time dependence greatly eases the solution of such equations. The balance equations of the mean variables are formulated by decomposing the dependent variables into a Favre mean and fluctuating component and ensemble averaging - see section 5.2. However, for the chemical reaction term (S_F) this introduces correlations which may not be modelled. The remainder of this section illustrates the methods which may be used to close this source term.

The simplest form of closure is achieved by replacing the instantaneous values of the scalar variables with their averaged counterparts. The interaction between the combustion chemistry and the turbulence is ignored entirely. Moss (1995) illustrates the effect of neglecting the turbulent fluctuations by considering the chemical reaction rate constant (k). Ignoring the turbulent fluctuations the rate constant becomes

$$k(\bar{T}) = A\,e^{-E_a/R\bar{T}} \tag{2.17}$$

This is an approximation to the true value $\overline{k(T)}$. For evaluation of the correct mean the statistics of the temperature are required. Moss (1995) considers the case where the temperature may take one of two equally probable values. Hence, the true mean value of the reaction rate constant is given by

$$\overline{k(T)} = \frac{1}{2}(k(T_1) + k(T_2)) \tag{2.18}$$

The corresponding mean temperature is

$$\bar{T} = \frac{1}{2}(T_1 + T_2) \tag{2.19}$$

Taking a representative value of E_a as 170 MJ kmol^{-1}, and 500 K and 2000 K for T_1 and T_2 respectively (corresponding to typical reactant and product temperatures). The ratio of the modelled mean reaction rate to the true mean is

$$k(\bar{T}) / \overline{k(T)} \approx 5\times10^{-3} \tag{2.20}$$

Clearly, the use of mean scalar values to evaluate reaction rate source terms leads to a profound under-prediction of the reaction rates.

Magnussen and Hjertager (1976) suggest a reaction model, suitable for use in premixed and diffusion flames, based on the Spalding (1971) eddy break up model. Under the assumption of fast chemistry, it may be assumed that the reaction rate will be determined by the mixing of the fuel and oxidant eddies at the molecular level. This small scale mixing is described by the dissipation rate of the eddies. The mean reaction rate is given by

$$\bar{S}_F = A\frac{\epsilon}{k}\mathrm{MIN}\left(\overline{\rho Y_F},\ \frac{\overline{\rho Y_O}}{\phi},\ B\frac{\overline{\rho Y_P}}{1+\phi}\right) \qquad (2.21)$$

where A and B are constants, ϵ is the dissipation rate of the turbulence kinetic energy, k is the turbulence kinetic energy, and MIN indicates that the smallest of the terms in the brackets is used to evaluate the reaction rate. Magnussen and Hjertager (1976) apply this combustion reaction rate to the modelling of turbulent premixed and diffusion flames. The agreement achieved with experiment is generally good for the mean temperature, velocity, and major species profiles. However, this model completely ignores the influence of the finite rate flame chemistry and therefore may not be used for the prediction of intermediate species.

It was discussed in section 2.4 that Bilger (1976) showed that for any diffusion flame the instantaneous thermo-chemical state of the mixture may be described by functions of the mixture fraction (a conserved scalar), under the assumptions of infinite reaction rate, equal diffusion coefficients for all the species, unity Lewis number, and adiabatic conditions. This applies for all diffusion flames, laminar or turbulent, with chemistry of arbitrary complexity, as long as the reaction rates may be assumed to be infinitely fast. Hence, the flame structure in conserved scalar space may determined from a flamesheet or equilibrium calculation; where the reactant mixture, corresponding to a particular value of the mixture fraction at the inlet conditions of pressure and temperature, is allowed to reach equilibrium. However, for this to be exploited within the context of a turbulent flame calculation the spatial distribution of the conserved scalar and its statistics must be known. This has led to the development of presumed probability density function (PDF) methods. A general form for the conserved scalar PDF is assumed. The exact form of this PDF at each spatial

location is determined from a limited number of moments obtained from solution of their respective balance equations. The normalised Beta function is commonly used to describe the statistics of the mixture fraction. This function has the form

$$P(\xi) = \frac{\xi^{\alpha-1}(1-\xi)^{\beta-1}}{\int_0^1 \xi^{\alpha-1}(1-\xi)^{\beta-1} d\xi} \qquad (2.22)$$

the coefficients α and β are functions of the mixture fraction mean and its variance. The mixture fraction mean and variance are obtained from solution of their respective balance equations - see sub-section 5.3.2. Knowledge of the mixture fraction statistics allows mean scalar properties to be determined from the state relationships

$$\bar{\Phi} = \int_0^1 \phi(\xi) P(\xi) d\xi$$

$$\overline{\phi'^2} = \int_0^1 (\phi(\xi) - \bar{\Phi})^2 P(\xi) d\xi \qquad (2.23 - 24)$$

Bilger (1977) showed that in real laminar diffusion flames the flame properties correlated well with the mixture fraction. Liew et al. (1981) supposed that the state relationships used in turbulent flame calculations should have the structure of a laminar diffusion flame, in mixture fraction space. These state relationships may be obtained experimentally or from diffusion flame calculations. Liew et al. (1981) report that a large improvement in the prediction of flame species, especially minor species such as CO, may be achieved by using laminar flame state relationships as opposed to assuming that the flame is in local equilibrium. However, the laminar flame state relationships are not unique, but are functions of the hydrodynamic strain rate. The strain rate is related to the scalar dissipation rate

$$\chi = 2D(\nabla\xi)\cdot(\nabla\xi) \qquad (2.25)$$

where D is the diffusion coefficient and ξ is the mixture fraction. The scalar dissipation rate may be thought of as a characteristic residence time. As the value of χ in the reaction zone is increased, a point will be reached where the chemistry will no longer be able to

keep up with the transport of energy away from the reaction zone and the flame will extinguish. Liew et al. (1984) have investigated the effect of strain on turbulent methane / air jet flames. Scalar properties in the calculation are represented by a pair of flamelets, corresponding to burning and extinguished states. The contribution from each flamelet is determined by the local probability of burning. This probability is obtained from the local distribution of scalar dissipation rate values. Liew et al. (1984) find that for open turbulent jet flames the effect of strain is small and confined to near burner regions.

A time-dependent solution is not necessary for the chemical source term to be described exactly. The mean chemical source term is given exactly by

$$\bar{S}_F = \int\int\int\int S_F(T, \rho, Y_F, Y_O)\, P(T, \rho, Y_F, Y_O)\, dT\, d\rho\, dY_F\, dY_O \qquad (2.26)$$

where $P(T, \rho, Y_F, Y_O)$ is the joint probability density function for temperature, density, and the mass fractions of the fuel and oxidant. Transport equations for such joint probability density functions may be solved and, hence, chemical source terms represented exactly. However, this method is computationally very expensive and the dimensions of the scalar spaces investigated is quite small. Despite this calculations for jet flames have been performed. Chen et al. (1989) report such a calculation for a methane / air turbulent jet diffusion flame. The combustion chemistry is described by both a five scalar reduced mechanism and a four scalar constrained equilibrium model.

2.6 Modelling Soot Formation

2.6.1 Soot Formation Chemistry

It is generally accepted that there are four steps to soot formation from a gaseous fuel. These are fuel pyrolysis, particle nucleation, and particle surface growth and coagulation. Of course, soot particles in diffusion flames will also eventually be subject to some degree of oxidation. The soot formation process is slow when compared to the reaction rates of the combusting gases. However, soot particles containing 10^6 - 10^{12} carbon atoms may form in only a few milliseconds. For diffusion flames the sooting propensity of a fuel generally correlates with the fuel type, with the sooting tendency following the trend aromatics > alkynes > alkenes > alkanes.

The rate limiting steps of the soot formation process are not of the fuel pyrolysis, but of nucleation and surface growth. Evidence suggests that soot formation proceeds via poly-aromatic hydrocarbons (PAHs). Experiments investigating the shock tube pyrolysis of acetylene reveal a 'bell' shaped dependence of the soot yield with temperature. Frenklach et al. (1983) explain this by the existence of two parallel reaction pathways. The acetylene will pyrolyse to form intermediate aliphatic species. These intermediate species will then interact to form aromatic species. The aromatic species will then either fragment back to aliphatic compounds or undergo further addition by aliphatic compounds to eventually form soot. This reaction scheme may be illustrated as

$$C_2H_2 \rightarrow X \rightarrow \begin{matrix} \xrightarrow{+M} X \\ A \\ \xrightarrow{+X} S \end{matrix} \qquad (2.27)$$

where X represents the intermediate aliphatic compounds, A the aromatics, and S the soot. At low temperatures the 'polymerisation' reaction is dominant ($A \xrightarrow{+X} S$) and the formation of soot is limited by the rate at which the aromatic structures may be formed. However, at higher temperatures the fragmentation reaction rate increases and the soot yield is determined by competition between the formation and destruction of the aromatic compounds. Frenklach et al. (1984) carried out a detailed kinetic analysis of the routes to soot formation in the shock tube pyrolysis of acetylene. Three reaction classes were found

to be the rate limiting steps in the formation of soot. The first of these is abstraction of a hydrogen atom from an aromatic species by a hydrogen atom

$$A\text{-}H + H \rightarrow A\cdot + H_2 \qquad (2.28)$$

The second is addition of acetylene to the radical formed

$$A\cdot + C_2H_2 \rightarrow A\text{-}C{\equiv}CH + H \qquad (2.29)$$

The final reaction is cyclisation to an aromatic ring

$$A\cdot_i\text{-}C{\equiv}CH + C_2H_2 \rightarrow A\cdot_{i+1} \qquad (2.30)$$

where the *i* indicates the number of aromatic rings in the molecule.

The results from this study showed that PAH formation and growth proceeds along only one or two dominant reaction pathways. For shock tube pyrolysis of acetylene sequential addition of acetylene dominates the PAH growth. Under different conditions other reaction steps may initiate the PAH production, but acetylene addition begins to dominate as the reaction progresses.

Frenklach and Wang (1990) considered the detailed modelling of soot particle nucleation and growth in laminar premixed hydrocarbon flames. The model consisted of three parts initial PAH formation, PAH growth, and spherical particle formation and growth. The initial stages of PAH production were modelled using reactions of the type given above. Particle nucleation was considered to be the process where PAH molecules, beyond a certain size, were allowed to grow by the hydrogen abstraction / acetylene addition reaction. These PAH molecules were also allowed to coagulate, forming clusters of PAH molecules. These clusters were assumed to be solid phase soot and were allowed to undergo mass addition and loss by surface reactions. The surface mass addition reaction was also considered to be the hydrogen abstraction / acetylene addition - Frenklach (1989). Mass loss from the soot particles was considered to be due to reaction with molecular oxygen and the hydroxyl radical. The results of this modelling study are as follows. The particle inception is determined by PAH coagulation. The average, computed, soot particle contains up to 10^5 carbon atoms. However, the average PAH size is only up to 50 carbon atoms.

This indicates that the size of an incipient particle should be approximately 1 nm. The surface growth of soot particles is determined by two processes, acetylene addition and condensation of PAHs at the particle surface. The relative contribution of these two processes changes with flame conditions. The main contribution of PAH condensation occurs in the early stages of PAH coagulation.

Puri et al. (1994) conducted a study into the oxidation of soot in laminar hydrocarbon diffusion flames. Three flames were investigated, fuelled by methane, methane / butane, and methane / 1-butene, burning in air. A coannular burner was used. Hydroxyl radical concentrations were measured using laser induced fluorescence. A thermophoretic sampling technique was used to remove soot from the flame for particle size measurements by transmission electron microscopy. Soot volume fraction and velocity data has also been obtained for these flames - Richardson (1993). Results indicate that the OH concentration is lowered in the presence of soot particles. The greater the soot concentration the greater the effect on the OH concentrations. This is shown to be the result of reactions of the OH radical with the soot particles rather than a reduction in temperature caused by radiative heat loss from the soot. The oxidation rate of the soot by the hydroxyl radical is found by subtracting from the total oxidation rate the rate of oxidation due to molecular oxygen, obtained from the expression of Nagle and Strickland-Constable (1962). The contribution to the oxidation rate from the hydroxyl radical is found to dominate that from molecular oxygen. Garo et al. (1990) also determined that the hydroxyl radical is the dominant oxidising species in a methane / air diffusion - see section 2.2.

2.6.2 Soot Formation Models

The chemistry of soot formation is highly complex. Detailed kinetic models have been developed - Frenklach et al. (1984) - but the number of separate reactions (approximately 600) and species (180) do not presently allow the extension of such schemes to turbulent combustion calculations. Hence, models have been developed to describe the sooting process. The closure of the source terms in these models is subject to the same problem outlined in section 2.5. Therefore, the assumption used for source term closure represents an integral part of the model and in this respect different applications of the same soot

formation model are in effect different soot models.

Khan et al. (1971) propose a single step mechanism for the production of soot mass. This model has been used more recently by Coppalle and Joyeux (1993) for the prediction of soot formation in a turbulent ethene / air jet diffusion flame. The production rate of the soot mass concentration is given by

$$\frac{dM}{dt} = C P_F \Phi^3 e^{-\frac{E_a}{RT}} \tag{2.31}$$

where M is the soot mass concentration, C is a constant (assigned the value of 0.1 by Coppalle and Joyeux (1993)), P_F is the unburnt fuel partial pressure, Φ is the equivalence ratio, and E_a / R is the activation temperature which is assigned a value of 20 000 K. Two expressions were considered for modelling the soot burnout. The first expression was the molecular oxygen oxidation rate of Nagle and Strickland-Constable (1962). The second expression is from Magnussen and Hjertager (1976) - see below. Source term closure was effected for the oxidation terms by replacing variables with their time means. Coppalle and Joyeux (1993) report a reasonable level of agreement, for the prediction of soot volume fraction in their turbulent jet ethene / air diffusion flame compared with experiment.

Tesner et al. (1971) suggest a two step model for soot formation. The first step represents the formation of radical nuclei and the second step represents the formation of soot particles from these radical nuclei. The rate of radical nuclei formation is expressed by

$$\frac{dn}{dt} = a_0 \rho Y_F e^{-\frac{E_a}{RT}} + (f - g)n - g_0 nN \tag{2.32}$$

where n is the concentration of the radical nuclei, a_0 is a constant, f is a linear branching coefficient, g is a linear termination coefficient, g_0 is a coefficient of linear termination on soot particles, and N is the concentration of soot particles. The formation rate of soot particles is given by

$$\frac{dN}{dt} = (a - bN)n \tag{2.33}$$

where a and b are constants. Magnussen and Hjertager (1976) used this model to predict the formation rate of soot in turbulent ethyne / air jet diffusion flames. Mean quantities were used to formulate the production rate source terms. The burnout of the soot was modelled by the following expressions

$$\frac{d\bar{M}}{dt} = A\,\bar{M}\,\frac{\epsilon}{k}$$

$$\frac{d\bar{M}}{dt} = A\,\frac{\overline{\rho Y_O}}{\phi_{Soot}}\,\frac{\epsilon}{k}\,\frac{\bar{M}\phi_{Soot}}{\bar{M}\phi_{Soot} + \overline{\rho Y_F}\phi} \qquad (2.34 - 35)$$

where ϕ_{Soot} is the stoichiometric oxygen requirement to burn 1 kg of soot. The expression yielding the lowest burnout value was employed. The reduction in radical nuclei was assumed to take the form

$$\frac{d\bar{n}}{dt} = \frac{1}{\bar{M}}\,\frac{d\bar{M}}{dt}\,\bar{n} \qquad (2.36)$$

Detailed comparisons of the predicted sooting structure of the flames with experiment show surprisingly good agreement for both the growth of the soot and its subsequent burnout.

Kennedy et al. (1990b) propose a single equation model for the production of soot volume fraction. The soot production rate is taken to be the sum of contributions from particle nucleation and surface growth processes. The surface growth rate is taken to be proportional to the particle surface area. A mono-disperse distribution of spherical particles is assumed, along with a fixed mean number density. The modelled production rate of soot volume fraction due to surface growth process is given by

$$\frac{df_V}{dt} = 6^{2/3}\,\pi^{1/3}\,N_{Avg.}^{1/3}\,f_V^{2/3}\,k(\xi) \qquad (2.37)$$

where f_V is the soot volume fraction, $N_{Avg.}$ is the assumed particle number density (taken to be 10^{-16} m^{-3}), and $k(\xi)$ is the surface area specific production rate of soot volume fraction. Metternich et al. (1991) apply this model to the prediction of soot volume fraction in a turbulent ethene / air diffusion flame. Soot oxidation by the OH radical and molecular

oxygen was considered. The PDF transport method was used for source term closure, with a transport equation solved for the joint PDF of the mixture fraction, enthalpy and the soot volume fraction. Detailed comparisons of the flame sooting structure are not reported. However, the evolution of the predicted soot volume fraction on the flame centreline is shown and compared with experiment. The prediction over-estimates the peak soot volume fraction on the centreline by approximately a factor of four.

Moss et al. (1988) propose a two-equation model of soot production. The soot is described by two parameters, the number density of soot particles and the soot volume fraction. The processes of particle nucleation, coagulation, surface growth, and oxidation are described in an approximate manner. The mean production rate of the particle number density is described by

$$\frac{d}{dt}\left(\frac{N}{N_A}\right) = C_\alpha \rho^2 X_{HC} T^{1/2} e^{-\frac{T_\alpha}{T}} - C_\beta T^{1/2}\left(\frac{N}{N_A}\right)^2 \qquad (2.38)$$

where N_A is Avogadro's number, C_α and C_β are model constants, X_{HC} is the mole fraction of a hydrocarbon precursor, and T_α is the activation temperature of the nucleation reaction. The first term on the right hand side represents the creation of particles by nucleation and the second term the reduction in number density due to coagulation. The formation of additional soot mass is assumed to take place through heterogeneous surface growth processes. Soot nuclei are assigned an initial mass of 144 kg kmol^{-1}, corresponding to 12 carbon atoms. Under these assumptions the formation of soot mass is given by

$$\frac{d}{dt}(\rho_{Soot} f_V) = 144\, C_\alpha \rho^2 X_{HC} T^{1/2} e^{-\frac{T_\alpha}{T}} + C_\gamma \rho X_{HC} T^{1/2} e^{-\frac{T_\gamma}{T}} N \qquad (2.39)$$

where C_γ is a model constant and T_γ is the activation temperature for the surface growth reaction. The first term on the right hand side represents the creation of soot mass due to nucleation processes and the second term represents the addition of soot mass through surface growth processes. The model constants are determined by the application of the model to a laminar flame calculation and detailed comparisons with experiment. Syed

(1990) applied this model to the prediction of the soot levels in a turbulent ethene / air jet flame. Source term closure was achieved by replacing the soot parameter with its time mean and using the presumed PDF / laminar flamelet approach to average the remainder of the source terms. The soot burnout was modelled by the molecular oxygen oxidation mechanism of Nagle and Strickland-Constable (1962), incorporated in the following expression

$$\frac{d}{dt}(\rho_{Soot} f_V) = -\omega (\pi N)^{1/3} (6 f_V)^{2/3} \qquad (2.40)$$

where ω is the surface specific oxidation rate given by Nagle and Strickland-Constable (1962). The closure of this source term was achieved as above, with the soot parameters being replaced by their time averages and the presumed PDF / laminar flamelet approach used to generate a suitable average for ω. This approach to source term closure ignores the correlations between the soot parameters and the gaseous species, as characterised by the mixture fraction. Syed (1990) reports good agreement for the predicted soot volume fractions with experiment, in the soot growth region of the flame, if the soot burnout term is not incorporated into the soot mass growth source term. Inclusion of the oxidation term led to a large under-prediction of the soot volume fraction at all flame positions. This indicates that the correlation between the soot properties and the gaseous species must be included to realistically capture the soot burnout rate.

Syed (1990) introduces a modification to the model of Moss et al. (1988). Syed (1990) models the soot formation rate in a laminar methane / air flame using a soot surface area dependent surface growth term. The rate of increase in soot mass is given by

$$\frac{dM}{dt} = 144\, C_\alpha\, \rho^2 X_{HC} T^{1/2} e^{-\frac{T_\alpha}{T}} + C_\gamma\, \rho\, X_{HC} T^{1/2} e^{-\frac{T_\gamma}{T}} N^{1/3} M^{2/3} \qquad (2.41)$$

where the second term on the right hand side represents the modified surface growth rate. This model accurately predicted the sooting trends in the laminar flame after adjustment of the model constants.

Leung et al. (1991) present a simplified mechanism for soot production in diffusion flames.

This mechanism also models in an approximate manner the processes of particle nucleation, surface growth, and coagulation. The soot is described by two parameters, the particle number density and the mass concentration. The intermediate species ethyne is assumed to be responsible for the processes of particle nucleation and surface growth. The rate of soot mass growth due to surface growth processes is taken to be proportional to the product of the acetylene concentration and the square root of the available soot surface area. Lindstedt (1991) applied this model to the prediction of the soot volume fraction in the Syed (1990) laminar methane / air diffusion flame. The evolution of the peak soot volume fraction with increasing height above the burner is not captured. This is likely to be because of the square root soot surface area dependence used in the surface growth term.

2.7 Predicting Flame Radiation

Thermal radiation plays an important role in determining the temperature field in a combustion system. Concentrations of trace species, such as soot, may be especially affected by heat losses due to radiation as their rates of production are usually highly temperature dependent. Thermal radiation may also have a large influence on the flame surroundings. It may, for example, determine the rate of fire spread in accidental fires. In practical devices, such as gas turbine combustors, thermal radiation may affect the lifetime of the device. For furnaces or boilers heat transfer by thermal radiation will determine the efficiency of the system. Clearly, an accurate predictive capability for flame radiation is highly desirable. Flame radiation is a highly complex phenomena and only a brief introduction is given in this section. A good review of radiative heat transfer in combustion systems is given by Viskanta and Mengüç (1987).

The distribution of radiation intensity is determined from the radiative transfer equation. The radiative transfer equation describes the transition of a beam of monochromatic radiation through an absorbing / scattering / emitting medium. In many combustion systems scattering may be ignored as gas molecules and soot particles scatter negligibly, as long as the wavelength of the radiation is much greater than their diameter. The monochromatic radiation intensity received at the origin from a single line of sight (of pathlength L) through an absorbing / emitting medium is obtained from the equation of radiative transfer - Siegel and Howell (1971) - which may be written as

$$I_\omega = \int_0^L \kappa_\omega \, I_{\omega,b} \exp\left(-\int_0^l \kappa_\omega \, dl' \right) dl \qquad (2.42)$$

where κ_ω is the spectral absorption coefficient and $I_{\omega,b}$ is the Planck blackbody distribution function. The complexity involved in solving this equation is associated with finding the form of the absorption coefficient. For gases this absorption coefficient shows an extremely complex form which varies with wavelength, temperature, and pressure. The remainder of this section discusses models which may be used to approximate κ_ω and solve the equation of transfer.

The spectral variation of the gaseous absorption coefficient arises from discrete changes in the energy levels of the emitting gas molecules. Joint transitions in the vibrational and rotational energy levels results in emission / absorption in the infrared region of the spectrum. Gaseous emission / absorption only occurs over discrete bands within the spectrum. Each band corresponds to a particular transition between vibrational energy states of the gas molecules. The bands are comprised of a large number of absorption / emission lines. These lines correspond to changes in the rotational energy states of the gas molecules, accompanying the transition in the vibrational energy state. As each line represents a transition between quantised energy states it might be expected that the line would be monochromatic. However, this is not the case and the lines have a finite width determined by various broadening mechanisms - Siegel and Howell (1971).

The most accurate calculation of flame radiation would consider each of these absorption lines separately. However, because of the large number of lines this is not possible. Therefore, band models have been developed. The 'narrow-band' model splits the spectrum into regions which are wide compared to the spacing between the individual absorption lines but are narrow compared with the widths of the absorption bands - Ludwig et al. (1973). These narrow bands are described by simple parameters. However, this model still requires a great deal of computational effort and its use has been restricted to post-process type calculations - for example Jeng et al. (1984) and Syed (1990).

A simplification of the narrow-band model is the wide band model - Tien and Lee (1982). Complete absorption / emission bands are modelled using empirical parameters obtained from fits to experimental data.

This simplest model of gas radiation ignores the spectral variation of the absorption coefficient entirely and assumes that the gas is a grey emitter. The total emissivity may be obtained from the spectral emissivity using the following relation

$$\epsilon = \frac{\int_0^\infty \epsilon_\lambda I_{\lambda,b}\, d\lambda}{\int_0^\infty I_{\lambda,b}\, d\lambda} = \frac{\pi \int_0^\infty \epsilon_\lambda I_{\lambda,b}\, d\lambda}{\sigma T^4} \qquad (2.43)$$

2 - Flame Soot and Radiation

The total emissivity for systems of CO_2 and H_2O are charted in Hottel and Sarofim (1967) as functions of the temperature and the product of the partial pressure and the pathlength. However, use of this approximation is only suitable for homogeneous, isothermal systems.

Soot is a continuum radiator and is approximately spectrally grey. Mie theory - Kerker (1969) - shows that, if the particle diameter is small compared with the wavelength of the electromagnetic radiation, then the spectral absorption coefficient is proportional to the volume fraction of the particles divided by the wavelength. The constant of proportionality is a function of the complex refractive index of the soot - see equation 3.15.

General solution of the radiative transfer equation for a combustion system requires integration of the equation over all paths, solid angles, and areas comprising the system. Such solutions are beyond the scope of this work but are reviewed by Viskanta and Mengüç (1987).

Chapter 3 - Turbulent Flame Experiments

3.1 Introduction

The existing measurement database on turbulent methane jet diffusion flames is extensive - see chapter 2 for examples. However, all studies have so far been deficient in one respect; soot property measurements have not been taken. At 1 atm laboratory scale methane flames are only lightly sooting and existing measurement techniques suffer a low signal to noise ratio. However, large scale methane fires, such as those encountered in hazards, soot heavily. This is due to the increased time scales under high-temperature, fuel-rich conditions. Given that the main radiating species from these hydrocarbon fuelled flames is soot the importance of its study is clear.

In this study only laboratory scale jet flames are considered. Measurements are made in an atmospheric pressure methane flame; but, in order to increase the soot yield to a level more representative of large scale flames, the operating pressure of the flame is also raised to 3 atm absolute. This has the effect of increasing the peak soot volume fractions in the flame by an order of magnitude and approximately doubling the radiative heat loss.

In order to operate at elevated pressure, the flame is confined in the Cranfield turbulent jet flame rig. A new burner is designed for use with methane in this rig; the final design reflecting a compromise between flame stability and physical size. The new burner design, circular with an exit diameter of 4.07 mm, precludes the extension of any existing methane flame database - eg. Jeng et al. (1984). Therefore, measurements needed for flame model validation have been taken. Given its pivotal role in modelling the turbulent diffusion flames in this work, mixture fraction measurements are made in order to characterise the turbulent mixing. Temperature measurements are taken to check the performance of the radiative loss model used in the flame calculations. In addition, the soot formation rate is very sensitive to temperature so an accurate prediction for the temperature field is vital if

the soot model is to be satisfactorily evaluated. Measurements of soot volume fraction are made to validate the soot model and to ensure that the soot volume fraction predictions used in the radiation intensity calculations are realistic. Finally, line of sight radiation intensity measurements are made for comparison with RADCAL predictions.

This chapter deals mainly with the experimental methods used for the acquisition of the dataset. There is also some analysis of the errors to which these measurements may be subject. The complete set of data recorded for the 1 and 3 atm turbulent methane flames is presented in the appendix.

3.2 Rig Geometry

During the course of this experimental study two rigs are used. The boundary conditions presented to the flame by these two rigs are identical.

The first rig is designed for studying turbulent jet flames at atmospheric and elevated pressure. The body of the rig comprises a pressure vessel, and consists of five main stainless steel sections (see figure 3.1). The bottom section is made from a blank flange. Through the centre of this flange passes a shaft upon which the burner is mounted. The gases for the main fuel flow and the premixed pilot pass through this shaft. Holes drilled in the flange admit the air for the co-flow. Bolted to this flange, forming the main body of the rig, are two sections of pipe. Between these is the measurement section, machined from a single billet of stainless steel. Four windows may be mounted in this section. These windows allow optical access to 75 mm of the flame's width. Two window types are utilised. Circular quartz windows, giving good optical access to the flame are generally used. However, for the radiation intensity measurements quartz is not a suitable optical material, as it absorbs strongly at wavelengths longer than approximately 2.5 μm. For the radiation intensity measurements the quartz windows are replaced by sapphire slot windows, these have the same width as the quartz windows but are only 10 mm in height. There is also provision for probes to be mounted on the measurement section, these probes may be traversed across the full width of the flame. At the top of the rig, closing the vessel, is the bursting disk and sonic-nozzle pressurising valve assembly. The burner has a vertical movement range of 300 mm and, coupled with the use of unequal length main tube sections which may be swapped, allows 425 mm of the flame's height (measured from the burner exit plane) to be investigated. The flame is contained by a Pyrex tube mounted inside the vessel. This Pyrex tube has an internal diameter of 155 mm. To allow optical and probe access to the flame the Pyrex tube is split into two sections separated by a slotted stainless steel spacer ring. The entire pressure rig is mounted on a movable platform. The platform may be traversed horizontally (perpendicular to the flame axis) over a range of approximately 150 mm. This allows the use of fixed optical systems on either side of the rig, with the ability to traverse the flame instead of the optics.

The second rig is designed for studying turbulent jet flames at atmospheric pressure only.

3 - Turbulent Flame Experiments

The rig is very similar to that previously described, but does not have the external pressure vessel. The flame is confined in a Pyrex tube of internal diameter 155 mm. This tube is split at around the mid-point and is separated by a stainless steel spacer, as before. However, in this case the spacer ring itself is machined to accept sapphire slot windows.

The high pressure rig is used for making nearly all the measurements on both the 1 atm and the 3atm flames. The only exception to this are the 1 atm radiation intensity measurements which, due to time limitations with the high pressure rig, were taken using the atmospheric pressure rig.

3.3 Burner Design

The burner design must satisfy several, possibly conflicting, criteria. The flame must be amenable to experimental measurement; on the other hand if the data is to be used for subsequent model validation, as in this case, the boundary conditions for the flame must be well defined. There may also be environmental considerations, such as the physical dimensions of the flame and heat output - both of these are concerns in this case. The flame is investigated inside a pressure vessel and, therefore, must not exceed the size constraints imposed by this vessel. The fume extraction system at Cranfield is, at the time of the experiments, limited in terms of the maximum throughput and temperature of the flowing gases. In the past, this fume extraction system has taken flames of up to ~ 20 kW heat output and this is considered as the limit here. In terms of the boundary conditions for the flame modelling, the most important consideration is the stability of the flame at the exit of the burner. The modelling approach adopted in chapter 5 utilises the laminar flamelet concept. This combustion model does not allow for degrees of partial premixing of the reactants. Hence, it is very important that the flame is stabilized at the exit of the burner; if the flame lifted partial premixing would result. This would also invalidate the boundary condition used for the soot - see chapter 5.

The constraints, therefore, on the design of the turbulent methane jet flame burner are: physical size of the flame, stability at high Reynolds numbers and heat release. The flame at elevated pressure will be smaller than that at atmospheric, for the same fuel mass flow rate, and will also be more stable due to the lower exit velocity. Therefore, only the atmospheric case is considered for the design of the burner.

The elevated pressure turbulent flame rig allows approximately 0.4 m of flame height to be investigated; measured from the burner exit plane. For turbulent flames, the flame height is determined by the diameter of the burner's exit not the exit velocity. Hawthorne et al. (1949) give the flame height for turbulent flames as

$$\frac{L}{d_B} = \frac{5.3}{C_T}\sqrt{\frac{T_F}{\alpha_T T_N}\left[C_T + (1 - C_T)\frac{M_S}{M_N}\right]} \qquad (3.1)$$

where: C_T is the mole fraction of the nozzle fluid in the unreacted stoichiometric mixture; α_T is the ratio of the number of moles of reactants to the number of moles of products for the stoichiometric mixture; M_S, M_N are the molecular weights of the surrounding and nozzle fluids respectively; T_N is the absolute temperature of the fluid in the nozzle; T_F is the adiabatic flame temperature; d_B is the nozzle diameter; and L is the flame height. For a turbulent methane/air flame the ratio L / d_B given by this equation is approximately 202. This would suggest a nozzle diameter of 2 mm would be suitable for full viewing of the flame in the pressure vessel.

For the flow in the burner tube to be turbulent a minimum Reynolds number of approximately 2300 must be attained. The Reynolds number is given by

$$\mathrm{Re} = \frac{\rho u d_B}{\mu} \tag{3.2}$$

Given that ρ/μ is a fixed property for the fuel, for the burner flow to be turbulent

$$u d_B = 2300 \frac{\mu}{\rho} \tag{3.3}$$

This gives a minimum value for $u d_B$ of 0.0377. Therefore if the nozzle diameter is 2 mm the minimum flow velocity for turbulent flow is 19 m s^{-1}. However, construction and testing of a prototype burner reveals that the flame has a tendency to lift long before the flow becomes fully turbulent. Following Stårner and Bilger (1985), several prototype burners were constructed with annular premixed pilot flames around the main flow orifice. The 2 mm piloted burner is unsuitable but a 4 mm diameter orifice shows a reasonable compromise between flame size and flame stability. However, even with a pilot flame the 4 mm burner gives a stable flame only to an exit Reynolds number of 5000. At this Reynolds number the mass flow rate is 10.3 g min^{-1} which gives a heat output of approximately 10 kW. The final burner design is shown in figure 3.2. The diameter of the main flow jet is 4.07 mm around this is an annulus (width 160 μm) through which the premixed gases for the pilot flow. The annulus is designed with a small width to prevent burn-back of the premixed pilot flame. Attention has been paid to the aerodynamics of the burner in an attempt to avoid recirculations around the base of the flame caused by the air co-flow, which may disturb the flame in the sensitive near burner region.

Mounted on the burner, below the level of the burner tip, is a diffuser for the air co-flow. This diffuser consists of two circular, perforated metal plates. The function of this diffuser is to flatten the velocity profile in the co-flowing air. The diffuser fills the diameter of the confining Pyrex tube.

3.4 Experimental Conditions

Two flames are investigated in the course of this study. The operating conditions for these flames are summarised in the table below.

Table 3.1

	Flame 1	Flame 2
Absolute Pressure / atm	1	3
Fuel Mass Flow / g min^{-1}	10.3	10.3
Air Mass Flow / g min^{-1}	708	708
Fuel Temperature / K	290	290
Air Temperature / K	290	290
Exit Reynolds Number	5000	5000

The pilot flame is a premixed mixture of methane and oxygen. This pilot flame is kept fuel rich to prevent overheating the burner tip. The methane flowrate for the pilot flame is < 2 % of the main fuel flowrate. At 3 atm the pilot flame shows a tendency to burn back to the premixing point. This is prevented by careful tuning of the ratio of O_2 to CH_4.

Flame 1 displays a visible flame height of around 600 mm, viewed with the external pressure vessel removed. This flame is shown in figure 3.3. Visual access to flame 2 is limited by the pressure vessel; but this flame appears to be smaller, with a height of approximately 400 mm.

3.5 Mixture Fraction Measurement

Two methods are used for making mean mixture fraction measurements in the turbulent flame. Both methods rely on a probe to draw gas samples from the flame. The technique employed most extensively infers the mixture fraction from the local carbon to nitrogen ratio. A sample of gas is continuously drawn from the flame through a quartz probe. The probe has an outside diameter of approximately 6 mm tapering to a tip with an orifice internal diameter of approximately 500 μm. Oxygen, flowing through a tube running along the centre of the probe, is mixed with the incoming sample gas near to the entrance of the probe. This mixture, of sample gas and oxygen, passes along the length of the probe over an electrically heated platinum catalyst (see figure 3.4). This probe was also used by Young (1993), and the reader is referred to Young (1993) for full details of the probe's design. All of the carbon bearing species, other than CO_2, oxidise to CO_2 and H_2O. This gives a product gas comprising of CO_2, H_2O, O_2 and N_2 only. This product gas is passed to a calibrated mass spectrometer, which is used to measure the mole ratio of carbon dioxide to nitrogen. The mixture fraction is obtained as follows

$$AFR = \frac{[N_2]}{[CO_2]} \frac{28 + (0.21 / 0.79) \times 32}{16} \tag{3.4}$$

$$\xi = \frac{1}{1 + AFR} \tag{3.5}$$

where AFR is the air to fuel mass ratio, $[N_2] / [CO_2]$ is the mole ratio of nitrogen to carbon dioxide and ξ is the mixture fraction. Young (1993) reported some problems using this probe in regions of high mixture fraction. Similar problems were encountered in the methane flame experiment, in the high ($\xi > 0.4$) mixture fraction regions near to the burner exit. Under these conditions the reaction between the oxygen and the sample gas, with its associated volumetric expansion, leads to flow reversal with oxygen leaving the tip of the probe. This confined the technique to regions in the flame with a mixture fraction below 0.4; from approximately 150 mm downstream of the burner exit.

Upstream of the 0.4 mixture fraction point the mixture fraction is measured more directly, by mixing a tracer species with the methane fuel. The tracer used is argon, mixed to give

a fuel gas stream consisting of 90 % methane and 10 % argon by volume. The gas sample drawn through the quartz probe is passed directly to the mass spectrometer. The mixture fraction is taken from the *AFR*, inferred from the ratio of argon to nitrogen - using the following relation

$$AFR = \frac{[N_2]}{[Ar]} \frac{28 + 0.21 / 0.79 \times 32}{1 \times 40 + 9 \times 16} \tag{3.6}$$

Only three data points in the data set are obtained using this technique; those at 50, 100 and 150 mm above the burner exit plane on the flame axis. All the experimental data is tabulated in the appendix. Figure 3.5 demonstrates the repeatability of the measurements. An estimate of the absolute uncertainty is obtained by calibrating the spectrometer with a gas of an accurately known composition, then measuring the carbon dioxide to nitrogen ratio of another gas with an accurately known composition. The effective measured mixture fraction of the second gas is calculated and this is compared with the known effective mixture fraction. The mean error calculated is 6 %. From figure 3.5 it may be seen that this error is of the same order as the repeatability of the measurement. Figure 3.5 also highlights another problem in the mixture fraction dataset. In the figure it is shown that the mean mixture fraction does not fall to zero at the edges of the flame, as would be expected. Examination of equations 3.4 and 3.5 reveals that for the mixture fraction to drop to zero the *AFR* must be infinity. This means that the concentration of carbon dioxide must fall to zero. In practice there is always a small background level of carbon dioxide present in the mass spectrometer so a mixture fraction measurement of zero is impossible. The minimum mixture fraction measured, corresponding to this background level of carbon dioxide, is approximately 0.02.

3.6 Temperature Measurement

Mean temperature measurements are made with a fine wire thermocouple of Pt - Pt 87 % / Rh 13 % (Type R). The diameter of the wires used for the thermocouple is 50 μm. These wires are flame welded to form a junction bead of < 200 μm diameter. The thermocouple junction is mounted on support wires, made from the same combination of materials, of 500 μm diameter. The support wires are passed through a dual bore ceramic tube, which is mounted in the stainless steel probe body. At one end of the ceramic tube the support wires are connected to a standard R type thermocouple connector, at the other the wires are bent outwards in the form of a 'V'. The support wires extend approximately 30 mm beyond the end of the ceramic tube, the widest end of the 'V' is approximately 20 mm across. It is at the wide end of the 'V' that the thermocouple junction is mounted. See figure 3.6 for a diagram of the thermocouple probe.

The thermocouple voltage is measured with an ADC system mounted in an IBM compatible computer, the ADC has a 12 bit resolution (1 in 4096). The temperature samples are taken at 1 kHz, 5000 samples are used to give a mean temperature at any given flame location.

The mean temperature values are corrected for the radiative loss from the bead of the thermocouple. Fristrom and Westernberg (1965) give a method for compensating for this heat loss from the thermocouple bead. If it is assumed that the only mechanism of energy transfer to / from the bead is by convection to the bead from the gas and radiative heat loss from the bead to the surroundings then an energy balance may be written for the bead

$$h(T_{Gas} - T_{Thermo.}) = \epsilon \sigma (T^4_{Thermo.} - T^4_{Wall}) \qquad (3.7)$$

No visible soot deposition on the thermocouple is apparent in either the 1 atm or 3 atm methane flame; hence, the bead emissivity (ϵ) may be taken as that for bright Platinum at 1500 K - a value of ~ 0.2.

The convective heat transfer coefficient is obtained from a correlation between the Nusselt number ($Nu = h d_s / k$) and the Reynolds and Prandtl numbers. The bead approximates to a sphere and Whitaker (1972) recommends an expression of the form

$$Nu = 2 + (0.4Re^{\frac{1}{2}} + 0.06Re^{\frac{2}{3}})Pr^{\frac{4}{10}}\left(\frac{\mu_\infty}{\mu_S}\right)^{\frac{1}{4}} \qquad (3.8)$$

The Nusselt number correlation used for the 1 atm flame differs from that used for the 3 atm flame. The radiative correction applied to the 3 atm flame temperature measurements uses the correlation given by equation 3.8 whereas the correction applied to the 1 atm uses the correlation reported by Young (1993). As the flame is turbulent, the instantaneous values for the properties needed for the heat transfer coefficient are not known. Hence, mean values are used for calculating the heat transfer coefficients. These are shown in the following table.

Table 3.2

	1 atm		3 atm	
	Value	Source	Value	Source
Viscosity (μ)	55.8 Pa s	Air at 1300 °C	55.7 Pa s	Air at 1500 K
Density (ρ)	0.218 kg m^{-3}	Air at 1300 °C	0.6966 kg m^{-3}	Air at 1500 K
Thermal Conductivity (k)	0.09 W m^{-1} K^{-1}	Air at 1300 °C	0.1 W m^{-1} K^{-1}	Air at 1500 K
Prandtl Number (Pr)	0.75	Air at 1300 °C	0.7	Air at 1500 K
Velocity (u)	8 m s^{-1}	Mean value	4 m s^{-1}	Mean value

The ratio of viscosity at the bead surface to the viscosity at infinity (μ_∞ / μ_S) is taken as unity. With a typical bead size of 150 μm the maximum correction applied to the temperature data is approximately 100 K.

The temperature measurements are found to demonstrate excellent repeatability, an example of which is shown in figure 3.7. The complete set of temperature measurements are tabulated in the appendix.

3.7 Soot Volume Fraction Measurement

Laser extinction tomography is the technique used for making measurements of mean soot volume fraction in the turbulent methane flames under study. The technique relies on a mathematical inversion of path-integrated extinction data to give the extinction coefficient as a function of position. This extinction coefficient may be related to the volume fraction of the soot.

The intensity of a ray of electromagnetic radiation travelling through an absorbing medium, with an absorption coefficient κ, is described by the Beer-Lambert law

$$I(L) = I_0 \, e^{-\int_0^L \kappa(l)\, dl} \tag{3.9}$$

The experiment involves measuring the mean value of the natural logarithm of the ratio of I to I_0 at various points across the width of the flame, as shown in figure 3.8. A 5 mW Helium-Neon laser is used as the source of electromagnetic radiation, a large area (100 mm^2) photodiode is employed as the detector. At each point on the traverse this average measurement represents the mean value of the integral in equation 3.9. I_0 is the laser intensity measured at the photodiode when the laser beam is not passing through the flame.

Assuming the flame to be axisymmetric on average, equation 3.9 may be re-written in terms of the extinction coefficient as a function of radius

$$\ln\left(\frac{I(x)}{I_0}\right) = -2\int_x^R \frac{\kappa(r)\, r\, dr}{(r^2 - x^2)^{0.5}} \tag{3.10}$$

where x is the shortest distance from the flame centreline to the chord that the ray passes along and R is the maximum radius of the flame. The mean extinction profile obtained - $\overline{\ln\,(I(x)\,/\,I_0)}$ - may be inverted in three different ways to give the mean extinction coefficient as a function of radius for the flame - $\overline{\kappa(r)}$. These three reconstruction methods are 'onion peeling', Abel transformation and Fourier convolution. Hughey and Santavicca (1982) outline these techniques and compare them in terms of their ability to reconstruct reacting

and non-reacting flowfields from simulated absorption data. Their conclusion is that each reconstruction process could possibly yield 'artifacts' which are not actually present in the flowfields. Therefore, they recommend the use of more than one of these methods to identify which features are real and which are artifacts of the reconstruction. Two reconstruction methods are used in this work: 'onion peeling' and Fourier convolution.

The 'onion peeling' technique divides the flow field into n concentric rings, where n is the number of absorption measurements taken. Each ring is considered to be homogeneous. Hence, equation 3.10 may be written as

$$\ln\left(\frac{I}{I_0}\right)_i = -\sum_{j=1}^{n} l_{ij}\,\kappa_j \qquad i = 1, n \tag{3.11}$$

where l_{ij} is the path length of the ith laser beam in the jth annulus. Solution for κ_j involves inverting the path length matrix. A disadvantage of this method is that, as the extinction coefficient is solved for sequential rings from the outside inwards, errors tend to build up to a maximum at the centre of the flowfield. Full derivation of the Fourier convolution method is given in Shepp and Logan (1974). A disadvantage of the Fourier convolution method is the behaviour of the reconstruction at discontinuities in $\kappa(r)$, where an oscillating overshoot is shown at the discontinuity.

Following the procedure of Young (1993), before reconstruction of the experimental data, the data is smoothed by fitting a high-order polynomial. Using the smoothed experimental absorption datasets no difference is found between the results of the two reconstruction algorithms used.

The extinction of electromagnetic radiation by soot particles is related to: the size of the particles, the refractive index of the particles, the wavelength of the incident radiation and the number density of the particles. For spherical particles the extinction coefficient may be written as

$$\kappa_{Ext.,\lambda} = \int_0^{\infty} N \pi r^2 Q_{Ext.}(\lambda, m, r)\, dr \tag{3.12}$$

The extinction of the radiation includes contributions from absorption and scattering. If the soot particles are small in comparison to the wavelength of the radiation ($2\pi r/\lambda \ll 1$), the Rayleigh limit, the component arising from the scattering of the radiation is negligible in comparison with the absorption - ie. $Q_{Ext.} \approx Q_{Abs.}$. If, also, the soot particles are assumed to be spherical then the absorption efficiency is given by the Lorentz-Mie theory - Kerker (1969) - as

$$Q_{Abs.} = -8\pi \frac{r}{\lambda} \Im\left(\frac{m^2 - 1}{m^2 + 2}\right) \tag{3.13}$$

Where $\Im$ indicates the imaginary part. Substituting $m = n - ik$ into equation 3.13 gives for the absorption efficiency

$$Q_{Abs.} = \frac{48\pi nkr}{\lambda(4n^2k^2 + (n^2 - k^2 + 2)^2)} \tag{3.14}$$

This may be substituted into equation 3.12 to give the absorption coefficient for soot in the Rayleigh limit

$$\kappa_{Abs.,\lambda} = \frac{36\pi nk}{\lambda(4n^2k^2 + (n^2 - k^2 + 2)^2)} \int_0^{\infty} N \frac{4}{3} \pi r^3 dr \tag{3.15}$$

where the integral is just the volume fraction of the soot particles. The laser used in these experiments is a Helium-Neon laser operating at 632.8 nm. The value of the complex refractive index used in this work is that of Mullins and Williams (1987) for propane soot at 632.8 nm. This refractive index has a value of $m = 1.92 - 0.45i$. The refractive index value was chosen to maintain continuity with the work of Syed (1990). The implications of choosing this value for the refractive index will be discussed later in this chapter.

The soot particles may be expected to reach a maximum diameter of 30 nm, based on laminar flame measurements - Garo (1984), in the 1 atm flame. In the 3 atm flame, where the measured mean absorption is an order of magnitude greater, this maximum particle diameter may be expected to reach 60 nm. Hence, the Rayleigh condition is certainly satisfied in the 1 atm flame but in the 3 atm flame some inaccuracy may be expected

because of the larger particle size.

The repeatability of the measurement is good in the regions of the flame where the soot volume fraction is high (> 0.5 ppm). Figure 3.9 presents two measurements of the radial soot volume fraction profile in the 3 atm flame at 350 mm above the burner exit plane. All the soot volume fraction profiles are presented in the appendix.

The errors in this measurement have four principal sources, these are: errors in the measurement of the mean extinction profile, error in the value of the refractive index chosen, erroneous assumption of the particles being within the Rayleigh limit and erroneous assumption of spherical soot particles.

The extinction profile measurement is subject to errors arising from four sources. The first problem is due to radiation from the flame falling on the photodiode, giving a false reading. This difficulty may be largely eliminated by placing an aperture and filter in front of the photodiode. The aperture is sized to allow the laser beam to pass through; but to block the optical path from the flame to the detector. Obviously, this cannot completely block the flame radiation so a band pass filter is also used. The band passed being centred around the laser wavelength.

The second problem is due to the changes in refractive index encountered by the laser beam as it passes through the flame. These refractive index changes cause the beam to deviate from its normally straight path. This deviation is only milliradians but over the half metre distance between the flame and the detector can cause large movement of the incident beam over the surface of the detector and the filter. If the surfaces of the filter and detector were completely homogeneous this would cause no problem, as long as the beam remained on the detector's surface. This error is kept to a minimum by ensuring that the surfaces of the filter and detector are kept clean. The magnitude of the signal caused by beam deviation is approximately 0.1 % of the full I_0 value.

The third inaccuracy in the extinction profile measurement is caused by the slight fluctuation in the power output of the laser over time. The I_0 value is measured once at the beginning of the traverse, and this value is used for calculating the value of $\overline{\ln (I(x) / I_0)}$ at

each point on the traverse. Clearly, if the laser intensity varies during the course of the traverse the measurement will be subject to error. This error is minimized by allowing the laser ample time to warm-up, as the power fluctuations are greatest in this warm-up period, and by completing each traverse in the minimum time. The laser power fluctuations are approximately 1 % of the full scale I_0 value. A method of continuously monitoring the laser power was also attempted using the arrangement shown in figure 3.10. A beam splitter is used to send a pre-flame fraction of the laser beam to a second photodiode, the laser power incident on this second photodiode being proportional to I_0. Hence, the I_0 value can be recorded simultaneously with the corresponding value of I. This setup presents problems because of the output from the laser being non-polarized. This requires a polariser to be placed in the system to give a constant split ratio from the beam splitter. The polarised output from the laser fluctuates by approximately ± 30 % of the mean value. Overall, an unidentified problem causes this system to give errors larger in magnitude than the non-polarised, non-power monitoring system. This problem may be due to the polariser not polarising perfectly; hence, the ratio from the beam splitter would not be constant.

The last inaccuracy, to which the extinction profile measurement is subject, is caused by inhomogeneities in the transmission characteristics of the rig windows. Even when newly cleaned the transmission of the windows can cause a 1 % variation in the laser signal. For measurements in the 3 atm flame, where the soot loadings are relatively high, this variation in window transmission presents no problem. However, for the 1 atm flame measurements the windows were removed from the rig. This caused a slight flame distortion, due to air entrainment through the window orifices, but this was largely confined to the flame region above the measurement plane.

Extinction profiles in the 1 atm flame are recorded at 300, 350 and 425 mm above the burner exit plane. The peak mean absorption is encountered at the 425 mm height, this peak absorption has a value of only 5 % - see figure 3.11. A 1 % variation in the power output of the laser, therefore, gives an error of 20 % in the measured signal. At 3 atm the peak absorption measured is approximately 20 % - 250 mm from the burner exit plane. The laser power fluctuation gives only a 5 % error at this height. Clearly, these errors in the extinction profile are at a minimum near the centre of the profile, where the absorption is at its highest.

The second principal error is due to uncertainty in the value of the refractive index, used for relating the absorption coefficient to soot volume fraction. The soot volume fraction is related to the absorption coefficient by equation 3.15. This may be rewritten as

$$f_V = f(m)\,\lambda\,\kappa_{Abs.,\lambda} \tag{3.16}$$

where $f(m)$ is given by

$$f(m) = \frac{4n^2k^2 + (n^2 - k^2 + 2)^2}{36\,\pi\,nk} \tag{3.17}$$

Various workers have proposed a value for the complex refractive index of soot. A selection of these values are shown in the following table, along with the corresponding values of $f(m)$.

Table 3.3

Author	Fuel	m	λ / nm	$f(m)$
Dalzell and Sarofim (1969)	Propane Acetylene	1.56 - 0.52*i* 1.57 - 0.44*i*	650	0.218 0.256
Lee and Tien (1981)	Iso-octane Polystyrene Plexiglass	1.9 - 0.55*i*	632.8	0.275
Mullins and Williams (1987)	Methane Propane n-Heptane Toluene	1.93 - 0.39*i* 1.92 - 0.45*i* 1.89 - 0.44*i* 1.89 - 0.46*i*	632.8	0.391 0.338 0.337 0.323
Chippet and Gray (1978)	Propane	1.9 - 0.35*i*	Visible	0.420

Although the values for m shown here are constants, Habib and Vervisch (1988) show that the value m depends on the wavelength and also the carbon to hydrogen ratio of the soot. The values of soot volume fraction extracted from the local extinction coefficients are directly proportional to the value of $f(m)$ used. In table 3.2 it is shown that the possible

values for $f(m)$ vary by approximately a factor of 2. If it is assumed that the actual value for the soot lies somewhere in this range then the value of m used in this study ($m = 1.92 - 0.45i$) may cause the measured values of soot volume fraction to be subject to an error of up to ± 30 %.

The third principal error in the measurement of the soot volume fraction is due to the assumption that the particles are in the Rayleigh limit ($2\pi r/\lambda \ll 1$). Selamet and Arpaci (1991) plot the percentage error using the Rayleigh limit instead of the exact solution for values of the size parameter α. Where α is given by

$$\alpha = \frac{2\pi r}{\lambda} \tag{3.18}$$

λ is the incident radiation wavelength - 632.8 nm for the He-Ne laser used in this work. In the 1 atm flame, where the soot particles may be expected to reach 30 nm diameter, the value of the size parameter is 0.15. In the 3 atm, where the soot particles may be up to 60 nm in diameter, the value of α is 0.3. These values of α yield errors of approximately 5 % and 10 % respectively.

The last significant error is that due to the assumption of spherical particles. Thermophoretic sampling of soot with subsequent examination by transmission electron microscopy has been performed on a laminar ethene diffusion flame by Megaridis and Dobbins (1988). The results of this study show that the soot is a chain-like agglomeration of near spherical primary particles. The size of these primary particles is less than 40 nm. Megaridis and Dobbins (1988) give the average number of primary particles per agglomerate as 34. Kumar and Tien (1989) examine the extinction and scattering characteristics of randomly oriented agglomerates. Kumar and Tien (1989) introduce the diameter of an equivalent sphere, this is the diameter of a sphere that exhibits the same extinction or scattering cross section as the agglomerate. They find that the ratio of this equivalent diameter to the diameter of a primary particle is proportional to the cube root of the number of primary particles in the agglomerate. If the proportionality constant is unity then the effective extinction from an agglomerate of N particles is the same as the extinction from N separate particles. Numerical results given by Kumar and Tien (1989) indicate that this proportionality constant is approximately unity for random clusters of

primary particles numbering less than 40. Hence, the effect of non-spherical soot clusters is ignored in this study.

Summing the errors from each of the four principal sources reveals that the mean soot measurement may be subject to an overall error of approximately ±50 % in both of the flames studied. The error is similar for each of the flames despite the relatively high soot loadings of the 3 atm flame. This is due to the increasing importance of light scattering from the larger soot particles formed in the 3 atm flame. This cancels out any increase in the signal to noise ratio encountered in this flame.

3.8 Radiation Intensity Measurement

Mean and instantaneous spectrally resolved radiation intensity measurements are made in both the 1 atm and the 3 atm turbulent methane flames. Rees Instruments scanning monochromators are used for these measurements. The system includes a number of small scanning monochromators which are connected to a control unit, this control unit interfaces to an IBM compatible computer. Control of the system is via software running on the computer. The monochromators are small enough to be mounted on an optical rail. The monochromators comprise of a spectrometer, which contains a motor driven, constantly spinning diffraction grating, and a detector unit which sends an analogue signal, the magnitude of which is proportional to the incident radiative energy, to the main control unit. The control unit also monitors the grating position. Hence, by simultaneously monitoring the grating position and detector signal, spectrally resolved measurements may be taken. The gratings spin inside the monochromators at 12 Hz. Therefore, the time taken for a scan across the full wavelength range of the monochromator is 1/24 s. Two separate detector/grating combinations are used; the first covers the range 600-1900 nm, the second overlaps the first to cover the range 1500-5000 nm. The shorter wavelength unit uses a germanium detector, the longer wavelength unit a cooled lead selenide detector. Second order blocking filters are used in conjunction with the two detector units. These are long pass filters designed to prevent lower wavelength spectral details appearing at positions in the spectra of twice their original wavelength. Two filters are used with the germanium detector, these cover the ranges 600-1100 nm and 1100-1900 nm. Three filters are used with the lead selenide detector, these are used over the ranges 1500-2000 nm, 1650-3000 nm and 2450-5000 nm.

A simple optical arrangement, consisting of a lens, an aperture and the monochromator slit, defines the ray collected by the monochromators. The monochromator slit width is 0.89 mm for both the grating/detector combinations used. The lens material is Ca Fl_2. This arrangement is shown in figure 3.12. Each instantaneous measurement recorded by the spectrometer / computer system is a path integral of the properties along the ray. Also, the ray itself is not one dimensional but due to the optics used is almost rectangular in cross section. The major dimension of this cross section is parallel to the axis of the flame and varies across the width of the flame from approximately 5 mm, on the side of the flame

nearest to the monochromator, to approximately 10 mm, on the far side. The minor cross sectional dimension varies from approximately 2 mm, on the side on the flame nearest to the monochromator, to approximately 5 mm, on the far side. The optics are aligned using a He-Ne laser. The signal strength recorded by the detector is very sensitive to the angle of the monochromator unit to the incident radiation. This angle is adjusted until the maximum signal strength is seen on the He-Ne line.

The system is calibrated with a Spembly furnace, which approximates a theoretical black body. This furnace comprises of an electrically heated, hollow carbon sphere, with a hole in one side, contained in an insulated gas tight vessel, that is purged with argon. It is this hole which is considered as a black body surface. A Ca Fl_2 window allows optical access to the carbon sphere. The transmittivity of this window is flat across the spectral interval studied and has a value of 0.935. A calibrated photovoltaic sensor gives the temperature of the furnace.

The experimental procedure for recording a calibrated spectrum is as follows. The first step is to calibrate the grating position / wavelength sensor in the monochromator system unit. This is achieved by passing the signal from a He-Ne laser into the monochromator. The He-Ne laser has several output orders at well defined wavelengths. By determining the grating position corresponding to one of these orders wavelength calibration is accomplished. The next step is to perform a dark level calibration for the detector, this establishes a base detector output voltage in the absence of any radiation. Once these calibrations have been completed the flame spectra are recorded. The last step is to record a spectrum from the black body furnace. This spectrum is used to calibrate the flame spectra. The calibration is carried out at each wavelength using the following equation

$$I_\lambda = \frac{M_{\lambda,F}}{M_{\lambda,b}} \tau_{Win.} I_{\lambda,b} \qquad (3.19)$$

where I_λ is the calibrated flame spectral measurement, $M_{\lambda,F}$ is the uncalibrated flame spectrometer measurement, $M_{\lambda,b}$ is the spectrometer measurement made on the furnace, $\tau_{Win.}$ is the transmission factor for the window and $I_{\lambda,b}$ is the Planck distribution function - Planck (1959), given by

$$I_{\lambda,b} = \frac{2 h c_0^2}{\lambda^5 (\exp(h c_0 / \lambda k T) - 1)} \tag{3.20}$$

Mean and instantaneous radiation intensity measurements are made in both the 1 atm and the 3 atm flames. The measurements are made on optical paths that pass perpendicularly through the axis of the flames. Two mean intensity measurements are taken at each vertical measurement station with each grating/detector/filter combination. Each mean measurement is the average of 500 samples. These two datasets are compared to check the repeatability of the measurement, see figure 3.13, and are then averaged to give a final mean of 1000 samples. The individual mean spectra from each grating/detector/filter combination are joined in the regions of overlap. Figure 3.14 reveals that the measurements made in the 1500-2000 nm region are redundant and therefore these measurements are not used. The other four measurement sets (600-1100, 1100-1900, 1650-3000 and 2450-5000 nm) are joined at 1100, 1750 and 2750 nm. At these points the spectra are found to overlap / join perfectly, see figure 3.14. The mean radiation data for the 1 and 3 atm flames are presented in the appendix. In figure 3.15 an example of the spectra recorded for both the 1 atm and the 3 atm flames is shown. The spectra recorded in the 3 atm flame exhibit a 'hole' in the 4300 nm CO_2 band. This 'hole' does not disappear after calibration. There are two possible causes for such a spectral 'hole'. The first is a hardware problem with the monochromator system. The 1 atm flame measurements, that exhibit no such 'hole' in the spectra, were made before those in the 3 atm flame. A fault may have developed in the intervening period. The second cause may be due to the rig in which the measurements were made. The radiation measurements in the 1 atm flame were made using the atmospheric flame rig - see section 3.2 - obviously the measurements in the 3 atm flame were made in the elevated pressure rig. An undesirable feature of this elevated pressure rig is the existence of a nearly stagnant region of gas between the Pyrex flame tube and the rig windows - see figure 3.16. It is likely that combustion products fill this space. The relatively cool CO_2 would absorb some of the flame radiation possibly creating the spectral 'hole'. This possibility is examined in chapter 6.

Instantaneous, 'single-shot' spectra are also recorded at a single height in the 1 and 3 atm flames. The optical path of the spectrometer again passes perpendicularly through the axis

of the flames, as for the mean measurements. The height of this optical path is 250 mm above the burner exit plane. Because the time taken for a single spectral scan is 1/24 s the wavelength points in each spectra are not necessarily correlated, one would expect the time scales in these flames to be much shorter than 1/24 s. However, from these 'single-shot' spectra radiation statistics at single wavelength points may be determined. For each flame approximately 150 'single-shot' spectra are recorded using two of the grating/detector/filter combinations. The two grating/detector/filter combinations cover the ranges 1100-1900 nm and 2450-5000 nm. For each set of spectra, four wavelength points are chosen at which the intensity statistics are calculated. In the 1 atm flame these points are 1650, 2834, 3332 and 4359 nm. In the 3 atm flame these points are 1700, 2846, 3342 and 4435 nm. These points are chosen to represent the peaks of the main gas band and soot radiation in each of the flames, based on the position of these peaks in the mean spectra at this height. At each wavelength point the range in radiation intensity, from zero to the maximum recorded at that point, is divided into 10 equally spaced 'bins'. The first 'bin' covering the region from 0 to 10 % of the maximum, the second from 10 to 20 %, continuing up to the tenth 'bin' covering the region from 90 to 100 % of the maximum. The data from the 'single-shot' spectra are then sorted into these 'bins', giving the relative frequencies for the intensity variations. The data is normalized by dividing each relative frequency by the total number of 'single-shot' spectra. This yields a discrete representation of the probability density function (PDF) of radiation intensity at each of these wavelength points. In figure 3.17 the discrete PDF of radiation intensity for the 1 atm flame at 4359 nm is shown. A Gaussian fit is also shown on this figure. The 'bin' centre values (5, 15,...,95 %) are used for this Gaussian fit. The complete set of PDFs for both flames are given in the appendix.

There are two main sources of error that may affect these radiation intensity measurements.

The first error would result from the misalignment of the optical components, particularly when changing grating/detector units or moving the optical system from flame measurements to furnace measurements. However, the near perfect joining of the spectra recorded using different grating/detector units would indicate that this is not a problem.

The second source of possible error is the temperature measurement of the black body furnace used for spectra calibration. Equation 3.19 shows that the calibrated flame intensity

at any wavelength position is proportional to the Planck distribution function at that wavelength. The value of the Planck distribution function is determined using the measured furnace temperature. Hence, the percentage error in the spectral intensity values are proportional to the percentage change in the Planck distribution function which would arise from a difference between the measured value of temperature and the real temperature value. The furnace temperature measured for all the recorded black body spectra is approximately 1975 K. Figure 3.18 plots the percentage change in the Planck distribution function versus wavelength for temperature changes of -50 K, -25 K, +25 K and +50 K from 1975 K. Figure 3.18 shows that for an error in the measured temperature of ±50 K, the error in the measured spectra is less than 20 % at all wavelengths greater than 1 micron.

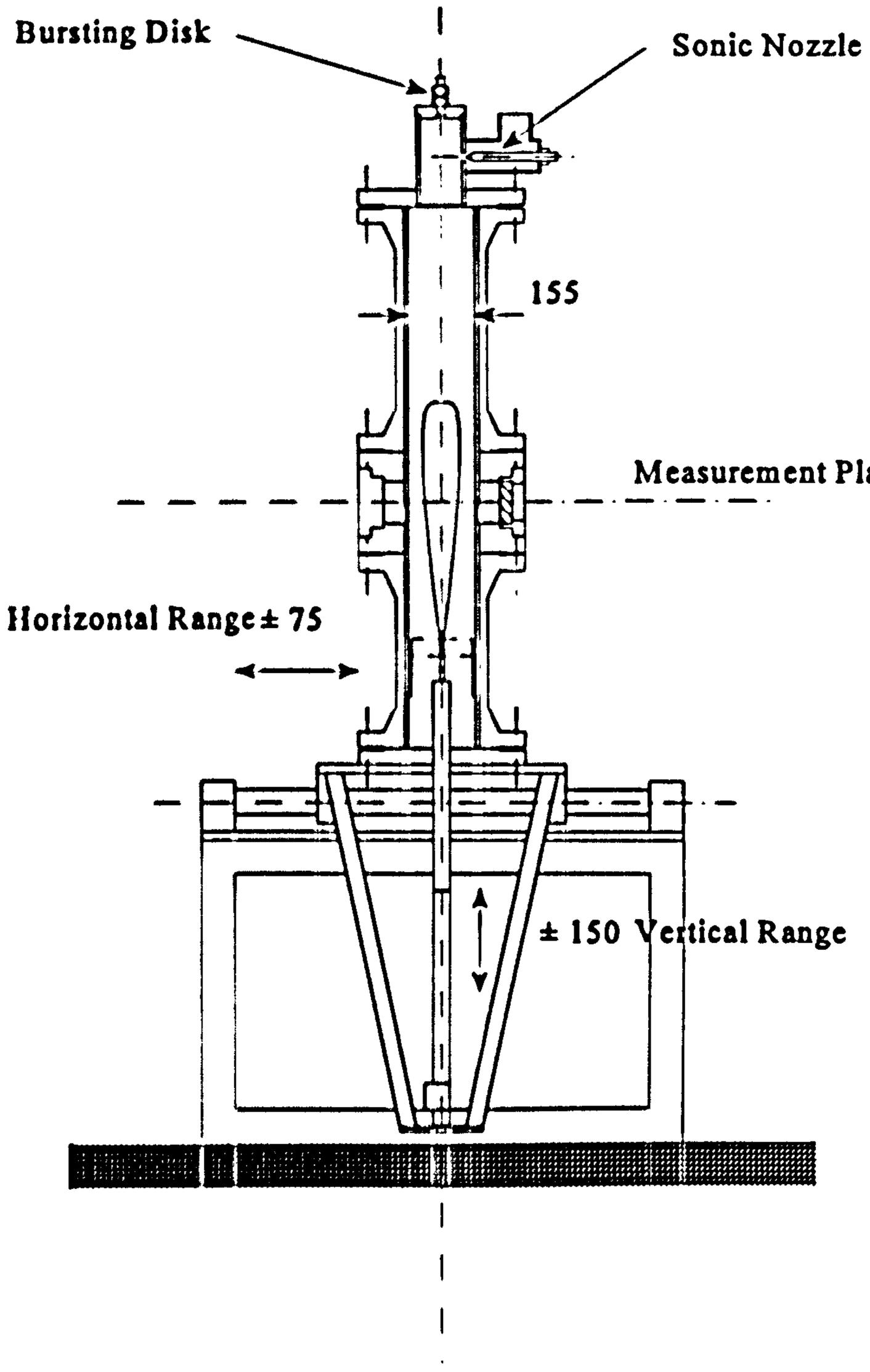

Figure 3.1. Simplified cross sectional view of the high pressure jet flame rig. All dimensions are in mm.

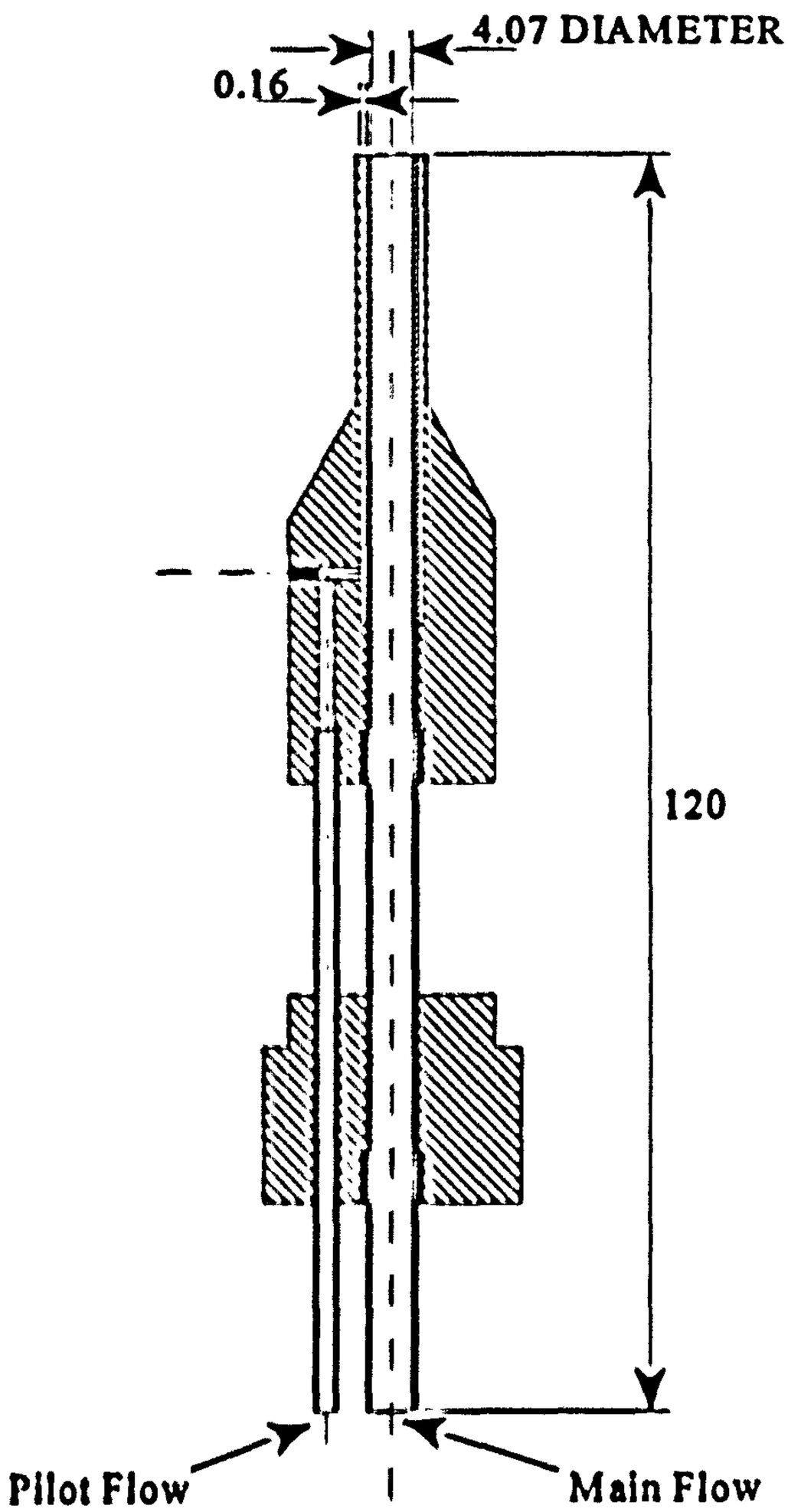

Figure 3.2. Sectional view of the methane burner used in this study. All dimensions are in mm.

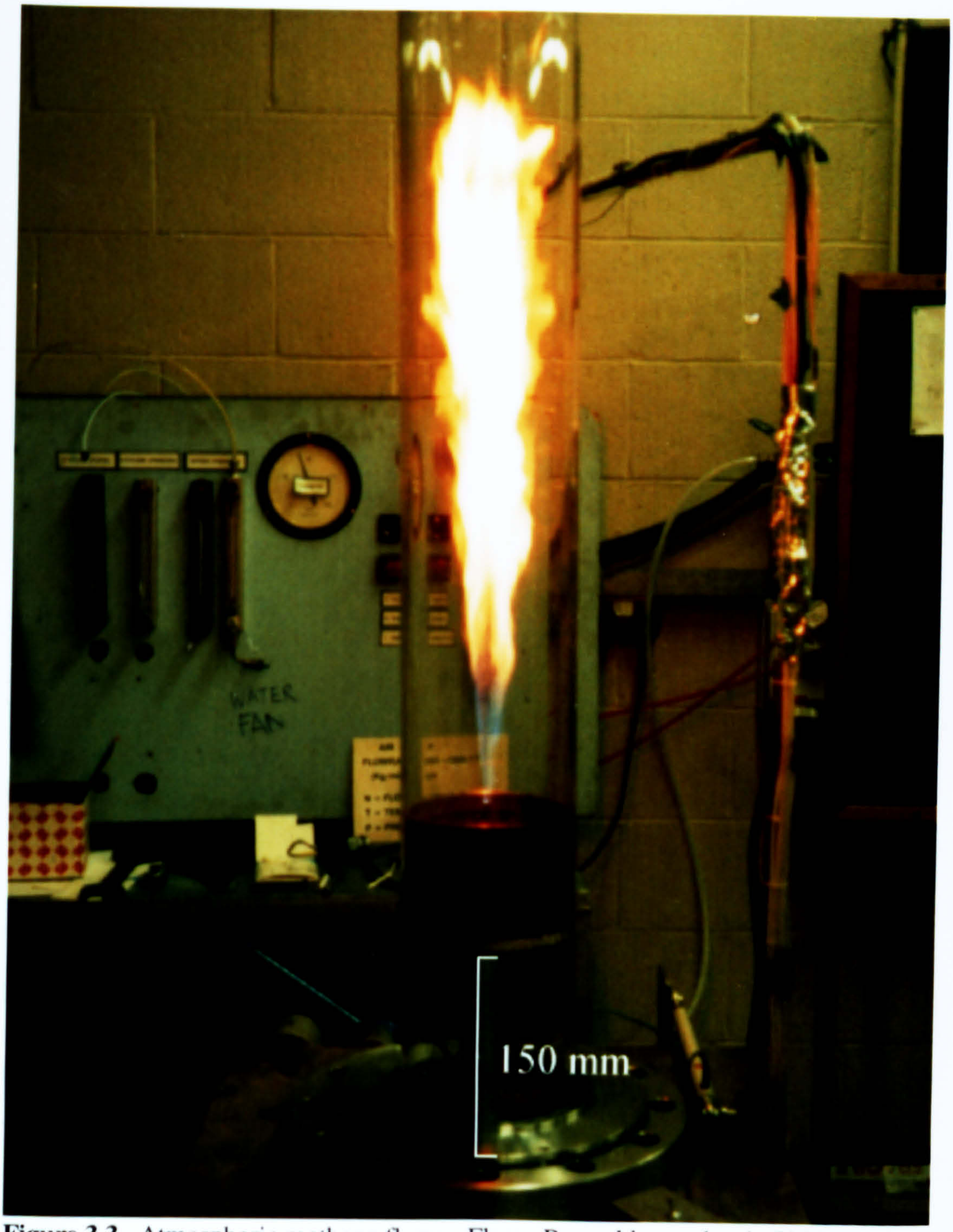

Figure 3.3. Atmospheric methane flame. Flame Reynolds number is 5000 based on the conditions at the nozzle exit.

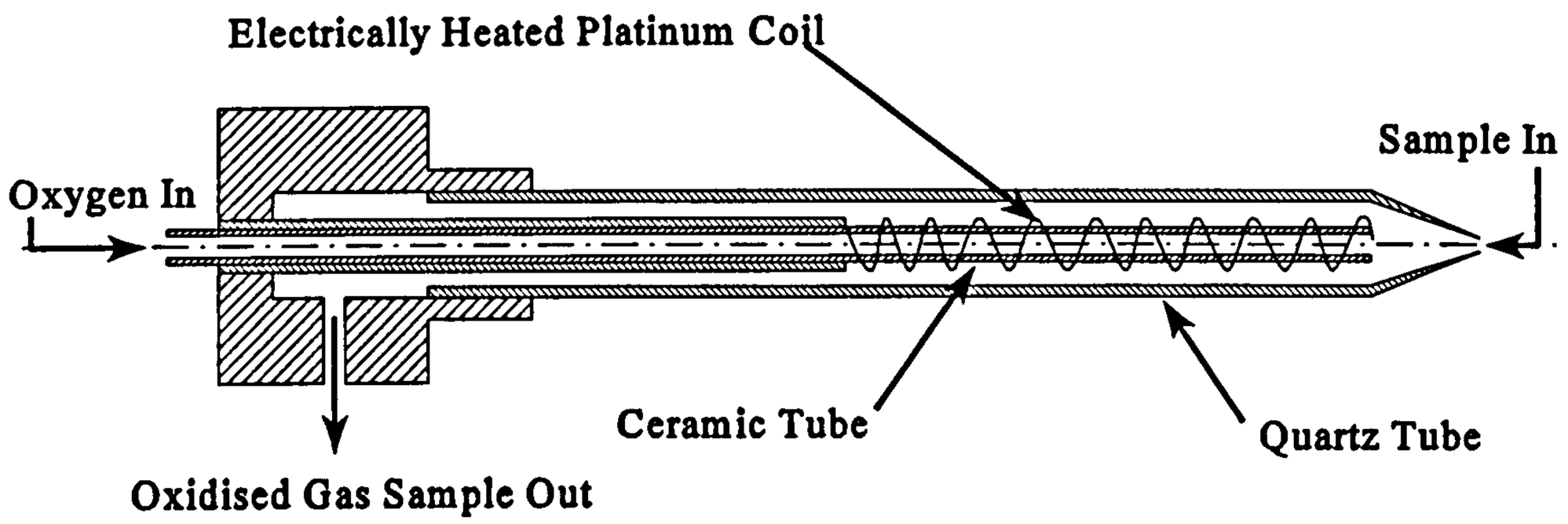

Figure 3.4. Simplified sectional view of the mixture fraction probe used in this work.

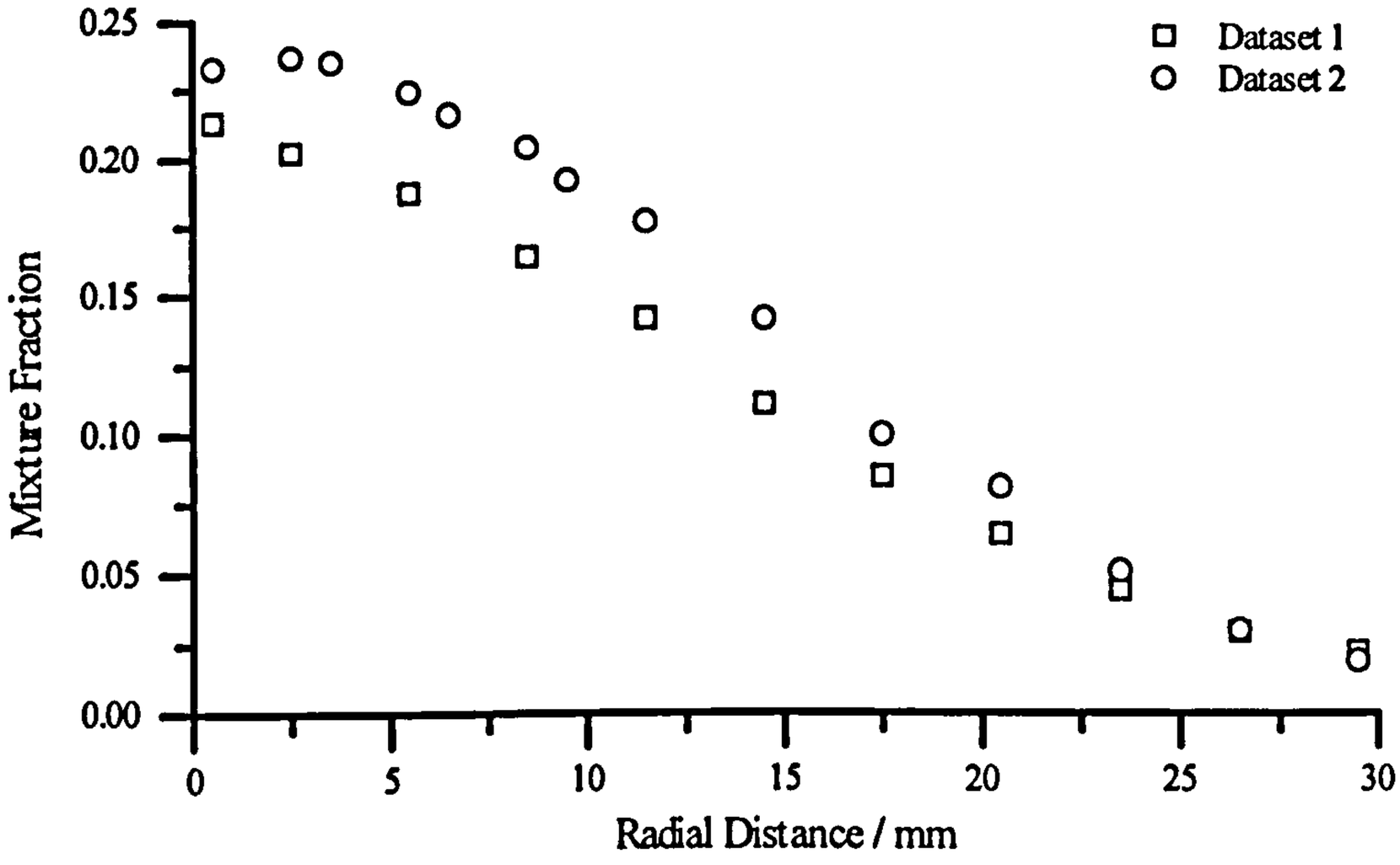

Figure 3.5. Repeatability of the mixture fraction measurements. Profiles taken from the 1 atm flame at a height of 200 mm above the exit plane of the burner.

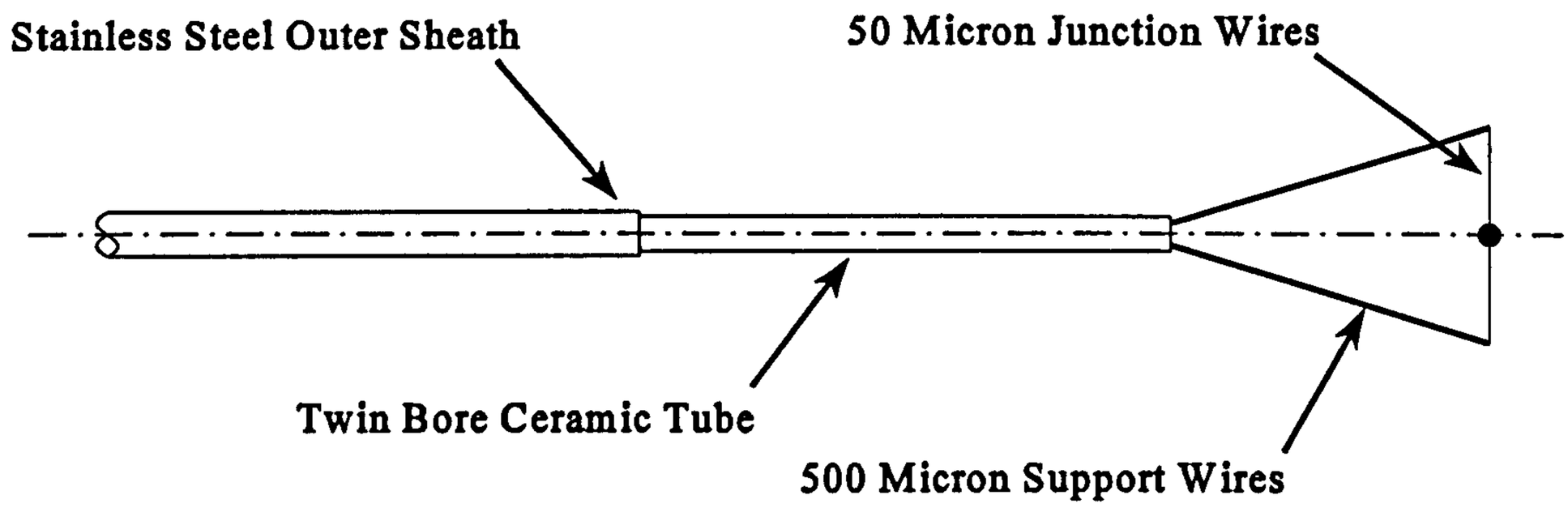

Figure 3.6. Diagram of the thermocouple probe used in this work.

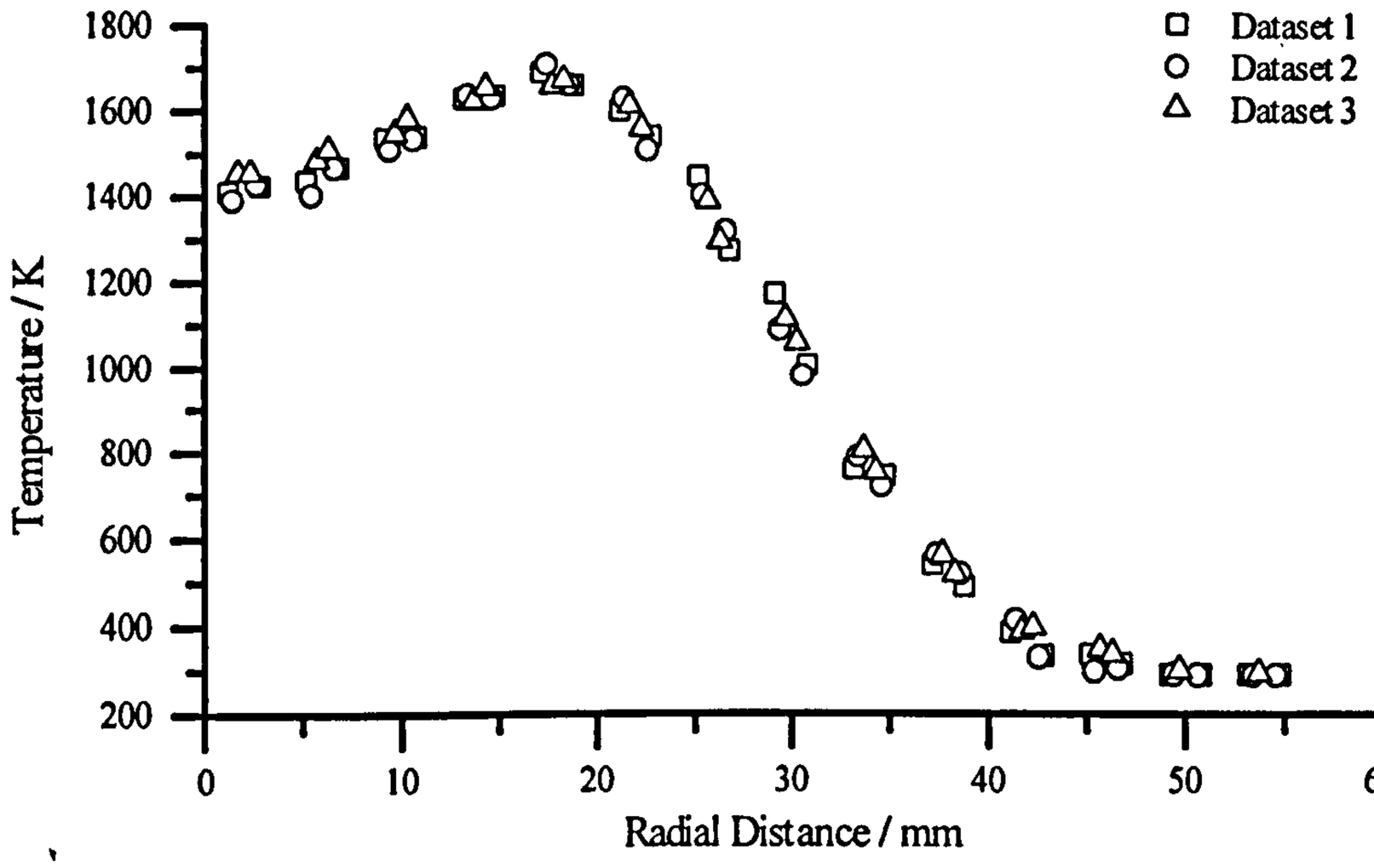

Figure 3.7. Repeatability of the temperature measurements. The radial profile shown is from the 1 atm flame at a height of 250 mm above the exit plane of the burner.

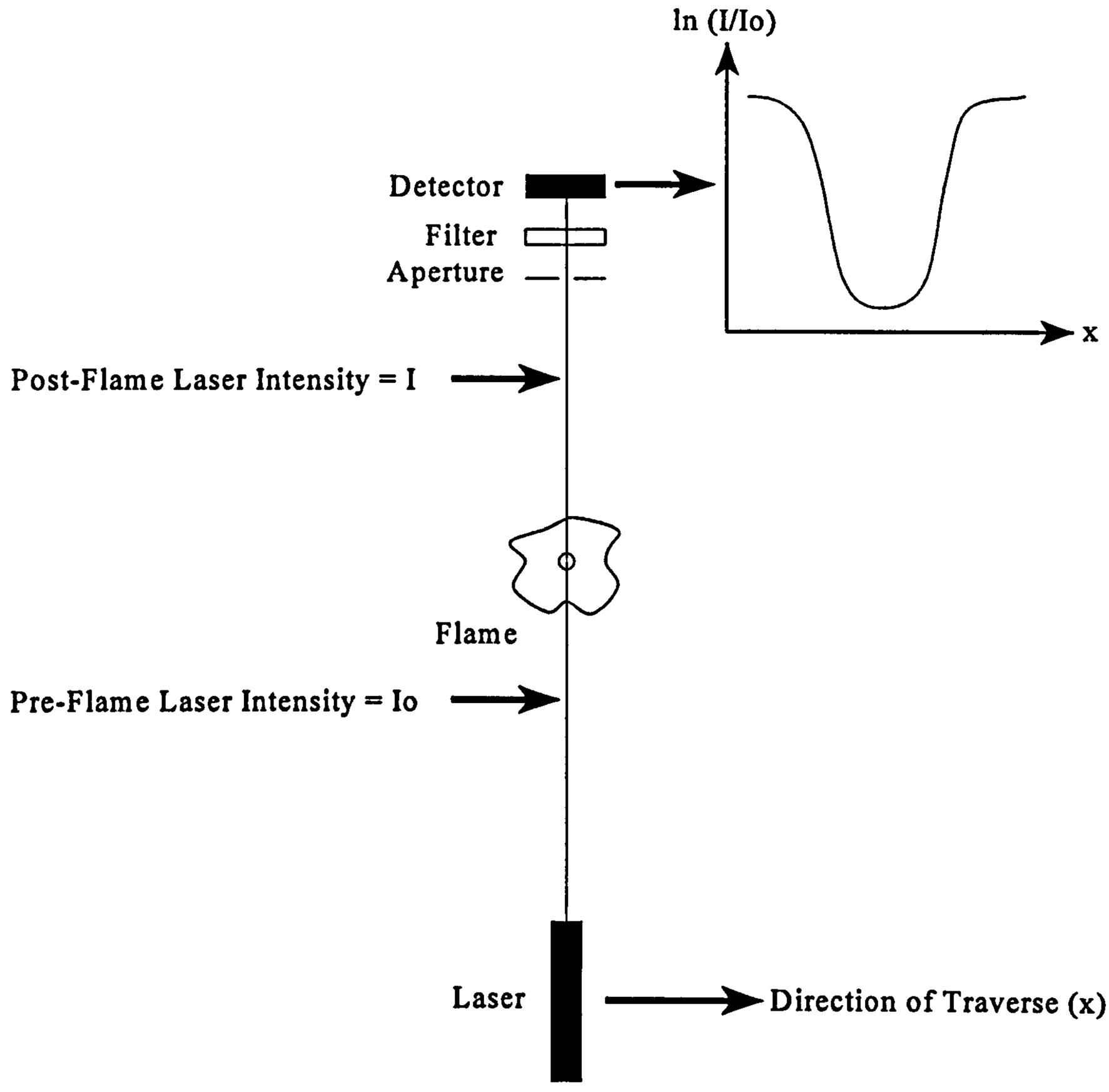

Figure 3.8. Schematic of the soot measurement experiment.

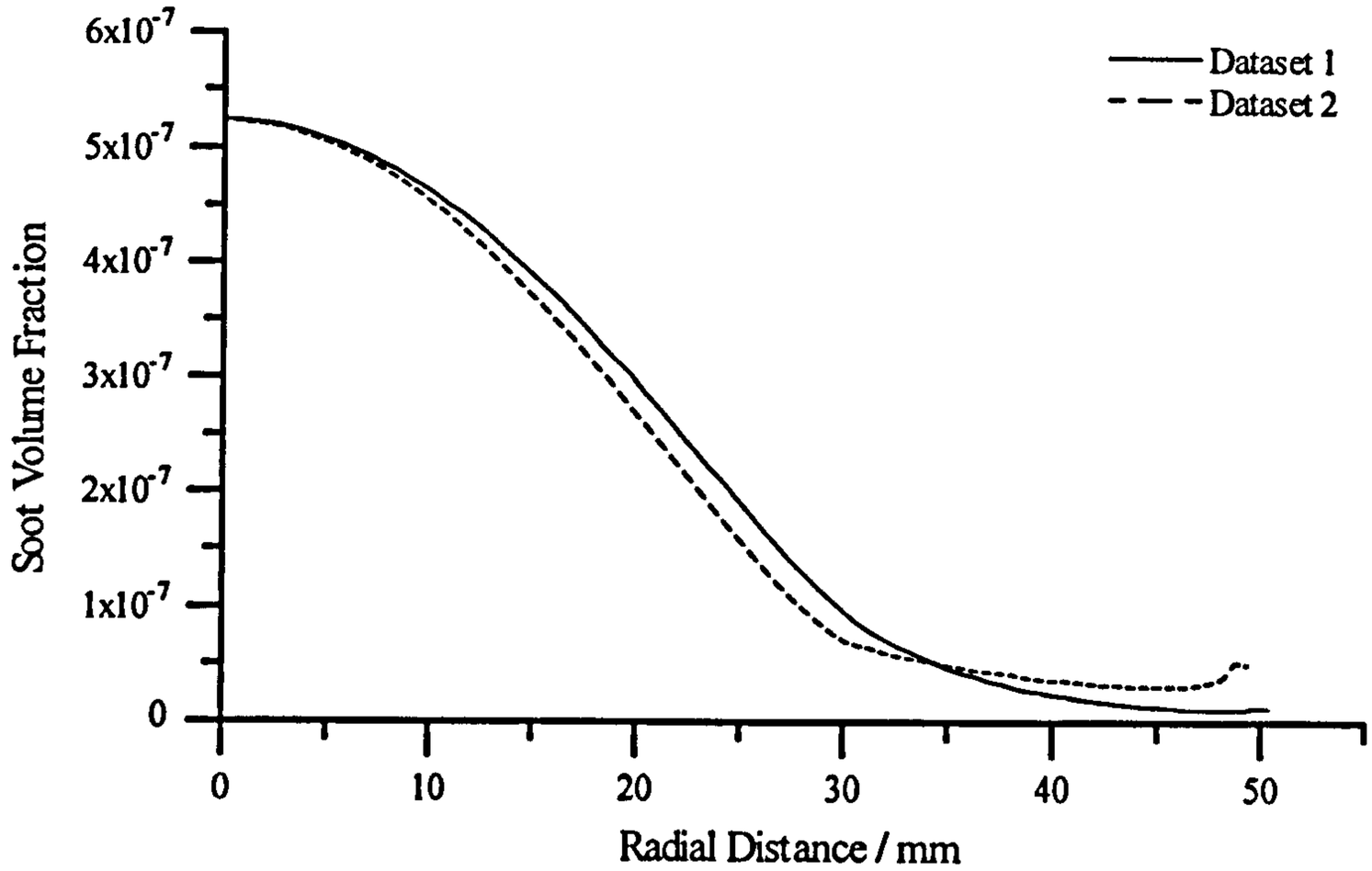

Figure 3.9. Repeatability of the soot volume fraction measurements. Profiles shown are from the 3 atm flame at a height of 350 mm above the exit plane of the burner.

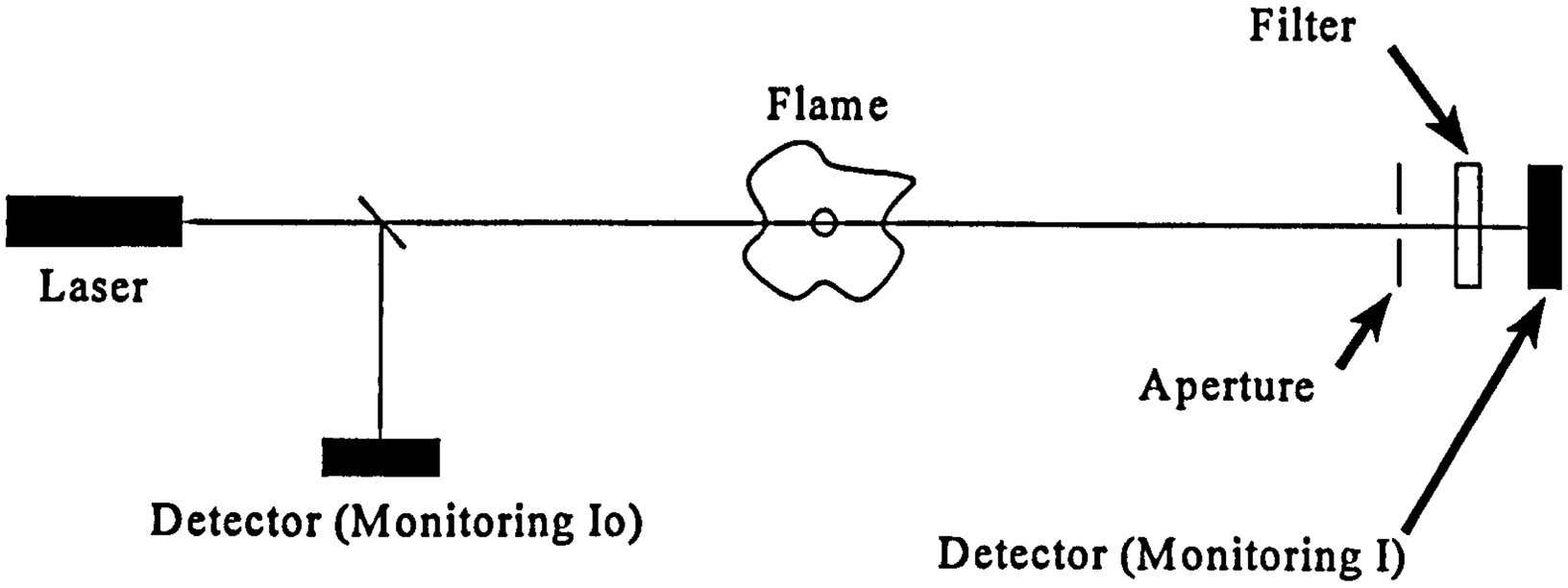

Figure 3.10. Schematic of soot measurement experiment incorporating continuous monitoring of the laser intensity.

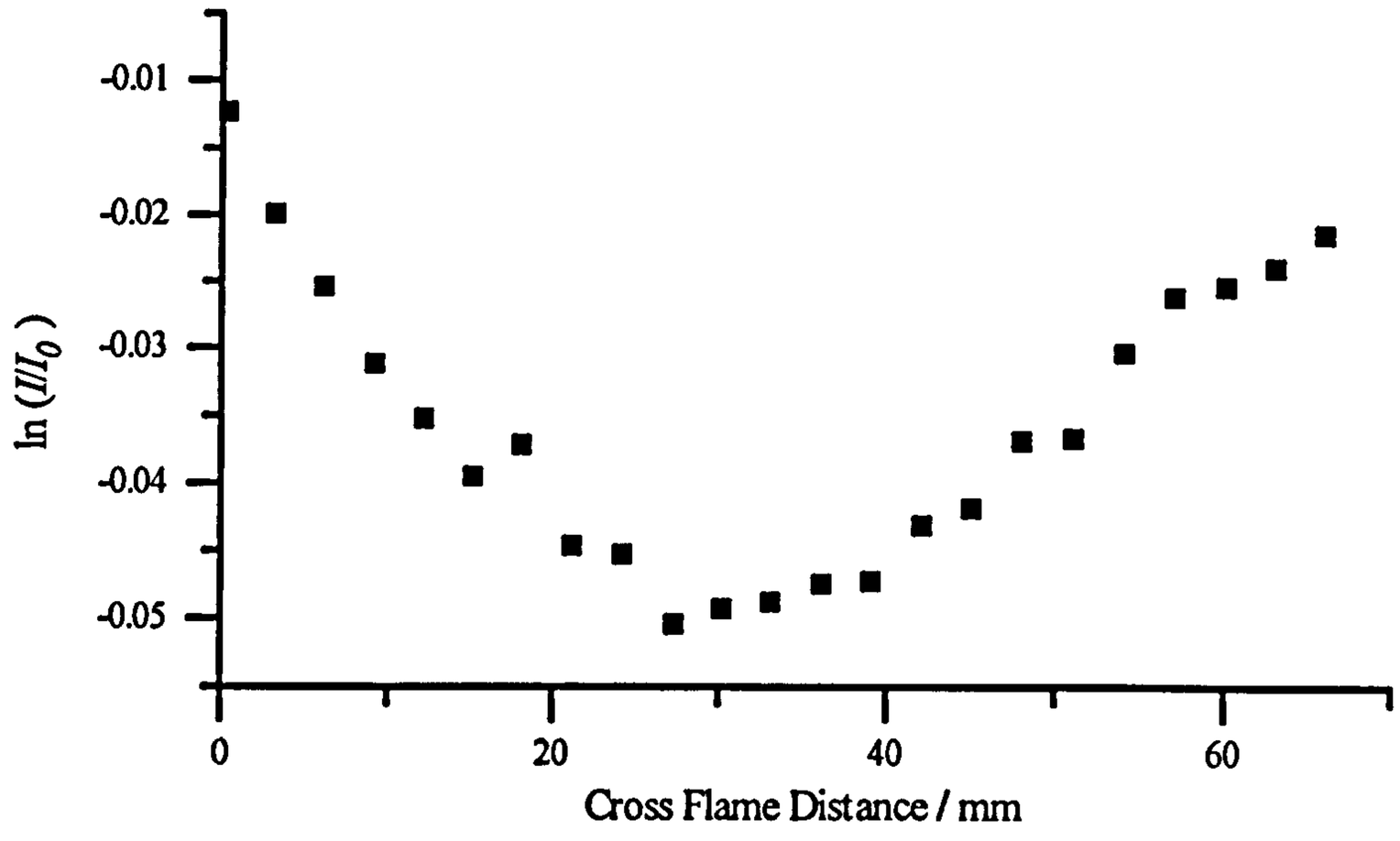

Figure 3.11. Absorption profile in the 1 atm flame. The height of the traverse above the burner exit plane is 425 mm.

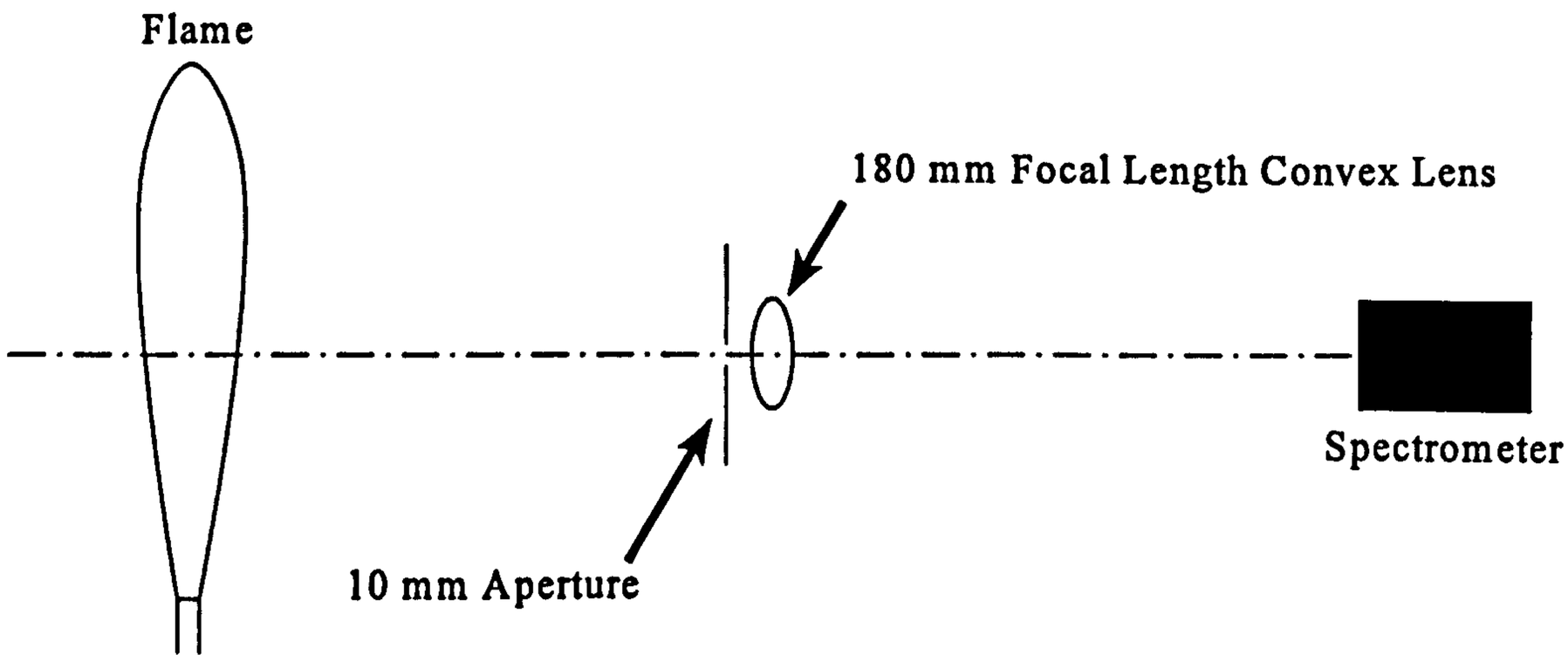

Figure 3.12. Schematic of the optical setup used for making the measurements of radiation intensity.

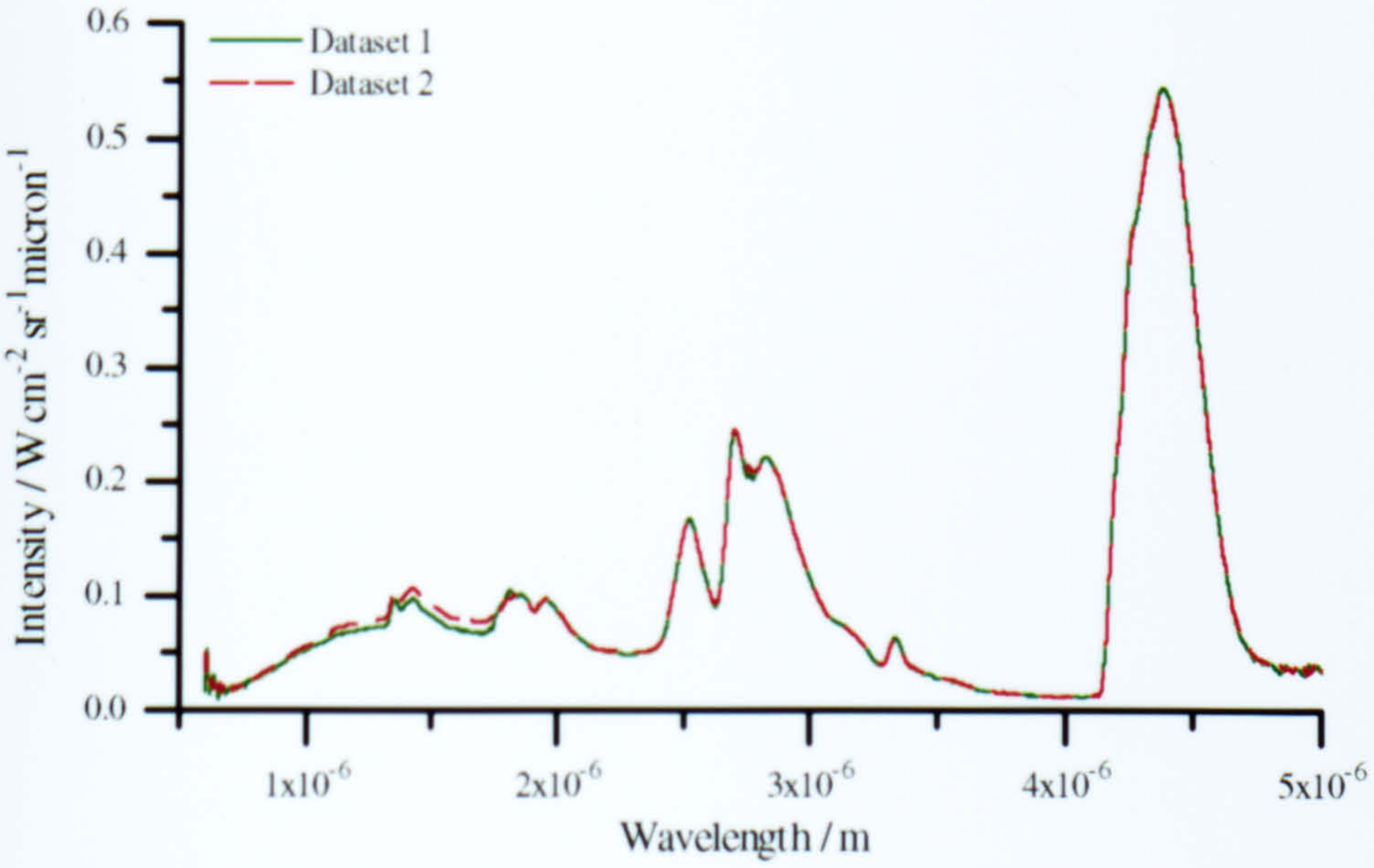

Figure 3.13. Repeatability of the measurement of radiation intensity. These spectra are recorded from the 1 atm flame at a height of 425 mm above the burner exit plane.

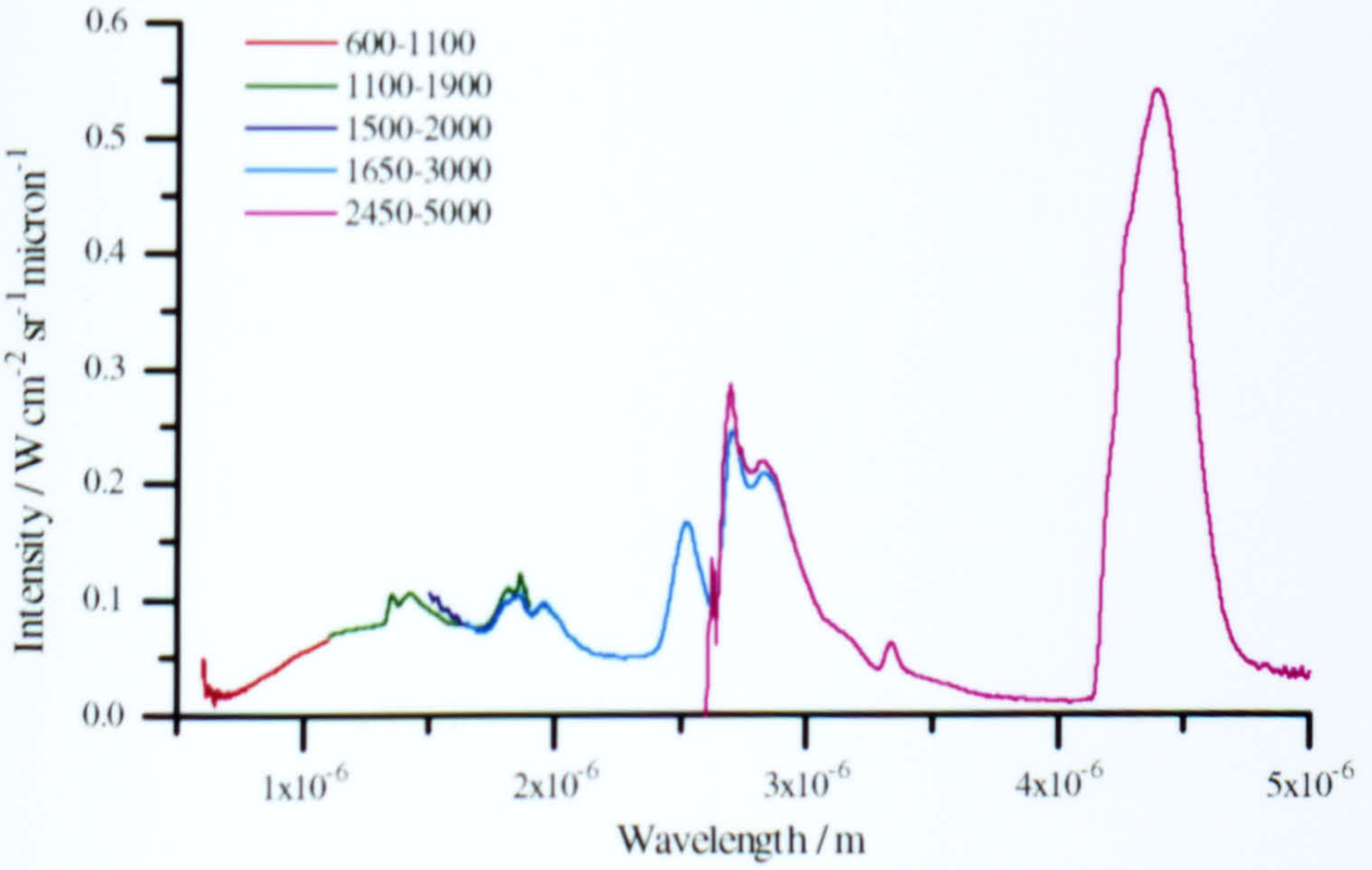

Figure 3.14. Contributions to the spectrum from the grating/detector/filter combinations used in this study. The legend gives the range of each grating/detector/filter combination in nm.

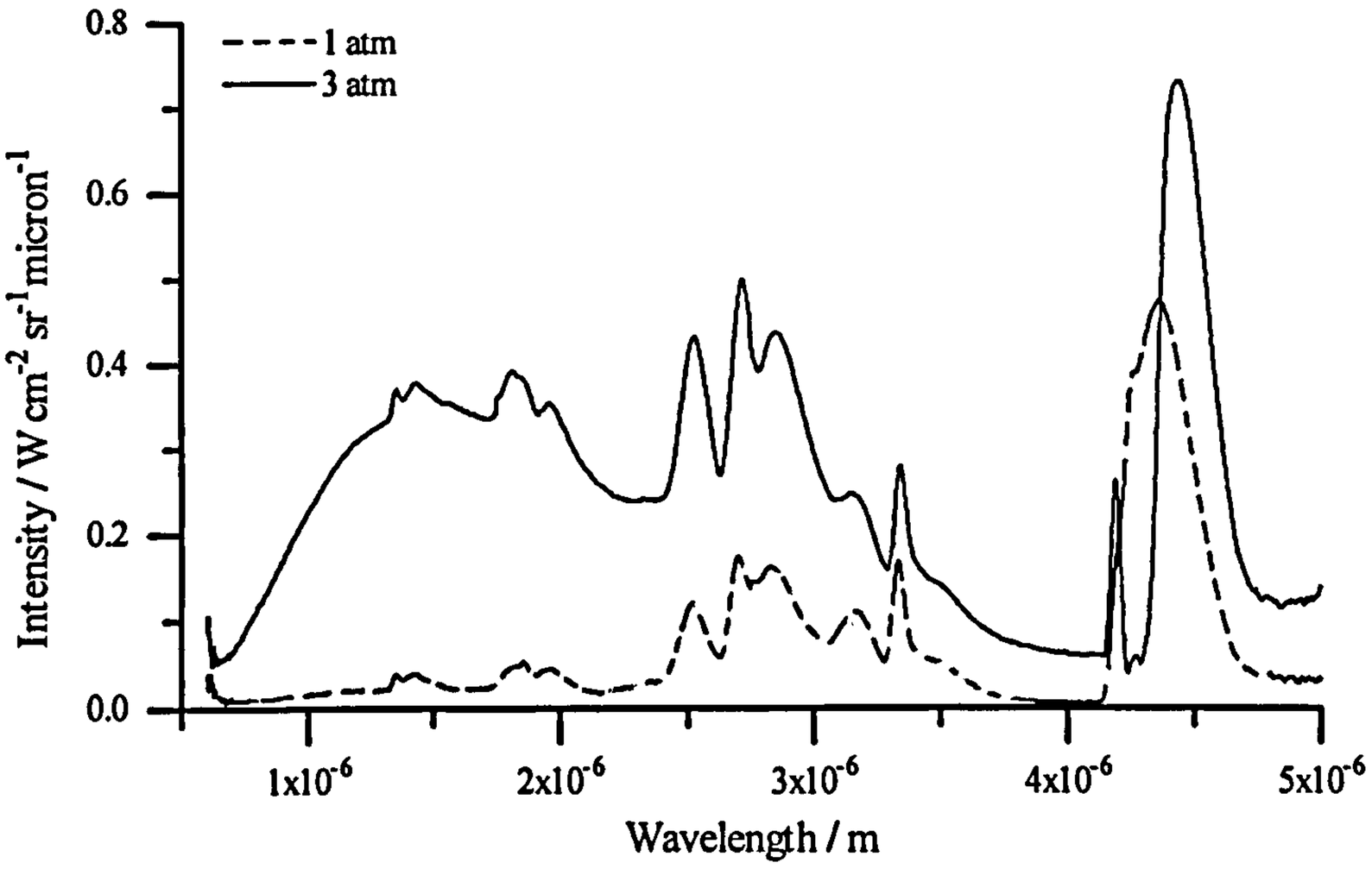

Figure 3.15. Mean radiation intensity spectra at a height of 250 mm above the exit plane of the burner.

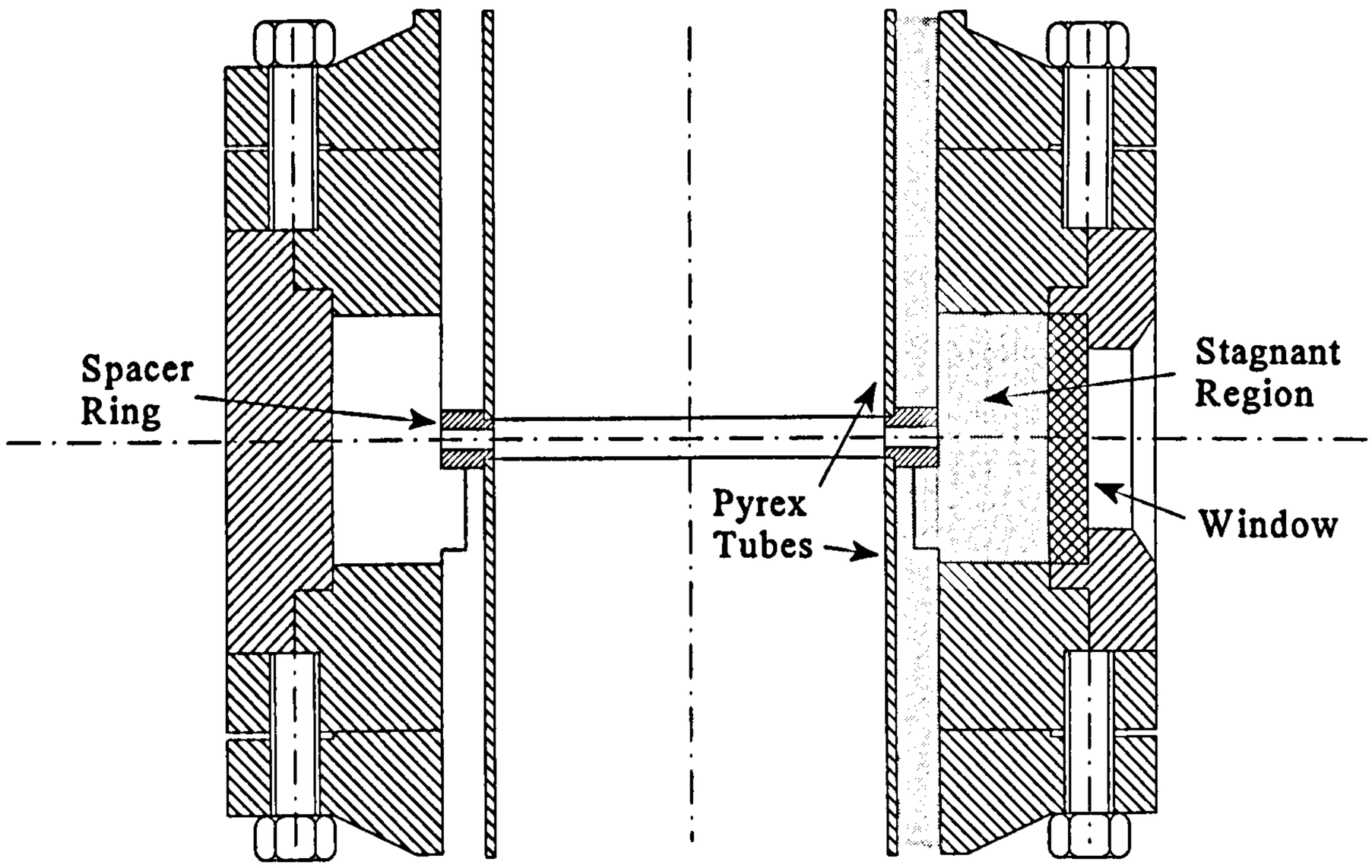

Figure 3.16. Cross section of the high pressure rig measurement section showing stagnant space (shaded) where combustion products may accumulate.

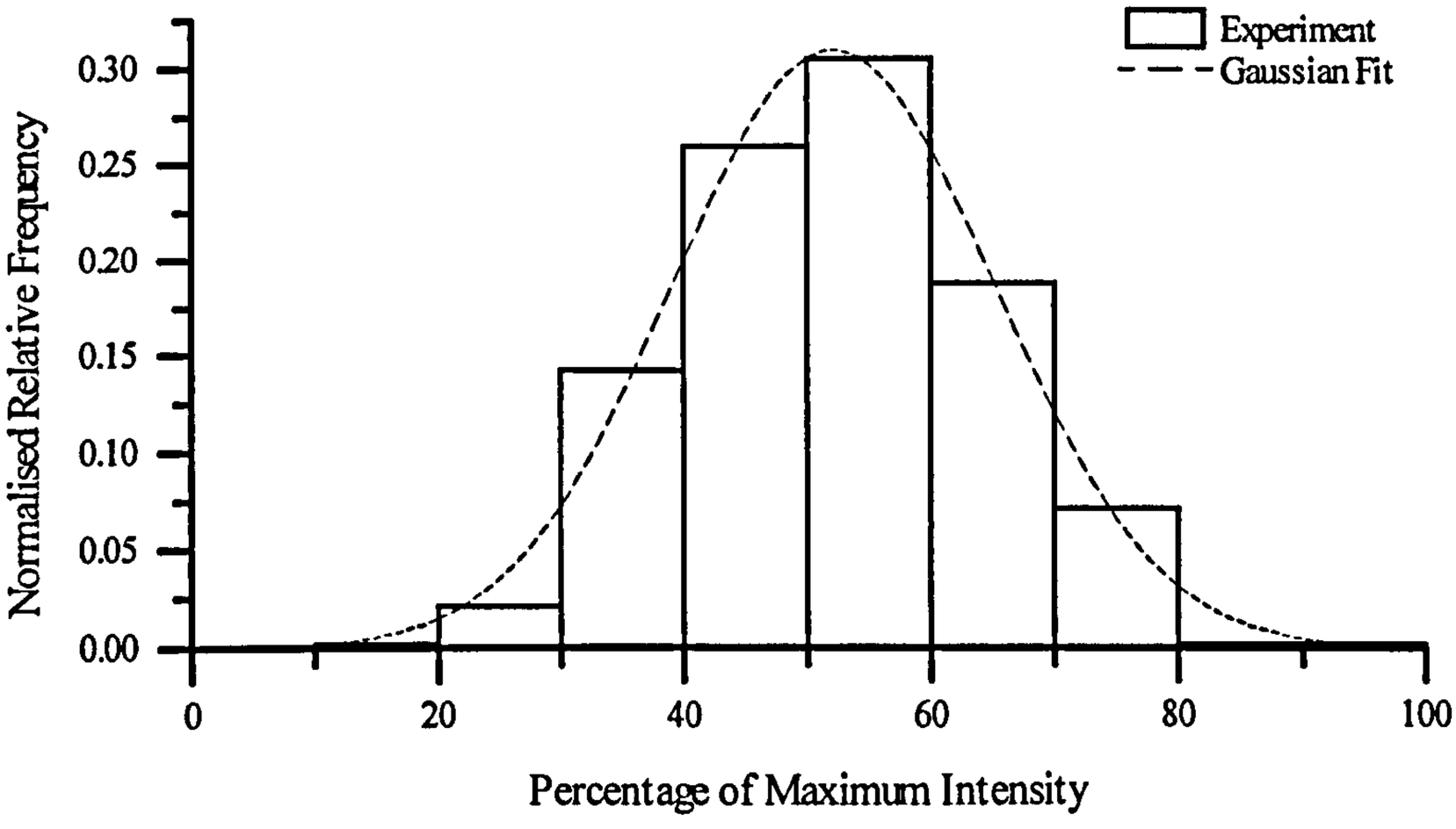

Figure 3.17. Experimental discrete PDF of radiation intensity. This PDF is taken from the 1 atm flame dataset. The wavelength is 4359 nm. The maximum intensity recorded is 0.90664 W cm^{-2} sr^{-1} $micron^{-1}$. The mean value of intensity is 52.4 % of this maximum value.

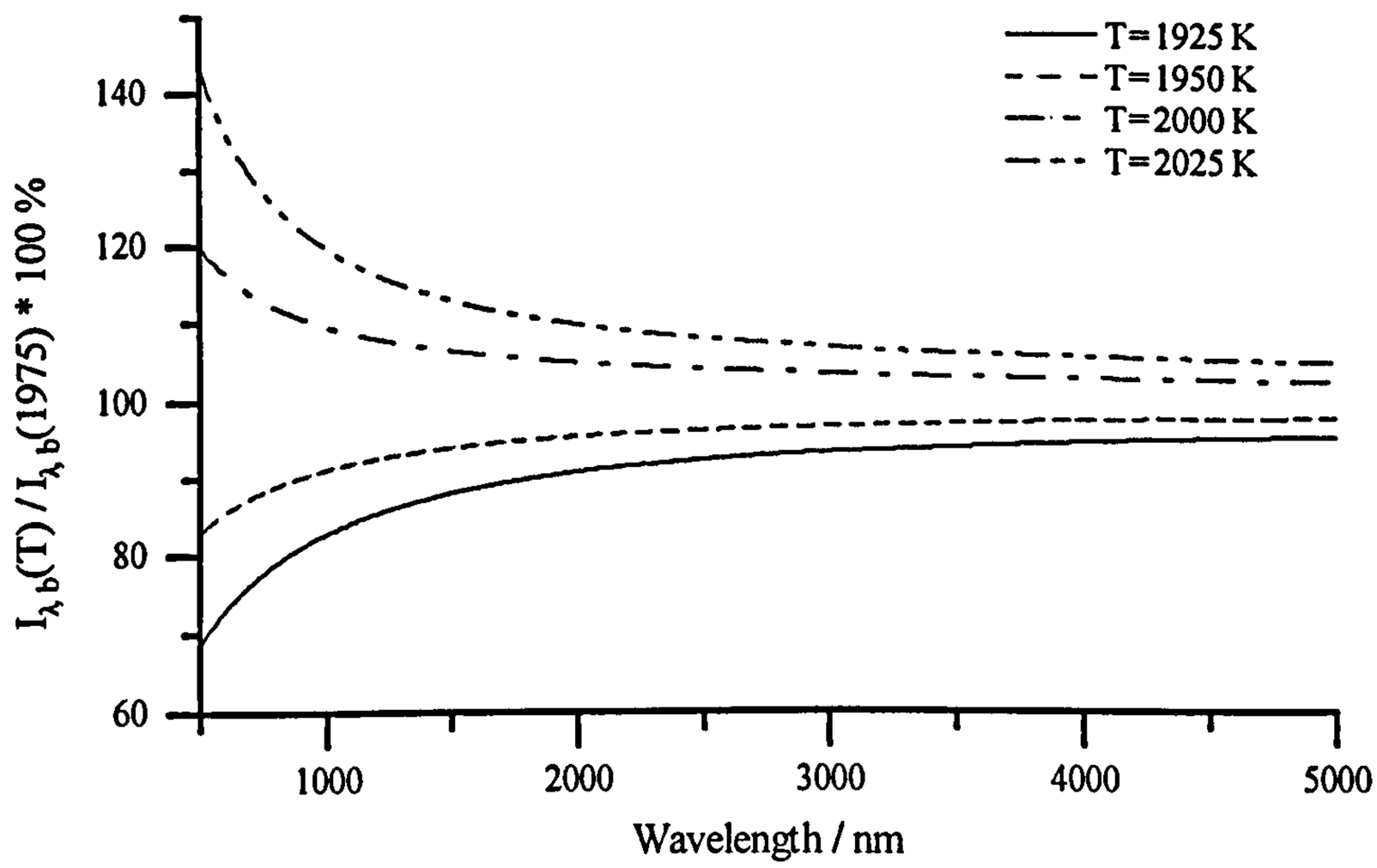

Figure 3.18. Percentage change in the Planck distribution function for changes in the temperature relative to 1975 K.

Chapter 4 - Modelling Sooting Laminar Flames

4.1 Introduction

While recent progress has been made in modelling the detailed chemical aspects of soot production (see chapter 2), such models are not suitable for inclusion in turbulent flame calculations due to the complexity of closing chemical source terms in turbulent flows. The soot model development here, therefore, concentrates on an empirical approach to soot modelling - relying on experiment for model 'calibration'. The model calibration is performed by applying the soot model to a simulation of a laminar flame - the model constants being adjusted until the best fit to the experimental soot properties data, for the flame, is obtained.

The accuracy of the vector and scalar fields given by the flame simulation is of paramount importance; especially with respect to temperature, to which the soot formation rate is extremely sensitive. Previous approaches to modelling laminar flames (see chapter 2) have tended to either rely on the fast chemistry assumption, where the gaseous species and temperature are taken to be functions of mixture fraction, or have attempted to model the flame chemistry in a more detailed manner, with reduced or full chemical reaction schemes. Here the fast chemistry assumption is only applied to the gaseous chemical species, which are taken to be unique functions of mixture fraction. The temperature is determined from the flamelet composition and the enthalpy, which is derived from its own balance equation. This allows the soot model to be coupled to the flame's radiative loss by including the soot radiation in the enthalpy source term.

In section 4.2 the basic equations governing the vector and scalar fields for the laminar flame simulation are developed. The sub-sections of section 4.3 then describe in some detail the physical models required to close these equations; specifically the combustion model used, the momentum, mass and energy transport model, the radiative loss model and

the soot model.

The laminar flame of Syed (1990) has been used for the initial soot model calibration and further model comparisons have been made with the data sets provided by Mitchell et al. (1980a) and Garo (1984).

4.2 Governing Equations

For a full description of the vector and scalar fields in the laminar flame, equations for continuity, momentum conservation, energy conservation and species conservation must be solved.

The equation for conservation of a single species *i* may written as

$$\frac{\partial(Y_i \rho)}{\partial t} + \nabla \cdot \vec{m}_i = S_i \tag{4.1}$$

The mass flux vector for species *i* consists of two components, a convective component and a diffusive component. If the diffusion velocity may be represented by Fick's law then this mass flux vector is expressed as

$$\vec{m}_i = Y_i \rho \vec{u} - \rho D \nabla Y_i \tag{4.2}$$

Summing all the individual species conservation equations gives the continuity equation

$$\frac{\partial \rho}{\partial t} + \nabla \cdot (\rho \vec{u}) = 0 \tag{4.3}$$

If the only forces in the fluid are those arising from gravity, pressure and the viscosity of the fluid then the momentum conservation equation is

$$\rho \frac{\partial \vec{u}}{\partial t} + \rho \vec{u} \cdot \nabla \vec{u} = \rho \vec{g} - \nabla P + \nabla \cdot \tau \tag{4.4}$$

where τ is the deviatoric stress tensor. In a low speed, chemically reacting flow system the energy conservation equation may be written as

$$\rho \frac{\partial h}{\partial t} + \rho \vec{u} \cdot \nabla h = -\nabla \cdot \vec{q} + \dot{Q} \tag{4.5}$$

where h is the total specific enthalpy (chemical + sensible), $\vec{q}$ is the heat flux vector and $\dot{Q}$ is the volumetric energy source. If the Dufour effect is ignored, this is nearly always negligible, then the heat flux vector is given by

$$\vec{q} = -\lambda \nabla T - \rho D \sum_i h_i \nabla Y_i \qquad (4.6)$$

This system of NS+4 coupled partial differential equations, where NS is the number of species in the system, needs to be solved for a three-dimensional flame simulation. Note that the number of coupled partial differential equations is NS+4 not NS+5, as the continuity equation may replace one of the species conservation equations. Additional relationships are needed to close this set of equations, these are the equation of state

$$\rho = \frac{P}{RT} \sum_i X_i M_i \qquad (4.7)$$

and the relationship between temperature and enthalpy

$$h = \sum_i \left(\Delta h^\circ_{f,i} + \int_{T^\circ}^{T} C_{P,i} dT' \right) \qquad (4.8)$$

Also relationships will be needed for the viscosity and the diffusion coefficients, as these are not, in general, constant in a combusting system. The method used for generating the viscosity is introduced in sub-section 4.3.2, a relationship between the viscosity and the diffusion coefficients is presented later in this section.

The solution of this set of NS+4 partial differential equations is very time consuming, as the value of NS for a detailed representation of the combustion chemistry of a methane / air flame is 38, Warnatz (1981). There are, however, simplifications to the above set of equations that may be made without introducing unacceptable errors. The first simplification, that is applicable to many flow problems and certainly to the laminar flames modelled in this chapter, is to assume that the flow is steady (time invariant). Some flows, including the flames modelled here, may be approximated by fewer than three dimensions. This removes one of the momentum transport equations and all of the terms in the third dimension in the other conservation equations. This leaves NS+3, simplified, coupled partial differential equations; the solution of which is still a formidable task for anything other than the most powerful computers. Further, more substantial, simplifications may

be made if the transport coefficients, D, of all the species are considered equal and the Lewis number, $\mathrm{Le} = \lambda/(\rho C_p D)$, is taken as unity. With the exception of hydrogen, the diffusions coefficients for most gases are approximately equal. Under these assumptions transport equations for conserved scalars may be derived. Conserved scalars are unaffected by chemical reactions in the system and their transport equations have no source term. If $\dot{Q}$ is zero then, under the above assumptions, enthalpy is a conserved scalar. If the chemical reaction rates are infinitely fast then chemistry dependent scalars are unique functions of conserved scalars - Bilger (1976). If these functions, often called flamelets or state relationships, are known then solution of a single balance equation for a conserved scalar will give the entire scalar field for the flame. The most commonly used conserved scalar in practice is the mixture fraction, represented by the symbol ξ; this is defined as the mass fraction of elements originating in the fuel stream. The balance equation for the mixture fraction, in a steady flow, may be written as

$$\nabla\cdot(\rho \vec{u}\xi - \rho D \nabla\xi) = 0 \qquad (4.9)$$

This has reduced the two-dimensional laminar flame problem to a system of 4 coupled partial differential equations. In real flame situations the constraints imposed above - equal diffusion coefficients, unity Lewis number, infinitely fast reaction rate and zero heat loss - may be violated to some extent. However, experiment has shown that scalar properties correlate well with mixture fraction in laminar diffusion flames - Bilger (1977). The flamelet functions, therefore, may be obtained by experiment. A drawback to the use of experimental flamelets is that the minor species that may be needed for a soot calculation, for example ethyne and the hydroxyl radical, may not be amenable to experimental measurement. Also, the resulting flamelet may be affected by the geometry of the flame or the type of burner used, see for example figure 4.1 which compares experimentally derived temperature flamelets from two sources - Mitchell et al. (1980a) and Syed (1990). These two flamelets show considerable difference in the rich mixture fraction region. Laminar flame codes exist, see for example Warnatz (1981), which permit the computation of one dimensional flame geometries but incorporate full kinetic schemes for the hydrocarbon combustion. Codes such as these may be used to provide detailed information about the concentrations of minor species as functions of the mixture fraction.

4 - Sooting Laminar Flames

Simplifications in the derivation of the transport coefficients for species and energy may be made by the introduction of two dimensionless parameters Pr, the Prandtl number, and Sc, the Schmidt number. The Prandtl number is defined as $\mathrm{Pr} = C_p \mu / \lambda$, and represents the ratio of the rate of momentum transport to the rate of energy transport. The Schmidt number is defined as $\mathrm{Sc} = \mu / (\rho D)$, and represents the ratio of the rate of momentum transport to the rate of mass transport. In most combusting systems these dimensionless groups may be approximated as constants - usually $\mathrm{Pr} \approx \mathrm{Sc} \approx 0.7$ - reducing the problem of finding the appropriate transport coefficients to one of determining the viscosity only.

4.3 Physical Models

4.3.1 Combustion

Theoretical analysis of diffusion flame structure reveals that all chemistry dependent scalars may be reduced to functions of a single conserved scalar - eg. mixture fraction - under the constraints of infinite reaction rate, zero heat loss, equal species diffusivity and unity Lewis number - Bilger (1976). This reduction has been shown to apply in real combustion systems, within the limits of experimental accuracy, even though one or all of the above constraints may be violated to some extent - Bilger (1977). Use has been made of the conserved scalar assumption here, but the model has been extended to remove the constraint of zero heat loss. Species mole fractions are taken to be functions of mixture fraction only but temperature is a function of mixture fraction and enthalpy - eg. $X_i = f(\xi)$ but $T = f(\xi, h)$. The mixture fraction and the enthalpy are derived from independent transport equations.

Using this model the entire vector and scalar fields of the laminar flame may be predicted by solving just four partial differential equations; continuity, axial momentum, mixture fraction and enthalpy. This equation set is closed by assuming that the density and viscosity may be obtained from the local composition and temperature. The density is determined using the perfect gas law

$$\rho = \frac{P}{RT} \sum_i X_i M_i \qquad (4.10)$$

Two methods are used for determining the species mole fractions, as functions of mixture fraction. These two methods are introduced to demonstrate the influence of the combustion chemistry on the structure of the flame. In section 4.5 it will be demonstrated that the influence of the combustion chemistry has a profound affect on the temperature field prediction of the Mitchell et al. (1980a) laminar flame.

The first method is the predicted flame structure from the laminar flame code of Warnatz (1981). This code solves for the properties along the stagnation streamline of a counter-flow, Tsuji and Yamaoka (1969), burner. This code incorporates a detailed chemical

kinetics combustion model involving 38 species and 84 reactions for methane combustion. Inputs to the code include the composition of the two gas streams and their velocities, from which the strain rate is calculated. The strain rate is defined as the local fractional increase in the surface are of the flame per unit time. For the 1 atm calculation this strain rate is 90 s^{-1}. The output of the Warnatz code yields the species mass fractions, which are converted to mole fractions, as a function of distance in physical space. These functions in physical space are converted to functions in mixture fraction space using the relationship suggested by Bilger (1988)

$$\xi = \frac{2\,Y_C / M_C + 1/2\,Y_H / M_H + (Y_{O,\,Oxidant} - Y_O) / M_O}{2\,Y_{C,\,Fuel} / M_C + 1/2\,Y_{H,\,Fuel} / M_H + Y_{O,\,Oxidant} / M_O} \qquad (4.11)$$

where the subscripts *C*, *H* and *O* refer to Carbon, Hydrogen and Oxygen respectively; the subscripts *Fuel* and *Oxidant* refer to the mass fractions in the unmixed fuel and oxidant streams. Only the seventeen most significant species in the Warnatz code output are used in GENMIX for calculating the temperature, density and viscosity - those with mass fractions greater than 10^{-4} at any point in mixture fraction space. These species are: H, O, OH, CH_3, CH_2O, CH_3OH, C_2H_2, C_2H_3, C_2H_4, C_2H_6, CO, CO_2, H_2, H_2O, O_2, CH_4 and N_2. The flame structure, for the major species, as predicted by this code is shown in figures 4.2a - c.

The second method used to determine the species mole fractions, as functions of mixture fraction, is a flamesheet calculation. For this the reaction rate is assumed to be infinitely fast, the reaction consisting of a single step

$$a CH_4 + b(0.21\,O_2 + 0.79\,N_2) \rightarrow c CO_2 + d H_2O + e CH_4 + f O_2 + g N_2 \qquad (4.12)$$

The reaction zone is a plane, of infinitesimal thickness, located at the position where *a* and *b* are in the stoichiometric ratio; in this case at the position where $2a = 0.21b$. In this plane the concentrations of the fuel and the oxygen are zero and the product concentrations are at a maximum. The product composition at mixture fractions other than stoichiometric are determined by the diffusion of the species. For this calculation, the transport coefficients of all the species are considered equal and the Lewis number is unity. Under these conditions the coefficients, *a* - *g*, are given by

$$a = \frac{\xi}{M_{CH_4}} \quad \text{and} \quad b = \frac{1-\xi}{M_{Air}} \tag{4.13}$$

$$\text{If } a \geq \frac{0.21b}{2} \text{ then } c = \frac{0.21b}{2},\ d = 0.21b,\ e = a - c,\ f = 0,\ g = 0.79b \tag{4.14}$$

$$\text{If } a < \frac{0.21b}{2} \text{ then } c = a,\ d = 2a,\ e = 0,\ f = 0.21b - 2a,\ g = 0.79b \tag{4.15}$$

The flame structure, as predicted by this calculation, is shown in figures 4.3a - b.

During the flame simulation the local flame temperatures are obtained by inverting the total enthalpy equation

$$h = \sum_i Y_i h_i \tag{4.16}$$

Where the species mass fractions are a function of the mixture fraction only. The individual species enthalpies are functions of temperature only. These are determined from fifth order polynomials in T - McBride et al. (1993). Solution of equation 4.16 for T where the total enthalpy and the mixture fraction are local flame properties gives the local flame temperature.

4.3.2 Viscosity

The component viscosities are determined using the corresponding states method of Lucas - Reid et al. (1977). Basic kinetic theory gives the following expression for the viscosity of a gas

$$\mu = \frac{5}{16} \frac{(\pi MRT)^{1/2}}{\pi \sigma^2} \tag{4.17}$$

where M is the molecular weight in kg / kmol and σ is the molecular diameter. If there are intermolecular forces present this expression becomes

$$\mu = \frac{5}{16}\frac{(\pi MRT)^{1/2}}{\pi\sigma^2\,\Omega_v} \tag{4.18}$$

where Ω_v is the collision integral; this is unity in the absence of intermolecular forces. From equation 4.18, if σ^3 is associated with the critical volume (V_c) and V_c is assumed to be proportional to RT_c/P_c then a dimensionless viscosity may be defined

$$\mu_r = \zeta\mu = f(T_r) \tag{4.19}$$

$$\zeta = \left[\frac{(RT_c)(N_A)^2}{M^3 P_c^4}\right]^{1/6} \tag{4.20}$$

where $f(T_r)$ is a known function of the reduced temperature. The mixture viscosity is calculated using Wilke's method - Reid et al. (1977). This mixture viscosity is given by

$$\mu_m = \sum_{i=1}^{n}\frac{X_i\mu_i}{\sum_{j=1}^{n}X_j\phi_{ij}} \tag{4.21}$$

where ϕ_{ij} is given by

$$\phi_{ij} = \frac{[1 + (\mu_i/\mu_j)^{1/2}(M_j/M_i)^{1/4}]^2}{[8(1 + M_i/M_j)]^{1/2}} \tag{4.22}$$

4.3.3 Radiative Loss

The GENMIX laminar flame calculation includes an enthalpy transport equation and it is from this transported enthalpy, as well as the mixture fraction, that the local properties are inferred. If the enthalpy source is set to zero then the equation describes an adiabatic

flame. However, there is the possibility of including a source term in the enthalpy transport equation that accounts for the radiative heat loss from the flame. For ease of calculation the laminar flame is assumed to be optically thin - ie. no self absorption of radiation. In the lightly sooting methane flames in this study this approximation should be valid. Radiation from the two main radiating gaseous species, CO_2 and H_2O, and the soot is considered in the enthalpy source term. The enthalpy transport equation, for a unity Lewis number system with equal transport coefficients for all species, takes the form

$$\rho \frac{\partial h}{\partial t} + \rho \vec{u} \cdot \nabla h - \nabla \cdot \left(\frac{\mu}{\sigma_h} \nabla h \right) = -4 \kappa_T \sigma T^4 \tag{4.23}$$

The term on the right hand side is the radiative loss source term in the optically thin limit. κ_T, the total Planck mean emission coefficient, is given by

$$\kappa_T = \kappa_{CO_2} + \kappa_{H_2O} + \kappa_{Soot} \tag{4.24}$$

The Planck mean emission coefficient is defined as

$$\kappa(T) = \frac{1}{\sigma T^4} \int_0^\infty \kappa(T,\omega)\, B(T,\omega)\, d\omega \tag{4.25}$$

The Planck mean emission coefficients for the gaseous species (κ_{CO_2} and κ_{H_2O}) have been taken from Hubbard and Tien (1978). The Elsasser narrow-band model is used for calculating the emission coefficients of these gases. This model assumes that in a given spectral region equally spaced, equally intense, equally wide absorption lines exist. For further detail the reader is referred to Hubbard and Tien (1978).

The absorption / emission coefficient for the soot (κ_{Soot}) has been taken from Hall (1988). Hall (1988) gives the total radiative heat loss per unit volume from soot in the optically thin limit as

$$\dot{Q} = -2.97\times10^{-4} f_V T^5 \tag{4.26}$$

Equating this to $-4\,\kappa_{Soot}\sigma T^4$ yields the following expression for κ_{Soot}

$$\kappa_{Soot} = 7.4\times10^{-5}\frac{f_V T}{\sigma} \tag{4.27}$$

4.3.4 Soot

The soot model used in this work is a development of the model first introduced by Gilyazetdinov (1972). This model includes representations of the key processes of particle nucleation, coagulation and surface growth. Two model parameters describe the soot, *N*, the soot particle number density and, *M*, the mass concentration of the soot - Moss et al. (1988). If the soot particles are assumed to be spherical with a mono-disperse size distribution then the full set of soot characteristics may be modelled; particle diameter, surface area, etc.

Nucleation

Nucleation here describes the process where the first solid phase carbon is produced by homogeneous gas phase reactions. Following the discussion in chapter 2 the nucleation rate is taken to be proportional to the local ethyne concentration. The activation temperature for the nucleation reaction is taken to be that proposed by Lindstedt (1991). Hence, the nucleation rate is given by

$$\left(\frac{dN}{dt}\right)_{Nuc.} = aN_A\left(\frac{X_{C_2H_2}P}{RT}\right)^l e^{-\frac{21100}{T}} \tag{4.28}$$

where *a* and *l* are model constants.

Coagulation

The coagulation of the soot particles is related to their frequency of collisions with each other. If it is assumed that each collision will result in the coalescence of the particles then the coagulation rate is equal to the collisional frequency. This collisional frequency is governed by the size of the particles and the mean free path of the surrounding gas. There are two distinct regimes although the transition from one to the other is continuous. If the diameter of the particles (d_p) is much less than twice the mean free path of the surrounding gas (λ) then the frequency of collisions is governed by kinetic theory. The mean free path is given by

$$\lambda = \frac{RT}{\sqrt{2} N_A P \pi \sigma^2} \qquad (4.29)$$

where σ is the diameter of the gas molecules. Assuming the temperature in the sooting region to be approximately 1700 K and taking the molecular diameter of N_2 (0.36 nm) as a representative value for σ, then at 1 atm the mean free path is 400 nm and at 3 atm the mean free path is 134 nm. Typical soot particle diameters in methane flames will range up to about 60 nm at 3 atm. This would imply that the collisional frequency is governed by kinetic theory. Alternatively, if the particle diameter is much greater than twice the mean free path of the surrounding gas then particle diffusion determines the frequency of the collisions. When the diameter of the particle is comparable in size to the mean free path then the behaviour is somewhere between the gas-kinetic and diffusion regimes. Fuchs (1964) has developed a correction term for the diffusive expression of particle coagulation, that allows the evaluation of the collisional frequency in both regimes from a single expression. However, the complexity of this correction term prevents its inclusion in the model. It is recognized, however, that at higher pressures the gas-kinetic coagulation term used in this work may be in error. Puri et al. (1993) have measured the agglomeration rate of soot particle aggregates in a laminar ethene diffusion flame and found the gas kinetic expression to give reasonable agreement with the measured value.

For mono-disperse spherical particles, kinetic theory gives the particle collision frequency (and hence, the coagulation rate) as

$$\left(\frac{dN}{dt}\right)_{Coag.} = -\pi d_P^2 \left(\frac{4kT}{\pi m_P}\right)^{1/2} N^2 \qquad (4.30)$$

where m_P is the mass of a single particle and k is Boltzmann's constant. The mass of a particle is related to its diameter by

$$m_P = \rho_{Soot} \frac{\pi d_P^3}{6} \qquad (4.31)$$

Where the density of the soot (ρ_{Soot}) is taken to be 1800 kg m^{-3}. Hence, the coagulation rate becomes

$$\left(\frac{dN}{dt}\right)_{Coag.} = -\left(\frac{24 d_P kT}{\rho_{Soot}}\right)^{1/2} N^2 \qquad (4.32)$$

The assumption that the particles are mono-disperse in size and spherical allows the particle diameter to be written in terms of the soot mass concentration (M) and the particle number density (N). Hence, the diameter may be written as

$$d_P = \left(\frac{6M}{\pi \rho_{Soot} N}\right)^{1/3} \qquad (4.33)$$

Which allows the coagulation rate to be formulated as

$$\left(\frac{dN}{dt}\right)_{Coag.} = -\left(\frac{24R}{\rho_{Soot} N_A}\right)^{1/2} \left(\frac{6}{\pi \rho_{Soot}}\right)^{1/6} T^{1/2} M^{1/6} N^{11/6} \qquad (4.34)$$

Surface Growth

A soot particle grows by addition of gaseous species, mainly ethyne, at its surface - Frenklach et al. (1984) and Harris et al. (1988). Ethyne has been shown to be in abundance in the sooting regions of laminar methane / air flames - Smyth et al. (1985). The reaction

rate is limited by the concentration of the species available for addition and by the number of active sites on the surface of the soot. The number of active sites may be taken as proportional to some function of the surface area of the soot particle. Only simple functions of surface area are considered in this work, specifically surface area raised to a constant power. The total surface area per unit volume of a cloud of mono-disperse spherical particles is given by

$$A_{Total} = (\pi N)^{1/3} \left(\frac{6M}{\rho_{Soot}} \right)^{2/3} \tag{4.35}$$

The activation temperature for the surface growth reaction is the same as that proposed by Lindstedt (1991); hence, the appearance of soot mass due to surface growth processes may be written as

$$\left(\frac{dM}{dt} \right)_{Growth} = b \left(\frac{X_{C_2H_2} P}{RT} \right)^m e^{-\frac{12100}{T}} \left[(\pi N)^{1/3} \left(\frac{6M}{\rho_{Soot}} \right)^{2/3} \right]^n \tag{4.36}$$

where b, m and n are model constants.

Particle nucleation also contributes to the appearance of soot mass. However, the point at which a soot precursor may be considered as a soot nucleus is arbitrary. Following previous work, Syed (1990), an incipient particle is assumed to consist of 12 carbon atoms. This gives the rate of appearance of soot mass due to nucleation as

$$\left(\frac{dM}{dt} \right)_{Nuc.} = \frac{M_P}{N_A} \left(\frac{dN}{dt} \right)_{Nuc.} \tag{4.37}$$

where M_P (= 144 kg kmol^{-1}) is the mass of a soot nucleus.

The processes of soot mass growth and soot oxidation are reasonably well segregated in physical space in laminar flames. However, experience has shown that to ignore soot oxidation completely yields growth rates that are too small (see section 4.5). For these laminar flame simulations soot oxidation by the OH radical, the main oxidising species

(see chapter 2), has been included. Puri et al. (1994) give the oxidation rate of soot by the OH radical, assuming a collision efficiency of 0.04, as

$$\omega = 4.2325 \frac{X_{OH} P}{RT} \sqrt{T} \tag{4.38}$$

The rate of soot mass consumption, by oxidation, is therefore

$$\left(\frac{dM}{dt} \right)_{Oxi.} = -\omega \, (\pi N)^{1/3} \left(\frac{6M}{\rho_{Soot}} \right)^{2/3} \tag{4.39}$$

Combining equations 4.28 and 4.34 yields, for the net production of soot number density

$$\frac{dN}{dt} = a N_A \left(\frac{X_{C_2H_2} P}{RT} \right)^{l} e^{-\frac{21100}{T}} - \left(\frac{24R}{\rho_{Soot} N_A} \right)^{1/2} \left(\frac{6}{\pi \rho_{Soot}} \right)^{1/6} T^{1/2} M^{1/6} N^{11/6} \tag{4.40}$$

Combining equations 4.28 and 4.36 - 4.39 yields, for the net production of soot mass density

$$\begin{aligned} \frac{dM}{dt} = {} & M_P a \left(\frac{X_{C_2H_2} P}{RT} \right)^{l} e^{-\frac{21100}{T}} \\ & + b \left(\frac{X_{C_2H_2} P}{RT} \right)^{m} e^{-\frac{12100}{T}} \left[(\pi N)^{1/3} \left(\frac{6M}{\rho_{Soot}} \right)^{2/3} \right]^{n} \\ & - 4.2325 \frac{X_{OH} P}{RT} \sqrt{T} \, (\pi N)^{1/3} \left(\frac{6M}{\rho_{Soot}} \right)^{2/3} \end{aligned} \tag{4.41}$$

The constants a and b may only be established by running GENMIX and making comparisons with the experimental data. To determine the constant l number density measurements, taken at several different pressures, would need to be available. In the absence of such measurements, or any further insight, l has been taken to be unity. Estimates, however, may be made for the remaining two constants m and n.

In a plug flow for which the soot containing volumes are characterised by a constant

mixture fraction equations 4.40 and 4.41 may be integrated analytically. Of course this approximation is invalid for a quantitative analysis of real flames since the mixture fraction contours are not in general parallel to the stream lines - which the soot follows. For the purposes of illustration, ignoring the contribution to mass growth by nucleation (which is very small in practice) and neglecting oxidation, the soot mass growth may be represented by

$$\frac{dM}{dt} \approx \gamma \left(N^{1/3} M^{2/3}\right)^{n} \tag{4.42}$$

where γ is a function of mixture fraction and pressure only. Separating the variables and integrating gives

$$\frac{3}{3-2n} M^{1-2n/3} = \int_{o}^{t} \gamma N^{n/3} dt' \tag{4.43}$$

Two limits may be deduced for N as a function of time. If the number density has not reached saturation then, neglecting the coagulation rate, integrating equation 4.40 gives for the number density

$$N \approx \alpha t \tag{4.44}$$

Where α is a function of mixture fraction only. The alternative limit is reached when the number density becomes great enough for the coagulation rate to equal the nucleation rate. At this point the number density becomes saturated at the constant value $N = N_{Sat.}$. The value of $N_{Sat.}$ may be determined by setting equation 4.40 equal to zero and solving for N. Considering the unsaturated number density first, substituting equation 4.44 into equation 4.43 and performing the integration gives

$$M^{1-2n/3} = \frac{3-2n}{3+n} \gamma \alpha^{n/3} t^{1+n/3} \tag{4.45}$$

If the saturated value for the number density is substituted into equation 4.43 the result is

$$M^{1-2n/3} = \frac{3-2n}{3}\,\gamma\, N_{Sat.}^{n/3}\, t \qquad (4.46)$$

The soot mass concentration is related to the soot volume fraction by the soot density, $M = \rho_{Soot} f_V$. Incorporating this relationship into equations 4.45 and 4.46 and taking the natural logarithms of both sides gives, for equation 4.45

$$\ln f_V = \frac{3+n}{3-2n}\ln t + \frac{3}{3-2n}\ln\left(\frac{\gamma\,\alpha^{n/3}}{\rho_{Soot}^{1-2n/3}}\,\frac{3-2n}{3+n}\right) \qquad (4.47)$$

and for equation 4.46

$$\ln f_V = \frac{3}{3-2n}\ln t + \frac{3}{3-2n}\ln\left(\frac{3-2n}{3}\,\frac{\gamma\, N_{Sat.}^{n/3}}{\rho_{Soot}^{1-2n/3}}\right) \qquad (4.48)$$

In figure 4.4 the natural logarithms of the experimentally derived peak soot volume fractions, from the Syed (1990) laminar flame, are plotted against the natural logarithms of residence time taken from the GENMIX flowfield calculation. The gradient of the best fit line is 4.02. Inspection of equation 4.47 gives a value for *n* that is approximately unity. This implies a linear dependence, for the surface growth term, on particle surface area if the number density is unsaturated. Inspection of equation 4.48 gives a value of 9/8 for *n*. Suggesting that, if the number density is saturated for the majority of the growth region, the dependency for surface growth on the surface area is more than linear. Unfortunately, measurements of number density are not available for the Syed (1990) flame. Measurements of number density are available for the Mitchell et al. (1980a) flame; taken by Garo (1984). However, these measurements only appear to be reliable in the region where the soot volume fraction is in decline; where the number density is also in decline. The measurements of number density in the growth region of the soot show considerable scatter between 10^{17} and 10^{18} m^{-3}, at the radial positions where the peak soot volume fractions occur. Due to the lack of definitive experimental soot particle number density data for laminar methane flames the preferred value for *n* used in this work is unity. This value of unity compares well with the linear surface area dependence used by Syed (1990);

but is in contrast to the values of surface area dependence proposed by other workers. Lindstedt (1991) proposes a square root area dependence. Delichatsios (1994) declares that the growth of soot is not at all dependent on the surface area; but only depends on the local fuel mass fraction. The current model would approximate this if n is taken as zero. The effect of n on the GENMIX calculations is discussed in section 4.5.

If n is unity then, for a fixed value of residence time, from equation 4.45

$$M \propto \gamma^3 \tag{4.49}$$

where

$$\gamma \propto P^m \tag{4.50}$$

The turbulent flame experiments (chapter 3) reveal that for similar residence times the soot volume fraction is proportional to pressure squared. From equations 4.49 and 4.50 this gives a value for m of 2/3. It should be noted, however, that as the pressure is increased the mole fraction of ethyne also increases (see chapter 5). This suggests that 2/3 is the maximum value of m to be expected.

4.4 Computation

4.4.1 Flowfield Equations

The Wolfhard-Parker burner, of the type used by Syed (1990), may be considered as a two dimensional flow system if the slot length is infinite. Of course, in practice this length is not infinite; but it is large in comparison to the width of the slot. Ignoring the variation along the length of the slot gives two orthogonal coordinate directions x (the downstream distance) and y (the cross stream distance) along which variations are considered.
The cylindrical burner used by Mitchell et al. (1980a) is by nature a two dimensional system with the two coordinate directions x (downstream distance) and r (radial distance).
The GENMIX code is designed for solving steady, two dimensional boundary layer problems. This code solves the continuity equation, an equation for axial momentum and any number of user defined transport equations. An equation for cross stream or radial momentum is not solved because the grid used by the code follows the streamlines, by definition there is no convection across streamlines.

The boundary layer form of the two dimensional transport equation, in rectangular coordinates, for the general variable ϕ, is

$$u\frac{\partial \phi}{\partial x} + v\frac{\partial \phi}{\partial y} = \frac{1}{\rho}\frac{\partial}{\partial y}\left(\frac{\mu}{\sigma_\phi}\frac{\partial \phi}{\partial y}\right) + \frac{1}{\rho}S_\phi \qquad (4.51)$$

This is the form of the general transport equation solved by the GENMIX code. In equation 4.51, ϕ may represent specific enthalpy, mixture fraction or either of the two soot properties. However, the units of the variable ϕ are property / kg of gas mixture - eg. for enthalpy the units are J kg^{-1}. The units of the two soot parameters are, for N, particles m^{-3} and, for M, kg m^{-3}. The transported soot variables, therefore, are given by

$$\phi_N = \frac{N}{N_A \rho} \qquad (4.52 - 53)$$

$$\phi_M = \frac{M}{\rho}$$

Note that the transported soot number parameter, ϕ_N, has been normalised by Avogadro's number.

The diffusivity of soot is negligible in comparison to that of gases. To account for this the Prandtl / Schmidt numbers for the soot variables (σ_N and σ_M) are set to a high value. It is found, however, that if these Prandtl / Schmidt numbers are set to too high a value - giving a soot diffusivity of effectively zero - then there is some instability in the GENMIX calculation; cf. Kennedy et al. (1990). For this reason the Prandtl / Schmidt numbers for the soot variables are set to give a soot diffusivity one-thousandth of the bulk gas diffusivity. The Prandtl / Schmidt numbers for each of the transported variables are given in the table below.

Table 4.1

Transported Variable	Prandtl / Schmidt Number
u	1
ξ	0.7
h	0.7
ϕ_N	700
ϕ_M	700

However, particles in non-isothermal media are subject to forces which cause movement other than merely convective or diffusive motion. One such force is thermophoresis, caused by gas molecules impacting the particle on opposite sides with differing mean velocities. In this way soot particles are carried along the temperature gradient, away from the high temperature regions of the flame. Fuchs (1964) gives the thermophoretic velocity of the particles, for particles smaller than the mean free path of the gas, as

$$v_{Thermo.} = \frac{-3}{4(1 + \pi/8)} \frac{\mu}{\rho T} \frac{\partial T}{\partial y} \qquad (4.54)$$

The movement of particles due to thermophoresis is treated as a source term in the GENMIX calculation. This thermophoretic source is given by

$$S_{\phi,\,Thermo.} = \frac{\partial}{\partial y}(\rho\, v_{Thermo.}\, \phi) \qquad (4.55)$$

Where, in this instance, ϕ may represent either ϕ_N or ϕ_M.

The source terms for the transport equations solved by the GENMIX code are summarised in the following table.

Table 4.2

Transported Variable	Source Term (S_ϕ)
u	$-\frac{\partial P}{\partial x} - \rho g$
ξ	0
h	$-4\kappa_T \sigma T^4$
ϕ_N	$\frac{1}{N_A} \cdot \frac{dN}{dt} + S_{\phi_N,\,Thermo.}$
ϕ_M	$\frac{dM}{dt} + S_{\phi_M,\,Thermo.}$

4.4.2 Geometry

The Mitchell et al. (1980a) flame geometry is shown in figure 4.5. The burner consists of two concentric tubes connected to a perforated brass disc which acts as the burner plate. The fuel issues from the central circular orifice of radius r_o = 6.35 mm and the air from the surrounding annulus of radius R = 25.4 mm. Methane was supplied with a flowrate of 0.228 g min^{-1} and the air co-flow with a flowrate of 13.48 g min^{-1}. The two gas streams are shielded from the ambient air by a Pyrex tube of inner radius R. The flame geometry used in the laminar flame experiments performed by Syed (1990) is shown in figure 4.6. This flame is planar and issues from a three slot Wolfhard-Parker burner. Fuel flows from the central slot of width 6 mm and air from the outer two slots each of 9 mm width; the

slots are 47 mm in length. The burner is mounted inside an enclosure, 90 mm x 90 mm, through which there is an air co-flow of an unspecified rate. The methane flowrate through the central slot was 0.552 g min^{-1} and the air flowrate through each of the two air slots was 3.864 g min^{-1}.

4.4.3 Initial and Boundary Conditions

The Syed (1990) laminar flame is modelled with GENMIX in planar mode. Only half of the burner's width is modelled, the flow being symmetrical about a plane running through the centre of the fuel slot. This burner half width is represented by two hundred cross-stream nodes. The inner node represents a boundary of planar-symmetry and the outer node a free-boundary; representing the position where the free stream values of mixture fraction, enthalpy and axial velocity are attained. Each of the other nodes represents the position of the computational cell centres. The initial conditions for five variables need to be specified at the upstream boundary. These variables are axial velocity, mixture fraction, enthalpy, soot number density, and soot mass density. However, one of the biggest problems to arise, when modelling laminar flames, is the specification of these initial conditions; especially if they are to be specified at the burner exit. At the low burner exit velocities usual for laminar flames - around 5 cm s^{-1} - axial diffusion becomes significant and the boundary layer approximation becomes invalid. However, for this flame the experimental profiles of mixture fraction and temperature are available at the plane 2 mm above the burner exit; a position at which the flow would have accelerated sufficiently, due to buoyancy forces, to enable the boundary layer approximation to be used. Therefore, the calculation is started at this height using the experimentally obtained profiles for these two variables. In fact the actual mixture fraction profile used is a fit of the experimental data, assuming the mixture fraction to have a Gaussian profile following the form of

$$\xi = a\, e^{-\frac{y^2}{b}} \tag{4.56}$$

The constant a is set to the experimental, centreline mixture fraction value and b such that the mixture fraction is at the correct value to give the temperature maximum at the position

indicated by experiment. This mixture fraction profile matches the experimental profile very closely. If an adiabatic initial enthalpy profile is assumed then the resulting temperatures are greatly in excess of the experimental temperature data, on the rich side of stoichiometric. To give the correct initial temperature condition the initial enthalpy profile is perturbed from the adiabatic. This, however, still leaves the initial velocity profile unspecified. The initial velocity profile that is used, in the flame simulations, is obtained as follows. The calculation is started from the burner exit plane using uniform mass-averaged velocity profiles for the fuel and air streams; a mixture fraction of unity in the fuel stream and a mixture fraction of zero in the air stream; and the enthalpies for the fuel and air streams set to their adiabatic values (these are the burner exit conditions that would be expected in the absence of axial diffusion). The velocity profile, obtained using these initial conditions, at 2 mm above the burner is then perturbed by multiplying the profile by the experimental temperature profile divided by the GENMIX temperature profile - eg. $u(y) = u(y)_{GENMIX}(T(y)_{Expt.}/T(y)_{GENMIX})$ - because the temperature profile, using the adiabatic initial conditions, and that obtained from experiment were not the same. The resulting velocity profile is used as the initial condition for all the subsequent calculations - the calculations starting at the 2 mm height. The soot variables, soot number density and soot mass density, are set to zero at this height. No boundary conditions are required at the downstream edge of the integration domain, as the calculation is parabolic. The initial conditions used by GENMIX for the calculation of the Syed (1990) flame are shown in figure 4.7.

The Mitchell et al. (1980a) flame is axi-symmetric and again only half of the flame's width is modelled, the grid for this flame extending from the centre of the burner to the inner surface of the confining tube. Two hundred nodes are used along this radius, the inner node representing a boundary of axi-symmetry and the outer node representing a wall boundary. This wall boundary is considered to be impervious to matter, there is no slip between it and the gas and the wall is assumed to be at a constant temperature of 290 K. The experiments presented by Mitchell et al. (1980a) do not include measurements at the burner exit plane and in the modelling of the flame, and also the modelling performed later with Smooke et al. (1989), the conditions at the burner exit plane are taken to be those obtained in the absence of back diffusion and include a uniform mass-averaged velocity profile across both the fuel and the air regions - eg.

In the fuel region: $0 \le r \le r_o$; $\xi = 1$; $u = u_{Fuel}$

And in the air region: $r_o < r < R$; $\xi = 0$; $u = u_{Air}$

However, as in the calculation of the Syed (1990) flame, employing these simple initial conditions in the GENMIX calculation leads to large errors in the predicted profiles at the first measurement station; as well as an over prediction of the flame length - similar observations are cited by Jones and Lindstedt (1988). Again this indicates a certain degree of axial diffusion, impossible to model in a parabolic code. Therefore, following Jones and Lindstedt, the experimental profiles obtained at the first measurement station - at a height of 12 mm - are used as the initial conditions. The axial velocity initial profile was taken directly from the measurements made by Mitchell et al. (1980a). Again, the mixture fraction was assumed to have a Gaussian profile following the form of

$$\xi = a\, e^{-\frac{r^2}{b}} \tag{4.57}$$

The constants a and b are set such that the mixture fraction was at the correct value to give the temperature maximum at the radial position indicated by experiment and the overall mass flux of fuel elements at this plane were the same as that in the Mitchell et al. (1980a) experiment. The mixture fraction profile obtained using this expression matched very closely the profile measured by Mitchell et al. (1980a). A more severe problem is that of matching the temperature profile of the gases to the profile measured at this height. If the temperature profile, corresponding to the mixture fraction profile, is taken from the adiabatic flamelet it is found that the temperatures on the rich side of the temperature peak are greatly in excess; regardless of the flamelet chemistry used - for example detailed chemistry or flamesheet calculation. This temperature difference, between the adiabatic flamelet values and the experimental values, is even greater than that observed in the Syed (1990) flame. It is not expected that the flame would have lost a significant amount of energy by radiative heat loss at this point, since the residence time for the gases is small. Therefore, it is suggested that the temperature difference is due to conduction to the burner plate and / or quenching of the flame in the near burner plate region. To obtain the correct temperature profile the initial enthalpy profile is perturbed from the adiabatic. Starting the flame calculation 12 mm from the burner plate leaves the problem of specifying the two

soot variables, as Mitchell et al. (1980a) made no soot measurements on this flame and Garo (1984) made no soot measurements at this height. Setting these variables to zero at this height may be expected to yield large errors, as the peak soot volume fraction measured by Syed (1990) at this height is far from negligible - approximately 10^{-8}. This problem is circumvented by mapping the soot properties, at 12 mm height, onto the mixture fractions - both from the Syed (1990) flame calculation. These soot properties, as functions of mixture fraction, mapped onto the initial mixture fraction condition are used as the initial soot conditions for the Mitchell et al. (1980a) flame calculation. The initial conditions used by GENMIX for this flame are shown in figures 4.8a - b.

4.4.4 Model Implementation

The GENMIX, Spalding (1977), code is well documented and its code structure will not be discussed here. However, the implementation of the combustion model will be explained in this section. For speed of execution, variables and the portion of the source terms that are functions of mixture fraction and enthalpy only are calculated before the runtime of the code. Values of these scalars are stored in files for discrete values of the mixture fraction and radiative loss. Files for temperature, density, viscosity, enthalpy, radiation emission rate, soot particle nucleation rate, particle coagulation rate, soot surface growth rate and soot oxidation rate are stored. The flame enthalpy is, of course, determined from its balance equation; however, the enthalpy file is needed for the operation of the combustion model. The files for the scalar values are laid out as shown in the table below.

Table 4.3

ξ_1	$\phi(\xi_1, X_{R,1})$	$\phi(\xi_1, X_{R,2})$	.	$\phi(\xi_1, X_{R,m})$
ξ_2	$\phi(\xi_2, X_{R,1})$	$\phi(\xi_2, X_{R,2})$	.	$\phi(\xi_2, X_{R,m})$
.	.	.	.	.
ξ_n	$\phi(\xi_n, X_{R,1})$	$\phi(\xi_n, X_{R,2})$	.	$\phi(\xi_n, X_{R,m})$

All the files contain the scalars for the same n values of mixture fraction (ξ) and m values

of radiative loss (X_R). Every scalar value in these files has a corresponding enthalpy value in the enthalpy file. The enthalpy values are calculated initially then the corresponding temperature values are calculated by inverting the enthalpy equation, using NASA polynomials which give enthalpy as a fifth order polynomial in T - McBride et al. (1993). From the temperature and the species mole fractions, which are functions of mixture fraction, all the other scalars may be calculated. The enthalpy values stored in the enthalpy file are calculated according to

$$h(\xi, X_R) = h_{Init.}(\xi) + (1 - X_R)(h_{Adia.}(\xi) - h_{Init.}(\xi)) \tag{4.58}$$

where $h_{Init.}(\xi)$ is the specific enthalpy of the product mixture, the composition of which is determined by ξ, at the initial reactant temperature (290 K for the Mitchell et al. (1980a) flame, 500 K for the Syed (1990) flame); $h_{Adia.}(\xi)$ is the enthalpy of the same mixture at the adiabatic product temperature; and X_R is the radiative heat loss fraction. Note that these are total enthalpies - chemical plus sensible. The adiabatic product enthalpy must be linearly related to the mixture fraction, because during the runtime of the code the local scalar values are found by comparing the transported values of mixture fraction and enthalpy with the values of mixture fraction and enthalpy in the enthalpy file. The transported enthalpy is a mixture property and in the absence of radiative loss will be linearly related to the mixture fraction, if the Lewis number is unity. The combustion model code firstly finds the pair of discrete values of mixture fraction, in the file, that bracket the value of the mixture fraction obtained from the transport equation. The pair of enthalpy values, for this mixture fraction, that bracket the transported enthalpy are then determined. Corresponding to each of this pair of enthalpy values is a value for each of the other scalars. The local scalar values are found by linear interpolation, using the transported enthalpy as the interpolating factor. For example, at a position in the flame the transported mixture fraction is ξ and the transported enthalpy is h. This mixture fraction will be bracketed by two of the mixture fraction values stored in the files, eg.

$$\xi_{Low} \leq \xi < \xi_{High} \tag{4.59}$$

where ξ_{Low} and ξ_{High} are two values in the file. Two enthalpy values are determined that bracket h, h_{Low} and h_{High}. These values are found by interpolating in mixture fraction

space at two discrete values of radiative loss, eg.

$$h_{Low} = h(\xi_{Low}, X_{R,High}) + \frac{\xi - \xi_{Low}}{\xi_{High} - \xi_{Low}}(h(\xi_{High}, X_{R,High}) - h(\xi_{Low}, X_{R,High})) \qquad (4.60)$$

where it should be noted that the higher value of radiative loss corresponds to the lower enthalpy. Associated with these two enthalpy values will be pairs of values of the other scalars. The local scalar values are found from these pairs by interpolating in enthalpy space

$$\phi(\xi, h) = \phi(\xi, h_{High}) + \frac{h - h_{High}}{h_{Low} - h_{High}}(\phi(\xi, h_{Low}) - \phi(\xi, h_{High})) \qquad (4.61)$$

The linear interpolation introduces a slight error, especially for functions that are strongly non-linear with temperature - such as the soot source terms. The error is, however, kept to a minimum by using a large number of mixture fraction and radiative loss points in the files. Fifty mixture fraction points are used with eight degrees of radiative loss.

4.5 Results and Discussion

GENMIX data are presented for the Syed (1990) flame and the Mitchell et al. (1980a) flame. The soot model has been calibrated in the Syed (1990) flame for six values of the ethyne concentration exponent (m) and three values of the area dependency exponent (n). Data are presented for three of these soot models applied to the simulation the Syed (1990) flame and for one of these models applied to the Mitchell et al. (1980a) flame. The temperature field calculated for the Mitchell et al. (1980a) flame using the Warnatz data differs greatly from the experimental data. To demonstrate the influence of the flame chemistry, this temperature field is compared to one obtained using the flamesheet data.

The constants derived for the soot model are summarised in the following table.

Table 4.4

Constant Set	a	b	m	n
1	5.4×10^{1}	0.6900×10^{1}	0.25	1
2	5.4×10^{1}	3.070×10^{1}	0.4	1
3	5.4×10^{1}	5.050×10^{1}	0.45	1
4	5.4×10^{1}	8.300×10^{1}	0.5	1
5	5.4×10^{1}	4.300×10^{2}	2/3	1
6	5.4×10^{1}	9.856×10^{2}	0.75	1
7	5.4×10^{1}	1.170×10^{4}	1	1
8	5.4×10^{1}	5.339×10^{4}	1	0.5
9	5.4×10^{1}	2.382×10^{4}	1	0.75
10	5.4×10^{1}	2.000×10^{3}	0.75	0.75

The constants a and b are obtained iteratively by setting the values of m and n for the soot model then repeatedly running the GENMIX code, making adjustments to a and b as necessary, until the best fit to the experimental soot data is achieved. This fit is assessed in terms of the growth of the peak soot volume fractions with height. For a given pair of

values of m and n the values of a and b are found to be unique - ie. it is not possible to perturb a and still get a fit to the experimental data by adjusting b. All the model calibrations have been performed by simulating the Syed (1990) flame, these simulations have included radiative loss from the gas and the soot and have included soot oxidation by the OH radical using the expression given by equation 4.39. The species data from the Warnatz laminar flame code has been used for all the species mole fractions.

The GENMIX data, obtained using constant set 7, are compared with the Syed (1990) experimental data in figures 4.9a - g. This GENMIX run includes radiative loss from the gas and the soot, the soot model includes the OH oxidation term. Warnatz species mole fractions are used in this and every other run for the Syed (1990) flame. The experimental profiles are generally well reproduced. The temperatures agree to within 50 K in the majority of the sooting region of the flame. Only above the 20 mm height does the temperature profile begin to show a deviation from the experimental data, with the temperatures towards the centre of the flame becoming over predicted. The spatial position of the temperature peaks are well reproduced by GENMIX at all heights in the flame. The mixture fraction profiles are also well predicted at all flame positions. The agreement of the soot model, using this set of constants, is satisfactory. However, although the growth of the maximum soot volume fraction with height and the position of this maximum is well reproduced, the centreline soot volume fractions are consistently low. The reason for the low soot prediction on the central plane is as follows. Soot is only produced in the high temperature ($T \geq 1400$ K), fuel rich regions of the flame. At low positions in the flame these conditions are only satisfied in a narrow region on the rich side of the flame front. At these low positions the residence time is comparatively large, the flow is still accelerating. As a result a narrow band of soot is formed low in the flame, away from the cool centre. The soot surface growth rate used for this calculation is proportional to the surface area. Hence, the mass growth rate of soot is greatest in this region where the soot has already formed. As the flow progresses away from the burner the temperature on the centreline begins to increase, but the flow velocity has also increased. The soot, therefore, that begins to form on the centreline has a shorter total residence time within which to form when compared with the soot that began to form next to the flame front close to the exit of the burner. Given that the growth rate is proportional to the surface area, the total mass of soot formed is proportional to residence time to the power of three or four (depending

on whether the number density is saturated or not). Hence, as the residence time under conditions favourable for sooting is lower on the centreline the reason for the lack of soot on the centreline is readily apparent.

The qualitative analysis of the soot model in section 4.3.4 indicates a linear dependence for the soot growth rate on surface area. However, to investigate the effect of this choice on the growth of soot other area dependencies have been explored. The model has been calibrated with area exponents of 0.5 (constant set 8) and 0.75 (constant set 9). The results for the GENMIX run made with constant set 8 are compared with those obtained using the linear surface area dependence in figure 4.10. This figure shows the growth of the peak soot volume fraction with height above the burner. Again the GENMIX run includes radiative loss from the gas and the soot and soot oxidation by the OH radical. The model has now failed to follow the growth of the soot maximum with height. Also, it is noted (but not illustrated) that the centreline soot values have increased by an order of magnitude. However, even with this increase the soot values on the centreline are well below those recorded experimentally. Obviously, changing the area dependency does not solve the centreline soot problem. Two causes may be responsible for this lack of agreement, on the centreline, between the model and the experimental data. The first possible reason is experimental error. This may be caused in three ways. The flame investigated by Syed (1990) is planar and flame properties are assumed to be invariant along lines running parallel to the major axis of the burner slot. The soot volume fraction is measured by the absorption of a laser beam running parallel to this major axis - see figure 4.6. Ideally the flame would consist of two flame sheets meeting some distance above the burner. However, in reality flame sheets are also present at the ends of the slots. Some soot will be present in these 'endflames' and the absorption by this soot will create errors in the measured soot values. Another cause of experimental error is the finite width of the laser beam. For the measurements in this flame the beam is focused at a point halfway along the width of the flame, giving a maximum beam diameter of 0.5 mm. The region around which the soot predictions disagree with the experimental data is approximately 2 mm centred around the axis of the flame. The gradient of the soot in this region is very large. The absorption of the laser beam is an average over the cross-section of the beam; any error in the position of the beam or flame flicker, therefore, will tend to increase the measured absorption. These experimental errors are difficult to quantify; but although these errors

must be present it is hard to imagine that they are solely responsible for the differences noted. The final possible source of experimental error may result from the absorption of the laser beam by species other than soot. Garo et al. (1986) note considerable absorption by poly-aromatic hydrocarbons (PAH) on the centreline of the Mitchell et al. (1980a) flame. The second possible cause for the discrepancy between the predicted soot profiles and the experimental data lies with the soot model. Before mass growth can occur soot nuclei must form. The activation temperature in the model for this process is higher than that for the mass growth process. Hence nuclei only form close to the flame front. These nuclei then undergo addition of mass by surface growth processes. The calculation does not allow these nuclei to diffuse, only allowing soot to grow in the regions where the nuclei have formed. However, the initial diffusivity of these soot nuclei will be close to that of the surrounding gas allowing the nuclei to diffuse to cooler regions where the temperature is too low for nuclei formation but is great enough for the surface growth processes. Unfortunately the model does not consider the soot nuclei as a separate species and therefore cannot allow for this diffusion of soot nuclei.

Figure 4.11 demonstrates the effect of the radiative loss on the soot production. The soot model for this GENMIX run uses constant set 7, with OH oxidation. The initial conditions are the same as for all the GENMIX runs but the radiative loss term has been set to zero. The soot levels show a marked increase.

Figure 4.12 removes the OH oxidation from the soot mass source term. Radiative loss from the gas and the soot is present. The soot profiles show an increase in the maximum of approximately 40 % at all heights in the flame. This shows that although the regions of soot growth and soot destruction, by oxidation, are segregated in physical space the effects of oxidation may not be ignored entirely in the soot growth region.

The model has been calibrated for ethyne concentration exponents (m) other than unity. The value of m is not found to affect the fit to the laminar data or the performance of the model in the 1 atm turbulent flame. Figure 4.13 compares the soot predictions for the Syed (1990) flame made with m set to 2/3 and 1, corresponding to constant sets 5 and 7. These GENMIX runs include soot oxidation by OH and radiative loss from the gas and the soot.

The soot model is also applied to the Mitchell et al. (1980a) flame. The results of this GENMIX calculation are shown in figures 4.14a - d and 4.15a - b. The calculation employs the Warnatz code for species mole fractions, gas and soot radiation is included, soot oxidation by the OH radical is incorporated and constant set 7 is used for the soot model. The agreement between the model predictions for this flame and the experimental data is less satisfactory than for the Syed (1990) flame. The axial decay of mixture fraction with height is well followed and indeed the flame height, as indicated by the position of the temperature maximum on the centreline, is captured perfectly. The radial spread of mixture fraction compares reasonably well with the experimental data. However, the agreement of the GENMIX temperature profiles with those from experiment is poor. The radial position of the temperature peaks are in agreement but GENMIX under predicts the magnitude of these maxima by approximately 200 K. Centreline temperatures are better represented by GENMIX; with an initial over prediction, reaching a maximum difference of approximately 100 K, followed by an under prediction, this under prediction again reaching a maximum of approximately 100 K. The poor agreement in the temperature field suggests that the soot model will give poor results for this flame, and this is the case. The experimental soot data shown here, for the Mitchell et al. (1980a) flame, is derived from the soot absorption data tabulated by Garo (1984). This absorption data has been re-analysed, employing the refractive index for soot used by Syed (1990), to achieve consistency with the Syed (1990) soot dataset. The growth of the soot volume fraction maximum with height, from GENMIX, is broadly in accord with the experimental data; but the form of the radial profiles show very poor agreement. Again the growth of soot on the centreline is the major problem. Given the lower predicted temperatures, the general under prediction of the soot maxima is expected. However, as in the case of the Syed (1990) flame the poor agreement in terms of the profile shape is less easily understood and, given the generally poor scalar field prediction, difficult to analyse. Garo et al. (1986) note that PAH absorption will be responsible for errors in the measured soot profiles. Prado et al. (1984) present radial profiles of laser light scattered by the soot particles. The shape of these profiles shows much better agreement with the form of the profiles predicted by GENMIX, with no particles appearing on the centreline of the flame. The Garo (1984) dataset also includes measurements of the number density of the soot particles. These number density measurements have been corrected for the change in refractive index. The particle number densities given by the model, of ~10^{17} particles per cubic metre, are

consistent with those measured by Garo.

The temperature agreement for the Syed (1990) flame is good; therefore, the poor temperature agreement for the Mitchell et al. (1980a) flame is unexpected. The effect of changing the flame chemistry is shown in figures 4.16a - b. For this GENMIX run the species mole fractions are provided by a flamesheet calculation. The soot levels have not been calculated and, therefore, there is no radiative loss from the soot. However, the CO_2 and H_2O concentrations are greater, than for the calculation using the Warnatz mole fractions, therefore the levels of radiative loss are similar. The temperature agreement has improved greatly, although there is still an over prediction on the flame centreline. The reasons for the generally poor agreement between the GENMIX predictions and the combined Mitchell et al. (1980a) / Garo (1984) dataset are uncertain, but two features of this dataset are notable. The first of these is the radiative correction for the thermocouple bead used for temperature measurement by Mitchell et al. (1980a). Syed (1990) states that a maximum radiative loss correction of ~60 K is applied to the thermocouple temperature measurements in his flame, whereas the correction used by Mitchell et al. (1980a) is ~200 K in the highest temperature regions. This suggests that Mitchell et al. (1980a) use a higher value for the emissivity of the bead than Syed (1990). The second point of note is that the soot measurements taken by Garo (1984) rely on tomographic inversion (see chapter 3) for retrieval of the soot volume fraction profiles. This process will inevitably result in a certain degree of error.

4.6 Conclusion

Two laminar flames have been modelled with varying degrees of success. The results for the Syed (1990) flame are good and encourage confidence in the accuracy of the soot model calibrations. The results for the Mitchell et al. (1980a) flame are not as good, but as noted in section 4.5 assessment of the model by comparison with the combined Mitchell et al. (1980a) / Garo (1984) dataset is slightly ambiguous. A linear dependence for the soot surface growth term is found to give the best agreement with the experimental data. The ethyne concentration exponent has been shown to not substantially affect the results for the laminar flame and discussion of this parameter is delayed until the next chapter. The main failing of the soot model is its inability to satisfactorily predict the growth of soot on the centreline of the laminar flame. However, until soot measurements in this flame region can be made unambiguously model development and validation beyond that accomplished in this chapter will be impossible.

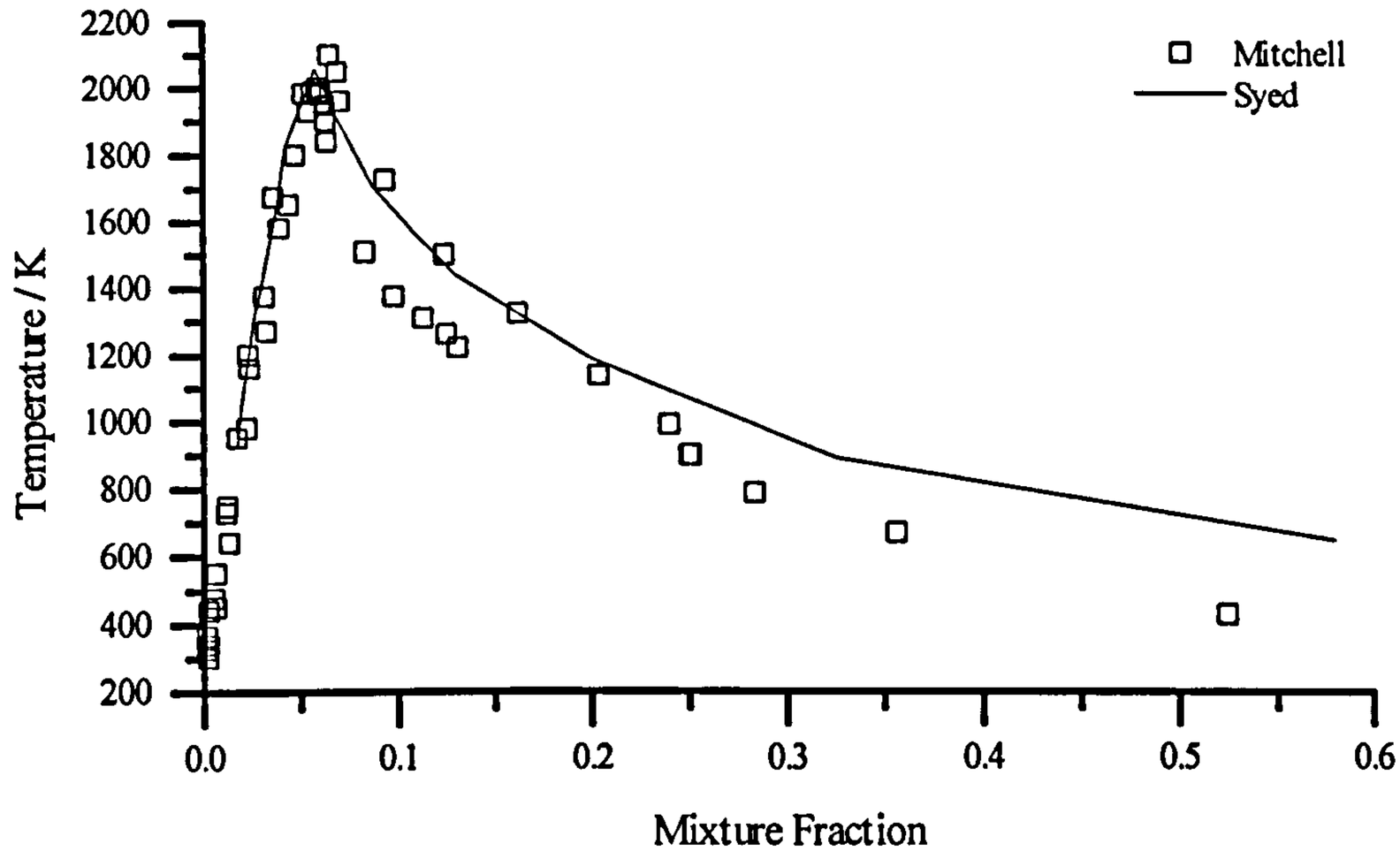

Figure 4.1. Experimental temperature - mixture fraction relationships, from the Mitchell et al. (1980a) and Syed (1990) laminar flame experiments.

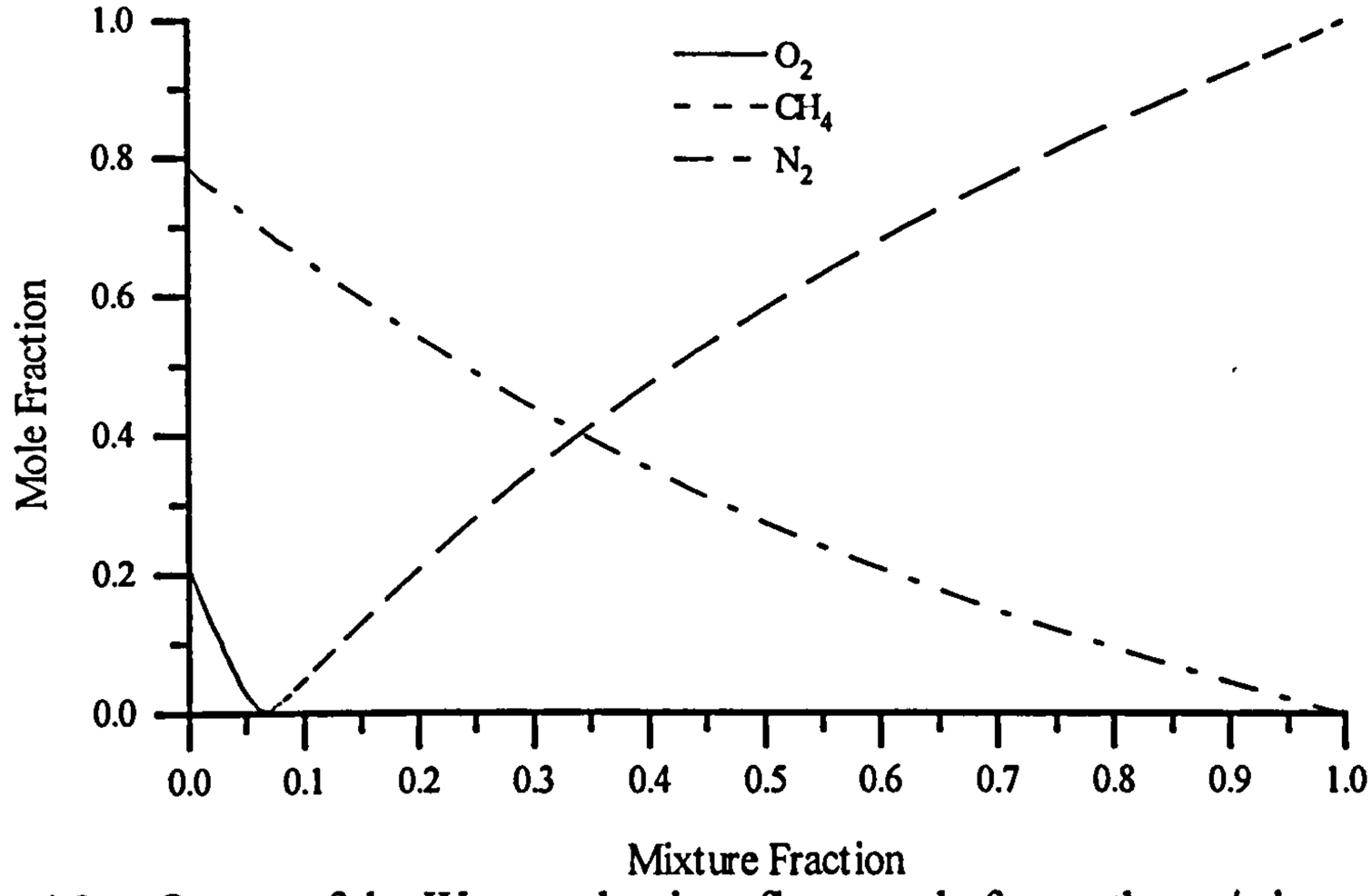

Figure 4.2a. Output of the Warnatz laminar flame code for methane / air combustion.

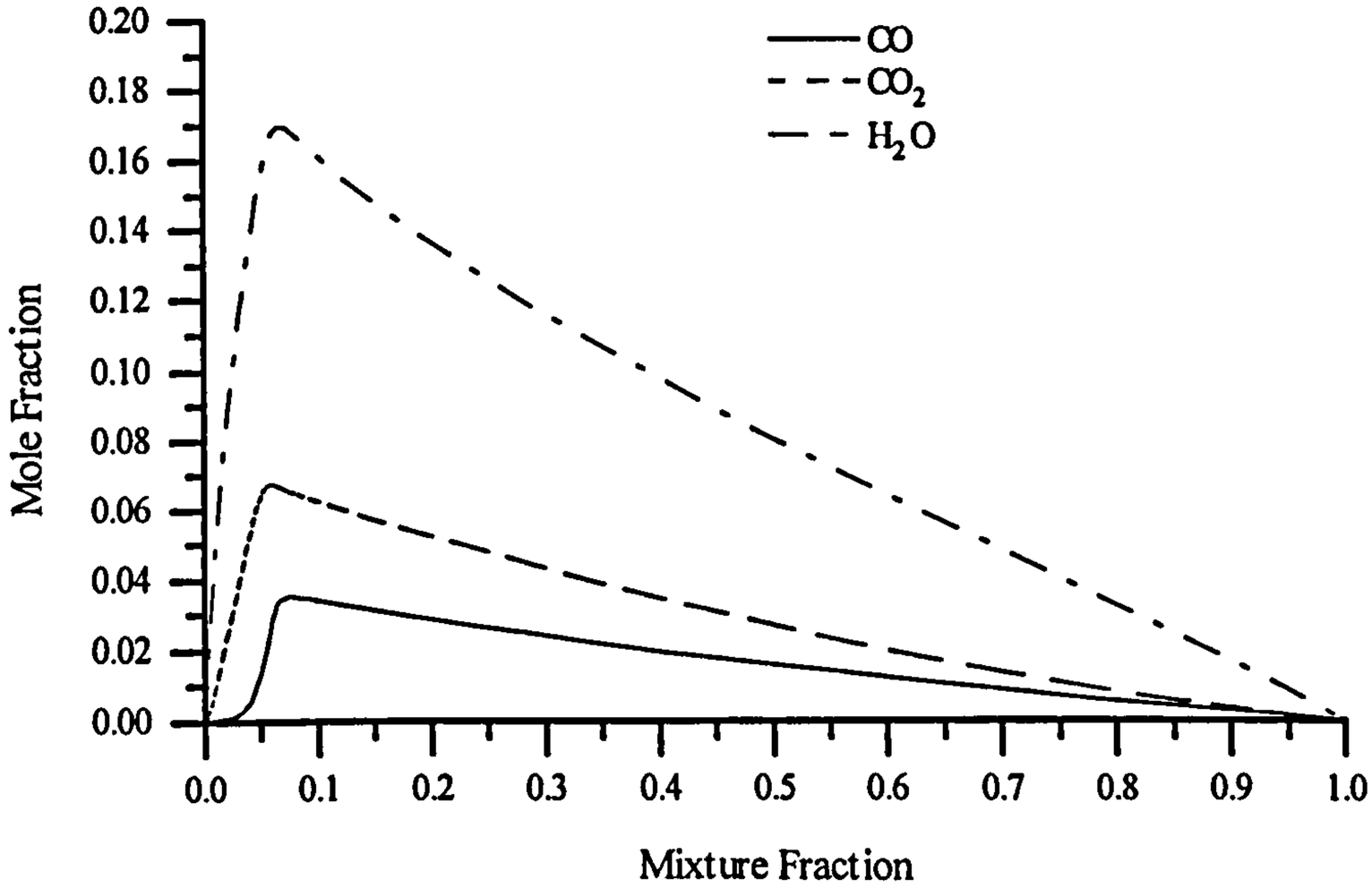

Figure 4.2b. Output of the Warnatz laminar flame code for methane / air combustion.

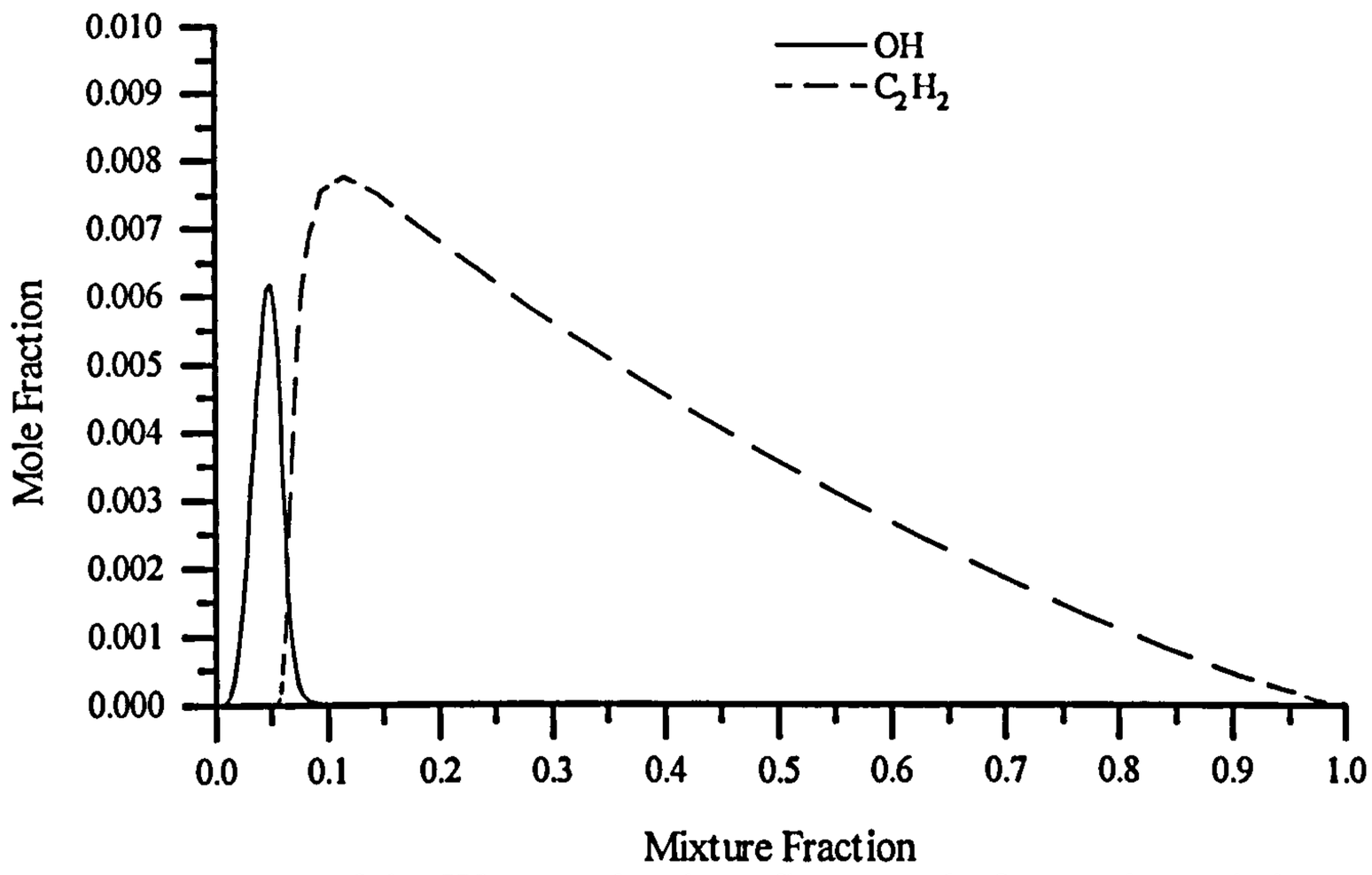

Figure 4.2c. Output of the Warnatz laminar flame code for methane / air combustion.

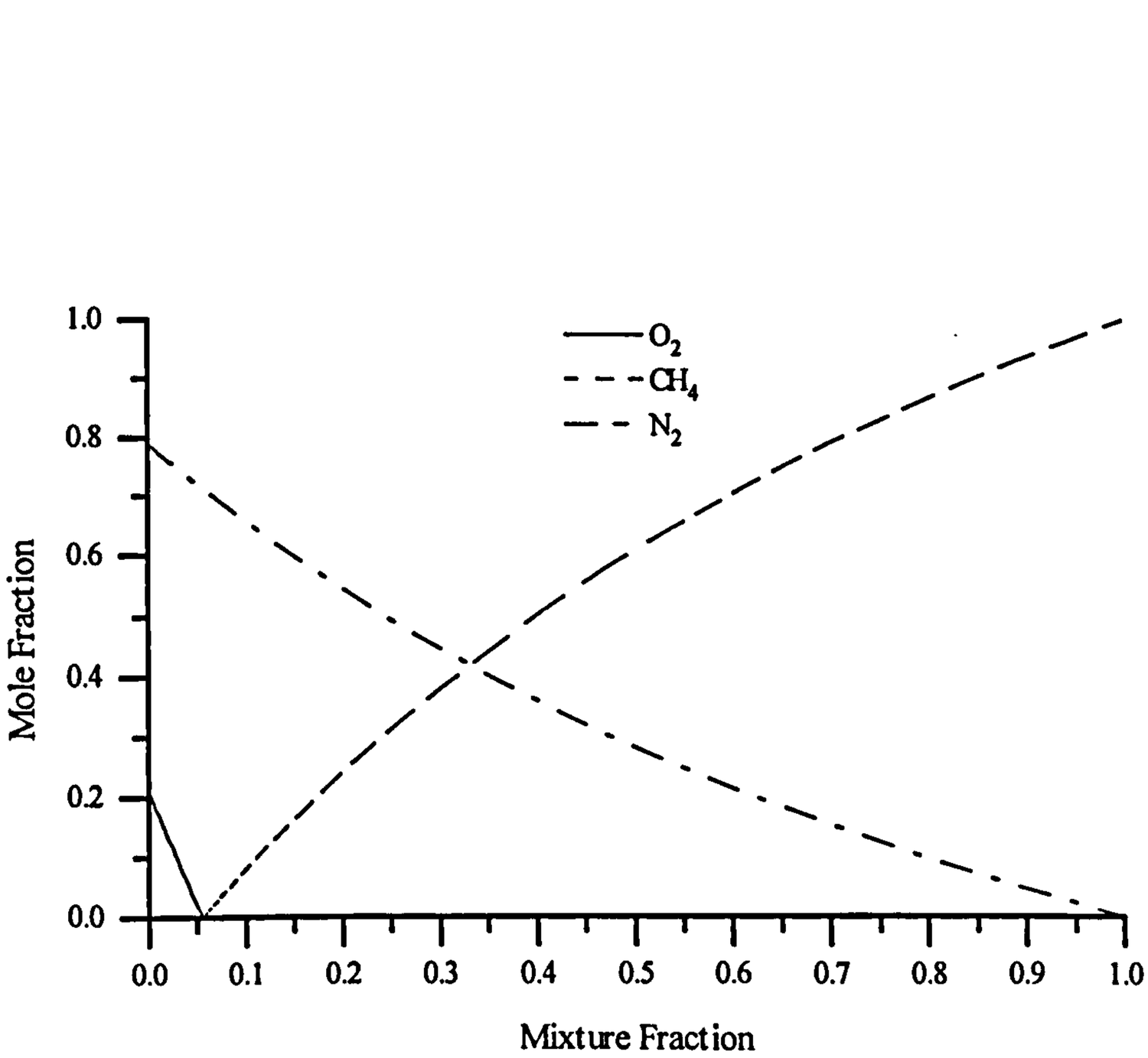

Figure 4.3a. Flamesheet species for methane / air combustion.

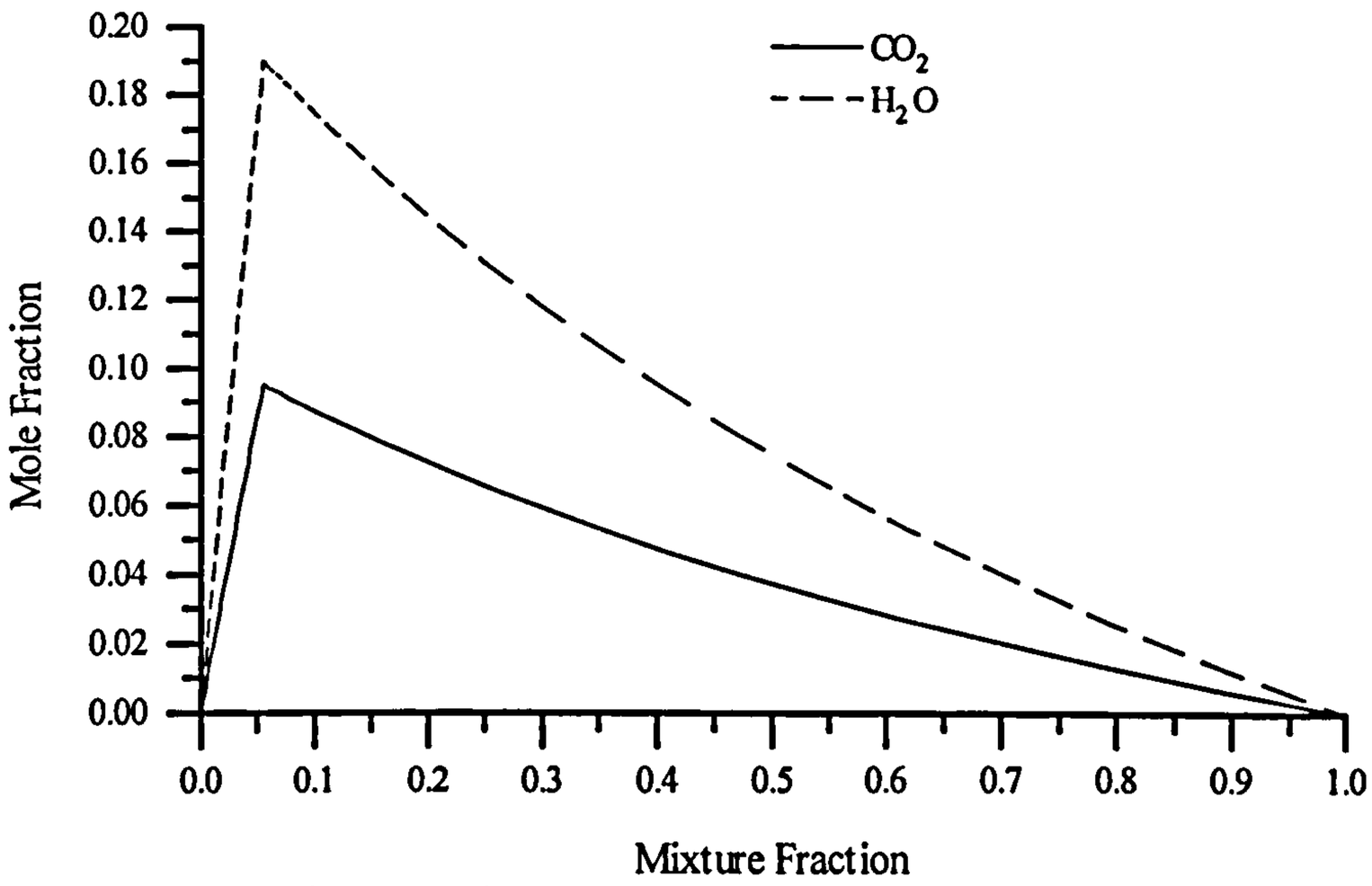

Figure 4.3b. Flamesheet species for methane / air combustion.

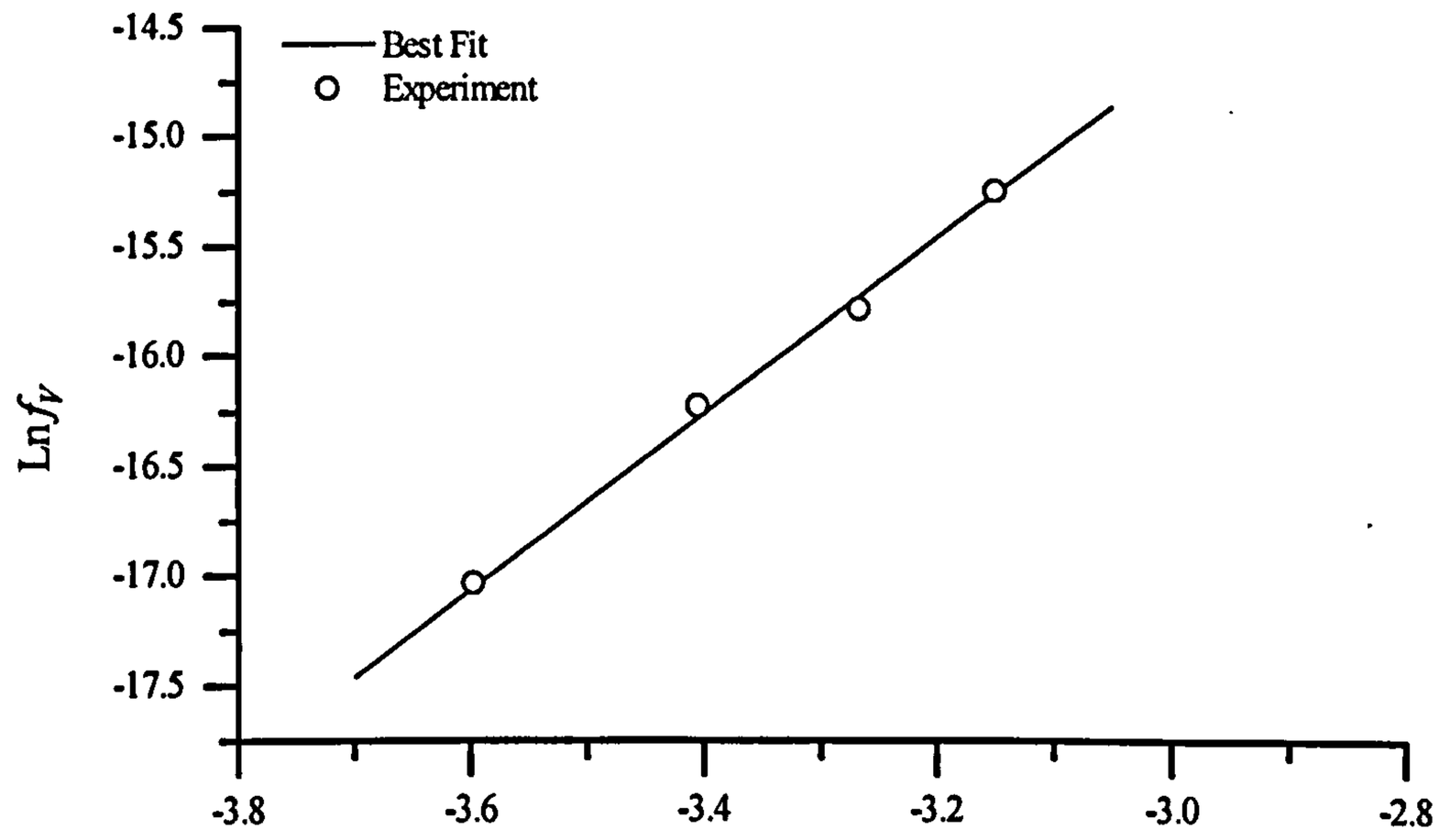

Figure 4.4. Natural log.s of peak soot volume fraction from the Syed (1990) experimental data set plotted against the natural log.s of residence time from the GENMIX calculation. The best fit line is also shown.

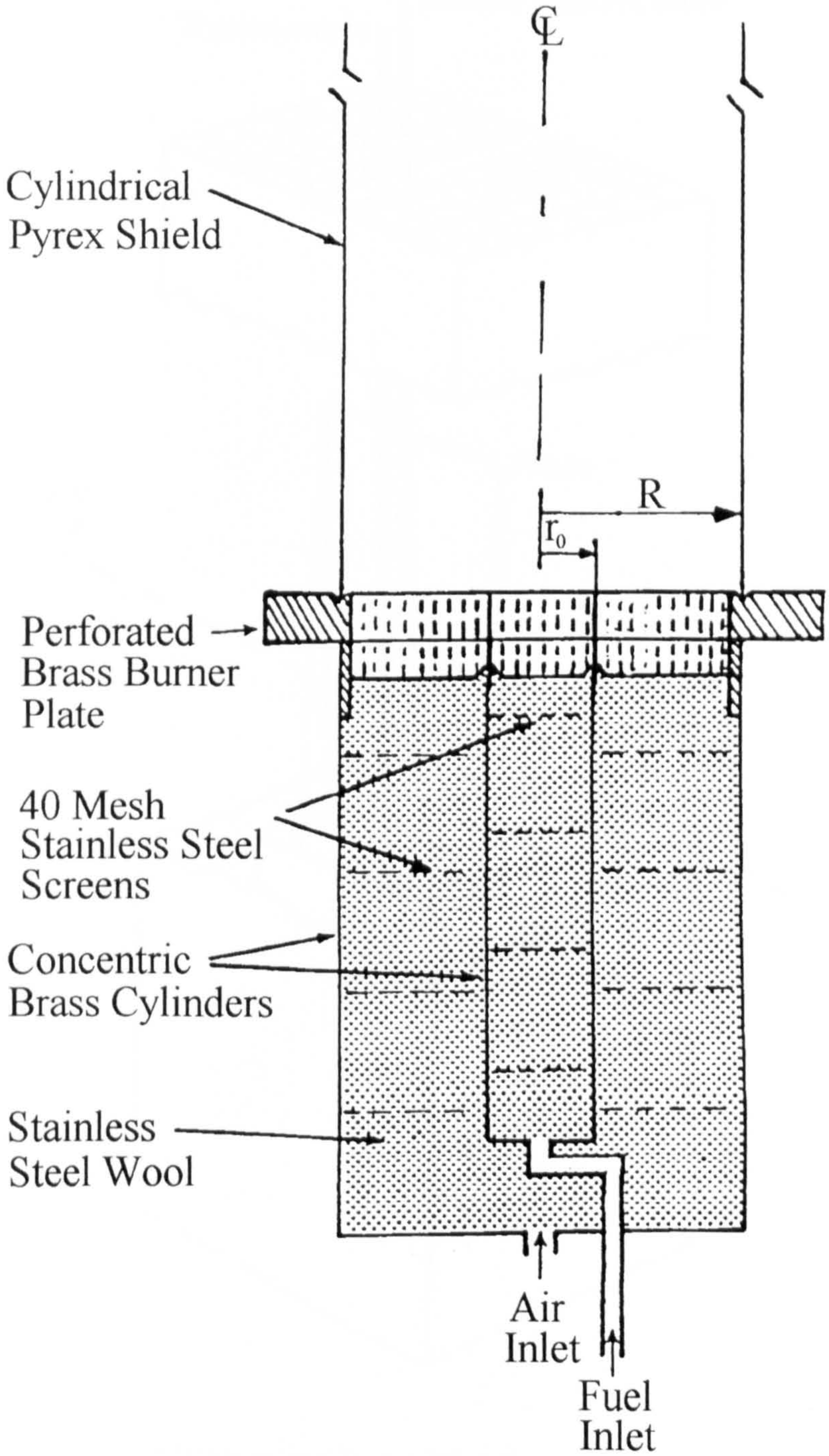

Figure 4.5. Mitchell et al. (1980a) laminar flame burner geometry.

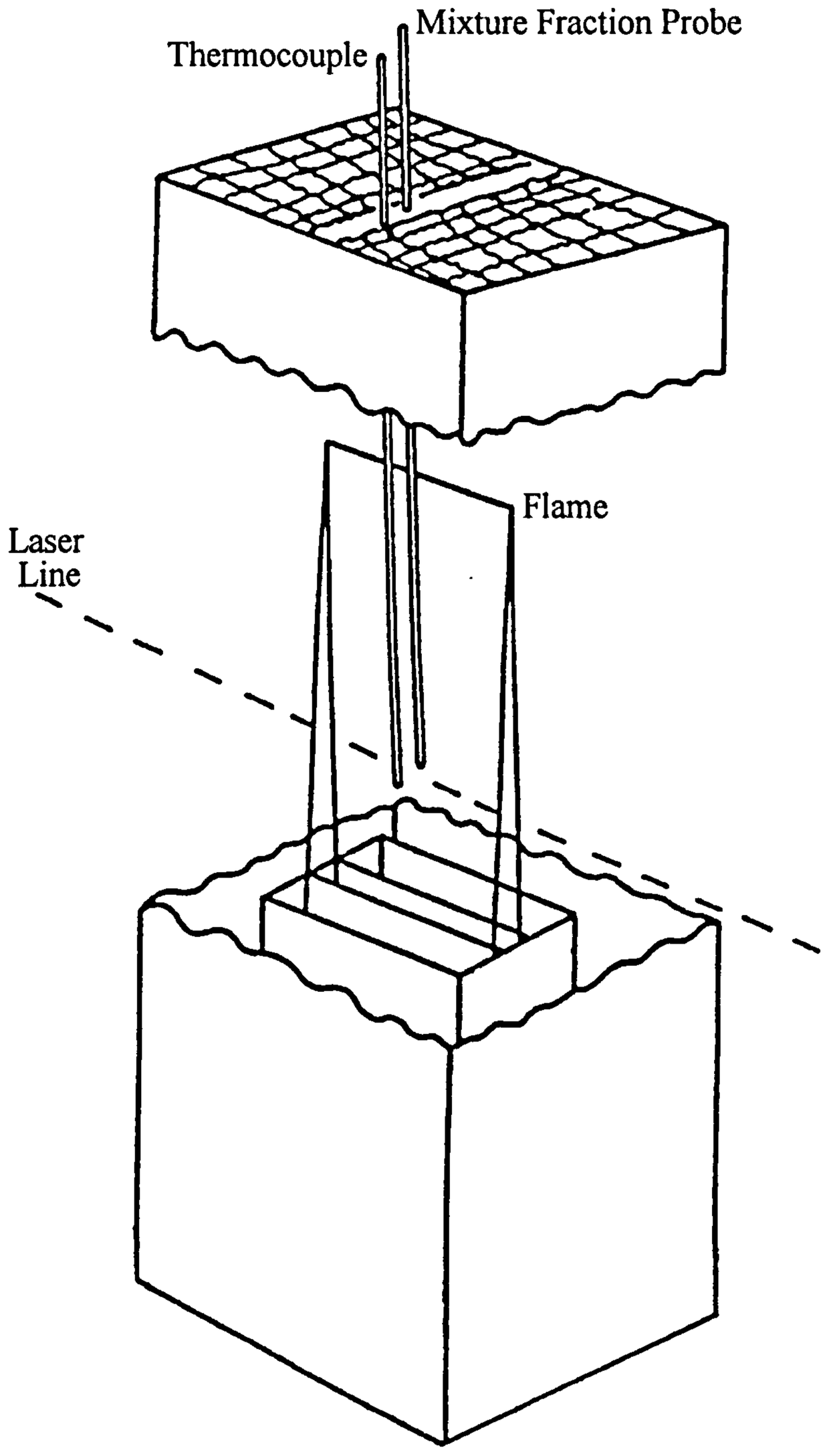

Figure 4.6. Syed (1990) laminar flame burner geometry.

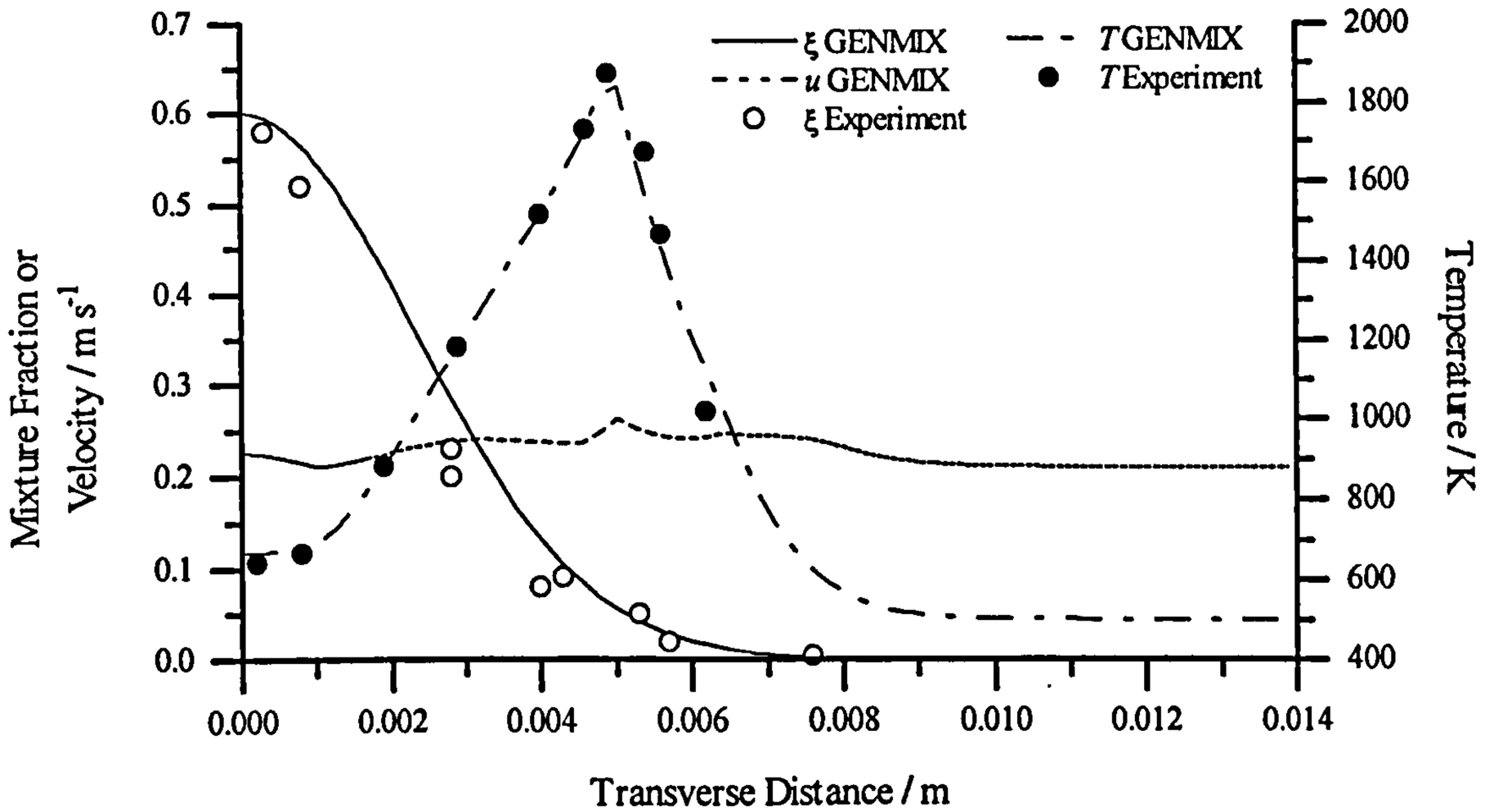

Figure 4.7. Initial conditions (2 mm above the exit plane of the burner) used in the GENMIX calculation of the Syed (1990) flame. The experimental values are shown for comparison.

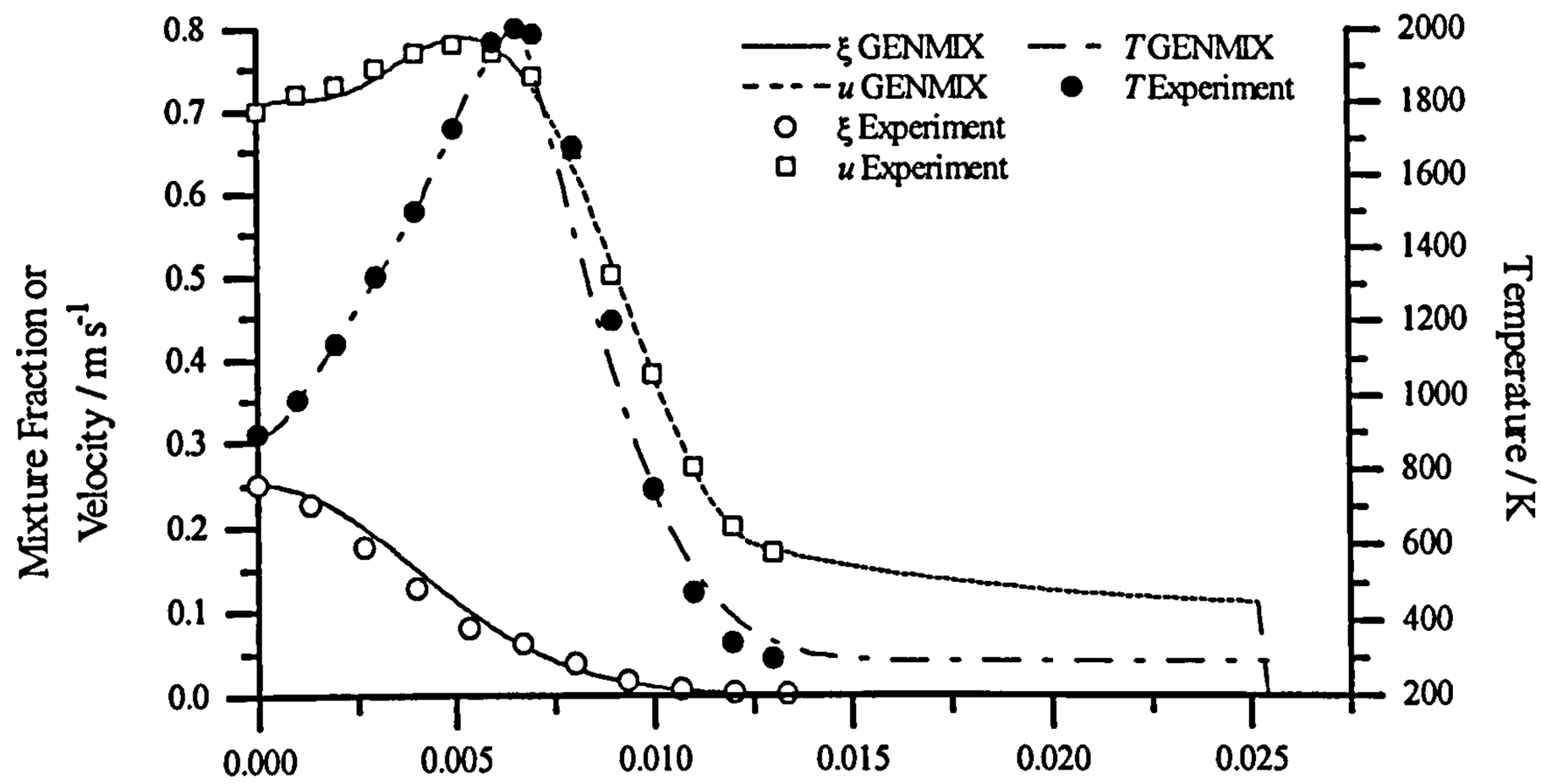

Figure 4.8a. Initial conditions (12 mm above the burner exit plane) utilised for the GENMIX calculation of the Mitchell et al. (1980a) flame. Experimental profiles are shown for comparison.

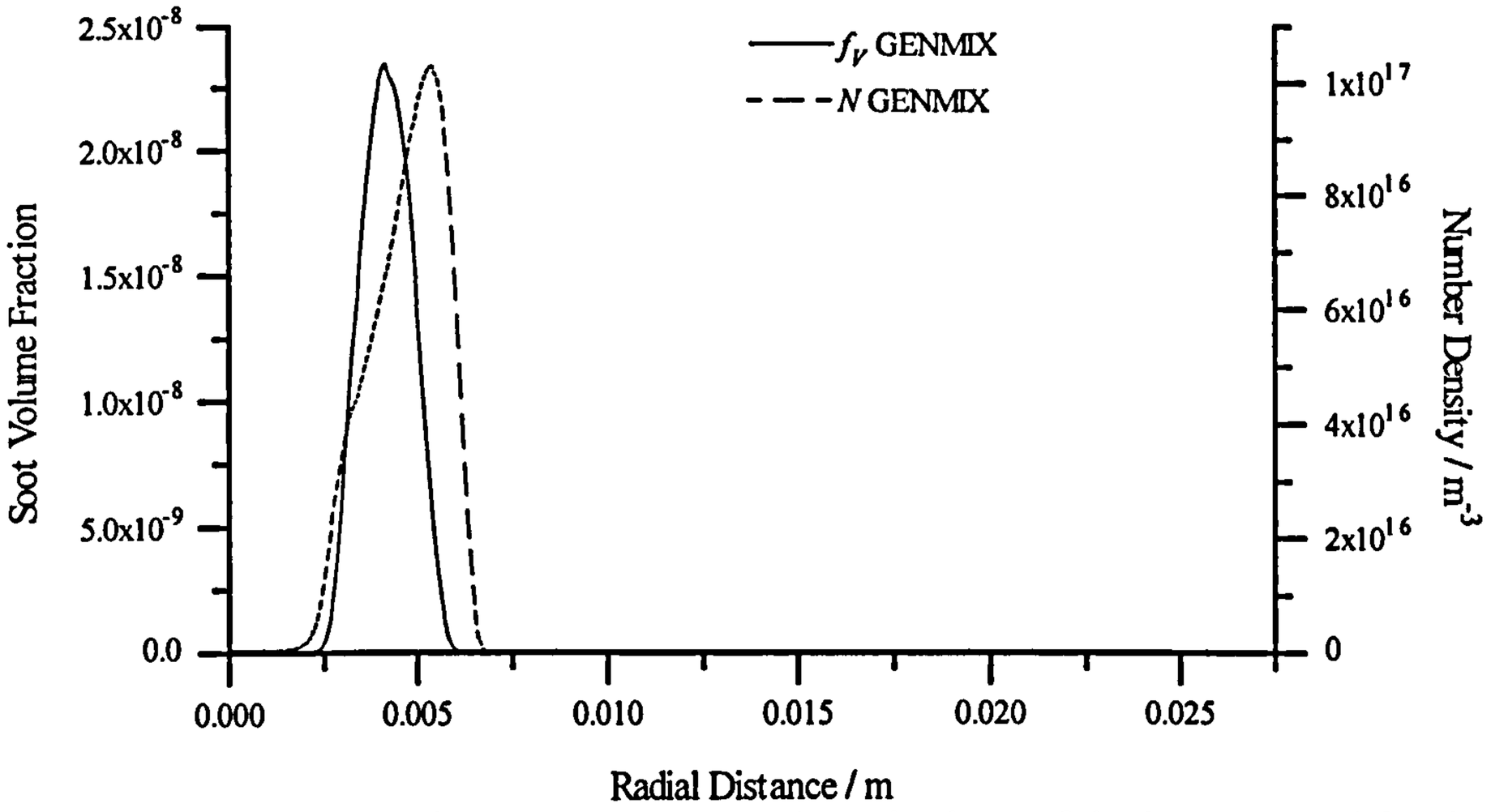

Figure 4.8b. Initial conditions (12 mm above the exit plane of the burner) used for the soot properties in the GENMIX calculation of the Mitchell et al. (1980a) laminar flame.

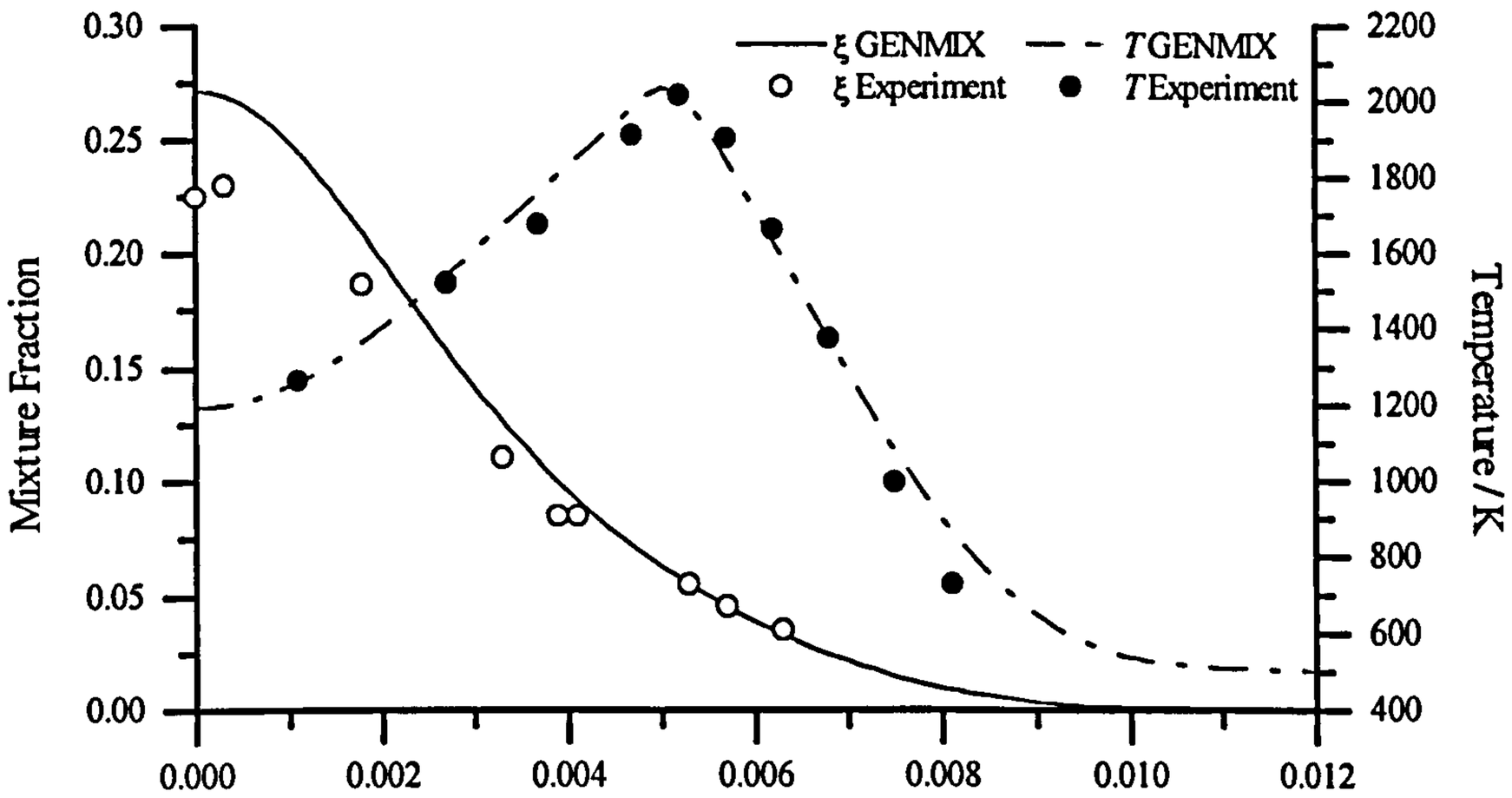

Figure 4.9a. Results of the GENMIX calculation for the Syed (1990) flame compared with experiment. Height shown is 10 mm above the exit plane of the burner. Constant set 7 is used in the soot model with soot oxidation by the OH radical. Radiative heat loss is included.

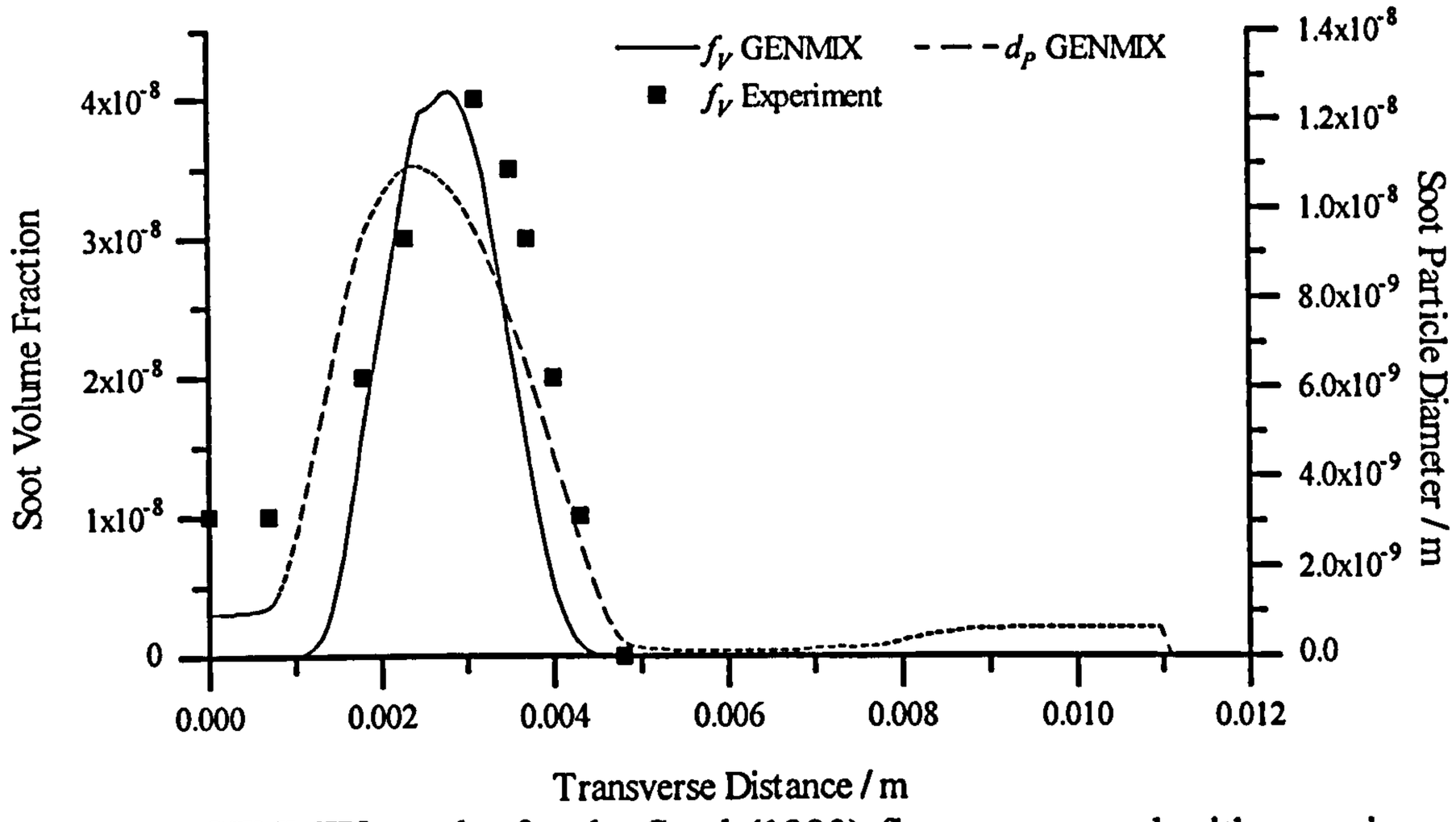

Figure 4.9b. GENMIX results for the Syed (1990) flame compared with experiment 15 mm above the burner exit plane.

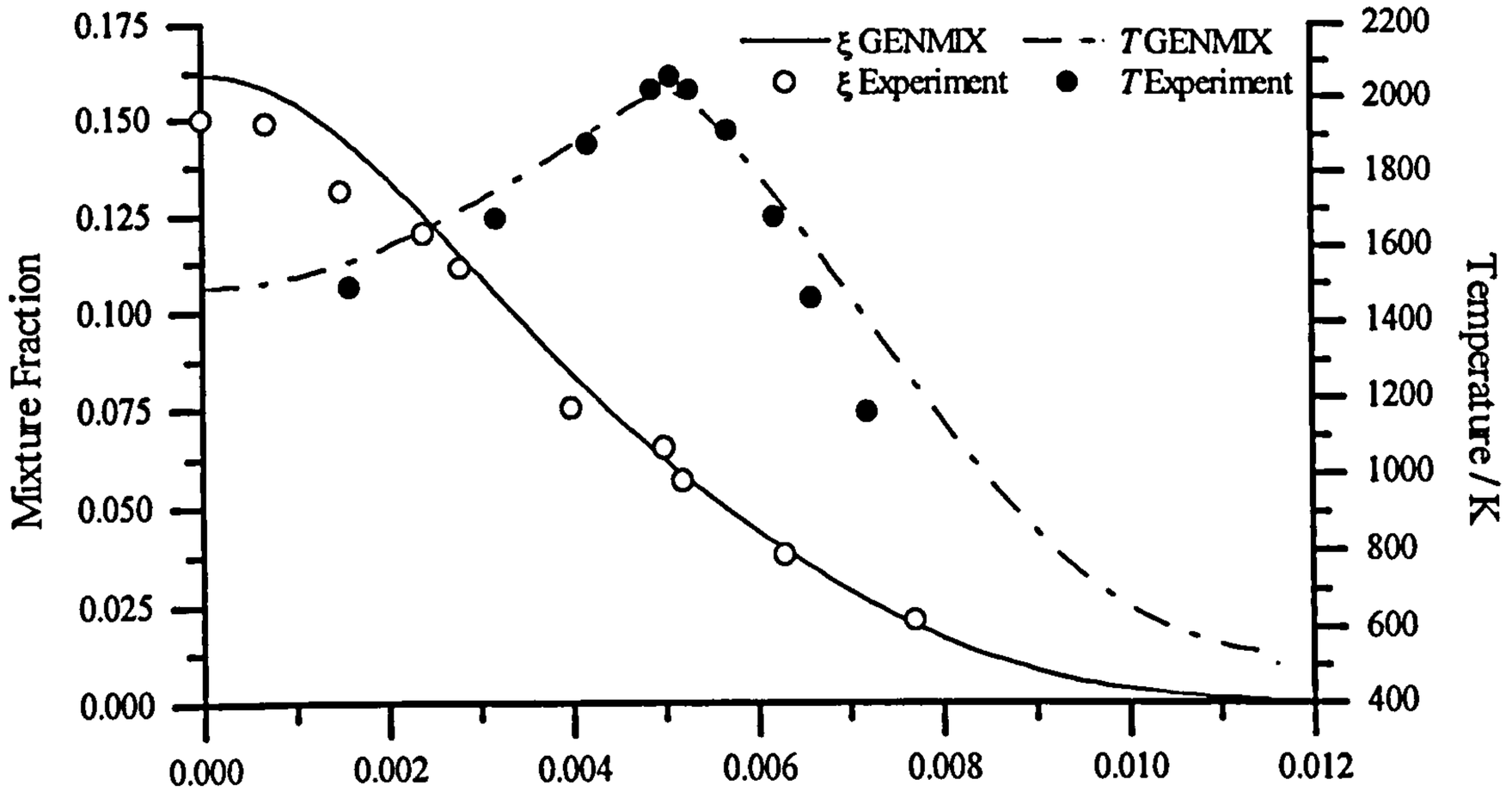

Figure 4.9c. GENMIX results for the Syed (1990) flame compared with experiment 20 mm above the burner exit plane.

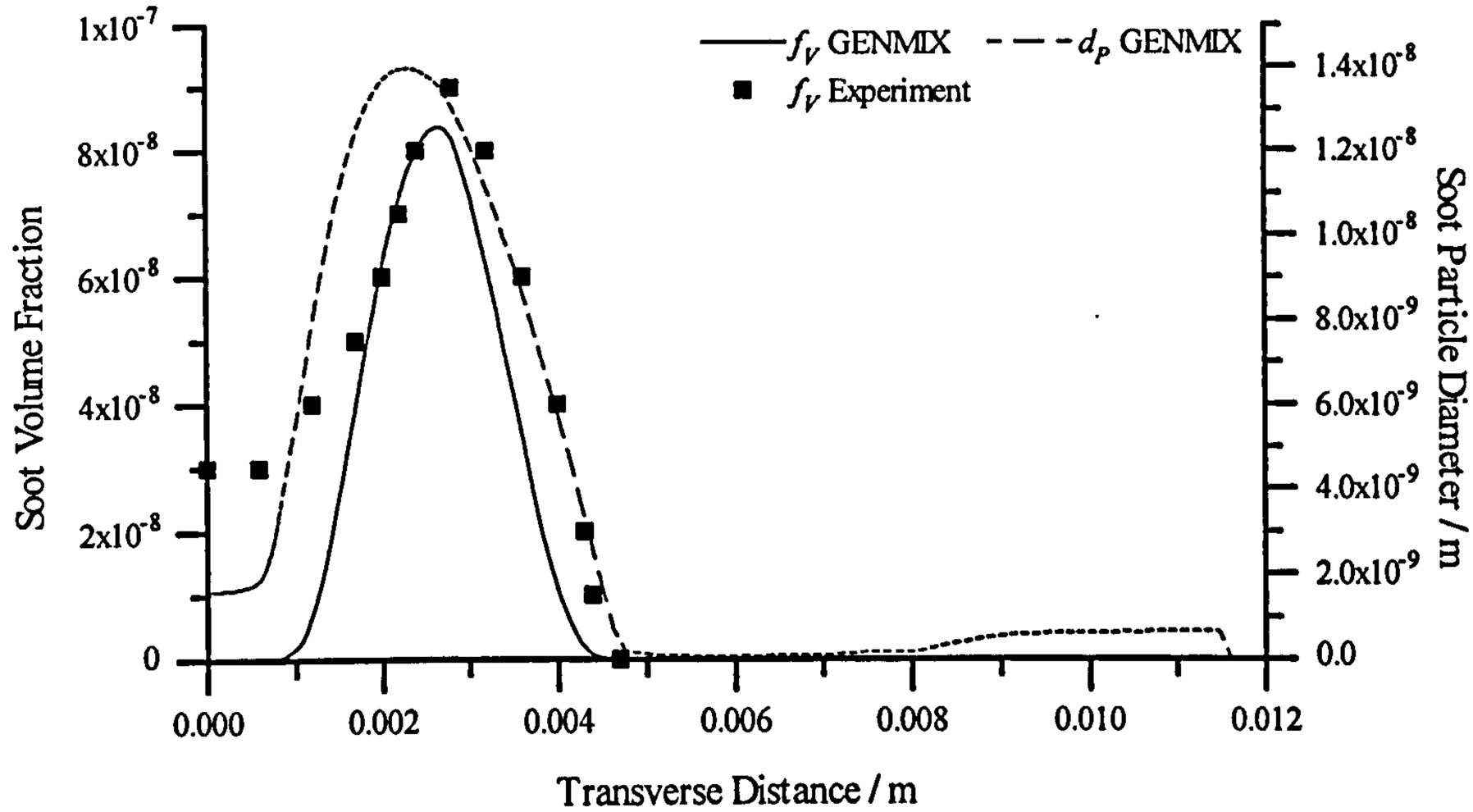

Figure 4.9d. GENMIX results for the Syed (1990) flame compared with experiment 20 mm above the exit plane of the burner.

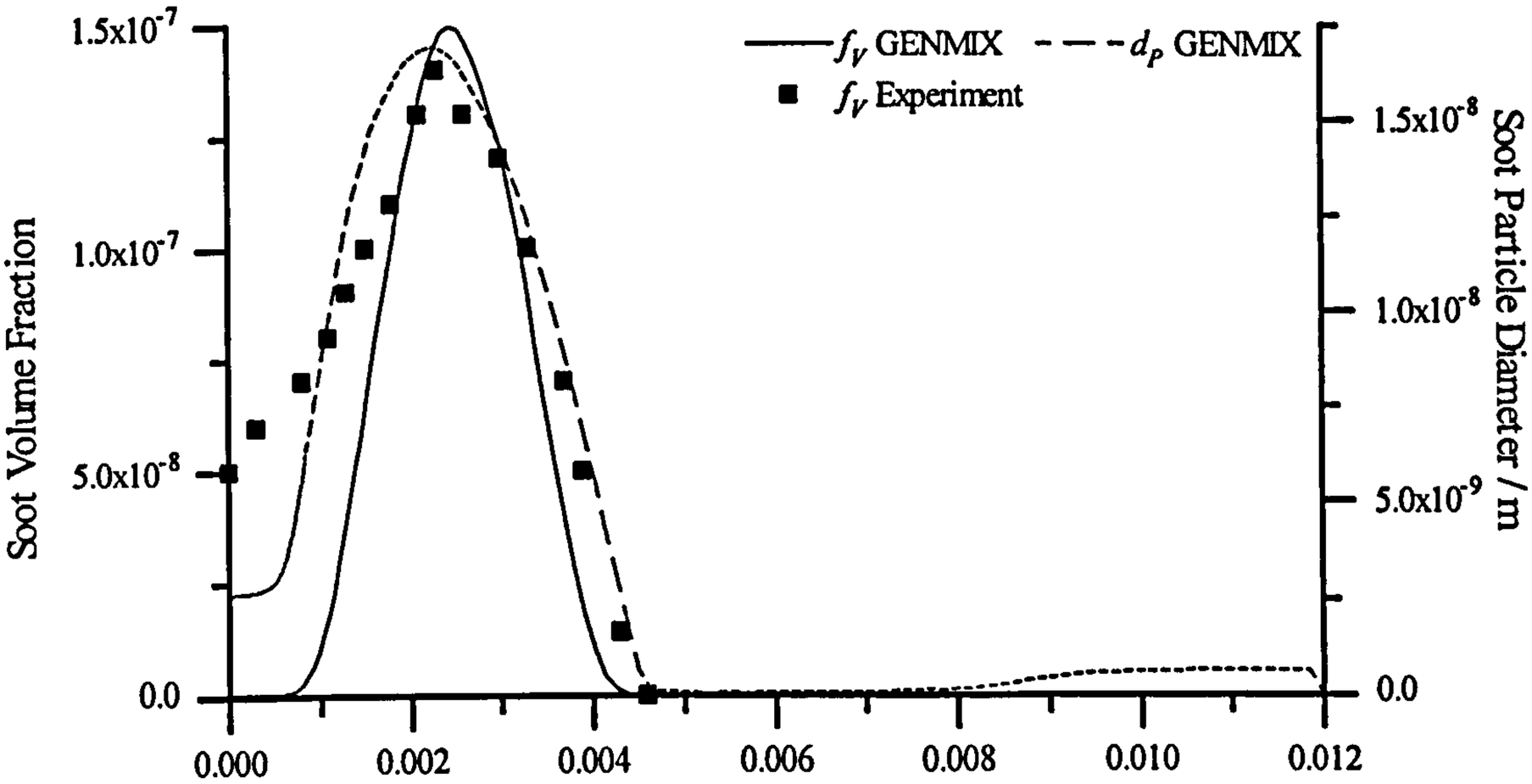

Figure 4.9e. GENMIX results for the Syed (1990) flame compared with experiment 25 mm above the exit plane of the burner.

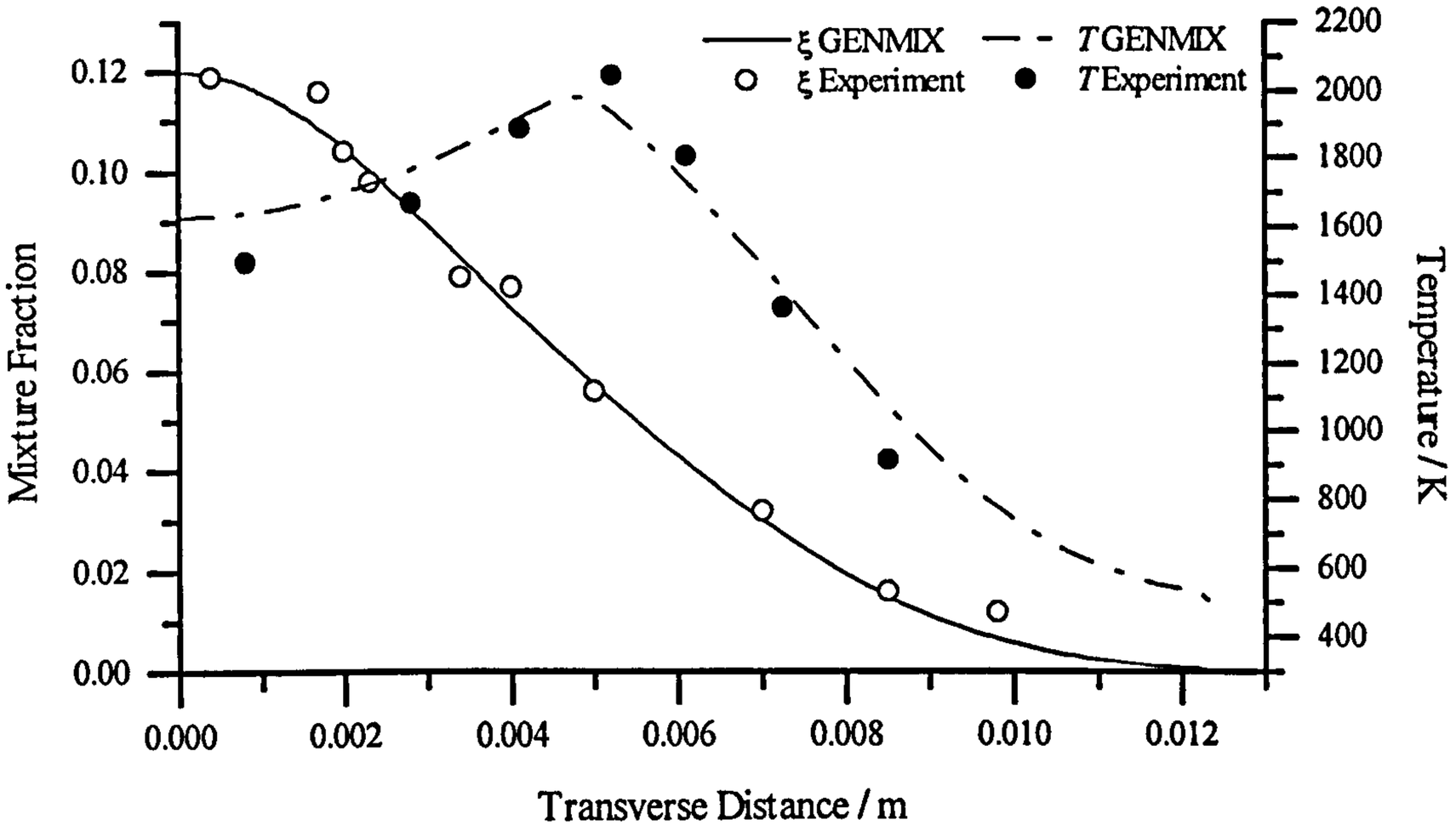

Figure 4.9f. GENMIX results for the Syed (1990) flame compared with experiment 30 mm above the exit plane of the burner.

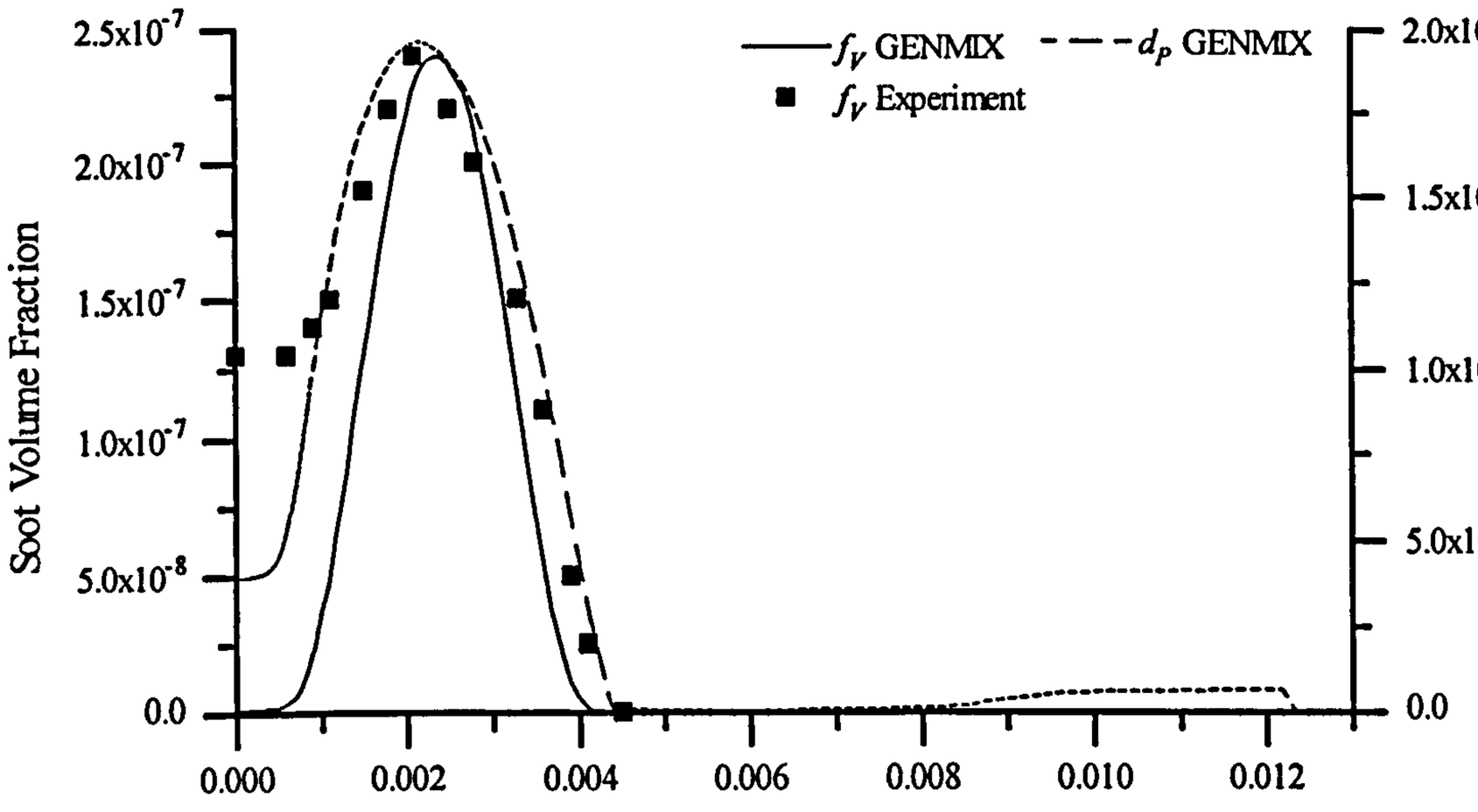

Figure 4.9g. GENMIX results for the Syed (1990) flame compared with experiment 30 mm above the exit plane of the burner.

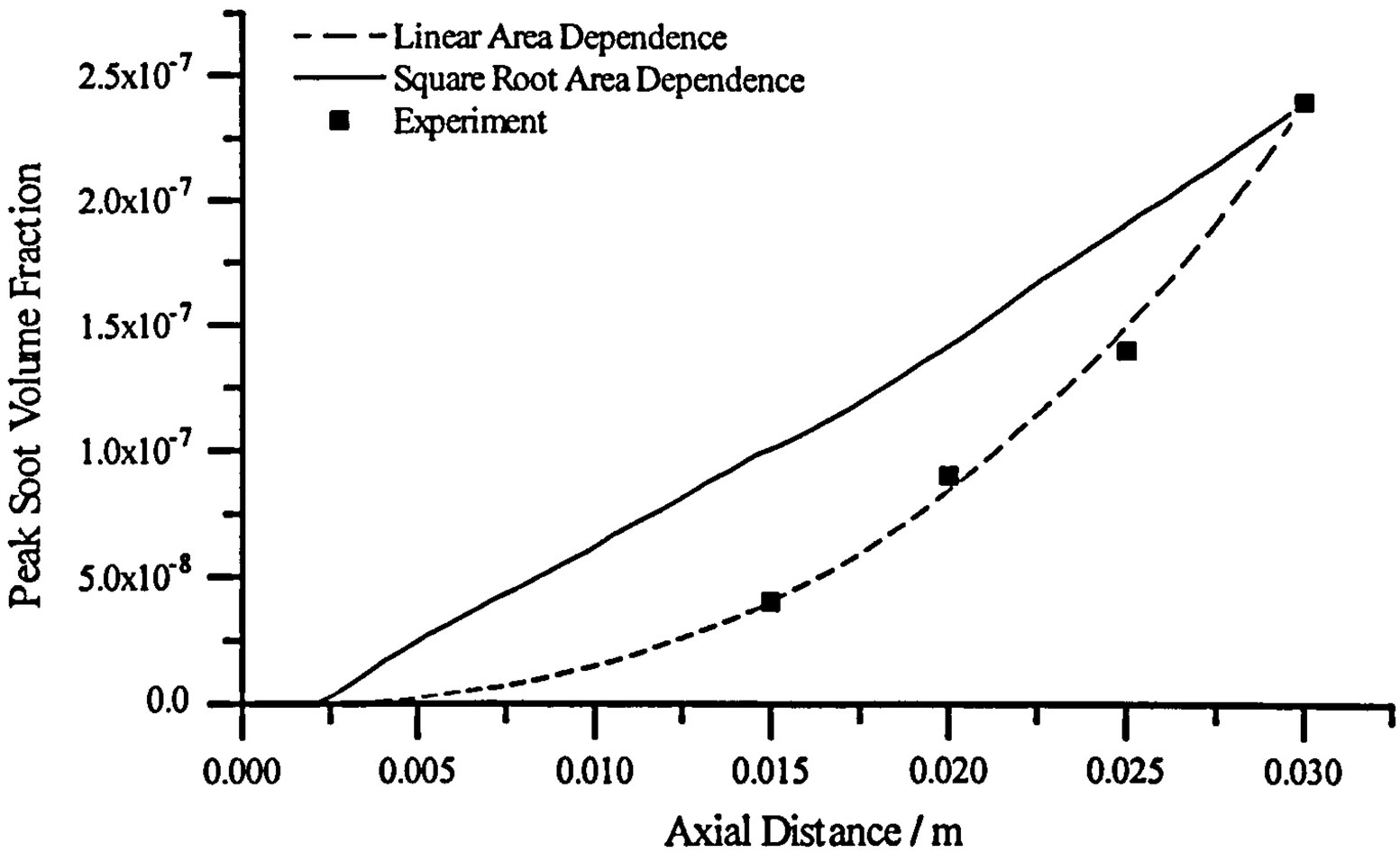

Figure 4.10. Axial variation of the peak soot volume fraction in the Syed (1990) flame. This figure compares the performance of the soot model with linear area dependence (constant set 7) and square root area dependence (constant set 8). Radiative heat loss and soot oxidation by the OH radical is included.

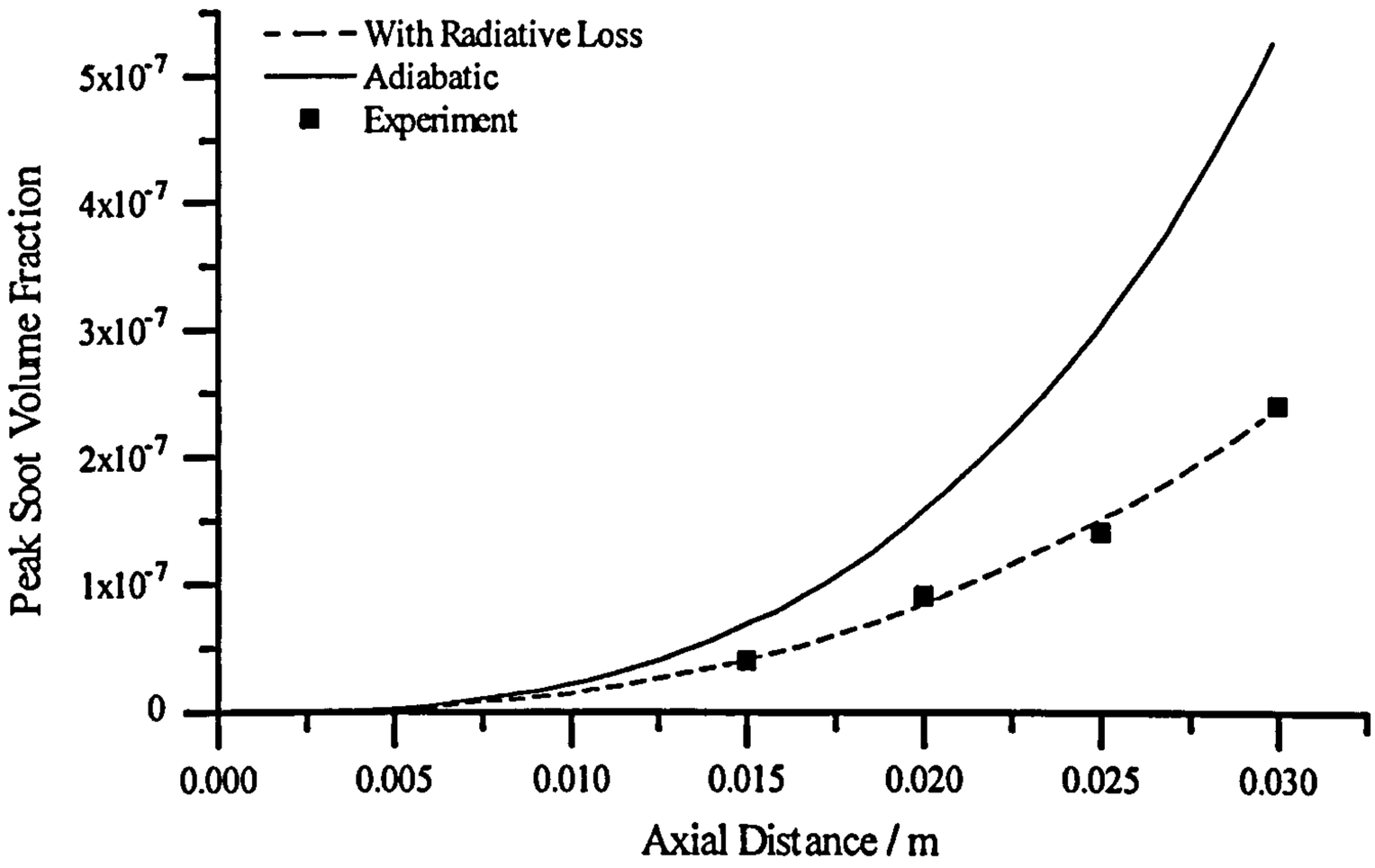

Figure 4.11. Axial variation of the peak soot volume fraction in the Syed (1990) flame. The soot model uses constant set 7 with soot oxidation by the OH radical included. The two lines show the effect of the radiative heat loss on the GENMIX calculation.

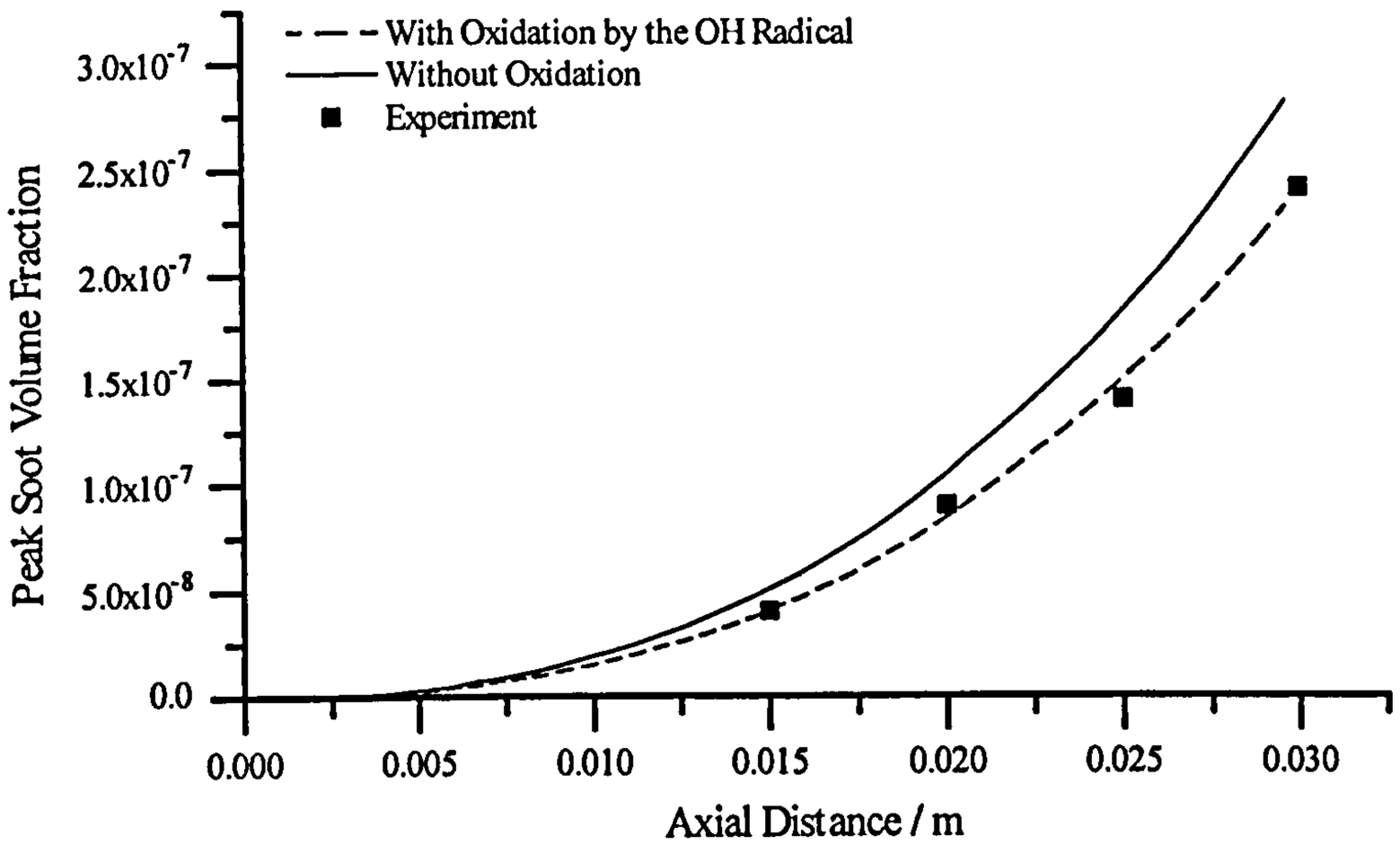

Figure 4.12. Axial variation of the peak soot volume fraction in the Syed (1990) flame. The GENMIX calculation uses constant set 7 in the soot model. Radiative loss is included. The two lines show the effect of neglecting the oxidation.

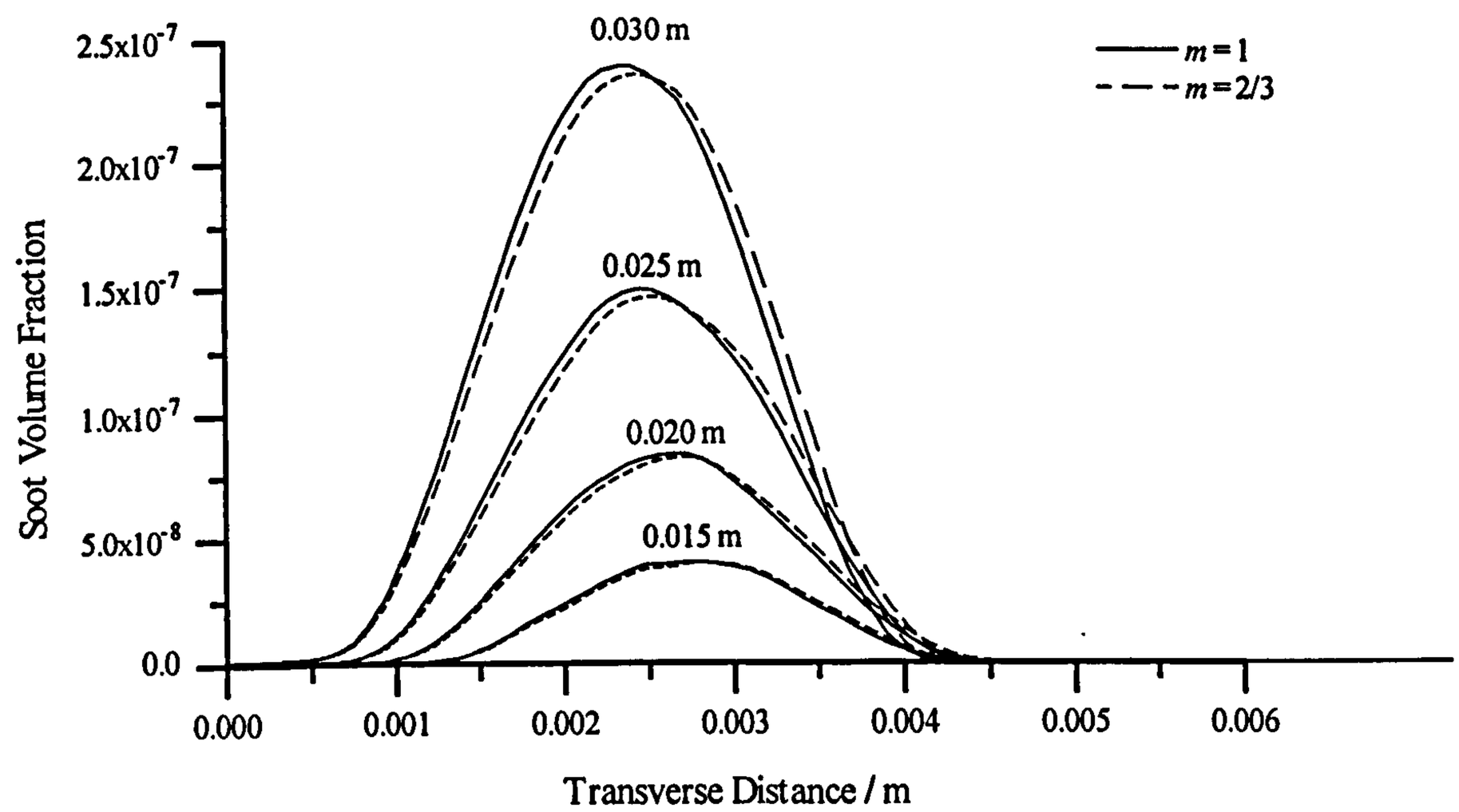

Figure 4.13. GENMIX results for the Syed (1990) flame. The figure illustrates the effect of changing the ethyne concentration exponent in the soot model.

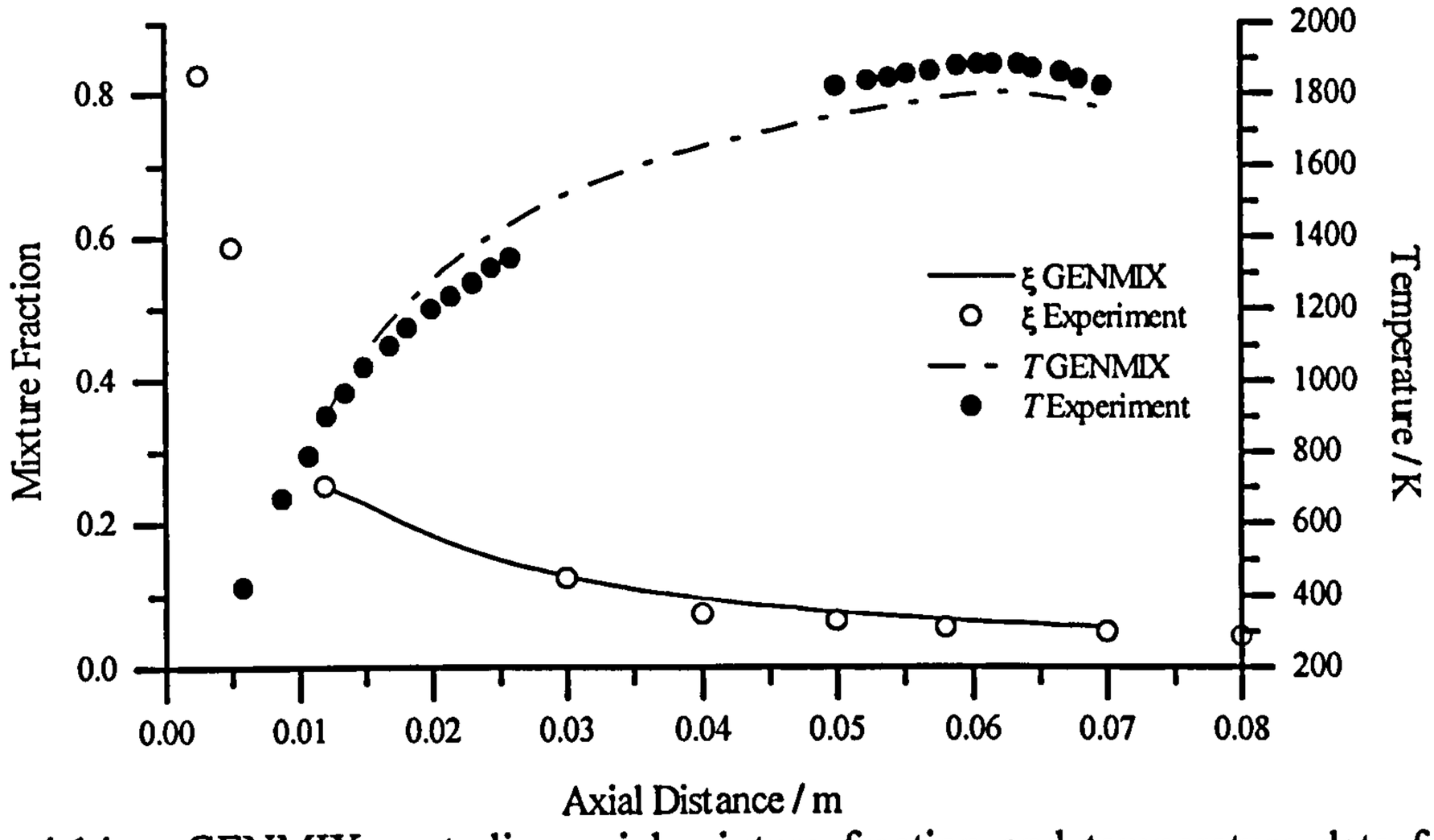

Figure 4.14a. GENMIX centreline axial mixture fraction and temperature data for the Mitchell et al. (1980a) laminar flame compared with experiment.

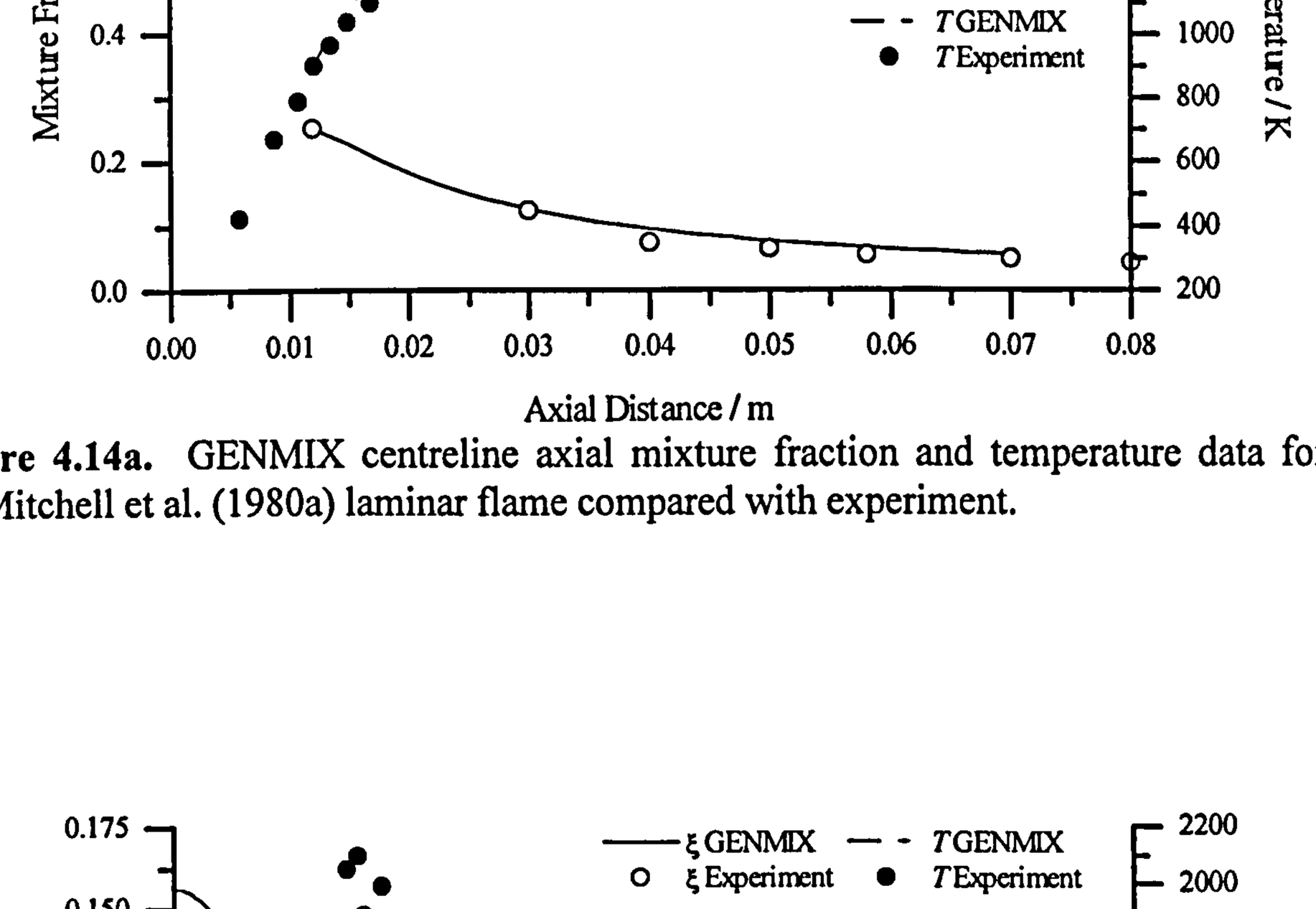

Figure 4.14b. GENMIX radial mixture fraction and temperature data for the Mitchell et al. (1980a) laminar flame compared with experiment 24 mm above the burner exit plane.

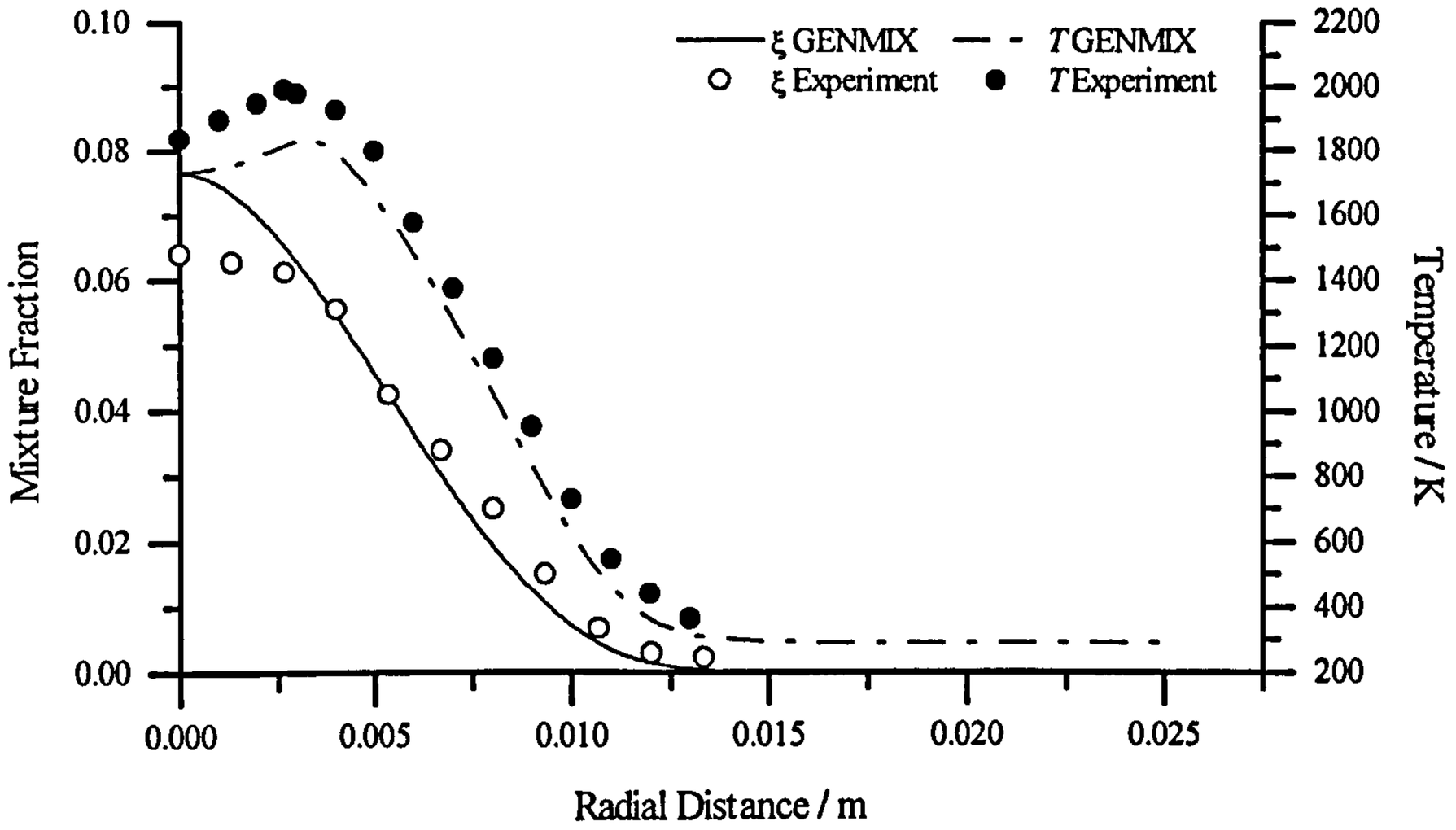

Figure 4.14c. GENMIX radial mixture fraction and temperature data for the Mitchell et al. (1980a) laminar flame compared with experiment 50 mm above the burner exit plane.

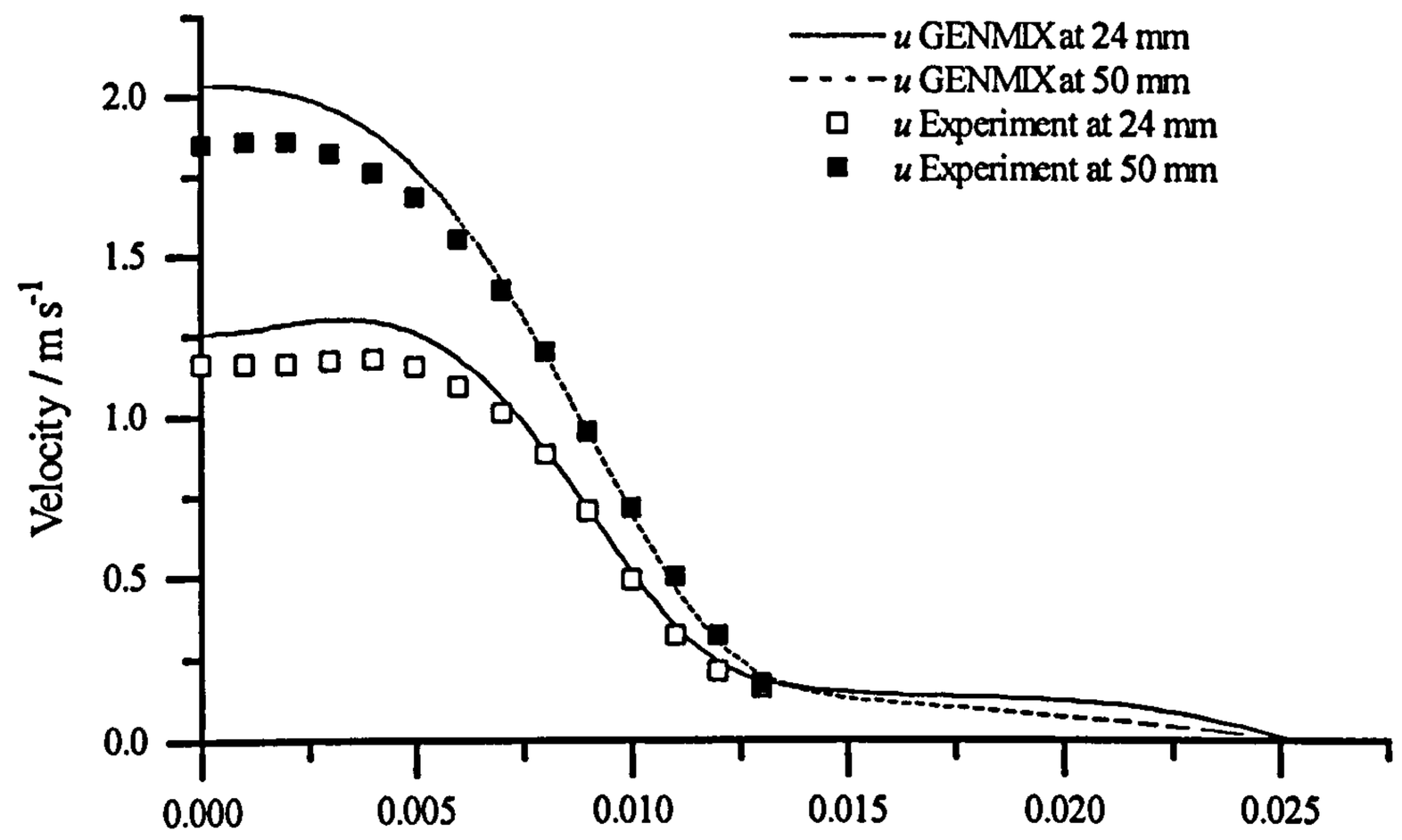

Figure 4.14d. GENMIX radial velocity data (axial component) for the Mitchell et al. (1980a) laminar flame compared with experiment at 24 mm and 50 mm above the burner exit plane.

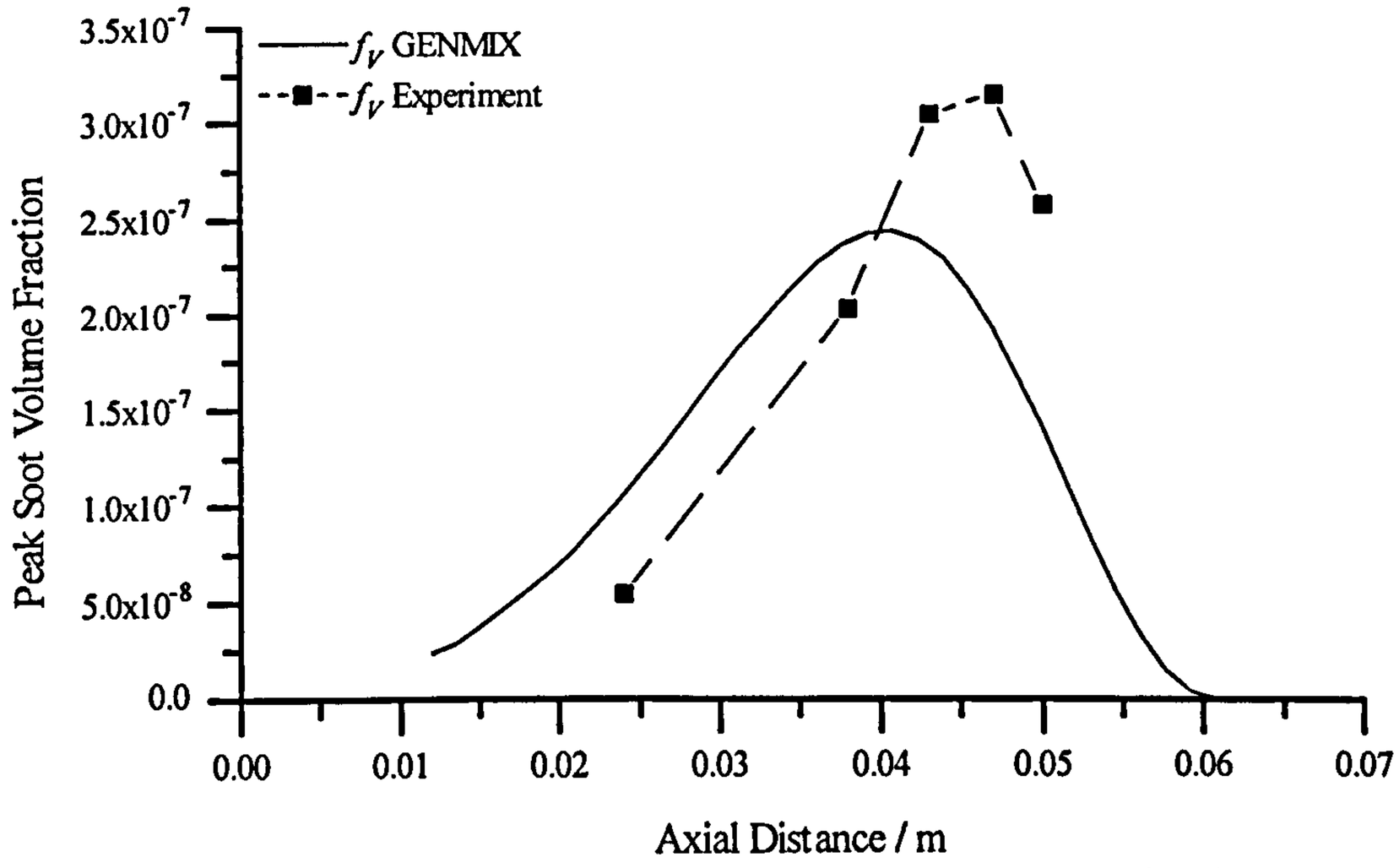

Figure 4.15a. GENMIX soot data for the Mitchell et al. (1980a) laminar flame compared with experiment. Figure shows the evolution of the peak soot volume fraction with height above the burner exit plane.

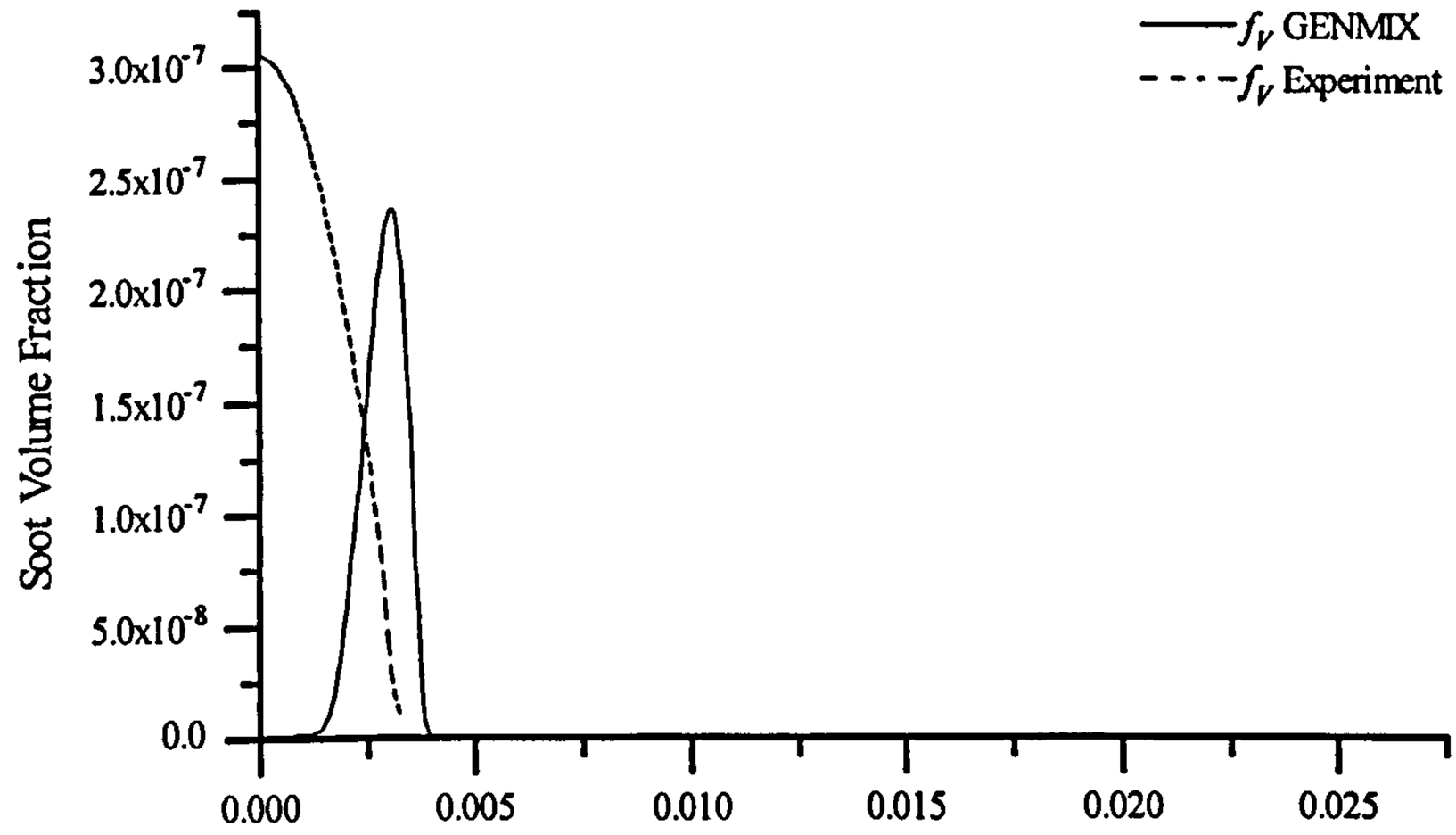

Figure 4.15b. GENMIX radial soot data for the Mitchell et al. (1980a) laminar flame compared with experiment at a height of 43 mm above the burner exit plane.

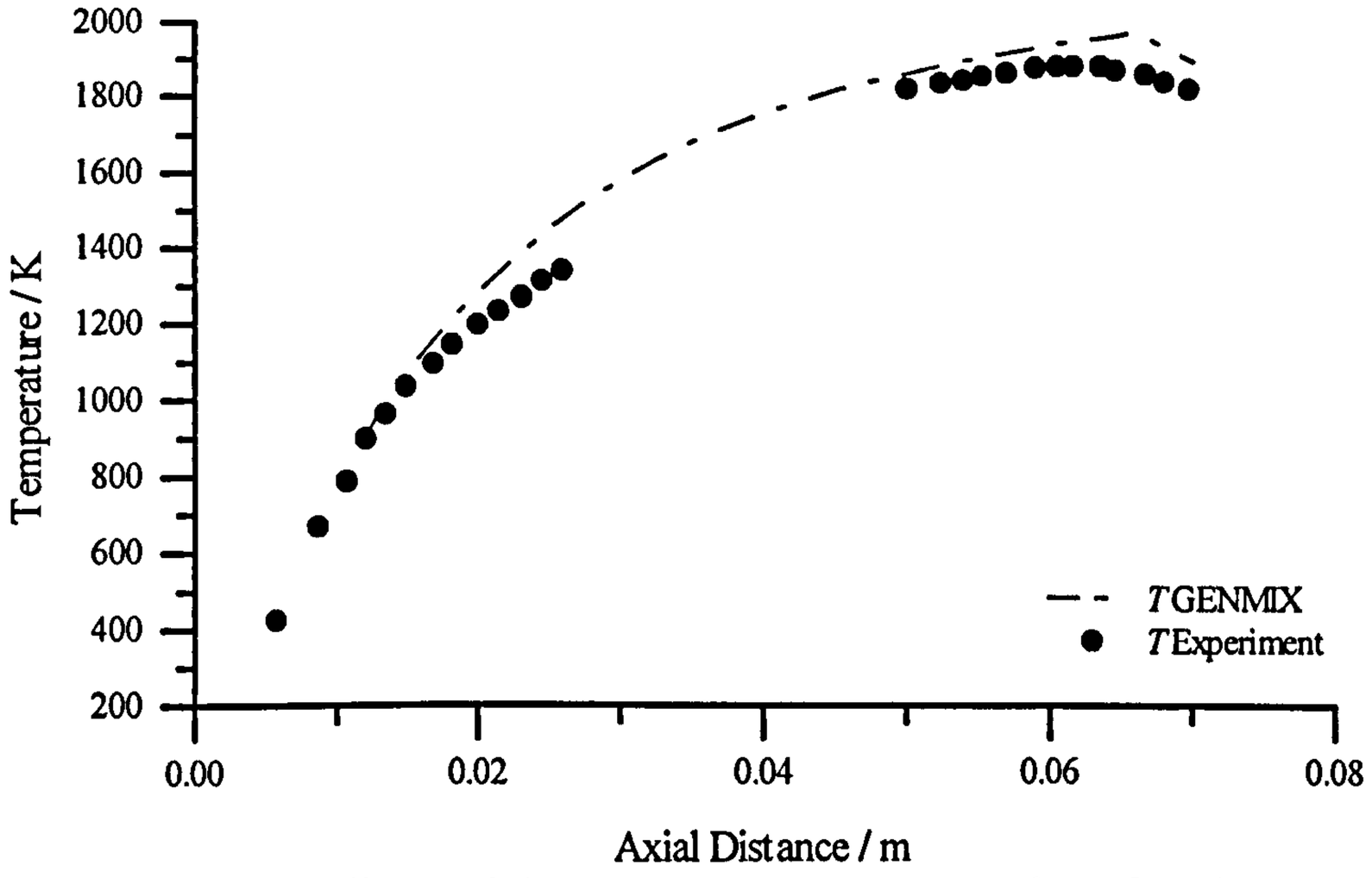

Figure 4.16a. Centreline axial GENMIX temperature data for the Mitchell et al. (1980a) laminar flame. Figure shows effect of using flamesheet temperature values.

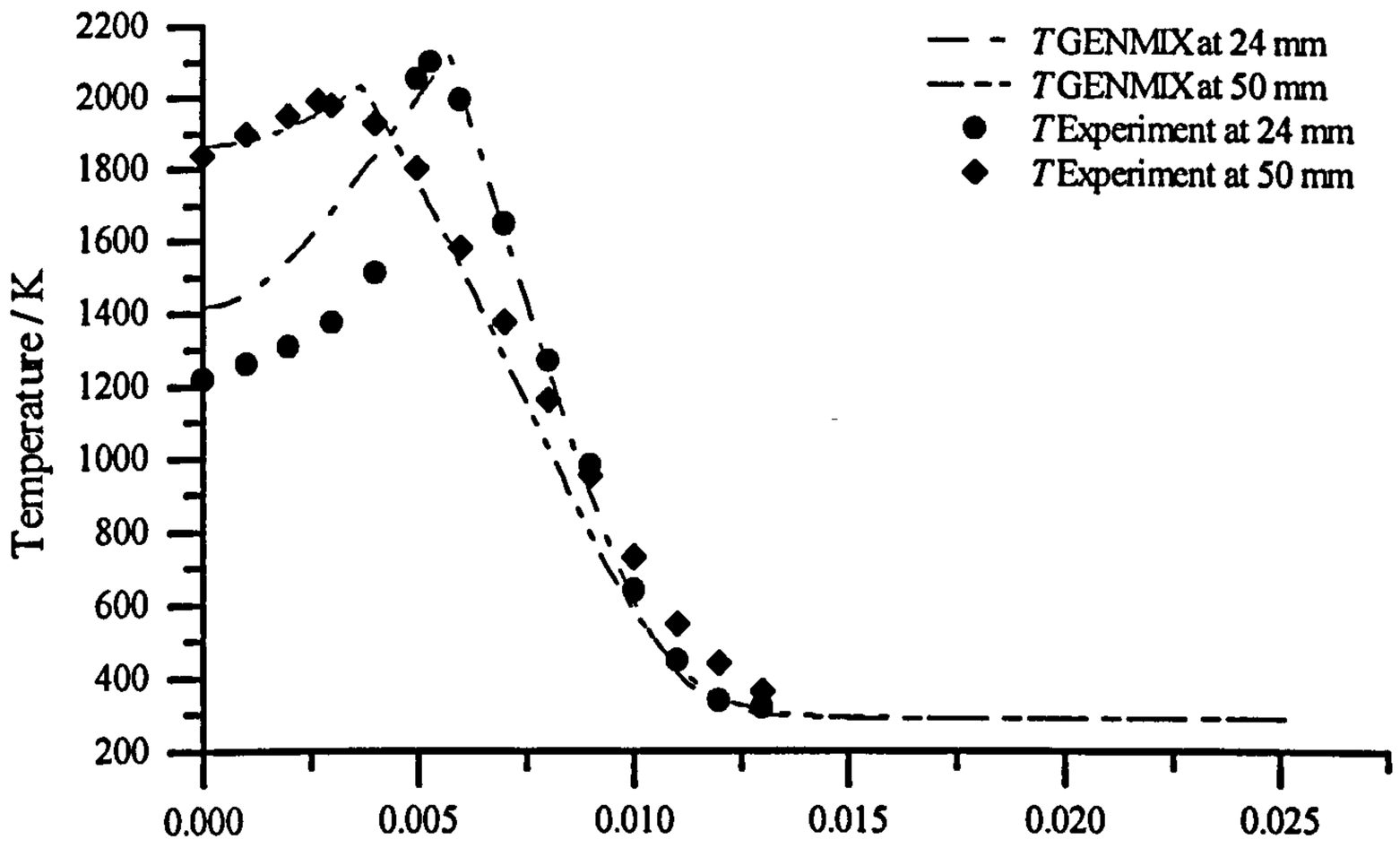

Figure 4.16b. Radial GENMIX temperature data, for the Mitchell et al. (1980a) laminar flame, compared with experiment. Figure illustrates the effect of using flamesheet values.

Chapter 5 - Modelling Sooting Turbulent Flames

5.1 Introduction

Turbulent, reacting flows may be described exactly by the Navier-Stokes equations and the appropriate equations of conservation for chemical species and energy. However, the complexity of this system of equations prevents their solution by analytical and numerical methods for all but the simplest of conditions. To compute practical combusting flow systems the effects of turbulence must be modelled.

The effects of turbulence are commonly accommodated by decomposing the dependent variables into mean and fluctuating components. Averaged transport equations may then be solved using conventional numerical methods to give the mean values of the dependent variables. There are two drawbacks to this method, when used in combusting flows. The first problem is that averaging the transport equations introduces additional terms, turbulent correlations, that may not be rewritten as functions of the mean variables. These terms require modelling for closure of the equation set. The second problem is that reaction rates are usually non-linear functions of the dependent variables - especially with respect to temperature. Therefore, attempts to close chemical source terms by evaluating mean reaction rates from mean properties will generally lead to substantial errors. Several approaches may be adopted to overcome this and these are discussed in chapter 2. Of these, the chemical source term closure is effected in this work by using the laminar flamelet combustion model.

The laminar flamelet model - Liew et al. (1981) - considers the turbulent flame to be composed of an ensemble of laminar flamelets. These flamelets are contorted by the turbulence, but their inner structure remains that of a laminar flame. If it may be assumed that all species have equal diffusion coefficients then the degree of mixing in the system may be described by a single conserved scalar - a scalar that remains unaffected by

chemical reactions. Bilger (1977) has shown that laminar diffusion flame structure may be substantially related to this single conserved scalar. An example of a conserved scalar is the mixture fraction, which for two-stream mixing is defined as the mass fraction of elements originating from the fuel stream. This conserved scalar is confined to values between zero and unity. The relationships between the dependent scalars and the conserved scalar are called flamelets. As these flamelets are usually non-linear functions of the conserved scalar the statistics of this conserved scalar must be known at a point in a turbulent flame for the determination of the local statistics of the dependent scalars. Obviously, for a complete statistical description of local flame properties the probability density function (PDF) of the conserved scalar must be known. The method adopted in this work, which has been used to good effect in the past, is to presume a simple function for this PDF. The exact shape of the presumed PDF at each location in the flame is determined from a limited number of moments, each moment obtained by the solution of its own transport equation. Two functions for the presumed PDF are commonly employed, the clipped Gaussian function and the Beta function. These functions may be defined by their first two moments - the mean and variance. The Beta function is more appealing as it is more easily manipulated mathematically, and the constraints imposed by the mean and variance limit the errors in the choice of the PDF shape.

The flamelet model, however, is only valid when the chemical time scales are much smaller than the time scales of the mixing process. Therefore, species that have slow formation rates - such as soot - are not unique functions of a conserved scalar. Although the soot properties may not be unique functions of a conserved scalar, the formation rate of soot - being dependent on the temperature and the concentrations of hydrocarbons with fast formation rates - may be taken as being approximately so. Also, in highly turbulent environments the time scales for the turbulent mixing process may approach those of the chemical reactions. This hydrodynamic straining of the flamelet will change its structure. However, the effect of strain on turbulent jet flames has been shown to be small - Liew et al. (1984) - and is neglected in this study. A further requirement for validity of the flamelet model is that the energy loss from the flame is zero. For flames of hydrogen or carbon monoxide this is nearly satisfied. However, for all hydrocarbon flames, even methane, the minimum energy loss by radiation is approximately 20 %. Following the suggestion of Syed (1990), this limitation may be overcome by using multiple flamelets, each flamelet

containing a different amount of radiative loss - Metternich et al. (1991), Young (1993), and Young and Moss (1995). The most appropriate flamelet for local flame properties may be selected by comparing the radiative loss incorporated in each of the flamelets with the local radiative loss - determined from a balance equation for the enthalpy.

The primary objective of the work contained in this chapter is to develop a fully coupled flame calculation; the soot formation rate being coupled to the radiative loss from the flame, this radiative loss being driven by the soot in the flame. The multiple flamelet strategy outlined above permits this coupling, in much the same manner as that achieved in chapter 4 for the laminar flame. However, an additional problem exists to those found in the laminar situation. As has already been stated, species that exhibit fast chemistry may be related to a single conserved scalar. If the statistics for this single scalar are known then the statistics for all other related scalars may be determined. The soot may not be related to this conserved scalar, and therefore its statistics are not easily determined. It may be imagined that the key factor in determining soot growth / oxidisation rates will be the correlation between the soot and its growth / oxidising species. The species primarily responsible for soot growth in simple paraffins, ethyne, shows a broad spread across mixture fraction space. Therefore, the correlation assumed between the soot and the mixture fraction will not affect the growth rate to a great extent. However, the principal soot oxidising species, the OH radical, exists as a sharp spike in mixture fraction space - see figure 5.2a. Hence, the correlation assumed between the soot and OH concentrations will be critical in determining the success of modelling the burnout of the soot. Four strategies for modelling this correlation in the soot source terms are evaluated. The first strategy, widely employed - eg. Syed (1990), Young (1993), Young and Moss (1995), Fairweather et al. (1992a), and Fairweather et al. (1992b), is to assume that the soot and the mixture fraction are entirely uncorrelated. However, the above argument suggests that this assumption will lead to incorrect growth and, more especially, oxidation rates. This does indeed prove to be the case - see section 5.5. The second strategy employed assumes that the soot is perfectly correlated with the mixture fraction. Laminar flame calculations show that the normalised profiles of the major soot properties show an almost constant form in mixture fraction space. There is some experimental evidence to suggest that this is also the case in turbulent flames - Sivathanu and Faeth (1990). The third strategy, proposed by Syed (1990), assumes that soot particles remain in the rich mixture fraction regions where they

are formed unless such regions become scarce. Oxidation will then occur as particles are forced into leaner regions. This oxidation condition depends on the local PDF of the mixture fraction. If the probability of attaining a mixture fraction greater than a critical value is below a set limit then oxidation will take place. The fourth strategy ignores the turbulence induced fluctuations entirely and formulates mean source terms using the mean soot properties and the mean species and temperature. A full discussion of these source term closures is deferred until sub-section 5.3.4.

In section 5.2 the basic equations describing the mean turbulent flow are developed from the laminar flow equations introduced in section 4.2. Section 5.3 introduces the physical sub-models needed to close this equation set. Sub-section 5.3.4 describes how the soot model developed in section 4.3.4 is applied to the turbulent flame calculation; in particular, the methods used for implementing the different correlation strategies outlined above. The present implementation of the multiple flamelet model is described in sub-section 5.4.4. The equations described in sections 5.2 and 5.3 are solved using the parabolic CFD code GENMIX - Spalding (1977) - and a comparison of the results of the flame modelling with the experimental data presented in chapter 3 and in the appendix are presented in section 5.5. The chapter ends with some conclusions in section 5.6.

5.2 Equations for Turbulent Reacting Flow

This section derives the partial differential equations necessary for modelling the turbulent jet flames investigated experimentally in this study. The flamelet combustion model simplifies the representation of the scalar field and allows the flowfield of an axi-symmetric turbulent flame to be described by four partial differential equations. These are the equations for mass continuity, axial velocity, enthalpy, and mixture fraction. Additional relationships relate the scalar variables, such as species mass fractions and temperature, to the mixture fraction and the enthalpy. The partial differential equations in time dependent, boundary layer, form are, for continuity

$$\frac{\partial \rho}{\partial t} + \frac{\partial}{\partial x}(\rho u) + \frac{1}{r}\frac{\partial}{\partial r}(r \rho v) = 0 \tag{5.1}$$

for velocity

$$\rho \frac{\partial u}{\partial t} + \rho u \frac{\partial u}{\partial x} + \rho v \frac{\partial u}{\partial r} - \frac{1}{r}\frac{\partial}{\partial r}\left(r \mu \frac{\partial u}{\partial r} \right) = \rho g - \frac{\partial P}{\partial x} \tag{5.2}$$

for enthalpy

$$\rho \frac{\partial h}{\partial t} + \rho u \frac{\partial h}{\partial x} + \rho v \frac{\partial h}{\partial r} - \frac{1}{r}\frac{\partial}{\partial r}\left[r \frac{\lambda}{C_P} \frac{\partial h}{\partial r} \right] = \dot{Q} \tag{5.3}$$

and for mixture fraction

$$\rho \frac{\partial \xi}{\partial t} + \rho u \frac{\partial \xi}{\partial x} + \rho v \frac{\partial \xi}{\partial r} - \frac{1}{r}\frac{\partial}{\partial r}\left[r \rho D \frac{\partial \xi}{\partial r} \right] = 0 \tag{5.4}$$

The similarity of the last three equations allows, through the introduction of the Prandtl / Schmidt number, the formation of a general transport equation for the dependent variable ϕ with a volumetric source equal to S_ϕ

$$\rho \frac{\partial \phi}{\partial t} + \rho u \frac{\partial \phi}{\partial x} + \rho v \frac{\partial \phi}{\partial r} - \frac{1}{r}\frac{\partial}{\partial r}\left[r \frac{\mu}{\sigma_\phi} \frac{\partial \phi}{\partial r} \right] = S_\phi \tag{5.5}$$

where σ_ϕ is the Prandtl / Schmidt number for ϕ. However, although a solution of these equations is necessary for a full description of the time dependent turbulent flow such a solution is computationally intractable. Fortunately many turbulent flows in practice, including the flames in this study, show behaviour that is statistically stationary. Any flame property that is averaged will show a stationary value as the number of samples comprising the average approaches infinity. The equations, therefore, may be solved in averaged form rendering the problem soluble. The averaged form of the equations are derived by decomposing the instantaneous flow variables (u, v, ϕ, etc.) into two components, a mean component and a fluctuating component. The instantaneous variables in the flow equations are replaced by these two components and the resulting equations are ensemble averaged. Hence, the time dependent terms become zero. If the instantaneous flow variables are replaced by a conventional Reynolds mean term and a fluctuating term, then terms appear involving cross correlations between the density fluctuations and the fluctuating components of the other flow variables. The solution to this problem is to use Favre averaging - Favre (1969). The Favre mean is a density weighted mean defined by $\tilde{x} = \overline{\rho x} / \overline{\rho}$, where the tilde indicates a Favre mean rather than a Reynolds mean. Replacing the velocity components u and v in the continuity equation with $u = \tilde{u} + u''$ and $v = \tilde{v} + v''$, and ensemble averaging, yields

$$\frac{\partial}{\partial x}(\bar{\rho}\tilde{u}) + \frac{1}{r}\frac{\partial}{\partial r}(r\bar{\rho}\tilde{v}) = 0 \tag{5.6}$$

Performing the same operation on the momentum transport equation yields

$$\begin{aligned}\bar{\rho}\tilde{u}\frac{\partial \tilde{u}}{\partial x} + \bar{\rho}\tilde{v}\frac{\partial \tilde{u}}{\partial r} = \bar{\rho}g - \frac{\overline{\partial P}}{\partial x} + \frac{1}{r}\frac{\partial}{\partial r}\left(r\mu\overline{\frac{\partial u}{\partial r}}\right) \\ - \frac{\partial}{\partial x}(\overline{\rho u''u''}) \\ - \frac{1}{r}\frac{\partial}{\partial r}(r\overline{\rho u''v''}) \\ - \frac{1}{r}\frac{\partial}{\partial \theta}(\overline{\rho u''w''})\end{aligned} \tag{5.7}$$

The additional stress terms on the right hand side, called the Reynolds stresses, arise from

the turbulent velocity fluctuations. These terms may not be expressed in terms of the mean variables and therefore need to be modelled. The modelling of the Reynolds stress terms is covered in sub-section 5.3.1.

Performing a similar operation on the transport equation for the general variable ϕ, replacing ϕ with $\phi = \widetilde{\phi} + \phi''$, yields

$$\bar{\rho}\,\tilde{u}\frac{\partial\widetilde{\phi}}{\partial x} + \bar{\rho}\,\tilde{v}\frac{\partial\widetilde{\phi}}{\partial r} = \frac{1}{r}\frac{\partial}{\partial r}\left(r\,\overline{\frac{\mu}{\sigma}\frac{\partial\phi}{\partial r}} \right) + \bar{S}_{\phi} - \frac{\partial}{\partial x}(\overline{\rho\,u''\phi''}) - \frac{1}{r}\frac{\partial}{\partial r}(r\,\overline{\rho\,v''\phi''}) - \frac{1}{r}\frac{\partial}{\partial\theta}(\overline{\rho\,w''\phi''}) \tag{5.8}$$

The last terms on the right hand side are called the turbulent scalar fluxes, and represent the enhanced mixing caused by the turbulence. Again, these terms may not be expressed as functions of the mean variables and must be modelled. This modelling is also covered in sub-section 5.3.1.

5.3 Physical Models

5.3.1 Turbulent Transport

The Reynolds stresses and turbulent scalar fluxes appearing in the averaged form of the transport equations for momentum and the general scalar ϕ require modelling for closure of this equation set. The transport of momentum and scalars by turbulent action is modelled by making an analogy with molecular motion. Molecular scalar or momentum transport takes place by the random motion of molecules, turbulent transport may therefore be thought of as transport occurring through the random motion of macroscopic turbulent eddies - Prandtl (1925). Hence, the turbulent transport of a fluid property may be related to the gradient of its mean.

The Reynolds stresses may then be written as

$$\overline{\rho u'' u''} = \frac{2}{3}\left[\bar{\rho} k + \mu_T\left(\frac{1}{r}\frac{\partial}{\partial r}(r\tilde{v}) + \frac{1}{r}\frac{\partial \tilde{w}}{\partial \theta} + \frac{\partial \tilde{u}}{\partial x}\right)\right] - 2\mu_T\frac{\partial \tilde{u}}{\partial x} \qquad (5.9)$$

$$\overline{\rho u'' v''} = -\mu_T\left(\frac{\partial \tilde{u}}{\partial r} + \frac{\partial \tilde{v}}{\partial x}\right) \qquad (5.10)$$

$$\overline{\rho u'' w''} = -\mu_T\left(\frac{\partial \tilde{w}}{\partial x} + \frac{1}{r}\frac{\partial \tilde{u}}{\partial \theta}\right) \qquad (5.11)$$

For the transport of a scalar a turbulent Prandtl/Schmidt number may be defined, allowing the turbulent scalar fluxes to be written as

$$\overline{\rho u'' \phi''} = -\frac{\mu_T}{\sigma_\phi}\frac{\partial \tilde{\phi}}{\partial x}, \quad \overline{\rho v'' \phi''} = -\frac{\mu_T}{\sigma_\phi}\frac{\partial \tilde{\phi}}{\partial r}, \quad \overline{\rho w'' \phi''} = -\frac{\mu_T}{\sigma_\phi}\frac{\partial \tilde{\phi}}{\partial \theta} \qquad (5.12)$$

where μ_T is the eddy viscosity.

This definition of eddy viscosity allows the Favre averaged transport equations to be recast in the following form

$$\bar{\rho}\,\tilde{u}\frac{\partial \tilde{u}}{\partial x} + \bar{\rho}\,\tilde{v}\frac{\partial \tilde{u}}{\partial r} = \frac{1}{r}\frac{\partial}{\partial r}\left(r\,\mu_T \frac{\partial \tilde{u}}{\partial r}\right) + \bar{\rho}\,g - \frac{\partial \bar{P}}{\partial x} \tag{5.13}$$

$$\bar{\rho}\,\tilde{u}\frac{\partial \widetilde{\Phi}}{\partial x} + \bar{\rho}\,\tilde{v}\frac{\partial \widetilde{\Phi}}{\partial r} = \frac{1}{r}\frac{\partial}{\partial r}\left(r\frac{\mu_T}{\sigma_\Phi}\frac{\partial \widetilde{\Phi}}{\partial r}\right) + \bar{S}_\Phi \tag{5.14}$$

The molecular contribution to the viscosity is usually small in comparison to the eddy viscosity and is ignored.

The k-ϵ model, Jones and Launder (1972), is used in this work to obtain the eddy viscosity. The eddy viscosity is determined from the turbulent kinetic energy (k) and its dissipation rate (ϵ) using the following relation

$$\mu_T = C_\mu \bar{\rho}\,k^2/\epsilon \tag{5.15}$$

This turbulent kinetic energy and dissipation rate are obtained from the solution of their respective transport equations

$$\bar{\rho}\,\tilde{u}\frac{\partial k}{\partial x} + \bar{\rho}\,\tilde{v}\frac{\partial k}{\partial r} = \frac{1}{r}\frac{\partial}{\partial r}\left(r\frac{\mu_T}{\sigma_k}\frac{\partial k}{\partial r}\right) + \mu_T\left(\frac{\partial \tilde{u}}{\partial r}\right)^2 - \bar{\rho}\,\epsilon \tag{5.16}$$

$$\bar{\rho}\,\tilde{u}\frac{\partial \epsilon}{\partial x} + \bar{\rho}\,\tilde{v}\frac{\partial \epsilon}{\partial r} = \frac{1}{r}\frac{\partial}{\partial r}\left(r\frac{\mu_T}{\sigma_\epsilon}\frac{\partial \epsilon}{\partial r}\right) + C_{\epsilon 1}\mu_T\frac{\epsilon}{k}\left(\frac{\partial \tilde{u}}{\partial r}\right)^2 - C_{\epsilon 2}\bar{\rho}\frac{\epsilon^2}{k} \tag{5.17}$$

The model constants C_μ, $C_{\epsilon 1}$, and $C_{\epsilon 2}$ were originally given as 0.09, 1.44, and 1.92 respectively - Jones and Launder (1972). However, the use of these constants in an axi-symmetric geometry over-predicts the spreading rate by approximately 40 %.

Following Young (1993) the correction to these constants by Rodi (1972) is used. This correction takes the form of the following changes to C_μ and $C_{\epsilon 2}$.

$$C_{\mu} = 0.09 - 0.04\left(\frac{r_{Half}}{\tilde{u}} \frac{d\tilde{u}}{dx} \right)_{CL}^{0.2} \tag{5.18}$$

$$C_{\epsilon 2} = 1.92 - 0.0667\left(\frac{r_{Half}}{\tilde{u}} \frac{d\tilde{u}}{dx} \right)_{CL}^{0.2} \tag{5.19}$$

where r_{Half} is the radius at which the mean axial velocity has dropped to half its centreline value and the subscript *CL* indicates that centreline values are to be used for the mean velocity and its axial gradient.

5.3.2 Combustion

The combustion model used in this study is a variation on the laminar flamelet model introduced by Liew et al. (1981). Bilger (1976) showed that diffusion flame structure may be expressed as functions of a single conserved scalar under the constraints of infinite reaction rate, equal species diffusivity, unity Lewis number and zero heat loss. Bilger (1977) extended this model by showing that in a real laminar flame, where some of the constraints may be violated, this is still the case. Liew et al. (1981) applied the conserved scalar approach to turbulent diffusion flames. However, in contrast to previous studies, where the state relationships were taken from a flamesheet or equilibrium calculation, the relationships between the chemistry dependent scalars and the conserved scalar were taken from a laminar flame. These state relationships are termed flamelets. The turbulent flame is assumed to comprise of an ensemble of these laminar flamelets. Each laminar flamelet is assumed to have the structure of an undisturbed laminar diffusion flame and therefore may be described by a single conserved scalar. Hence, if the statistics of this conserved scalar are known then mean flame properties may be determined.

The conserved scalar statistics are found using the presumed PDF method. The PDF of mixture fraction is assumed to be described by a Beta function at all positions in the flame. The Beta function is defined by two parameters only, the mean and the variance of the mixture fraction. The Beta function Favre PDF may be written as

$$\tilde{P}(\xi) = \frac{\xi^{(\alpha-1)}(1-\xi)^{(\beta-1)}}{\int_0^1 \xi'^{(\alpha-1)}(1-\xi')^{(\beta-1)}\,d\xi'} \tag{5.20}$$

where α and β are given by

$$\alpha = \tilde{\xi}\left(\frac{\tilde{\xi}(1-\tilde{\xi})}{\widetilde{\xi''^2}} - 1\right) \qquad \beta = \frac{\alpha(1-\tilde{\xi})}{\tilde{\xi}} \tag{5.21}$$

The mean mixture fraction and the mixture fraction variance are obtained from the solution of their respective balance equations. The balance equation for mean mixture fraction has no source term and in axi-symmetric, boundary layer form may be written as

$$\bar{\rho}\tilde{u}\frac{\partial\tilde{\xi}}{\partial x} + \bar{\rho}\tilde{v}\frac{\partial\tilde{\xi}}{\partial r} - \frac{1}{r}\frac{\partial}{\partial r}\left(r\frac{\mu_T}{\sigma_\xi}\frac{\partial\tilde{\xi}}{\partial r}\right) = 0 \tag{5.22}$$

The balance equation for the variance of the mixture fraction is obtained by multiplying the instantaneous equation for ξ by ξ'' and averaging. This balance equation is

$$\bar{\rho}\tilde{u}\frac{\partial\widetilde{\xi''^2}}{\partial x} + \bar{\rho}\tilde{v}\frac{\partial\widetilde{\xi''^2}}{\partial r} = \frac{1}{r}\frac{\partial}{\partial r}\left(r\frac{\mu_T}{\sigma_v}\frac{\partial\widetilde{\xi''^2}}{\partial r}\right) + C_{g1}\mu_T\left(\frac{\partial\tilde{\xi}}{\partial r}\right)^2 - C_{g2}\bar{\rho}\frac{\epsilon\widetilde{\xi''^2}}{k} \tag{5.23}$$

The constants C_{g1} and C_{g2} are set to 2.8 and 1.89 respectively, following Syed (1990) and Young (1993).

Once the mixture fraction PDF is known, the averages of all mixture fraction dependent variables may easily be found. Taking for example the general scalar variable ϕ, the Favre average may be found from

$$\widetilde{\Phi} = \int_0^1 \phi(\xi)\,\tilde{P}(\xi)\,d\xi \tag{5.24}$$

Reynolds means may also be determined as follows

$$\overline{\Phi} = \overline{\rho} \int_0^1 \frac{1}{\rho(\xi)} \phi(\xi)\,\tilde{P}(\xi)\,d\xi \tag{5.25}$$

Hence the Reynolds PDF may be written in terms of the Favre PDF as

$$P(\xi) = \frac{\overline{\rho}}{\rho(\xi)} \tilde{P}(\xi) \tag{5.26}$$

There are two major problems associated with this model. The first problem is associated with the finite rate chemical kinetics. Species which exhibit slow chemistry, such as soot, are not functions of a conserved scalar. Therefore, balance equations must be solved for the soot properties. Also, laminar flame properties are not themselves unique but are in fact a function of the hydrodynamic strain rate (stretch). Liew et al. (1984) investigated the effect of flame stretch in open turbulent methane / air jet diffusion flames. The results of this study indicated that the effect of flame stretch is confined to a region just downstream of the potential core on the axis and positions that, away from the centreline, move towards the burner. It was also found that the effect of flame stretch increased in significance as the exit velocity of the fuel jet was increased. The flames modelled by Liew et al. (1984) were all characterised by exit velocities far in excess of the flames in this study. Because of the low exit velocities characterising the flames investigated in this work and also the negligible effect of flame stretch over most of the flame volume, the effect of flame stretch has been ignored in this study. The second problem is that the model does not easily accommodate radiative heat loss. It may be argued that flamelets obtained experimentally from laminar flame data already include a certain degree of radiative loss. While this may be true to some extent, the problems associated with making measurements - particularly of temperature - in sooting laminar flames probably obscures the true effect of the radiative heat loss. Another method that has been employed is to create flamelets, using a computer code, perturbing the flamelets' enthalpy so that a fixed amount of energy loss is included -

Jeng and Faeth (1984). Flame calculations using both of these methods have been performed and the results for temperature are satisfactory - Jeng and Faeth (1984) and Syed (1990). However, soot production rates are extremely sensitive to temperature. The use of a single flamelet, to describe the production rate of soot, that includes a fixed amount of radiative loss would be expected to initially under-estimate the soot production rate in the lower region of the flame and possibly to over-estimate the production rate high in the flame, where the radiative loss is large. Syed (1990) suggests a means by which the radiative loss problem may be overcome. Syed's suggestion, further developed and implemented by Young (1993) and Young and Moss (1995), is to use a range of flamelets differentiated by radiative loss. The most appropriate flamelets at any particular location may be selected on the basis of the local radiative loss. Generally, local flame properties are determined by two parameters: the mixture fraction and the fractional radiative loss. Hence, mean scalar values may be found according to

$$\overline{\Phi} = \int_0^1 \int_0^1 \phi(\xi, X_R)\, P(\xi, X_R)\, d\xi\, dX_R \qquad (5.27)$$

where X_R is the heat loss fraction and is bounded between zero and unity. However, the derivation of such joint PDF information, between the mixture fraction and the heat loss fraction, is beyond the scope of this work. Therefore, some assumptions need to be made about the form of $P(\xi, X_R)$. The simplest form for this joint PDF is $P(\xi, X_R) = P(\xi)\,\delta(X_R)$ where $\delta(X_R)$ is a delta function centred on the local mean value of the heat loss fraction - cf. Gore et al. (1992). The local mean heat loss fraction may be obtained from the solution of an enthalpy transport equation that incorporates a radiative heat loss source term - see sub-section 5.4.4. A family of flamelets, one for each scalar, may be chosen where each flamelet includes this level of radiative loss. If the species mole fractions are assumed to be independent of the radiative loss fraction (hence, species mole fractions are functions of the mixture fraction only) then the radiative heat loss will affect the other scalar variables through the changes in temperature that it causes. The temperature flamelet incorporating the requisite degree of heat loss may be found by inverting the locally applicable enthalpy flamelet, which is formed as

$$h(\xi, X_R) = h_{Init.}(\xi) + (1 - X_R)(h_{Adia.}(\xi) - h_{Init.}(\xi)) \qquad (5.28)$$

where $h_{Init.}(\xi)$ is the specific total enthalpy of the product mixture at the initial reactant temperature and $h_{Adia.}(\xi)$ is the specific total enthalpy of the same mixture at the adiabatic product temperature. Inversion of the enthalpy / temperature relationship to give $T(\xi, X_R)$ allows the formation of flamelets for the other scalars - $\phi(\xi, X_R)$. The derivation of the heat loss fraction from an enthalpy transport equation requires that the adiabatic enthalpy / mixture fraction relationship, $h_{Adia.}(\xi)$, is linear. This is because in an adiabatic, unity Lewis number system the total enthalpy (chemical + sensible) is a conserved scalar and is, therefore, linearly related to the mixture fraction. The enthalpy obtained from an adiabatic transport equation is, obviously, a mixture property and hence is linearly related to the mixture fraction (assuming that their respective Prandtl / Schmidt numbers are identical), which is also a mixture property.

Obviously, as written above this method requires the derivation of a very large number of flamelets, to cover all the possible heat loss fractions encountered. The generation of such flamelets, especially during the runtime of any computer calculation would be extremely time consuming. In practice a finite number of flamelets are generated that cover the full range of heat loss fractions encountered. Flamelet values for a radiative loss that does not fall on any of the discrete radiative loss values chosen for this set may be found by interpolating between adjacent flamelets. A full description of this method is given in sub-section 5.4.4. Figures 5.1a - d illustrate the flamelet family of the soot particle nucleation function, soot particle surface growth term, temperature, and enthalpy for the X_R values of 0, 0.1, 0.2, and 0.4. Species mole fractions from the Warnatz laminar flame code are used to derive these flamelets - see later in this section.

The implication of the above model is that $X_R(\xi) = \bar{X}_R$ at any flame location. Analysis of the heat loss results given by laminar flame calculations of the type performed in chapter 4 indicate that this is not the case. The heat loss fraction is a function of the mixture fraction, even for flame regions of constant residence time. This is not surprising since the heat loss occurs by radiation from mainly soot and gases in the high temperature regions in mixture fraction space. Also, the heat loss fraction at the mixture fractions of zero and unity must always be zero - assuming that, as in this case, the reactants are at ambient temperature. Further examination of the laminar flame results show that, although the heat loss function varies in magnitude with residence time, the normalised profile has an almost

constant shape in mixture fraction space. This laminar profile of normalised heat loss versus mixture fraction may be exploited in the turbulent flame calculation by replacing X_R in equation 5.28 with $X_R(\xi)$. Where $X_R(\xi)$ is formed by multiplying the normalised heat loss function by a range of constant factors.

The source of appropriate flamelets must now be addressed. The requirement is for a source of species mole fractions as a function of mixture fraction at 1 and 3 atm. The temperature flamelets are, of course, formed by the inversion of the enthalpy flamelets; provided the species mole fractions and the adiabatic enthalpy / mixture fraction relationship are known. Flamelets for other properties may be formed from the species mole fractions and temperature. The density is determined according to the perfect gas law

$$\rho = \frac{P}{RT}\sum_i X_i M_i \qquad (5.29)$$

There are two potential sources for these species / mixture fraction relationships. The first such source is experimental measurement. However, the database for methane / air laminar flames which includes detailed studies of the species profiles is small and there are no measurements reported of detailed species profiles at elevated pressure. The second source is from a laminar flame code, that includes a detailed representation of the combustion chemistry. In this work the laminar flame code of Warnatz (1981) is used to derive the species information - see also section 4.3.1. This is a one dimensional laminar code which solves for the properties along the stagnation streamline of a counter-flow burner. The inputs to the code include the compositions of the fuel and oxidant streams and their velocities, from which the strain rate may be calculated. The output of the code gives the species mole fractions as a function of distance in physical space, these are converted to functions of mixture fraction using the relationship given in equation 4.11. The flamelets derived for the 1 atm turbulent flame calculation were calculated with a strain rate of 90 s^{-1}, the flamelets derived for the 3 atm turbulent flame calculation with a strain rate of 50 s^{-1}; reflecting the slightly more benign rates of strain found in the lower nozzle exit velocity 3 atm flame. The flamelets for the mole fractions of the significant species (CH_4, O_2, CO_2, CO, H_2O, C_2H_2, and OH) at both pressures are compared in figures 5.2a - c. The increase in the mole fraction of ethyne at the higher pressure is immediately apparent as is the decrease in the mole fraction of the OH radical. These differences have important

implications for the sooting behaviour of the 3 atm turbulent flame.

5.3.3 Radiative Loss

Energy loss by radiation from the soot and the two main gaseous radiating species (CO_2 and H_2O) in the optically thin limit is considered. The absorption coefficients for the gases and the soot are the same as those used in chapter 4. The highly non-linear relationship between the radiative loss source term and temperature prevents the use of mean properties in the formulation of the source. The instantaneous source term for radiative loss is given by

$$S_R = -4\kappa_T \sigma T^4 \tag{5.30}$$

where κ_T is the total Planck mean emission coefficient and is given by $\kappa_T = \kappa_{CO_2} + \kappa_{H_2O} + \kappa_{Soot}$. The emission coefficients for the gases are functions of mixture fraction only and therefore the means may be formed by weighting with the PDF of mixture fraction. However, the emission coefficient for the soot is a function of the mixture fraction and the soot volume fraction. This emission coefficient is of the form

$$\kappa_{Soot} = C T f_V \tag{5.31}$$

where C is a constant. For the mean emission coefficient of the soot the joint PDF for soot volume fraction and mixture fraction would be required. This is not available so the expression is modelled by assuming that the soot and the mixture fraction are entirely uncorrelated. This leads to the following form for the total mean radiative energy loss source term

$$\bar{S}_R = -(\overline{4\kappa_{CO_2}\sigma T^4} + \overline{4\kappa_{H_2O}\sigma T^4} + 4C\sigma\bar{f}_V\overline{T^5}) \tag{5.32}$$

where the numerical value of the constant (C) is 1.307×10^3 m^{-1} K^{-1}.

This form of the source term captures the main non-linearity in the temperature term. However, the radiative energy loss from the soot may be slightly under-predicted as it may be expected that there is a correlation between soot volume fraction and temperature. The

soot is formed in the fuel-rich, high temperature regions. Hence, the temperature of the soot is likely to be higher than the mean.

5.3.4 Soot

This sub-section describes the implementation of the soot model, developed in chapter 4, in the turbulent flame calculation. The model constants are determined by applying the model to a laminar flame calculation - see chapter 4. However, due to the lack of information available in the literature concerning the sooting structure of elevated pressure, laminar methane flames the value of the ethyne concentration exponent (m, cf. equation 4.41) is set by recourse to the turbulent flame data. As indicated in section 4.3.4 the value for this exponent is likely to be less than 2/3. The main problem surrounding the use of this model in the turbulent flame calculation, however, is closure of the soot production source terms in the turbulent flow.

The soot model describes the soot by two parameters: N, the number density of the soot particles, and M, the mass concentration of the soot. The assumption of spherical particles, with a mono-disperse size distribution, allows the surface area of the soot to be determined. The instantaneous net production of the soot number density is given by equation 4.40, and is reproduced here in the form

$$\frac{dN}{dt} = \alpha - \beta M^{1/6} N^{11/6} \tag{5.33}$$

where α and β are functions of the mixture fraction and radiative heat loss only, and may be defined by making reference to equation 4.40. Hence, if for the sake of example the radiative heat loss is ignored, the mean production rate of soot number density may be given exactly by

$$\overline{\frac{dN}{dt}} = \int_0^{\infty}\int_0^{\infty}\int_0^{1} (\alpha(\xi) - \beta(\xi) M^{1/6} N^{11/6}) P(\xi, N, M)\, d\xi\, dN dM \tag{5.34}$$

where $P(\xi, N, M)$ is the joint probability density function of mixture fraction, soot particle

number density, and soot mass concentration. Unfortunately, the form of this joint PDF is not known and its determination through PDF transport methods is beyond the scope of this work. Approximate representations are therefore needed. Four such possibilities are examined in this section, with the results given by each presented in section 5.5.

Uncorrelated Closure

In the first model the soot properties are assumed to be totally uncorrelated with the mixture fraction, and each other. This leads to the following form for the joint PDF

$$P(\xi, N, M) = P(\xi)\,P(N)\,P(M) \tag{5.35}$$

Substituting equation 5.35 into equation 5.34 and performing the integrations yields

$$\overline{\frac{dN}{dt}} = \bar{\alpha} - \bar{\beta}\,\overline{M^{1/6}}\,\overline{N^{11/6}} \tag{5.36}$$

The individual PDFs for the soot particle number density and the soot mass concentration are not known, so this expression is modelled as

$$\overline{\frac{dN}{dt}} = \bar{\alpha} - \bar{\beta}\,\bar{M}^{1/6}\,\bar{N}^{11/6} \tag{5.37}$$

Similarly, the equation for the mean production of soot mass concentration is

$$\overline{\frac{dM}{dt}} = M_P\,\bar{\alpha} + \bar{\gamma}\,\bar{N}^{1/3}\,\bar{M}^{2/3} - \bar{\omega}'\bar{N}^{1/3}\,\bar{M}^{2/3} \tag{5.38}$$

Where α, γ, and ω' are functions of mixture fraction only, and may be defined by making reference to equation 4.41.

Correlated Closure

The second possibility considered is that the soot properties are perfectly correlated with the mixture fraction. There is some experimental evidence to support this. Sivathanu and Faeth (1990) present probability functions for temperature conditioned on soot volume fraction for turbulent flames of several hydrocarbons. For maximal values of soot volume

fraction the temperature PDFs show the form of a single narrow peak indicating that the soot is associated with a limited temperature range. This is consistent with the soot properties being well correlated with the mixture fraction. At lower soot volume fractions the temperature PDF broadens and in some of the datasets hints at bimodality. This is to be expected as the lower values of soot volume fraction will correspond to two distinct regimes for the soot particles; that of the growth phase and the oxidation phase. The temperatures corresponding to these two regimes will be different and, therefore, the temperature PDFs will broaden as a result. Tait and Greenhalgh (1993) present two dimensional, instantaneous images of the soot volume fraction in turbulent propane jet diffusion flames. The images, recorded using laser induced incandescence (LII) of the soot particles, are qualitative but do provide useful information about the sooting structure of turbulent flames. One of the images, from a highly turbulent flame, is reproduced in this work as figure 5.3. The image shows a large soot feature at the top left position as well as very fine (100 micron thickness) sheets of soot convoluted by the turbulent flow. The fine features are likely to be soot sheets in cross section while the large feature is possibly a layer of soot aligned in the plane of the laser sheet. The image demonstrates the intermittent nature of the soot. The thickness of the soot sheets suggests that the soot is not randomly mixed by the turbulence with the gas phase but actually exists as laminar-like layers which are convoluted by the turbulence but have a structure similar to that found in laminar flames. Miake-Lye and Toner (1987) present soot images recorded using a laser scattering technique in natural gas fuelled low Reynolds number flames. The images also demonstrate the highly intermittent nature of the soot. Photographs taken simultaneously with the laser images show that all of the soot in the flame is highly luminous and therefore only exists in the high temperature regions of the flame, close to the flame front.

In laminar flames the soot particle number density and the soot mass concentration form functions of the mixture fraction that are approximately constant in shape but the magnitude of which varies. This may be exploited in the turbulent flame calculation by imposing these profiles, taken from a laminar flame calculation, on to the mean soot properties obtained from their respective balance equations. Hence, the joint PDF $P(\xi, N, M)$ may be replaced by $P(\xi)$. This allows mean soot properties to be calculated as

$$\bar{M} = \int_0^1 P(\xi)\, M(\xi)\, d\xi \tag{5.39}$$

Introducing the normalised profile of soot mass concentration in mixture fraction space $D_M(\xi)$, obtained from a laminar calculation

$$\bar{M} = \frac{\int_0^1 P(\xi)\, D_M(\xi)\, \bar{M}\, d\xi}{\int_0^1 P(\xi)\, D_M(\xi)\, d\xi} \tag{5.40}$$

By comparison of equation 5.39 with equation 5.40, $M(\xi)$ may be defined as

$$M(\xi) = \frac{D_M(\xi)}{\int_0^1 P(\xi)\, D_M(\xi)\, d\xi}\bar{M} = \frac{D_M(\xi)}{\bar{D}_M}\bar{M} \tag{5.41}$$

Similarly, for the soot particle number density

$$N(\xi) = \frac{D_N(\xi)}{\bar{D}_N}\bar{N} \tag{5.42}$$

However, the profile of soot particle number density in mixture fraction space is very nearly constant. Hence, to simplify the model the number density as a function of mixture fraction is taken to be $N(\xi) = \bar{N}$. The mean production rates for the soot properties may now be formulated as, for number density

$$\overline{\frac{dN}{dt}} = \bar{\alpha} - \overline{\beta\, D_M^{1/6}}\,\bar{N}^{11/6}\left(\frac{\bar{M}}{\bar{D}_M}\right)^{1/6} \tag{5.43}$$

and for mass concentration

$$\overline{\frac{dM}{dt}} = M_P \bar{\alpha} + \overline{\gamma D_M^{2/3}} \bar{N}^{1/3} \left(\frac{\bar{M}}{\bar{D}_M} \right)^{2/3} - \overline{\omega' D_M^{2/3}} \bar{N}^{1/3} \left(\frac{\bar{M}}{\bar{D}_M} \right)^{2/3} \qquad (5.44)$$

Note, that if the soot concentration profile was flat (a constant value in mixture fraction space), the model would reduce to equations 5.37 and 5.38.

The model needs a representative profile for $D_M(\xi)$ obtained from a laminar flame calculation. This presents a problem because the profile shape may be influenced by the flowfield of the laminar flame. To avoid any flowfield-specific features in the profile of soot mass concentration, a laminar GENMIX calculation is performed with the stream-wise velocity source term set to zero. The initial stream-wise velocity profile is flat with a value of 1 m s^{-1}. This effectively converts the stream-wise distance into residence time. Two hundred cross-stream nodes are used. Initially half of the nodes are pure methane fuel and half pure air. Because stream-wise diffusion is ignored, the overall calculation represents the time dependent result of a one-dimensional calculation for the initial gas mixture - where there is only diffusion. The soot mass concentration profile from the result of this calculation at 50 ms is normalised and used as the assumed distribution in the turbulent flame calculation - this distribution is shown in figure 5.4. The 50 ms residence time position is used for the soot profile as it approximately represents the residence time found in the turbulent flames in this study. Hence, the shape of the soot profile will reproduce the conditions found in the oxidation regions of the turbulent flame. However, the profile falls to a value of near zero at very lean and very rich mixture fractions. Therefore, to avoid 'division by zero' and 'arithmetic overflow' errors in the turbulent GENMIX calculation (cf. equations 5.43 and 5.44) a threshold value is set, which becomes the minimum value any point on the profile may fall to. It is discovered that, unfortunately, this threshold parameter exerts a large influence on the performance of the model. This is discussed in section 5.5.

Conditional PDF Closure

The third form for the production rates of the soot properties follows Syed (1990). Syed (1990) proposes that soot particles remain in the rich mixture fraction regions where they

are formed, until such regions become scarce. Oxidation then occurs as the soot particles are forced into leaner, oxidising regions. The condition for oxidation to take place depends on the local PDF of mixture fraction. If the probability of achieving a mixture fraction greater than a critical value is below a set limit then oxidation will ensue. Syed (1990) uses the uncorrelated form for the soot source terms (cf. equations 5.37 and 5.38). An extra parameter which may take a value of either zero or unity is used to control the oxidation. The source terms are, for number density

$$\overline{\frac{dN}{dt}} = \bar{\alpha} - \bar{\beta}\bar{M}^{1/6}\bar{N}^{11/6} \tag{5.45}$$

and for mass concentration

$$\overline{\frac{dM}{dt}} = \bar{\gamma}\bar{N}^{1/3}\bar{M}^{2/3} + M_P\bar{\alpha} - k\bar{\omega}'\bar{N}^{1/3}\bar{M}^{2/3} \tag{5.46}$$

k is determined by: $k = 0$ if $\bar{C} \geq P_0$ and $k = 1$ if $\bar{C} < P_0$, where $\bar{C}$ is given by

$$\bar{C} = \int_0^1 P(\xi)\,C(\xi)\,d\xi \tag{5.47}$$

The function $C(\xi)$ is defined by: $\xi < \xi_0$ then $C = 0$, $\xi \geq \xi_0$ then $C = 1$. The parameter ξ_0 is taken to be the value of mixture fraction at which the net mass concentration source term changes from a positive to a negative value - ie. at the point where $\gamma - \omega'$ changes from positive to negative. For the present soot model this is approximately at a mixture fraction of 0.06 and this is the value used for ξ_0. P_0 is the probability threshold. Three values for this threshold are used in this work 0.1, 0.25, and 0.5. The effect of changing this threshold parameter is discussed in section 5.5.

Mean Properties Closure

The final source term closure evaluated in this work ignores the effect of the turbulence entirely and formulates mean source terms from the mean properties. Replacing the instantaneous variables by their time averaged quantities yields the parameters α, β, γ, and ω'

in the form, for particle nucleation

$$\bar{\alpha} = a N_A \frac{\bar{X}_{C_2H_2} P}{R \bar{T}} e^{-\frac{21100}{\bar{T}}} \tag{5.48}$$

for particle coagulation

$$\bar{\beta} = \left(\frac{24 R}{\rho_{Soot} N_A} \right)^{1/2} \left(\frac{6}{\pi \rho_{Soot}} \right)^{1/6} \bar{T}^{1/2} \tag{5.49}$$

for surface growth

$$\bar{\gamma} = b \left(\frac{\bar{X}_{C_2H_2} P}{R \bar{T}} \right)^m e^{-\frac{12100}{\bar{T}}} \pi^{1/3} \left(\frac{6}{\rho_{Soot}} \right)^{2/3} \tag{5.50}$$

and for oxidation

$$\bar{\omega}' = 4.2325 \frac{\bar{X}_{OH} P}{R \bar{T}} \sqrt{\bar{T}} \pi^{1/3} \left(\frac{6}{\rho_{Soot}} \right)^{2/3} \tag{5.51}$$

The mean source terms are then given by equations 5.37 and 5.38.

5.4 Computation

5.4.1 Flowfield Equations

The GENMIX code - Spalding (1977) - is used to solve the system of equations introduced in section 5.2. This parabolic CFD code is designed to solve boundary layer flow problems of this type. The 1 and 3 atm flames investigated experimentally (see chapter 3) are both modelled; these flames are axi-symmetrical when time averaged. Using the turbulence model described in sub-section 5.3.1, the combustion model outlined in sub-section 5.3.2, and the soot model described in sub-section 5.3.4, eight transport equations are required to model these flames. These are equations for axial momentum, turbulence kinetic energy, turbulence kinetic energy dissipation rate, mean mixture fraction, mixture fraction variance, specific enthalpy, soot particle number density, and soot particle mass concentration. The Favre averaged, axi-symmetric form of the general transport equation solved by GENMIX is

$$\tilde{u}\frac{\partial\tilde{\phi}}{\partial x}+\tilde{v}\frac{\partial\tilde{\phi}}{\partial r}=\frac{1}{\bar{\rho}\,r}\frac{\partial}{\partial r}\left(r\frac{\mu_T}{\sigma_\phi}\frac{\partial\tilde{\phi}}{\partial r}\right)+\frac{1}{\bar{\rho}}\bar{S}_\phi \qquad (5.52)$$

where ϕ may represent any of the dependent variables mentioned above, σ_ϕ is the turbulent Prandtl / Schmidt number for ϕ, and S_ϕ is the volumetric source term of ϕ. The transported soot variables are not the mean particle number density and mean mass concentration, but are related to these quantities by

$$\tilde{\phi}_N=\frac{\bar{N}}{N_A\bar{\rho}} \qquad \tilde{\phi}_M=\frac{\bar{M}}{\bar{\rho}} \qquad (5.53)$$

The molecular diffusion coefficient of soot particles is very small compared to that of gases. In the turbulent flame calculation the soot is assumed to follow the bulk gas motion exactly, this results in a turbulent Prandtl / Schmidt number for both the soot properties of unity. In the laminar flame calculation thermophoretic transport of soot is included. Thermophoresis is the name given to the motion of particles in non-isothermal media resulting from the net force on the particles due to gas molecules impacting the particle on

different sides with different velocities. Thermophoresis results in particles travelling along the temperature gradient, away from the regions of higher temperature. However, in the turbulent calculation only mean property information is available. Mean temperature properties will not reflect the instantaneous temperature field that the soot experiences. The soot exists in thin layers within which the temperature gradients may be very large, but not necessarily aligned with the mean temperature gradient. For this reason thermophoresis is omitted from the turbulent calculation.

The turbulent Prandtl / Schmidt number for the mixture fraction is set to a value of 0.7. This value is found to give the best agreement with the experimental mean mixture fraction field and also agrees with the value used by Syed (1990). The Prandtl / Schmidt number for the specific enthalpy is also set to 0.7. The value of this Prandtl / Schmidt number must match that used for the mixture fraction for the radiative loss combustion model to perform correctly - see sub-section 5.3.2.

The turbulent Prandtl / Schmidt numbers for each of the dependent variables are summarised in the following table.

Table 5.1

Transported Variable	Turbulent Prandtl / Schmidt Number
$\tilde{u}$	1
$\widetilde{\xi}$	0.7
$\widetilde{\xi''^2}$	0.7
$\tilde{h}$	0.7
k	1
ϵ	1.3
$\widetilde{\phi}_N$	1
$\widetilde{\phi}_M$	1

5.4.2 Geometry

The flames modelled in this section show properties that are axi-symmetrical when time averaged. The flames are confined in the rig described in section 3.2. This rig confines the flames in a Pyrex flowtube with a circular cross section of internal diameter 155 mm. In the centre of this tube, aligned with its axis, is the methane burner - see also figures 3.1 and 3.2. This is also circular with an exit diameter of 4.07 mm.

5.4.3 Initial and Boundary Conditions

The turbulent jet flames modelled are axi-symmetrical when time averaged, this allows the use of a two dimensional grid in the GENMIX code. This grid extends for half of the flames' width. This flame half-width is represented by one hundred cross-stream nodes. Initially twenty of these nodes are positioned in the burner stream and eighty in the co-flowing air stream. The inner node, that at the centre of the burner, represents the axis of symmetry and the outer node represents the inner surface of the confining Pyrex tube.

The initial conditions for the eight dependent variables need defining at the lower boundary of the computational domain (the burner exit plane). These variables are axial velocity, mean mixture fraction, mixture fraction variance, turbulence kinetic energy, turbulence kinetic energy dissipation rate, specific enthalpy, soot particle number density, and soot mass concentration. The initial conditions for each flame are set as follows.

<u>1 atm Flame</u>

Axial Velocity: Flat velocity profiles are used in both the fuel and the air streams. The fuel and velocities are given their mass averaged values. For the fuel stream this is 20.3 m s^{-1} and for the air stream this is 0.55 m s^{-1}.

Mixture Fraction, Mean and Variance: The mean mixture fraction is assigned a value of unity in the fuel stream and zero in the air stream, corresponding to pure fuel and pure air respectively. Unlike low exit velocity laminar flames, upstream diffusion is

insignificant. The mixture fraction variance is given a value of zero in both the fuel and air streams.

Turbulence Kinetic Energy and Dissipation Rate: The turbulence kinetic energy follows the equation $k = 0.003\,u^2$ in both the fuel and air streams - Syed (1990). The dissipation rate of the turbulence kinetic energy in both the fuel and air streams is set according to $\epsilon = k^{3/2} / r_{Burner}$, by relating the integral length scale to the radius of the burner.

Specific Enthalpy: The specific enthalpy is given the value of methane enthalpy at 290 K in the fuel stream and air enthalpy at 290 K in the air stream. Methane enthalpy at 290 K is -4.6805×10^{-6} J kg^{-1} and air enthalpy at 290 K is -8.2436×10^{-3} J kg^{-1}.

Soot Particle Number Density and Mass Concentration: The soot properties are both assigned a value of zero at the exit plane of the burner.

<u>3 atm Flame</u>

Axial Velocity: Flat velocity profiles are used in both the fuel and the air streams. The fuel and velocities are given their mass averaged values. For the fuel stream this is 6.77 m s^{-1} and for the air stream this is 0.18 m s^{-1}.

Mixture Fraction, Mean and Variance: The mean mixture fraction is assigned a value of unity in the fuel stream and zero in the air stream, corresponding to pure fuel and pure air respectively. The mixture fraction variance is given a value of zero in both the fuel and air streams.

Turbulence Kinetic Energy and Dissipation Rate: The turbulence kinetic energy follows the equation $k = 0.0003\,u^2$ in both the fuel and air streams. It should be noted that the value of the constant in this expression is an order of magnitude lower than in the expression used for the 1 atm case. Syed (1990) notes that an order of magnitude change in the value of this constant affects the results only in the near burner region. In the 3 atm flame the temperature profile measured 50 mm above the burner exit plane shows a very high peak value of 1848 K (see appendix). This indicates that a certain degree of relaminarization is

taking place close to the exit of the burner. This relaminarization is caused by the increase in the molecular velocity due to the combustion heat release. A fit to the molecular viscosity, determined using the method given in section 4.3.2, shows that $\mu \propto T^{3/4}$. The temperature profile at this height given by GENMIX using the same initial parameter for k as used for the 1 atm flame fails to capture this temperature peak. A lower value for the constant in the expression for the initial value of k raises the temperature peak. This effect arises from the effect that k has on the source term of mixture fraction variance. The calculation downstream is unaffected however. The dissipation rate of the turbulence kinetic energy in both the fuel and air streams is set according to $\epsilon = k^{3/2} / r_{Burner}$, as in the 1 atm flame calculation.

Specific Enthalpy: The specific enthalpy is given the value of methane enthalpy at 290 K in the fuel stream and air enthalpy at 290 K in the air stream.

Soot Particle Number Density and Mass Concentration: The soot properties are both assigned a value of zero at the exit plane of the burner.

5.4.4 Model Implementation

Sub-section 5.3.2 describes the multiple flamelet combustion model used to effect the chemical source term closure in this study. This sub-section describes the implementation of the model in the GENMIX code. The model uses a range of flamelets, each flamelet including a fixed level of radiative heat loss. At any flame location the most appropriate flamelet is chosen by comparing the levels of heat loss in the flamelets with the local heat loss obtained from an enthalpy transport equation. As the number of flamelets in any set is finite, in practice this means choosing two flamelets that bound the local heat loss and interpolating between them. Two methods of flamelet selection are reviewed below.

The first method determines the local heat loss fraction from the transported enthalpy. Two flamelets for each scalar may then be chosen from the flamelet library that have bounding values of the radiative loss fraction. Weighting with the PDF of mixture fraction yields two mean values of the scalar property which may be interpolated between using the heat loss

fraction obtained from the enthalpy transport equation. The scheme is as follows. Firstly, the local heat loss fraction must be determined from the mean transported enthalpy. The enthalpy flamelet is generally given by (cf. equation 5.28)

$$h(\xi, X_R) = X_R\, h_{Init.}(\xi) + (1 - X_R)\, h_{Adia.}(\xi) \tag{5.54}$$

Forming the mixture fraction Favre PDF weighted mean of $h(\xi, X_R)$ and equating to the transported enthalpy yields

$$\tilde{h} = X_R \int_0^1 h_{Init.}(\xi)\, \tilde{P}(\xi)\, d\xi + (1 - X_R) \int_0^1 h_{Adia.}(\xi)\, \tilde{P}(\xi)\, d\xi \tag{5.55}$$

where $\tilde{h}$ is the Favre mean enthalpy given by the enthalpy transport equation. This may be rearranged to give X_R

$$X_R = \frac{\tilde{h} - \int_0^1 h_{Adia.}(\xi)\, \tilde{P}(\xi)\, d\xi}{\int_0^1 (h_{Init.}(\xi) - h_{Adia.}(\xi))\, \tilde{P}(\xi)\, d\xi} \tag{5.56}$$

The relationship between the adiabatic product enthalpy ($h_{Adia.}$) and the mixture fraction (ξ) is linear. Therefore the Favre PDF weighted mean of $h_{Adia.}(\xi)$ becomes

$$\int_0^1 h_{Adia.}(\xi)\, \tilde{P}(\xi)\, d\xi = \int_0^1 (a\xi + b)\, \tilde{P}(\xi)\, d\xi = a\widetilde{\xi} + b \tag{5.57}$$

where the constants a and b are given by $a = h_{Fuel,290\,K} - h_{Air,290\,K}$ and $b = h_{Air,290\,K}$. Substituting this result into equation 5.56 yields a simplified expression for X_R

$$X_R = \frac{\tilde{h} - (a\widetilde{\xi} + b)}{\int_0^1 h_{Init.}(\xi)\, \tilde{P}(\xi)\, d\xi - (a\widetilde{\xi} + b)} \tag{5.58}$$

Scalar flamelets are labelled according to the heat loss fraction used in their definition.

Hence, two flamelets for each scalar may be chosen that have bounding values of heat loss fraction. Scalar values may then be found by linear interpolation between PDF weighted, bounding flamelets.

As an example, if the bounding values of radiative loss are $X_{R,Low}$ and $X_{R,High}$ then $X_{R,Low} \le X_R < X_{R,High}$. Two PDF weighted values for each scalar are determined, corresponding to each bounding value of the heat loss fraction

$$\bar{\Phi}(X_{R,Low}) = \int_0^1 \phi(\xi, X_{R,Low}) P(\xi) d\xi \tag{5.59}$$

$$\bar{\Phi}(X_{R,High}) = \int_0^1 \phi(\xi, X_{R,High}) P(\xi) d\xi \tag{5.60}$$

Hence, the mean scalar value is given simply by

$$\bar{\Phi} = \bar{\Phi}(X_{R,Low}) + \frac{X_R - X_{R,Low}}{X_{R,High} - X_{R,Low}} (\bar{\Phi}(X_{R,High}) - \bar{\Phi}(X_{R,Low})) \tag{5.61}$$

Or, if the flamelets are represented by discrete values and the integration is numerical, it may be more efficient to interpolate between these discrete values before the integration. The major disadvantage of this method is immediately apparent. In the derivation of the expression for X_R, the heat loss fraction is taken to be a constant not a function of the mixture fraction. This does limit the generality of this method.

Because of the disadvantage given above, the following method is implemented for flamelet selection in the version of the GENMIX code used in this study. This method was developed by Young (1993) but a full description is not given. For completeness a full explanation is given here. Rather than deriving the local heat loss fraction from the enthalpy transport equation, integrated flamelet enthalpies are compared with the transported enthalpy for flamelet selection. Two enthalpy flamelets are found that, when weighted by the mixture fraction PDF, have mean enthalpy values that bound the mean transported enthalpy. In practice this results in integrating successive enthalpy flamelet

pairs until the appropriate flamelet pair is found. Because the level of radiative loss is unlikely to change greatly from one computational step to the next, the previous flamelet pair is used as the starting point. Corresponding to each enthalpy flamelet is the family of flamelets for the other scalars. When the enthalpy flamelets are found that bound the transported enthalpy the corresponding flamelets for the other scalars are weighted by the mixture fraction PDF. The local scalar values are then found by linear interpolation between the scalar pairs. An example best illustrates this scheme.

The mean transported enthalpy is $\tilde{h}$. Two flamelets are determined that have mean enthalpies that bracket this transported enthalpy.

$$\tilde{h}_{Low} = \int_0^1 h(\xi, X_{R,High})\,\tilde{P}(\xi)\,d\xi \tag{5.62}$$

$$\tilde{h}_{High} = \int_0^1 h(\xi, X_{R,Low})\,\tilde{P}(\xi)\,d\xi \tag{5.62}$$

where $\tilde{h}_{Low} < \tilde{h} \le \tilde{h}_{High}$ and it is noted that an inverse relationship exists between enthalpy and radiative loss fraction. Pairs of mean values for the other scalars are also determined by weighting the corresponding flamelets with the PDF of mixture fraction and integrating

$$\overline{\Phi}_{Low} = \int_0^1 \phi(\xi, X_{R,High})\,P(\xi)\,d\xi \tag{5.64}$$

$$\overline{\Phi}_{High} = \int_0^1 \phi(\xi, X_{R,Low})\,P(\xi)\,d\xi \tag{5.65}$$

The desired mean scalar value is found by linear interpolation using the transported enthalpy as the interpolating factor

$$\overline{\Phi} = \frac{\tilde{h} - \tilde{h}_{High}}{\tilde{h}_{Low} - \tilde{h}_{High}}\left(\overline{\Phi}_{Low} - \overline{\Phi}_{High}\right) + \overline{\Phi}_{High} \tag{5.66}$$

It is evident that this method is not as computationally efficient as the first method given. However, because the form of $X_R(\xi)$ may be entirely arbitrary the method is more general. The effect of the form of $X_R(\xi)$ on the results is discussed in section 5.5.

5.5 Results

The first set of GENMIX results presented are those obtained for the 1 atm flame. The calculation includes radiative heat loss from the soot and the gas phase. The soot model used in this calculation is defined by the constant values of $m = 1$ and $n = 1$ (constant set 7); linear soot growth dependence on ethyne concentration and soot surface area. The closure of the soot source terms is effected by assuming that the soot properties are uncorrelated with the gas phase. Soot oxidation is omitted. The heat loss function is taken to be a constant across mixture fraction space. The results are compared with experiment in figures 5.5a - j. This calculation is taken to be the 'base case' for the 1 atm flame. The results for this calculation are generally good. The mean mixture fraction field is well predicted by the GENMIX code. The temperature profiles, both axial and radial, also show good agreement with experiment. The axial evolution of the centreline soot volume fraction is surprisingly well captured by GENMIX with a slight over-prediction at the 425 mm axial station (the highest position for which experimental values are available). This over-prediction at higher positions in the flame is to be expected due to the omission of soot oxidation from the calculation.

The GENMIX result for the centreline axial profile of soot volume fraction for the same calculation but with the inclusion of the soot oxidation term is shown in figure 5.6. Note that the enhanced mixing due to the turbulence allows comparisons of the soot model performance to be made on the basis of the centreline axial profiles alone. The soot oxidation source term is closed by assuming that the soot properties are uncorrelated with the gas phase. As predicted in section 5.1 the performance of the model is very poor with soot oxidation clearly dominating the growth term. The peak soot volume fraction is under-predicted by more than two orders of magnitude and the calculated axial position of the peak is reached before the experimental maximum. Some insight into the reason for this may be obtained by referring to figures 5.7 and 5.8. Figure 5.7 shows the flamelets of the soot growth and the soot oxidation functions, for the adiabatic and 10 % heat loss cases. Figure 5.8 shows the evolution of the normalised Beta function PDF of mixture fraction along the centreline of the flame. At each axial station the PDF has been normalised by dividing by the PDF's maximum value. Note that the axial variation of the PDFs' maxima coincides well with the experimental mean mixture fraction values, as would be expected

from the symmetrical PDF shape. From this figure it may be seen that in the soot growth region the PDF width in mixture fraction space is very wide. The soot oxidation function has a peak value approximately one order of magnitude greater than the soot surface growth function. Also, the position of the peaks for the oxidation and surface growth functions are very close in mixture fraction space. These two factors, the PDF spread and the closeness of the growth and oxidation functions, leads to a lack of discrimination between the growth and oxidation regions of the turbulent flame. The magnitude of the oxidation function ensures that it dominates the soot mass source term. The problem is exacerbated with increasing axial distance as the radiative loss decreases the growth term but has little effect on the oxidation.

A simple method of decreasing the effect of the oxidation function is to multiply the oxidation term by a constant (<1). The effect on the axial soot volume fraction of doing this is shown in figure 5.9. The conditions for this GENMIX calculation are the same as those above, except the oxidation component of the soot mass source term is multiplied by 0.015. The figure shows a massive improvement in the prediction of the soot volume fraction. The GENMIX prediction does not quite pass through the experimental points, although fine tuning of the oxidation factor would clearly allow this to happen. However, it is difficult to view this factor as anything other than a rather arbitrary means of achieving agreement with the experimental data. Although, Syed (1990) achieved a similar level of agreement in a turbulent ethene / air flame using the oxidation mechanism of Nagle and Strickland-Constable (1962) factored by the same amount. Despite this the generality of the value given here is not proven, but it would seem reasonable to suppose that values for different flames would require determination on an ad hoc basis.

Before moving on to the correlated soot model the effect of the flame's heat loss on the soot production rate and temperature field is examined. Figures 5.10a - b show the axial evolution of the soot volume fraction and the temperature along the centreline for an adiabatic GENMIX calculation of the 1 atm flame. The mixture fraction is not shown as the change from the case including heat loss is negligible. The soot model is the same as that used in the calculations above, with no oxidation. The peak temperature on the axis is now over-predicted by approximately 200 K. The effect of these higher temperatures on the performance of the soot model is great, with the model over-estimating the soot volume

fraction at the 425 mm axial station by approximately 400 %. The other issue to consider in relation to the heat loss is the form of the heat loss function itself ($X_R(\xi)$). In all the calculations so far, for each flame position, the heat loss function has been taken as a constant in mixture fraction space. Results from laminar flame calculations indicate that this is unlikely to be the case. Flamelets have been created using the normalised heat loss profile from a laminar flame calculation. However, the application to the turbulent flame of this flamelet set produces only negligible differences when compared with the results given by assuming that $X_R(\xi)$ is a constant in mixture fraction space at any particular flame location. Hence, $X_R(\xi)$ is taken to be a constant at each flame position.

Evidence presented in sub-section 5.3.4 (Sivathanu and Faeth (1990) etc.) suggests that there may be some correlation between the soot properties and the mixture fraction. The fully correlated model presented in sub-section 5.3.4 assumes that the soot properties correlate perfectly with the mixture fraction. A normalised state relationship for the soot mass concentration, obtained from a laminar flame calculation, is imposed on the local mean value of the soot mass concentration obtained from its transport equation. This normalised profile of soot mass concentration in mixture fraction space allows locally applicable soot 'flamelets' to be generated, which in turn allow the soot source terms to be calculated exactly. The normalised profile of the soot mass concentration versus mixture fraction is shown in figure 5.4. The profile drops to very low values at extreme rich and lean mixture fraction conditions. The source term includes the reciprocal of the local mean of this function. Therefore, to prevent 'arithmetic overflow' or 'division by zero' errors in the GENMIX calculation a threshold value of the function is set, below which the function value cannot fall. It is found that the value of this threshold exerts a large influence on the calculation. Figure 5.11 shows the centreline soot volume fractions from three GENMIX calculations, corresponding to the threshold values of 0.01, 0.001, and 0.0001. The figure shows that, bounded within the range of these values, a value of the threshold parameter does exist for which the model would give reasonable agreement with the experiment. However, this value may not be determined a priori and therefore the model would seem to yield no additional benefit over the simpler uncorrelated model with a factored oxidation term.

Syed (1990) proposes the use of a conditional oxidation term - see section 5.3.4. The

centreline soot volume fraction profile given by this model is shown in figure 5.12. The parameter P_0 is set to 0.1 and the soot model constants are as used above. This model still contains a degree of arbitrariness, in the selection of P_0. Values for P_0 of 0.25 and 0.5 have also been used and the effects on the results are large. The axial evolution of the soot volume fraction profile shows a trend that is not observed experimentally, with the onset of oxidation occurring suddenly, causing a steep drop in the soot volume fraction with increasing axial distance. Increasing the value of P_0 decreases the axial position at which the onset of oxidation occurs.

The last soot model source term closure to be discussed here is the mean properties closure (see sub-section 5.3.4). Local mean properties are used to generate the local mean soot source terms. Results from this closure are not illustrated but even with the oxidation term omitted the soot volume fractions are too low, by approximately a factor of 2. This is to be expected as the soot source terms are highly non-linear, especially with respect to temperature.

A more stern test of the performance of the soot model is its application to the 3 atm flame. The 3 atm flame, because of the higher soot volume fractions, has nearly double the radiative heat loss of the 1 atm flame. The effect of this increased heat loss on the soot model is more difficult to identify, however, due to the effect of the increased pressure on the soot model source terms for nucleation and surface growth. The first set of results presented for the 3 atm flame uses the soot model with linear dependence on ethyne concentration for the surface growth term (m = 1, constant set 7), oxidation has been omitted and the soot properties are taken as being uncorrelated with the mixture fraction. The analysis presented in chapter 4, sub-section 4.3.4 suggests that the maximum value for this exponent would be 2/3, this is supported by the results. Figures 5.13a - b present the centreline axial evolution of soot volume fraction and temperature. The centreline soot volume fraction at the 250 mm axial station is over-predicted by approximately a factor of 3. This in turn leads to a general under-prediction in the temperature field. A trial and error analysis of the exponent m leads to a value for m of 0.4 as giving the best agreement with experiment. Figures 5.14a - f present axial and radial data for the GENMIX calculation of the 3 atm flame. The soot model uses constant set 2 (m = 0.4, n = 1), the soot properties are assumed to be uncorrelated with the mixture fraction. Oxidation of the soot is included

with a constant multiplying factor of 0.015 being applied to the oxidation term. The peak soot volume fraction predicted on the centreline is in general agreement with experiment. The temperature profiles are well predicted at all heights. However, the form of the axial profile does not follow the experiment which is characterised by an initial rapid growth in soot volume fraction followed by a more rapid decay due to oxidation. Several reasons may account for the disparity between the GENMIX calculation and experiment. The peak soot volume fraction is determined by the balance between the surface growth term and the oxidation term. For this 3 atm calculation the factored oxidation term from the 1 atm calculation is carried over and the exponent m is adjusted to give the best fit to the data. However, as pointed out earlier in this section the oxidation factor is unlikely to be universal. An increase in the value of this multiplying factor would lead to a corresponding increase in the value of m. An increase in m would lead to more rapid initial soot growth, while the increased oxidation term would enhance soot burnout. The other element not yet considered here is the influence of the change in pressure on the particle nucleation term. In the absence of any experimental evidence of the behaviour of particle nucleation with changing pressure the ethyne concentration exponent is taken as unity (see equation 4.40). However, a better value for this exponent may be greater than unity. This would lead to an enhanced nucleation rate at higher pressures. As the coagulation rate will not change with increasing pressure, an increase in the nucleation rate will cause the number density to saturate more quickly. Also, the saturated number density will be higher. These increases will cause an increase in the available soot surface area low in the flame, which in turn will enhance the growth rate of the soot. When the oxidation component of the soot mass concentration source term begins to dominate the surface growth, the increased soot surface area will also enhance the burnout of the soot.

5.6 Conclusion

The purpose of this chapter is to demonstrate a fully coupled model for soot prediction in turbulent flames, that may allow the accurate prediction of the thermal radiation emitted from such flames. It has been confirmed that coupling the soot production rate to the radiative heat loss is necessary to accurately model the formation of the soot. The temperature field calculated with the multiple flamelet combustion model shows excellent agreement with the experimental measurements. The soot prediction for the 1 atm flame also shows excellent agreement in the soot growth region, if soot oxidation is omitted from the calculation. Current models are, however, inadequate for modelling the soot burn-out. The problem seems to lie with modelling the correlation between the soot and its oxidising species. The assumption that these species are uncorrelated is, from the results shown here, obviously entirely inappropriate. However, despite the failings of these models to accurately represent the soot burnout a qualitative assessment may be made as to which model captures the process in the most realistic manner. The visible flame length for the 1 atm flame is approximately 600 mm with no unburnt soot emitted from the flame as smoke. No soot measurements are available for the oxidation region of the 1 atm flame. However, the 3 atm flame data shows that the burnout rate for the soot is relatively gradual, almost mirroring the growth rate. In the 1 atm flame the decreased soot growth rate would probably lead to the soot burnout region being somewhat more pronounced than in the 3 atm flame. However, the sudden onset of oxidation as given by the conditional oxidation model (figure 5.12) appears to disagree with the experimental data. The uncorrelated, factored oxidation model gives good agreement during the growth phase of the soot. However, the subsequent burnout is decreased to an extent that at the 600 mm axial position the soot volume fraction is still of order 0.1 ppm. The fully correlated model of soot growth and oxidation gives the best agreement with the experimental data. From figure 5.11 it is apparent that a threshold value for the model that would allow the prediction to pass through the experimental points would completely burnout the soot before the 600 mm axial position. During the final stages of writing this thesis, after the modelling work on the turbulent flames was completed, some new evidence concerning the relationship between soot and the OH radical in turbulent flames emerged. Brookes et al. (in preparation) have investigated the instantaneous relationship between soot volume fraction and OH radical concentration in a methane fuelled turbulent jet flame using the

techniques of laser induced fluorescence (LIF) and laser induced incandescence (LII). Two counter-propagating laser sheets, one at 308 nm and the other at 1064 nm, were aligned vertically in the flame. The pulsed laser sheets were spatially co-located in the flame and temporally offset by approximately 50 μs. Two intensified CCD cameras, with appropriate filters, were employed to separately capture a two dimensional image from each laser pulse. The sheet at 308 nm resulted in an OH LIF signal and a scattering component from the soot, whereas the sheet at 1064 nm gave LII from the soot only. A typical example of the images captured is shown in figure 5.15. The images from each camera have been overlaid in this figure. The LIF and soot scattering is coloured blue and the LII signal is coloured red. Where two signals are spatially coincident, as in the case of scattering from the soot and LII from the soot, the result is purple. The figure clearly shows a highly organized structure, with bands of the OH radical lying outside sheets of soot. This lends further support to the concept of 'flamelet' like structures existing for the soot, and adds further credibility to the fully correlated form of the soot model.

The soot model shows reasonable agreement at elevated pressure, although considerable uncertainty remains surrounding the pressure dependence of both the surface growth and particle nucleation terms in the model.

Some of these soot and temperature field predictions will be used to generate post-processed, spectrally resolved flame radiative property predictions. These predictions of the flames' radiation are presented in the next chapter.

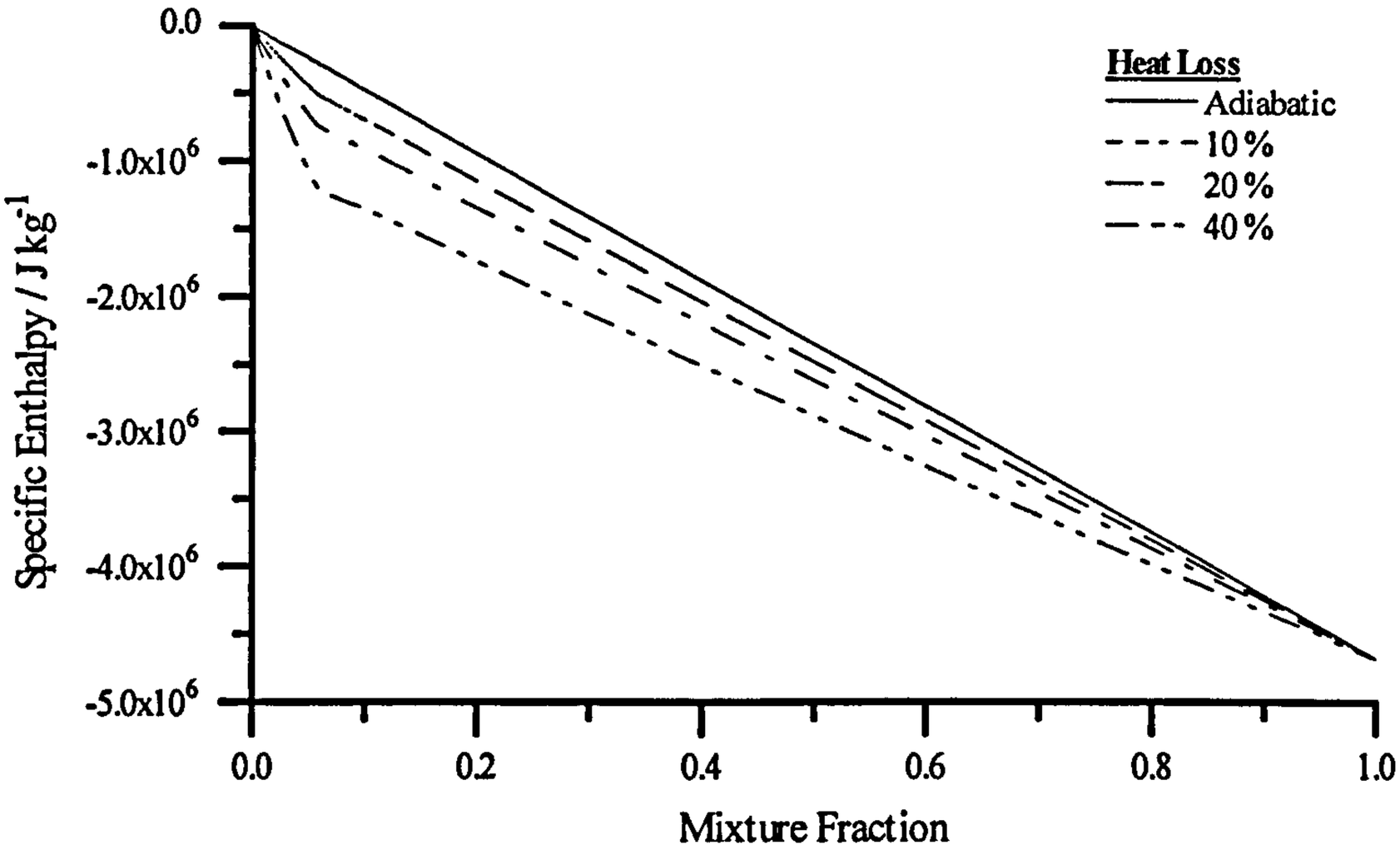

Figure 5.1a. Enthalpy flamelets for methane / air.

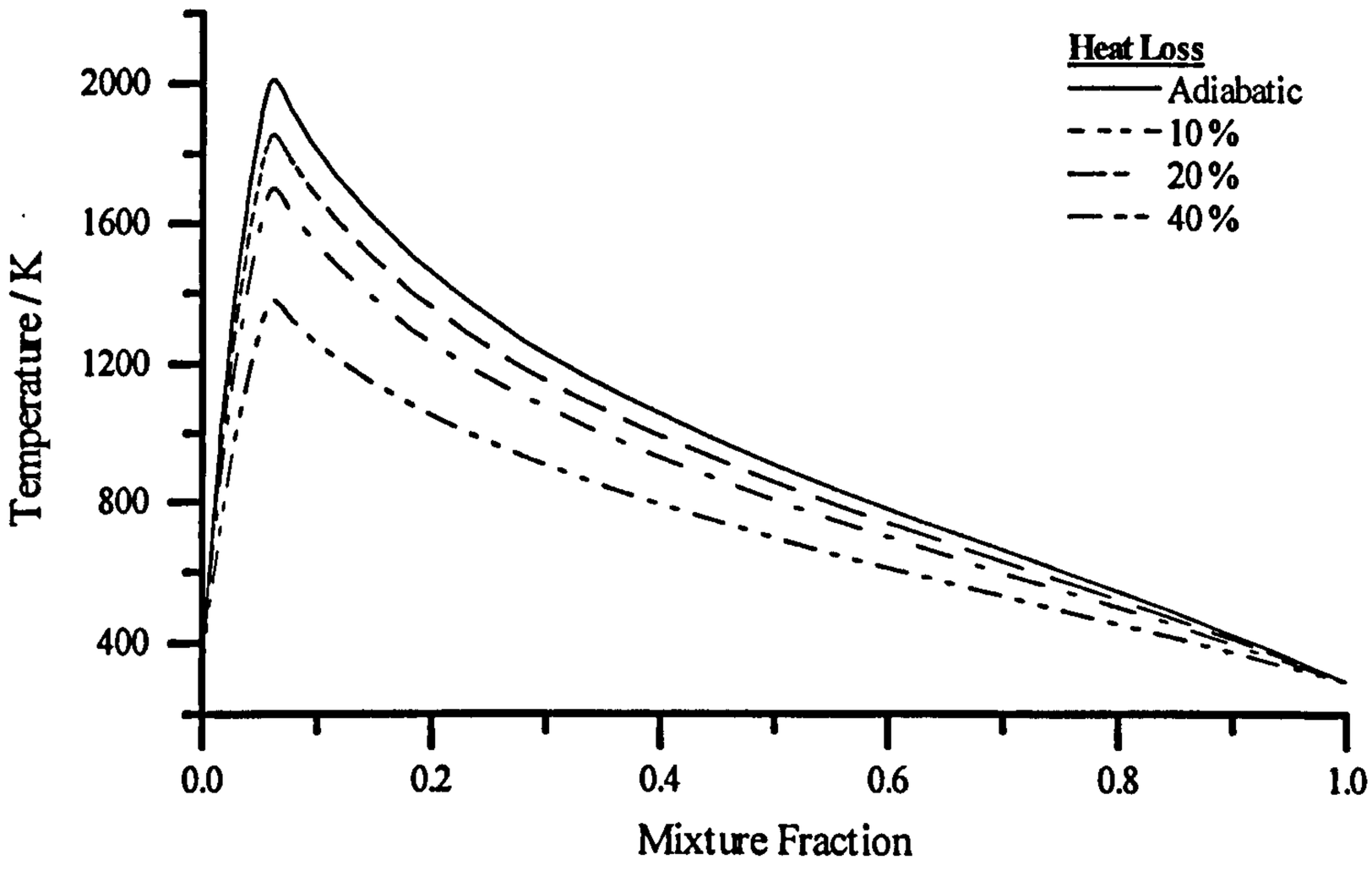

Figure 5.1b. Temperature flamelets for methane / air at 1 atm.

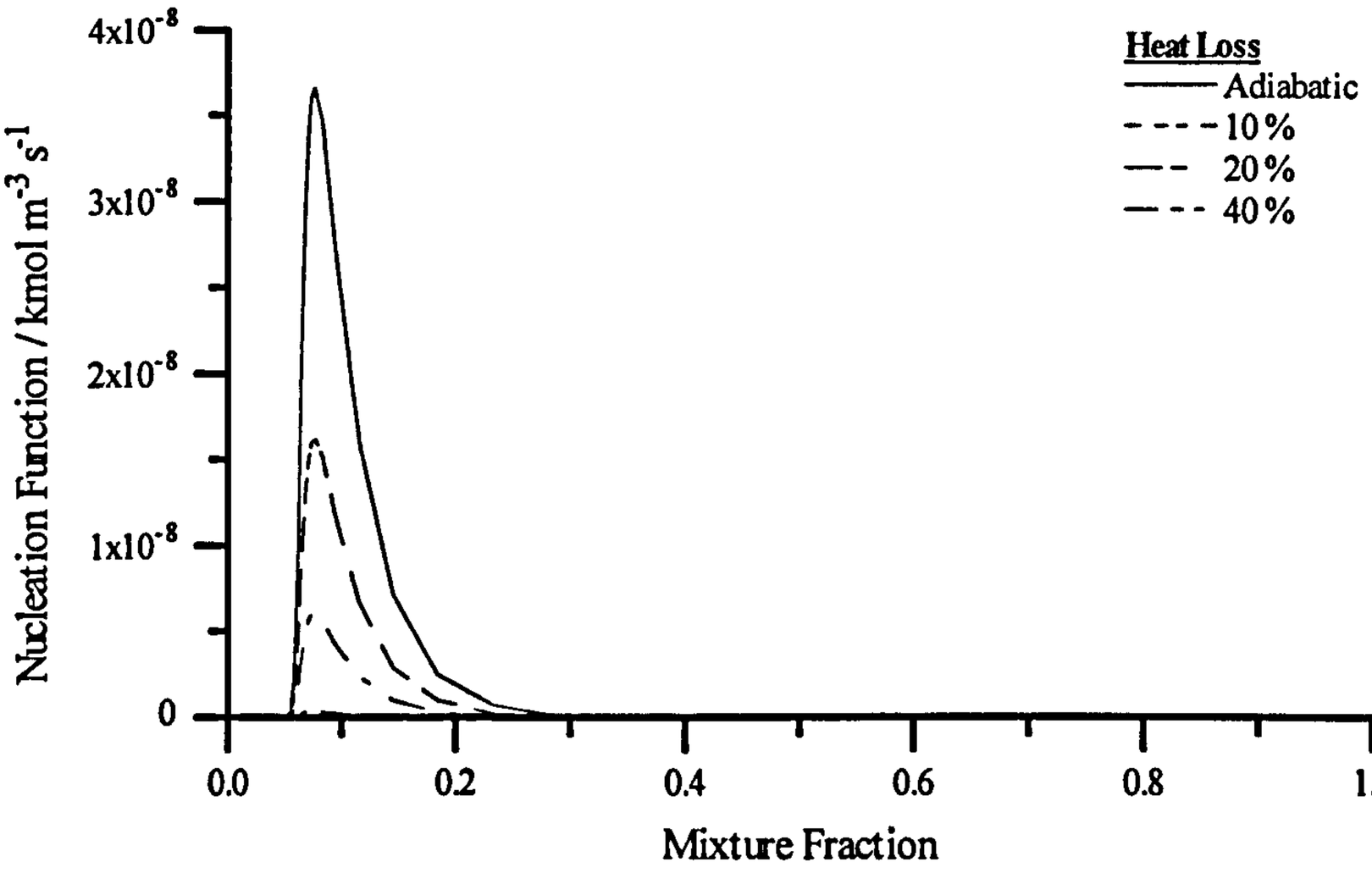

Figure 5.1c. Flamelets for the soot particle nucleation function using constant set 7 at 1 atm.

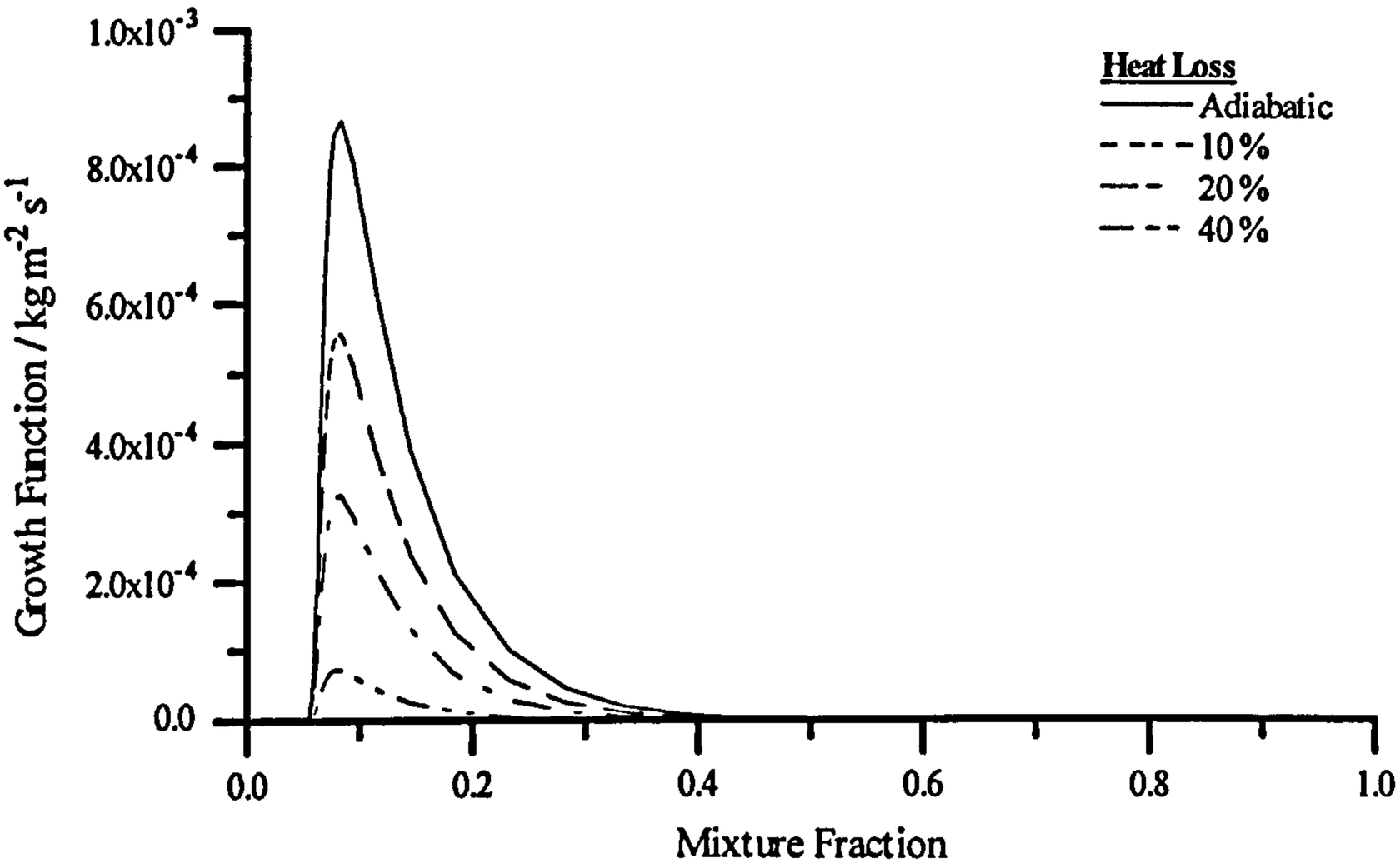

Figure 5.1d. Flamelets for the specific soot surface growth rate using constant set 7 at 1 atm.

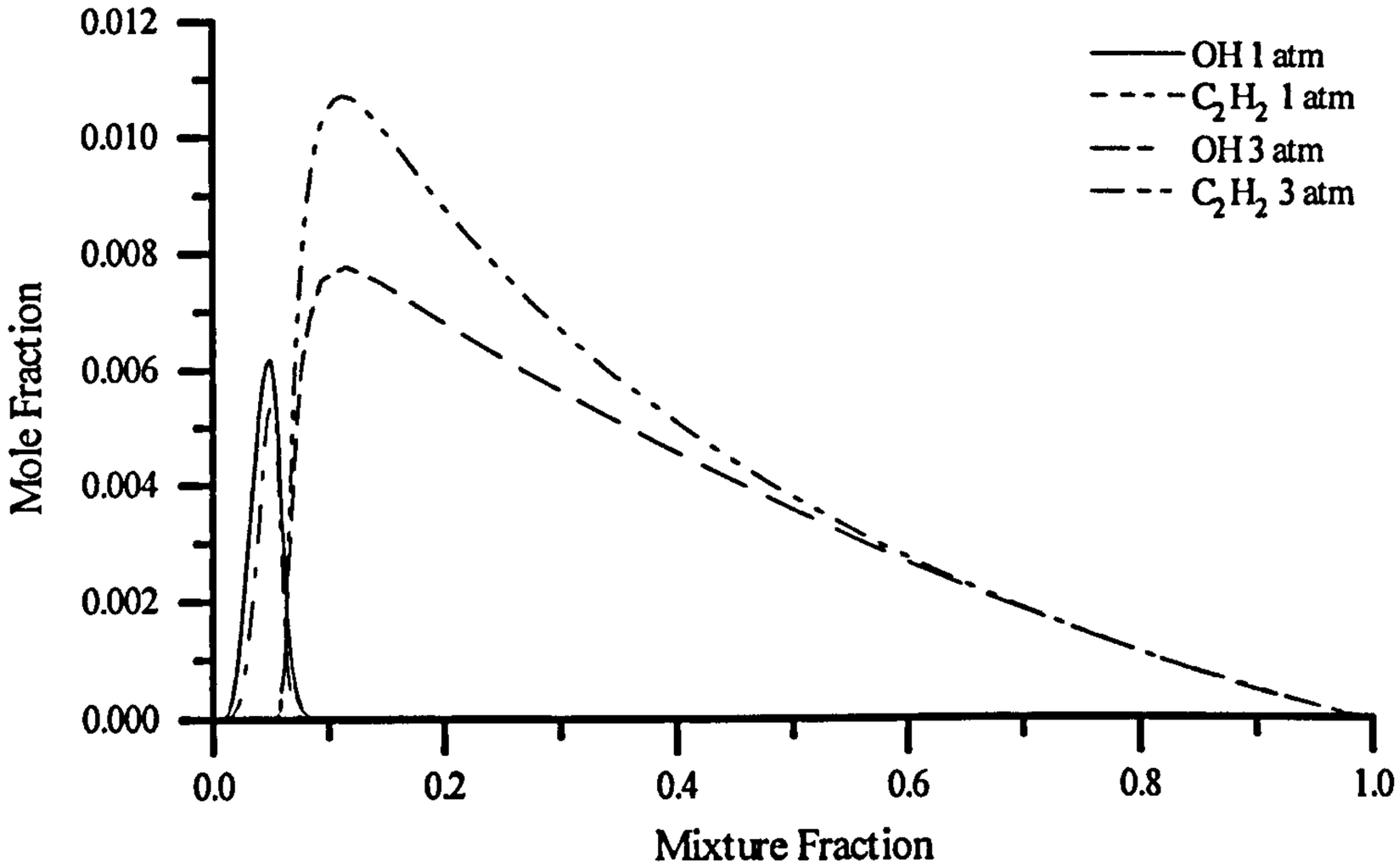

Figure 5.2a. Mole fraction flamelets for the OH radical and ethyne at 1 and 3 atm.

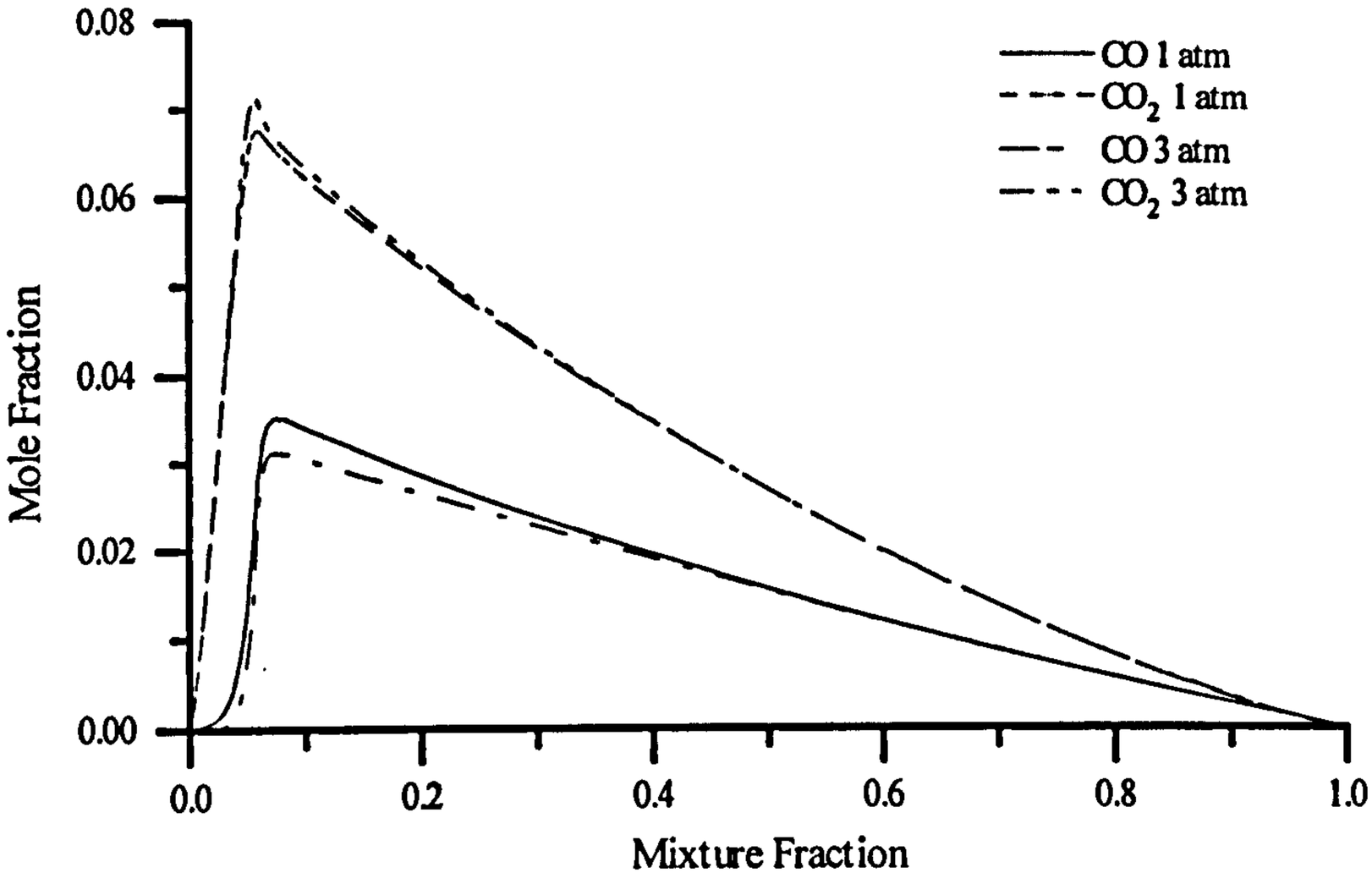

Figure 5.2b. Mole fraction flamelets for carbon dioxide and carbon monoxide at 1 and 3 atm.

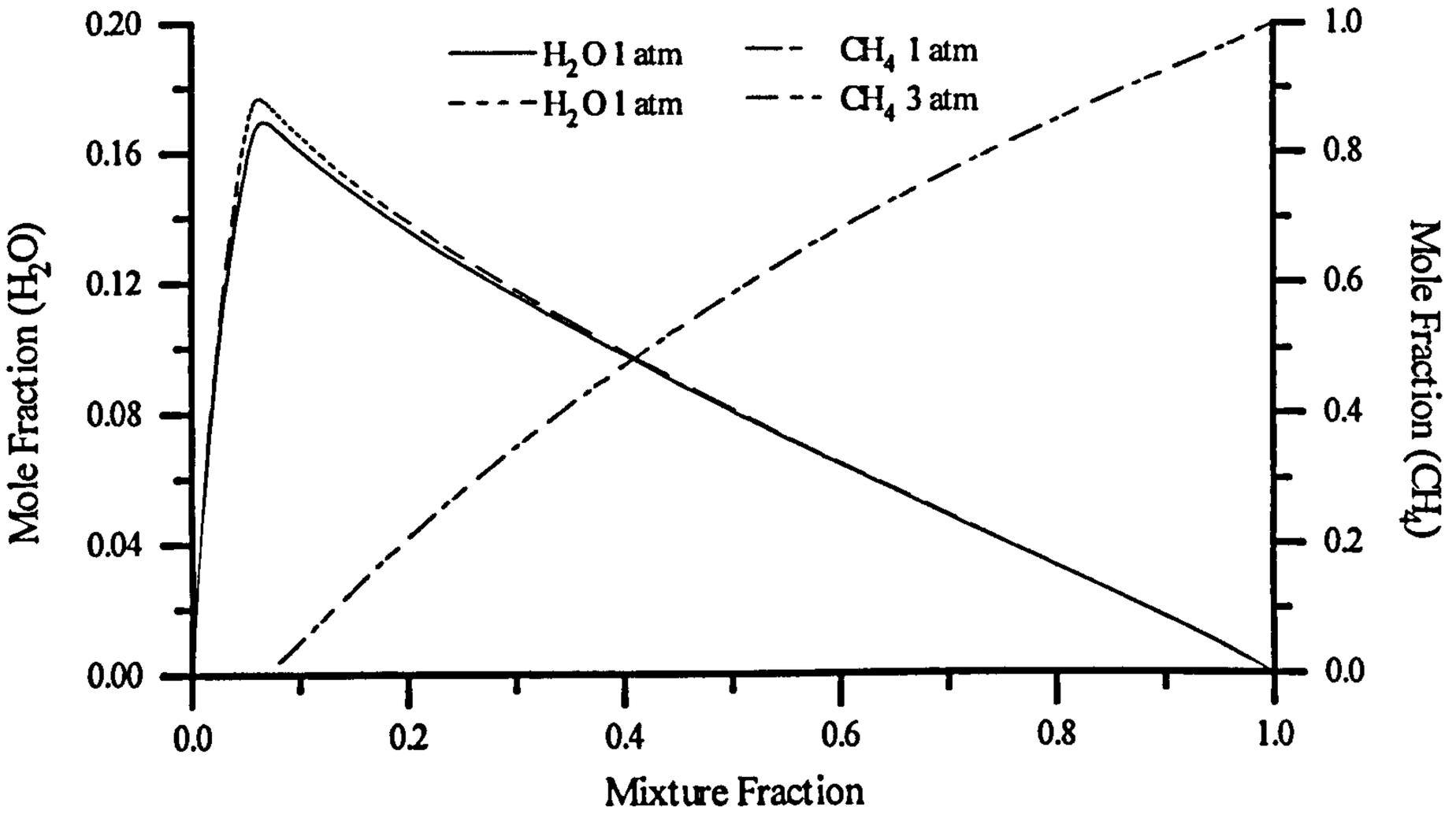

Figure 5.2c. Mole fraction flamelets for water and methane at 1 and 3 atm.

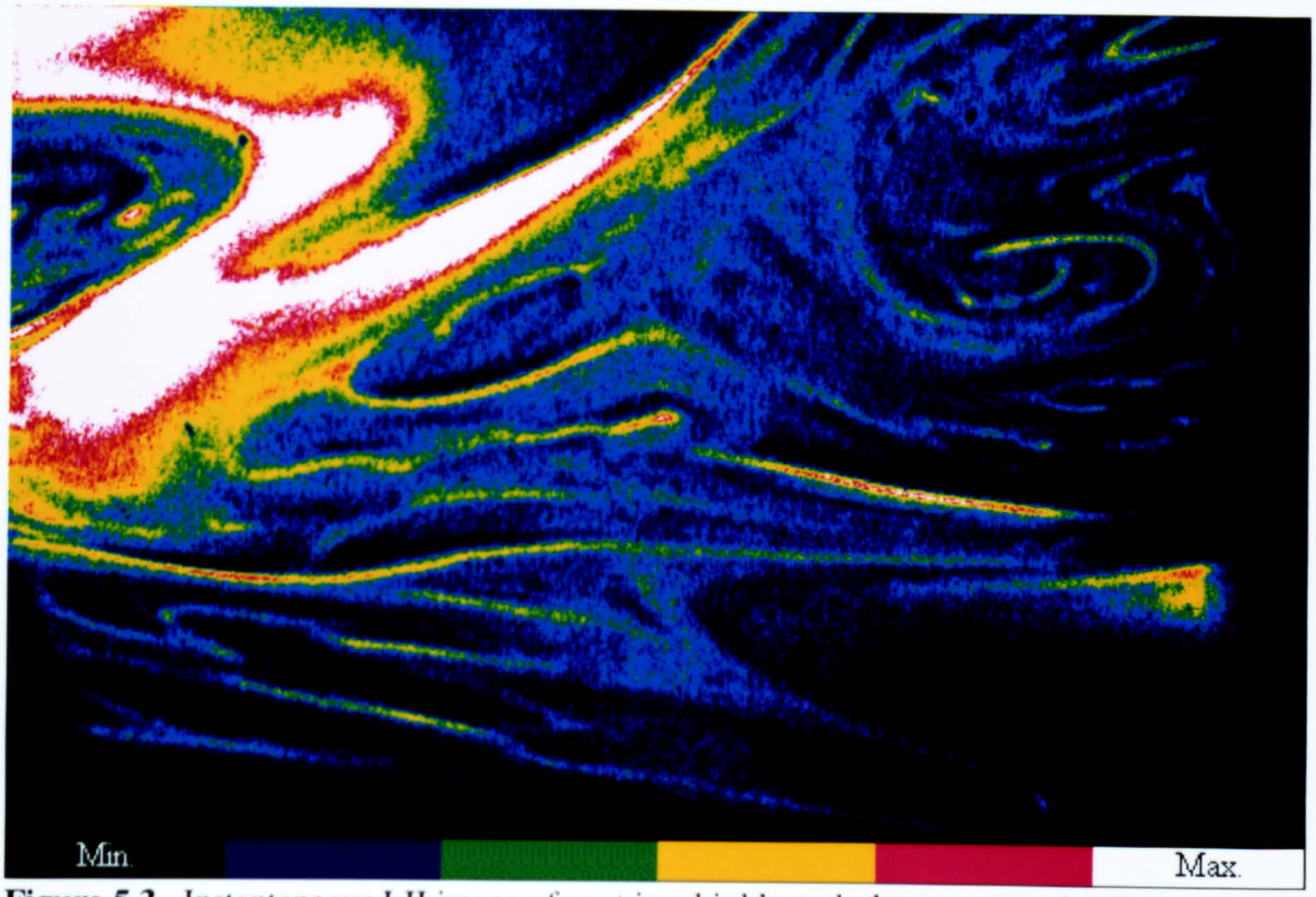

Figure 5.3. Instantaneous LII image of soot in a highly turbulent propane jet flame. Image taken from Tait and Greenhalgh (1993).

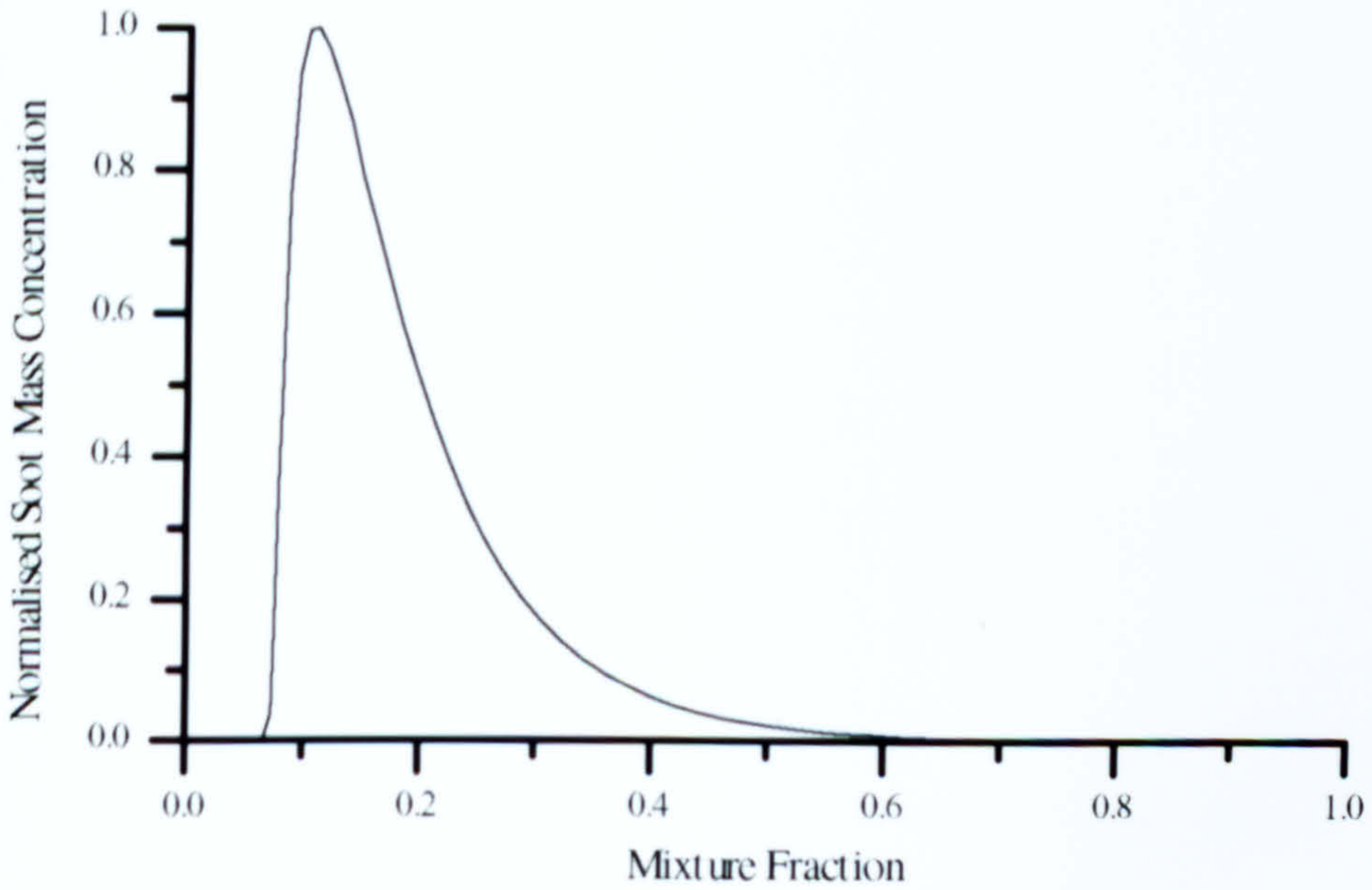

Figure 5.4. Normalised distribution of soot mass concentration in mixture fraction space.

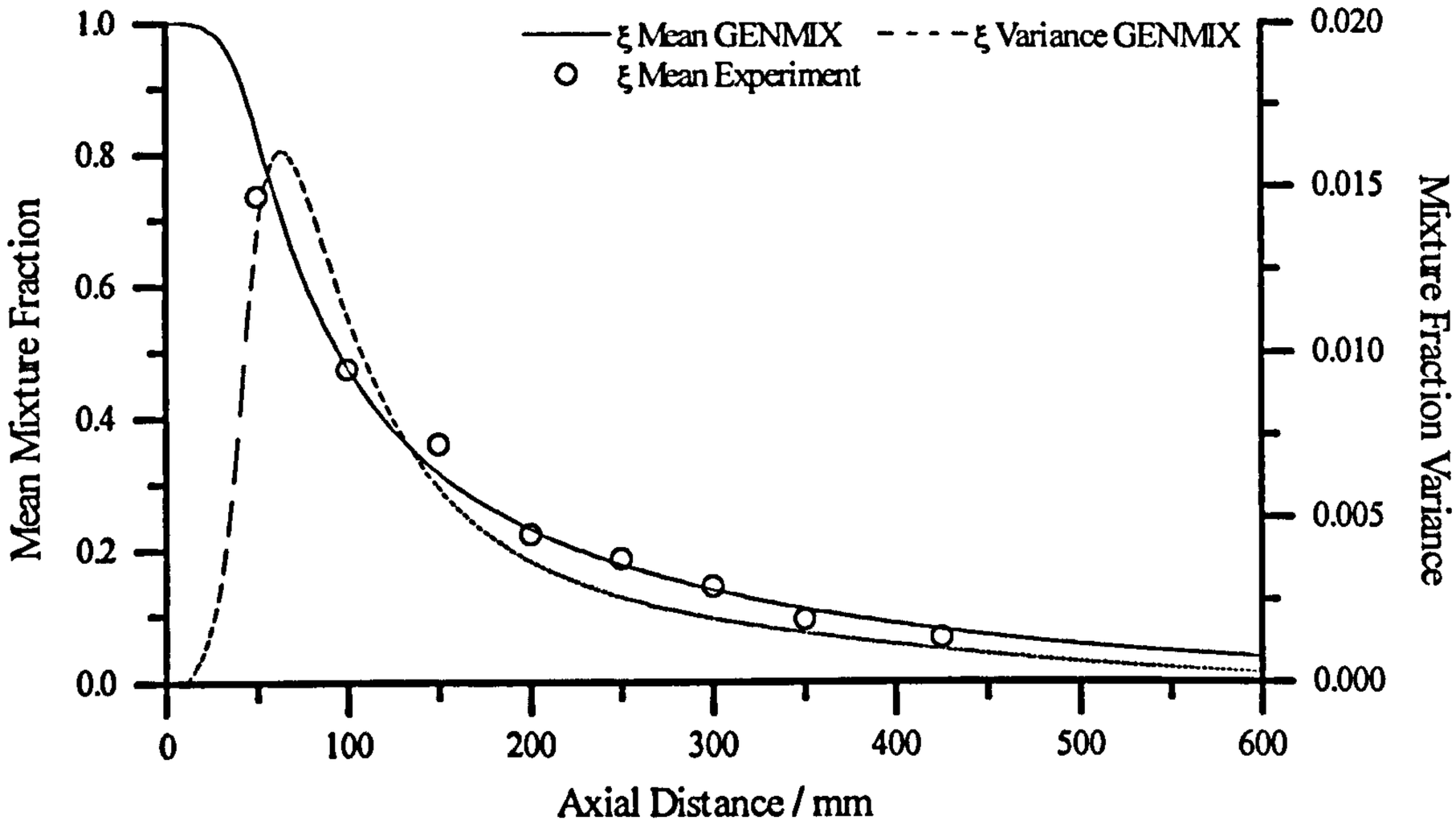

Figure 5.5a. Centreline GENMIX data compared with experiment for the 1 atm methane flame. Radiative heat loss is included in this calculation. The soot model uses constant set 7. The non-correlated soot model is implemented with soot oxidation omitted.

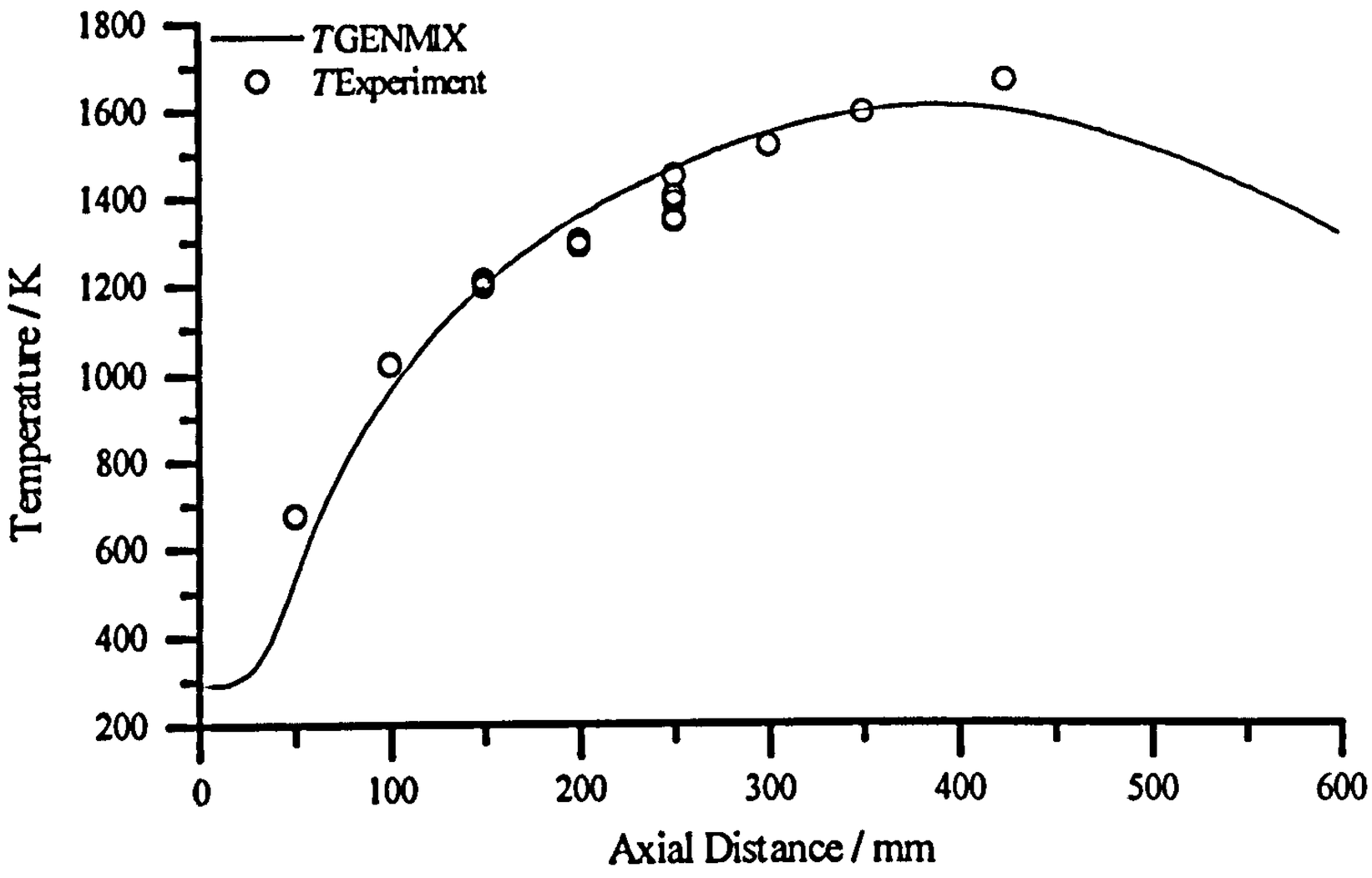

Figure 5.5b. Centreline GENMIX data compared with experiment for the 1 atm methane flame. Calculation details as above.

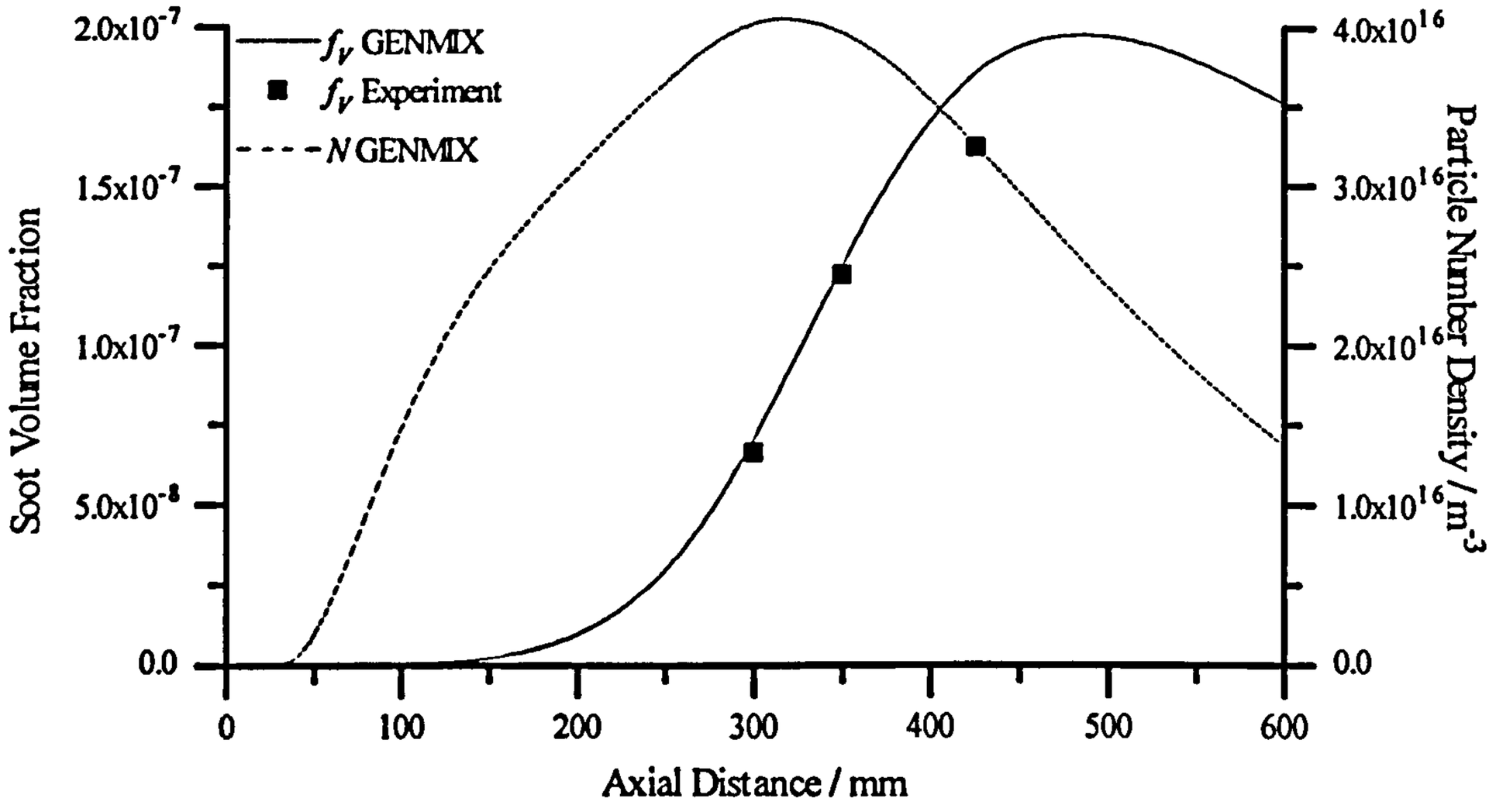

Figure 5.5c. Centreline GENMIX data compared with experiment for the 1 atm methane flame. Calculation details as above.

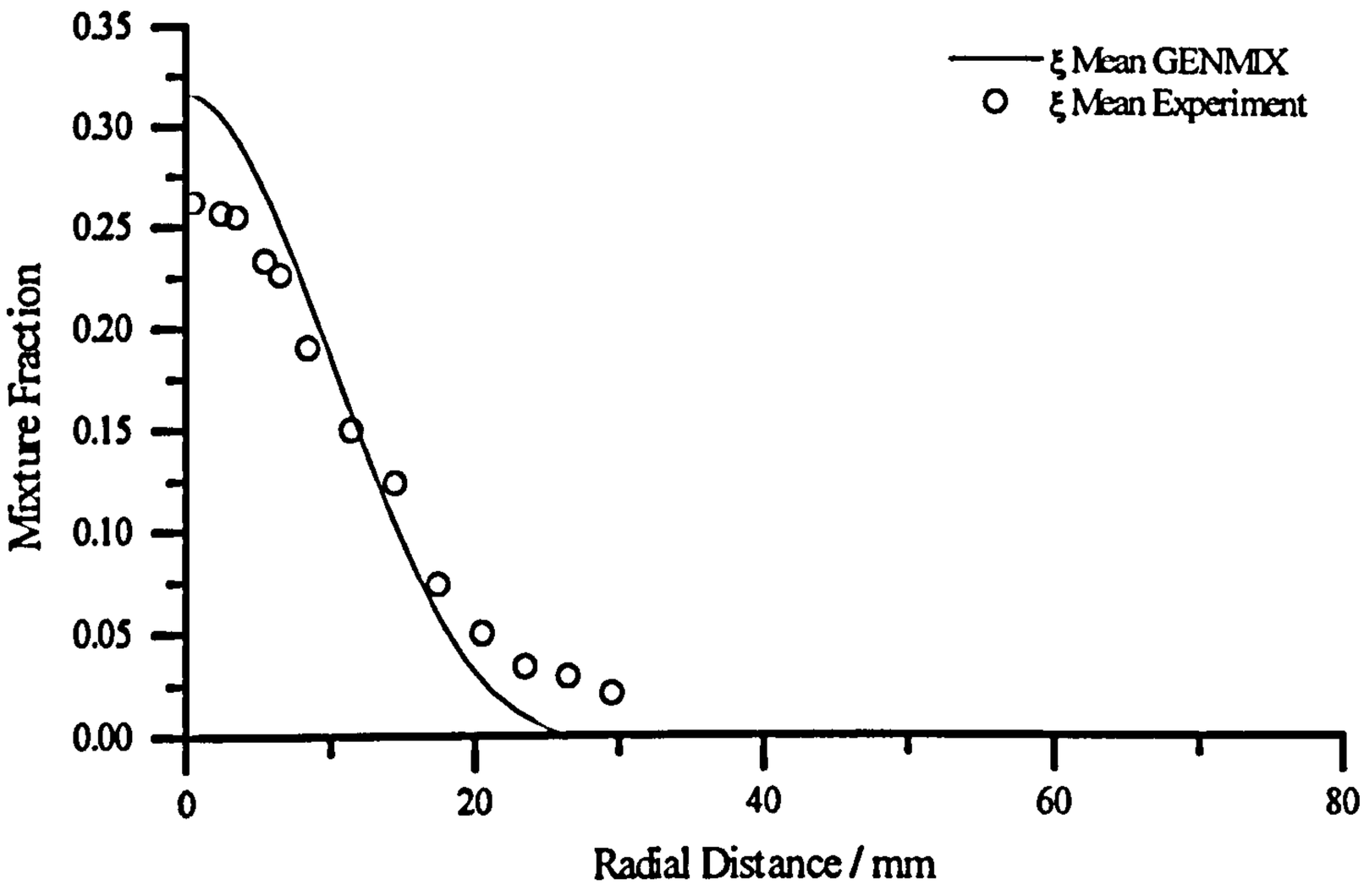

Figure 5.5d. Radial GENMIX data compared with experiment for the 1 atm methane flame at 150 mm above the burner exit. Calculation details as above.

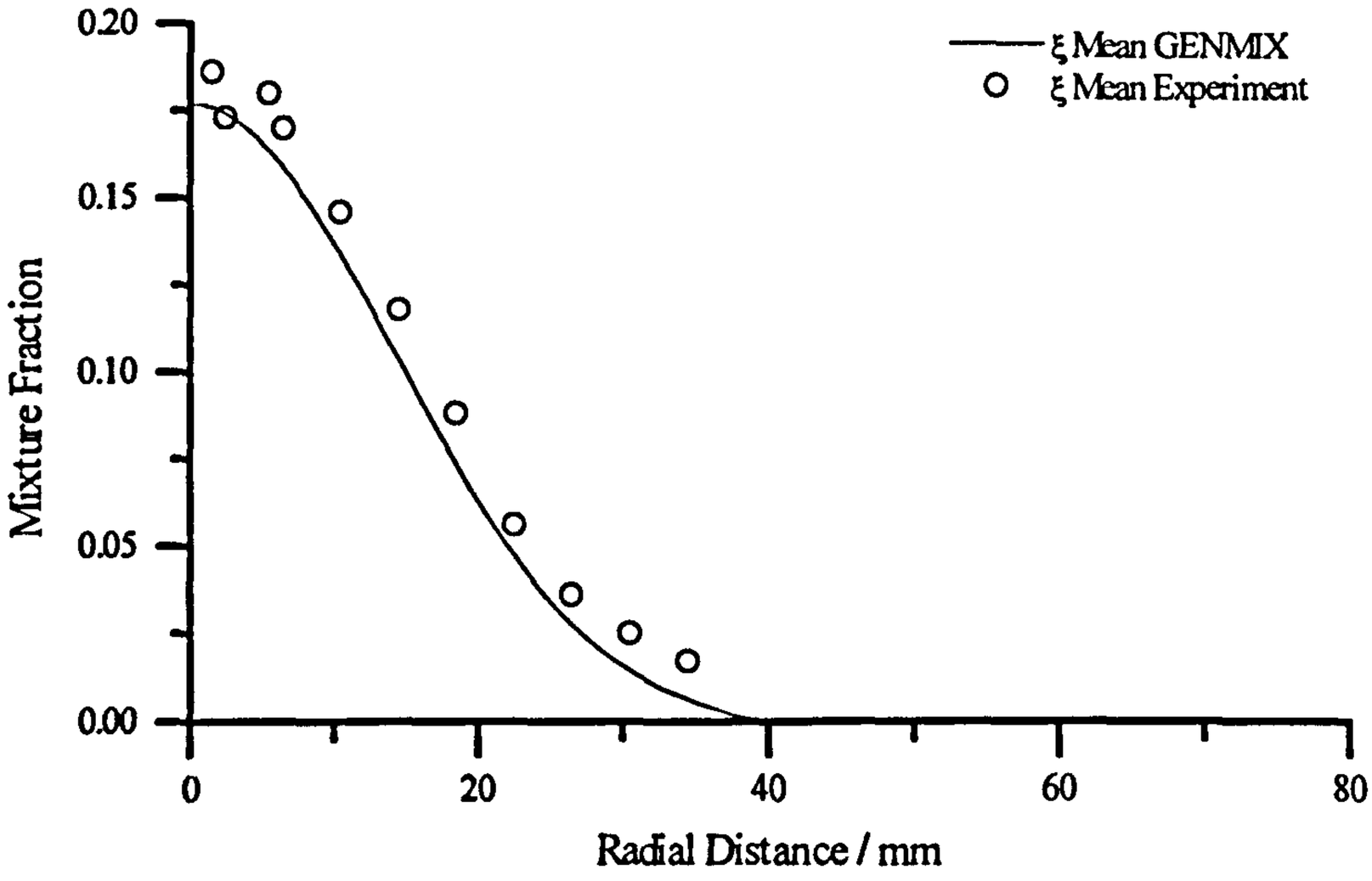

Figure 5.5e. Radial GENMIX data compared with experiment for the 1 atm methane flame at 250 mm above the burner exit. Calculation details as above.

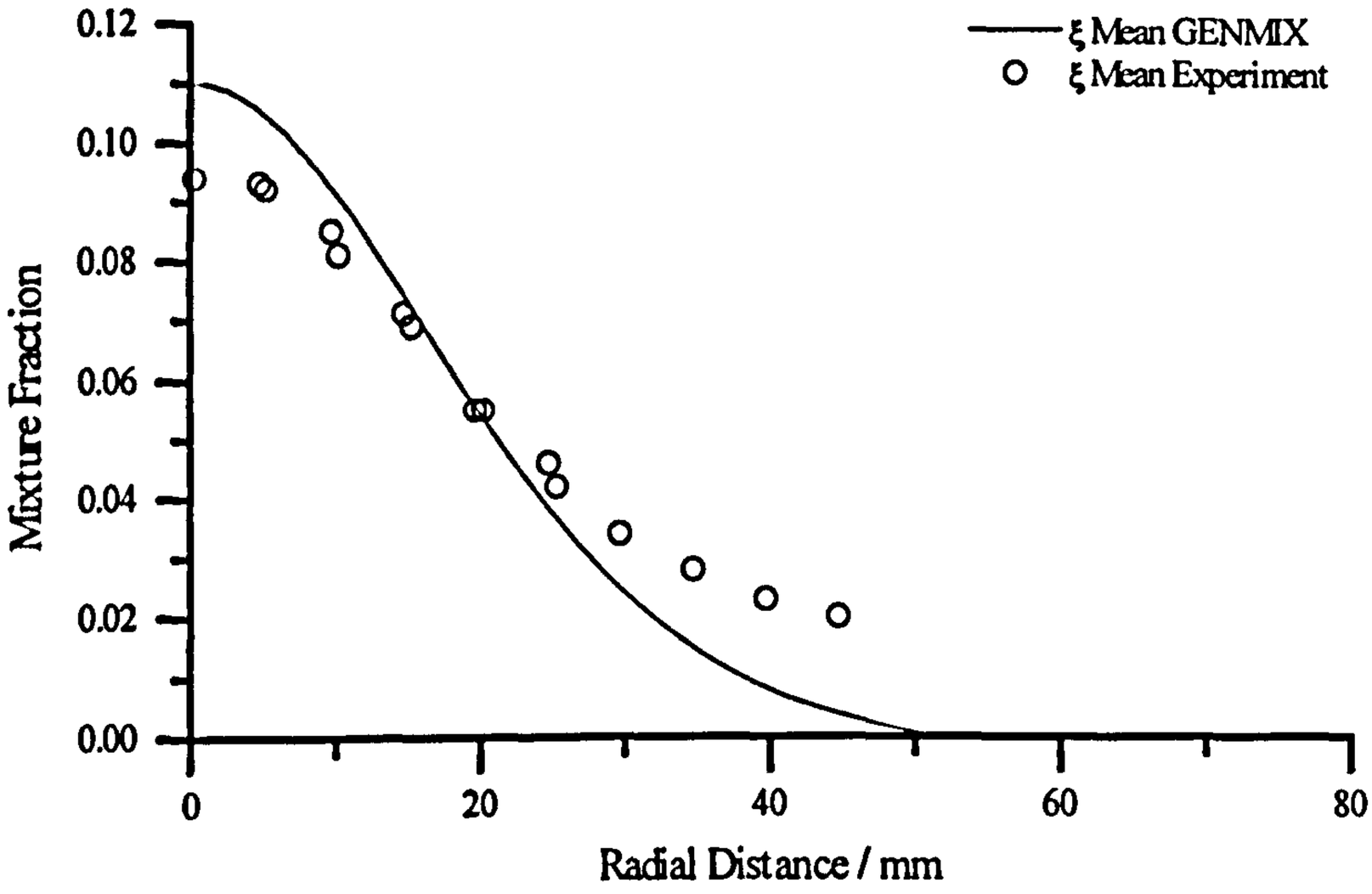

Figure 5.5f. Radial GENMIX data compared with experiment for the 1 atm methane flame at 350 mm above the burner exit. Calculation details as above.

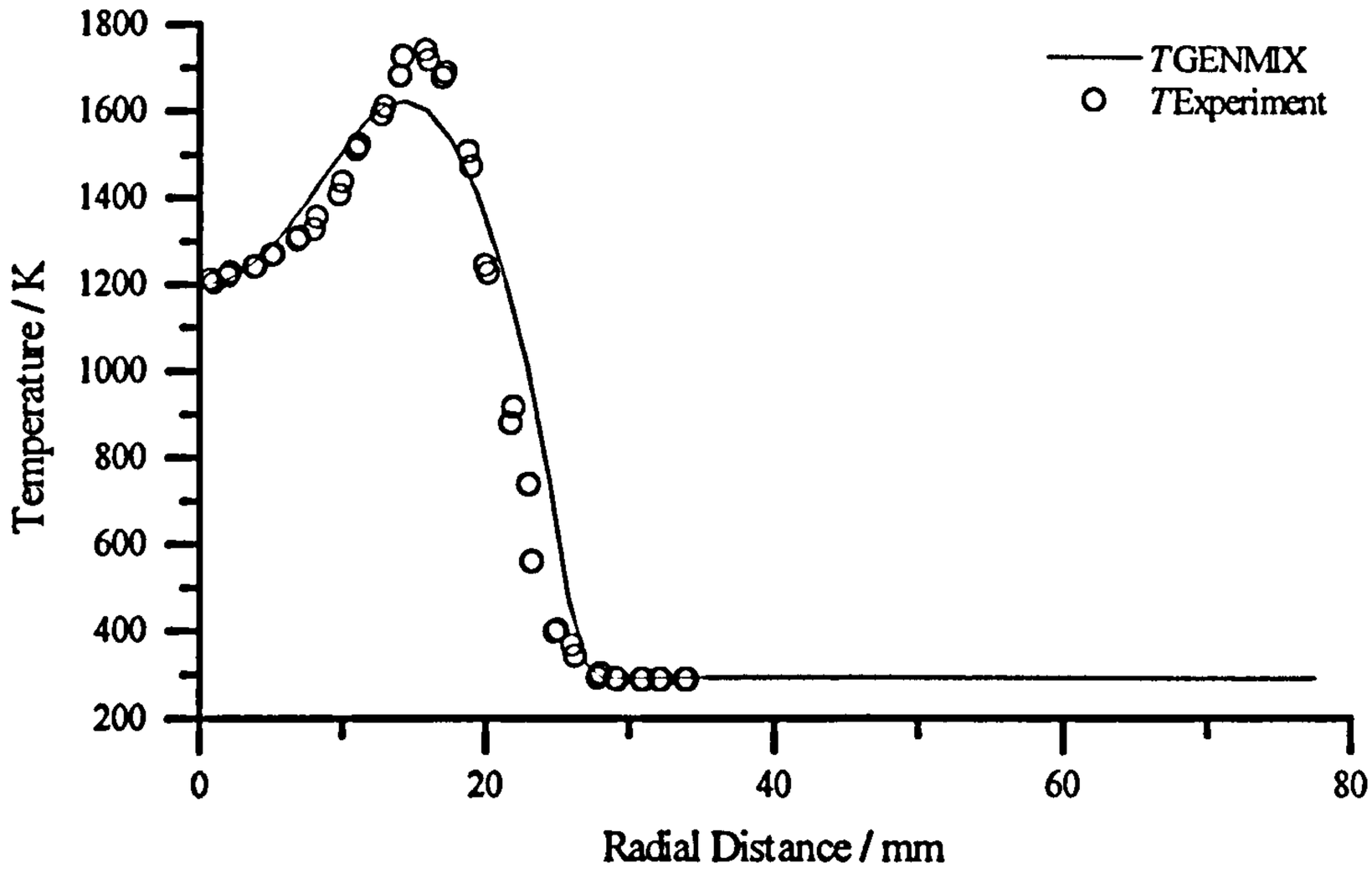

Figure 5.5g. Radial GENMIX data compared with experiment for the 1 atm methane flame at 150 mm above the burner exit. Calculation details as above.

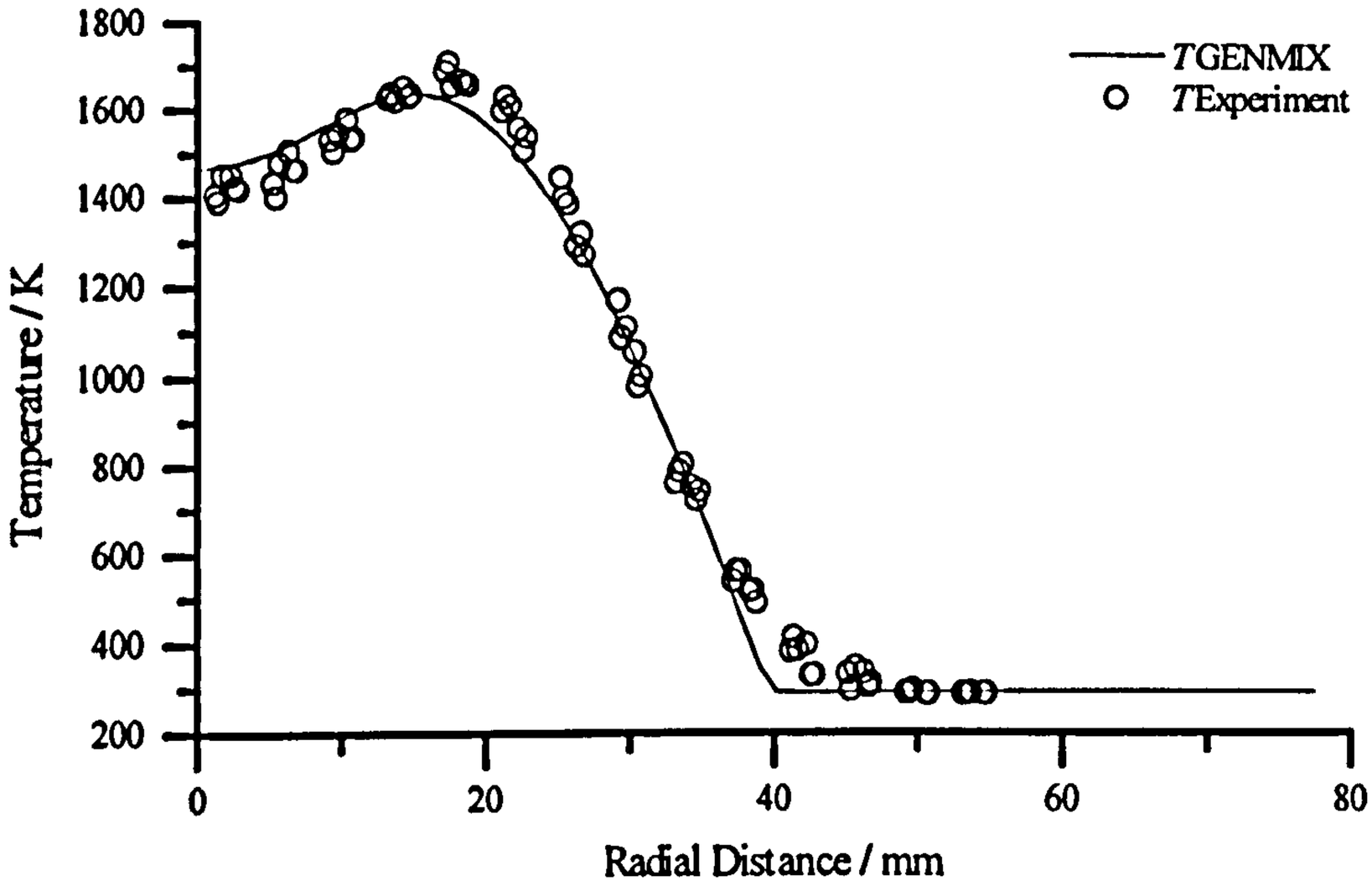

Figure 5.5h. Radial GENMIX data compared with experiment for the 1 atm methane flame at 250 mm above the burner exit. Calculation details as above.

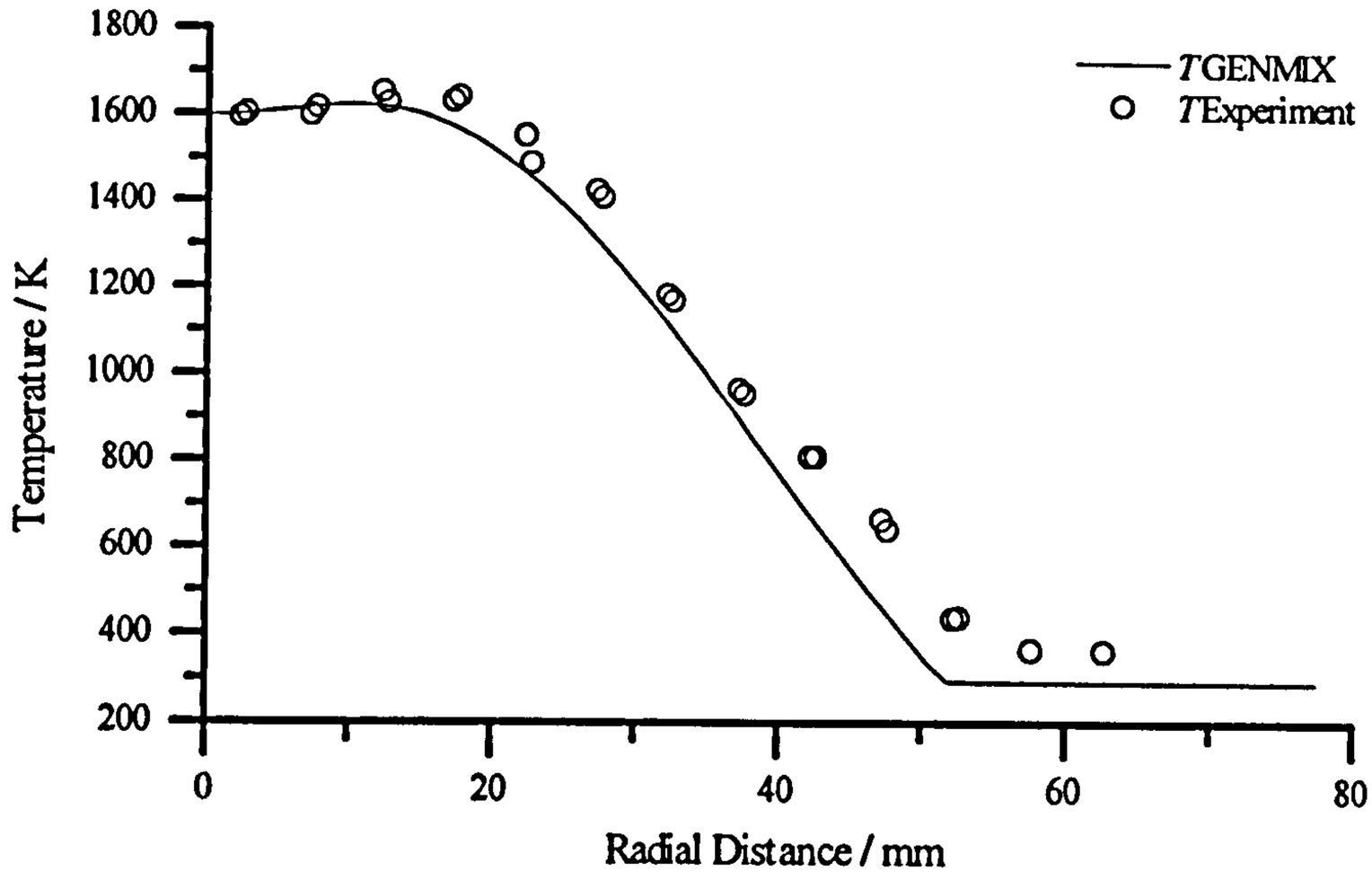

Figure 5.5i. Radial GENMIX data compared with experiment for the 1 atm methane flame at 350 mm above the burner exit. Calculation details as above.

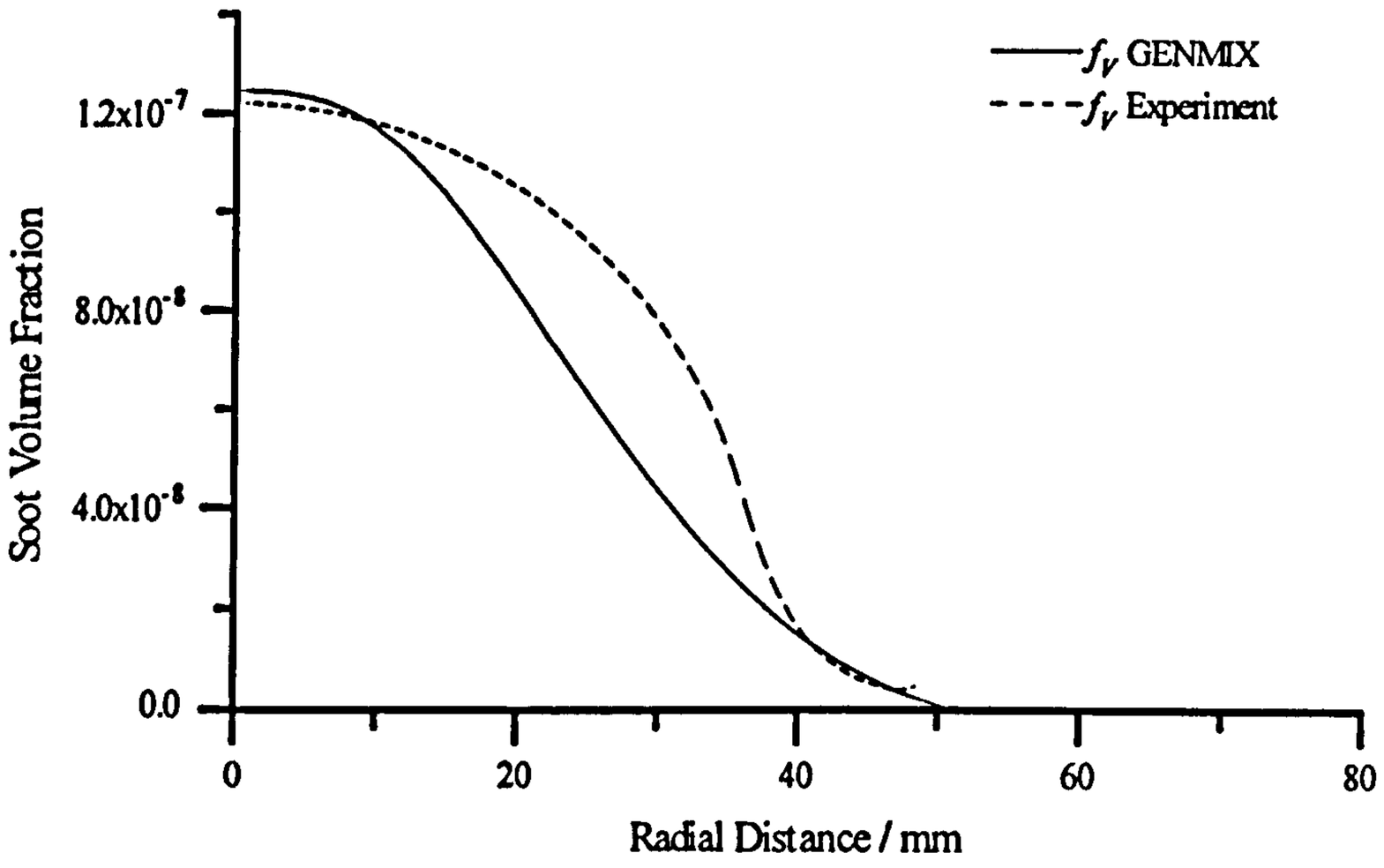

Figure 5.5j. Radial GENMIX data compared with experiment for the 1 atm methane flame at 350 mm above the burner exit. Calculation details as above.

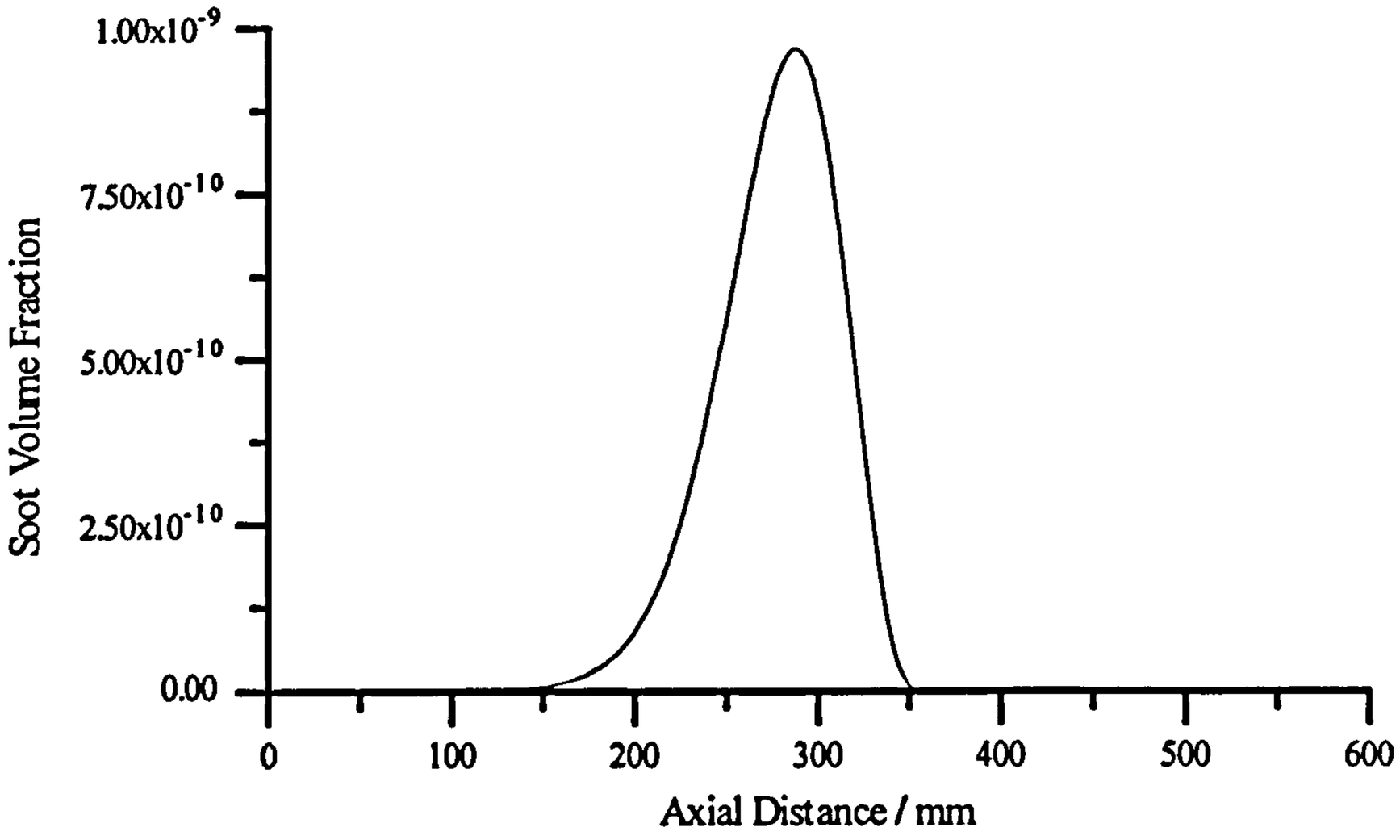

Figure 5.6. Axial evolution of the soot volume fraction given by GENMIX for the 1 atm flame. This calculation is identical to that in the previous figure except uncorrelated oxidation is included.

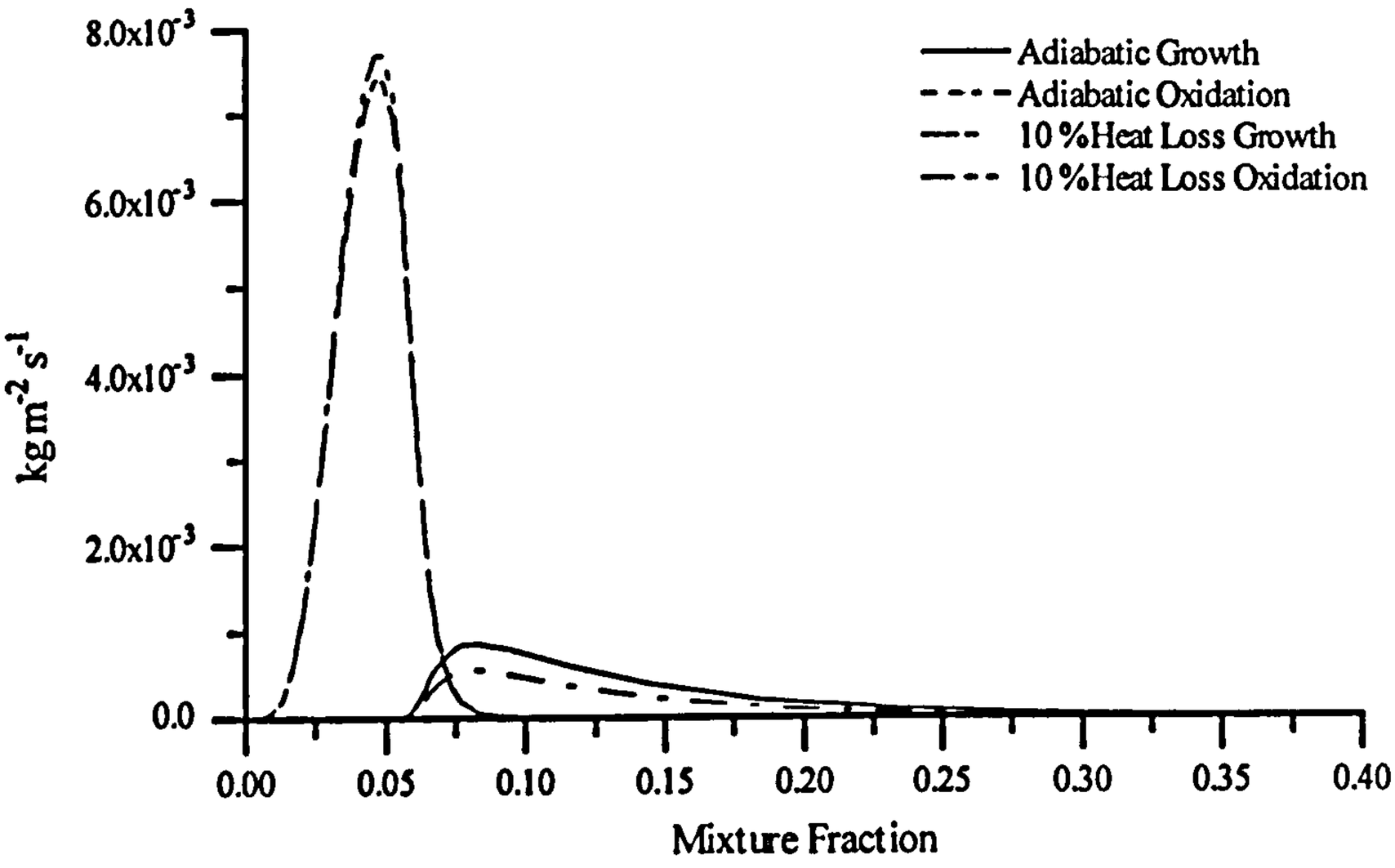

Figure 5.7. Comparison of the specific soot surface growth and oxidation functions at 1 atm.

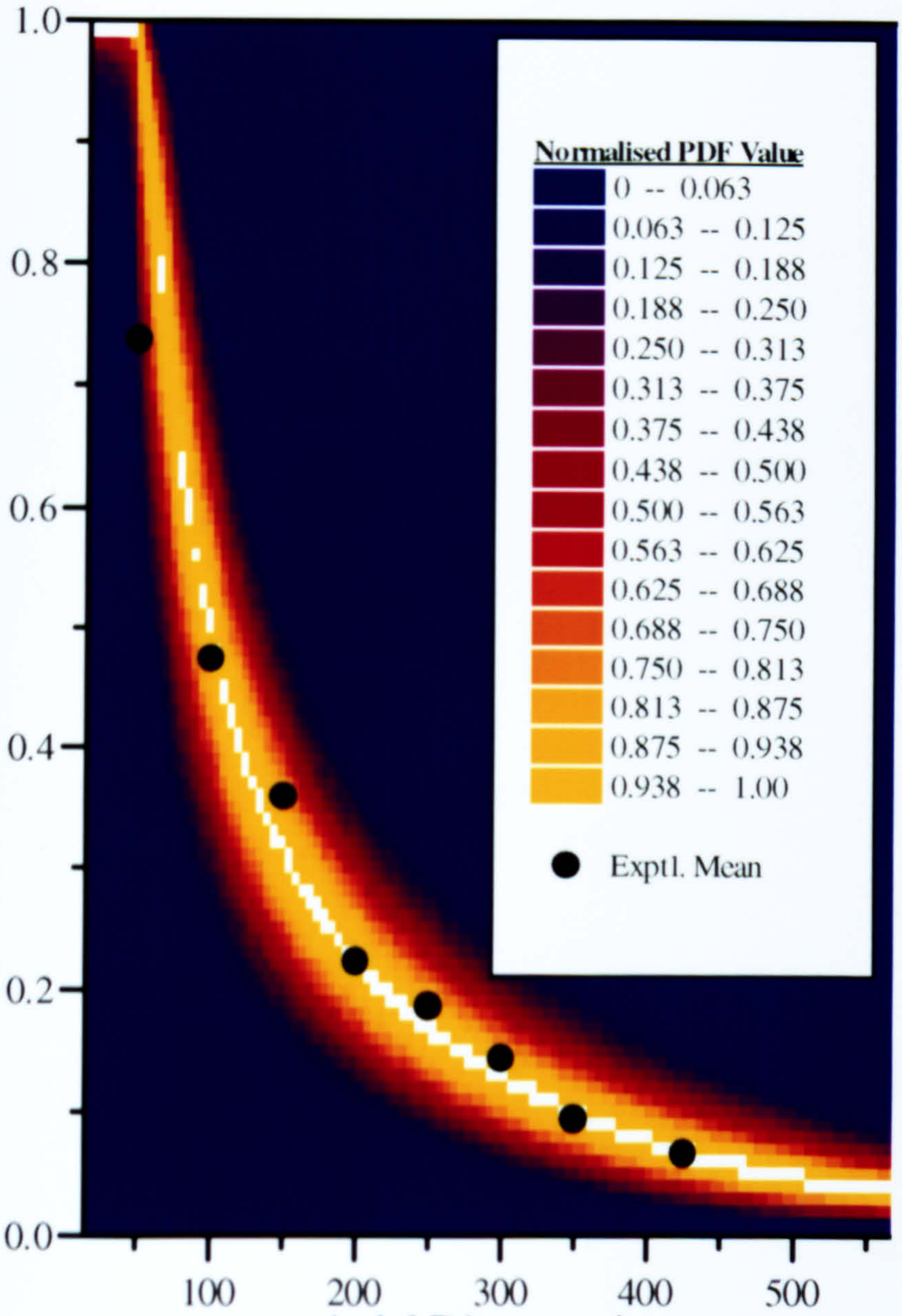

Figure 5.8. Axial evolution of the normalised mixture fraction PDF. Colours represent normalised PDF values.

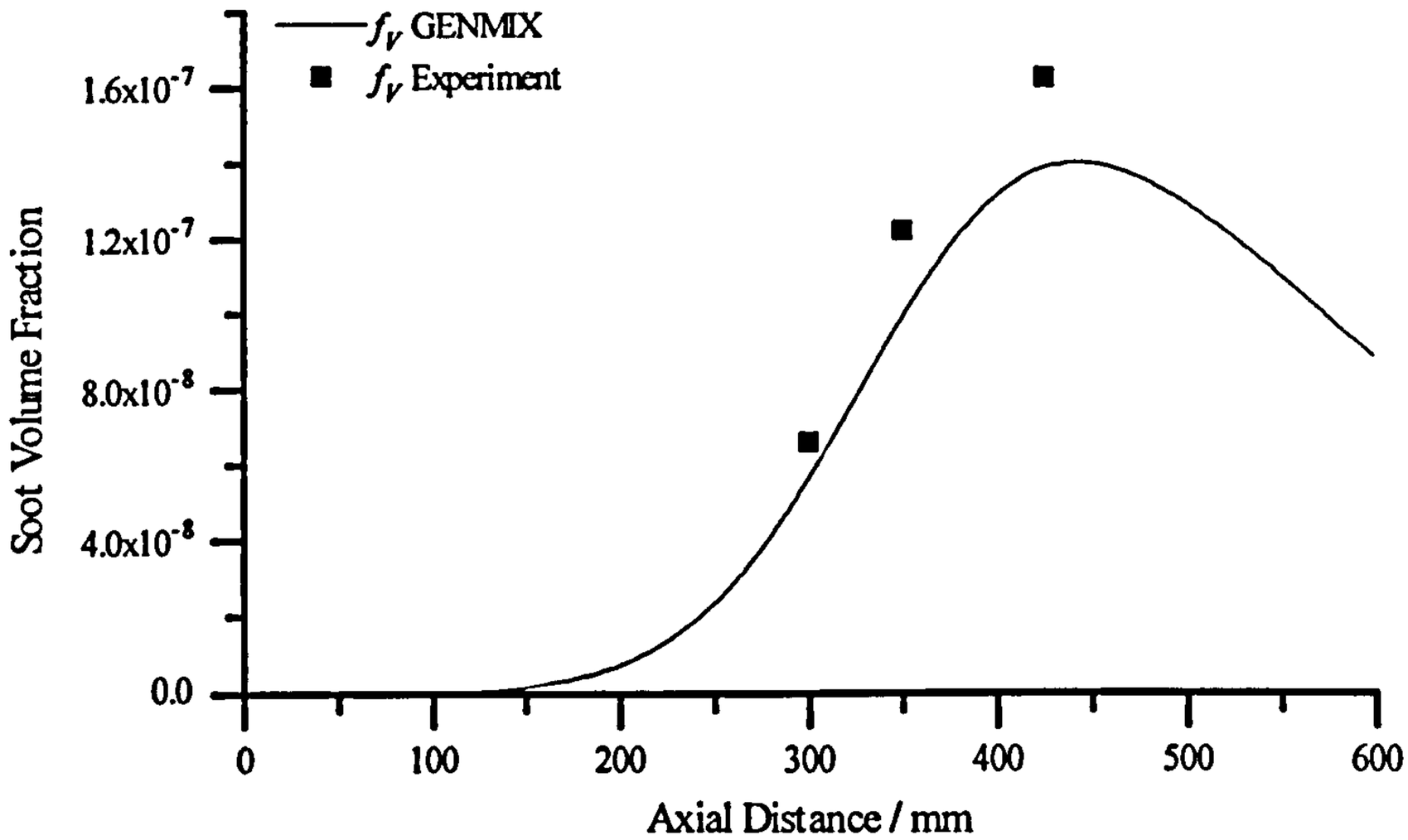

Figure 5.9. Axial evolution of the soot volume fraction in the 1 atm flame. The figure shows the result of using an uncorrelated oxidation term multiplied by a constant factor (0.015).

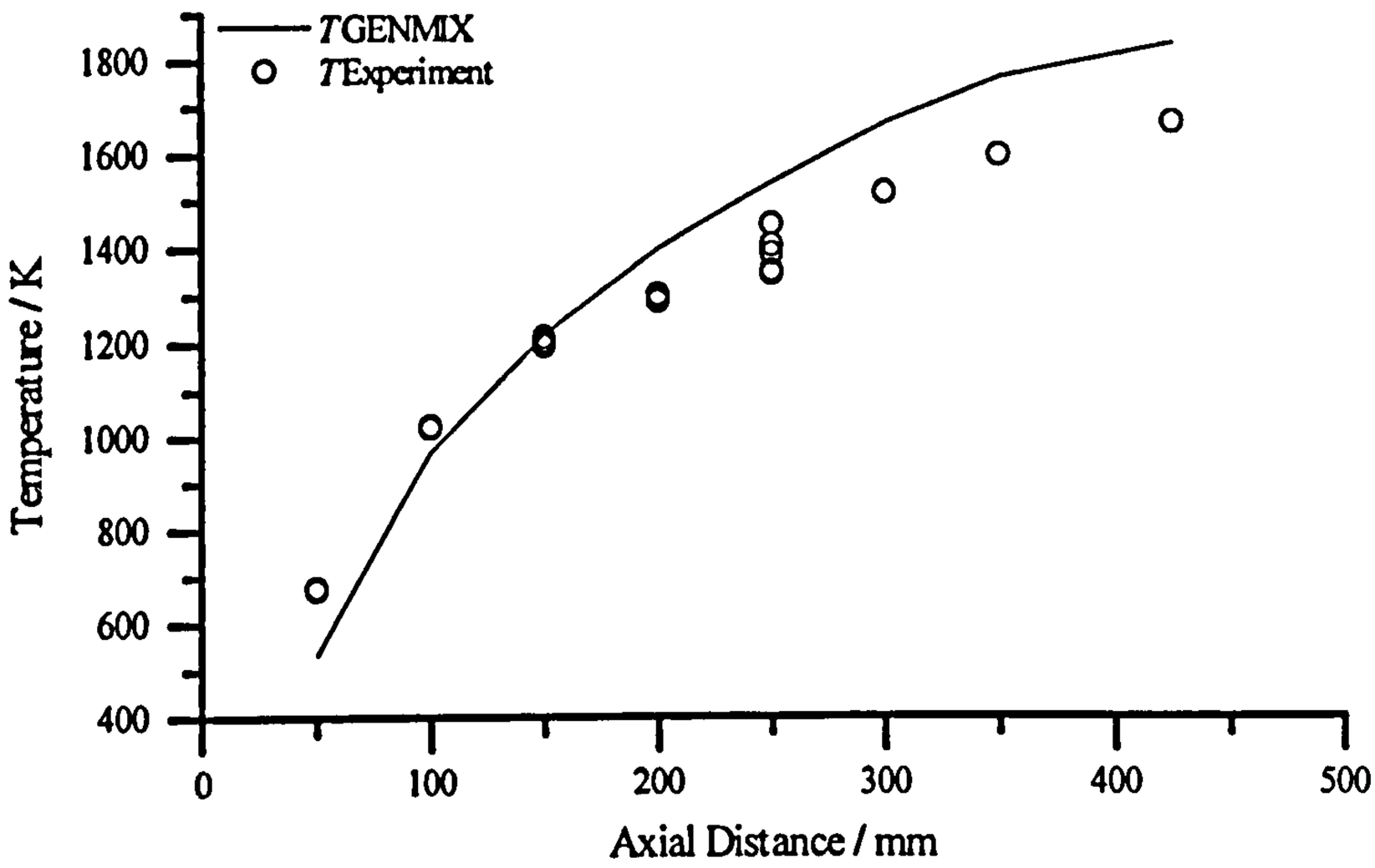

Figure 5.10a. Centreline GENMIX temperature data for the 1 atm flame. The figure shows the result of an adiabatic flame calculation.

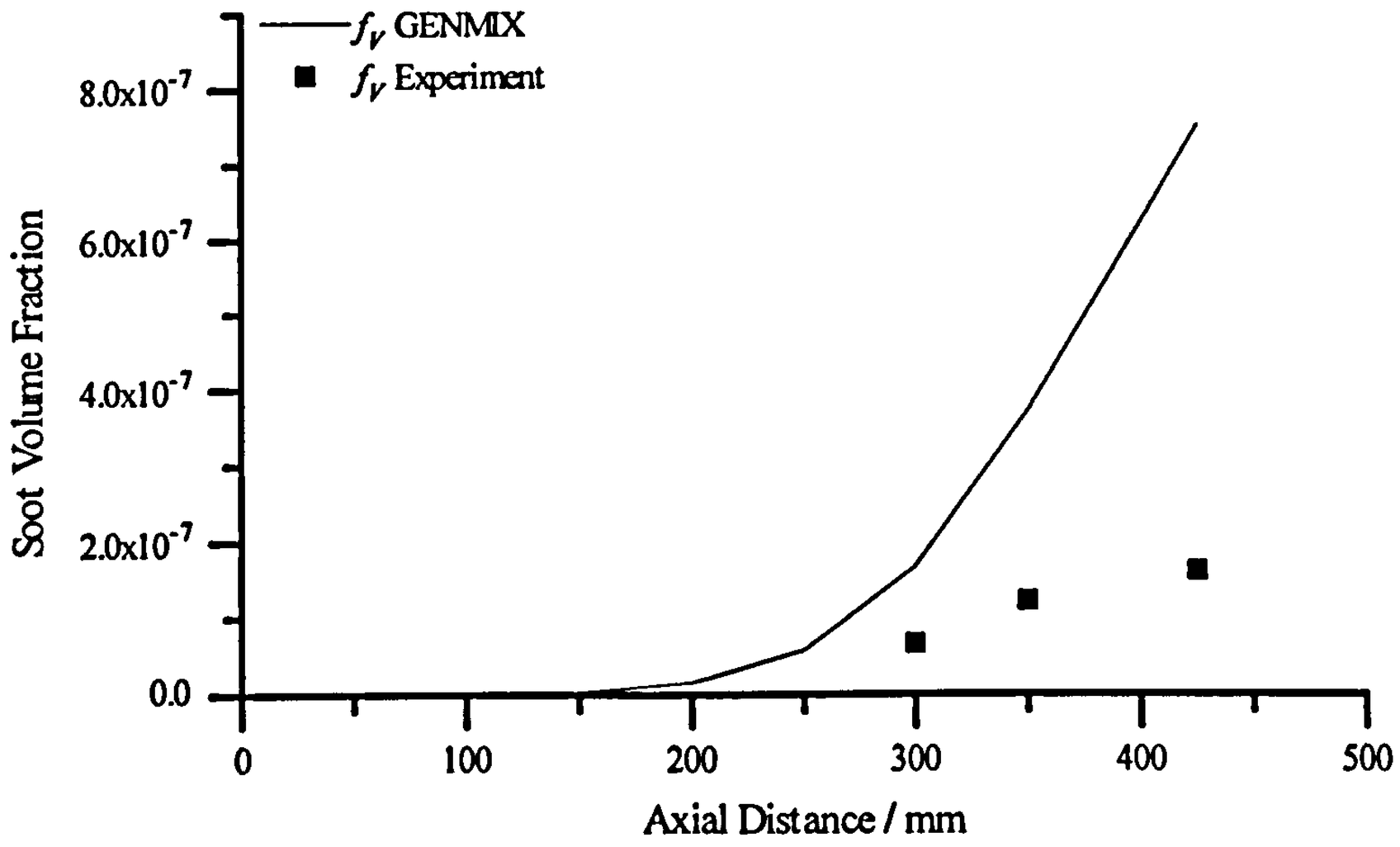

Figure 5.10b. Centreline GENMIX data for the 1 atm flame. Figure shows the effect of omitting the radiative heat loss on the soot volume fraction. The uncorrelated form of the soot model is used with constant set 7. Soot oxidation is omitted.

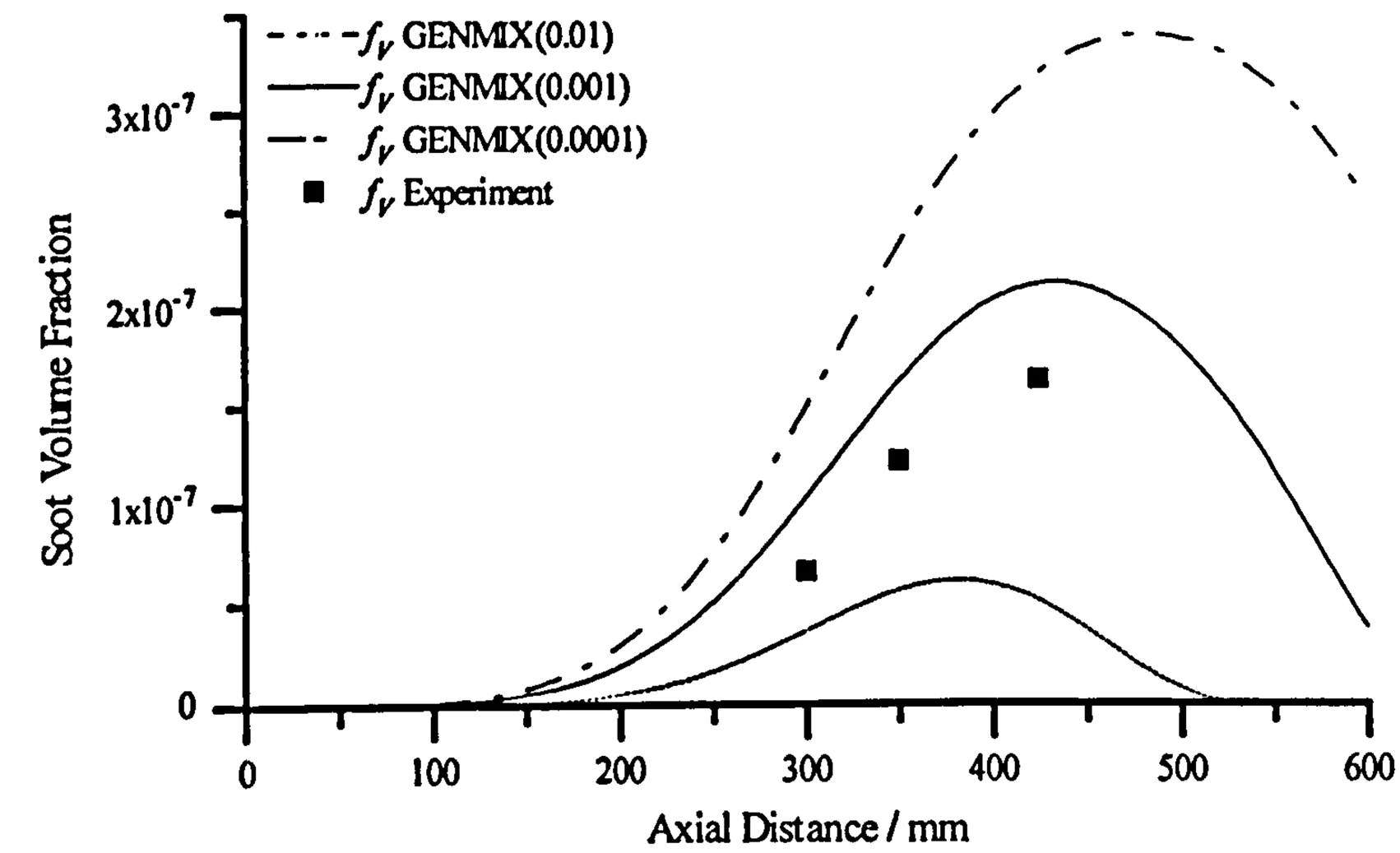

Figure 5.11. Axial evolution of the soot volume fraction in the 1 atm flame given by GENMIX using the fully correlated model of soot growth and oxidation. The figures in brackets shown in the legend indicate the threshold value used in the model.

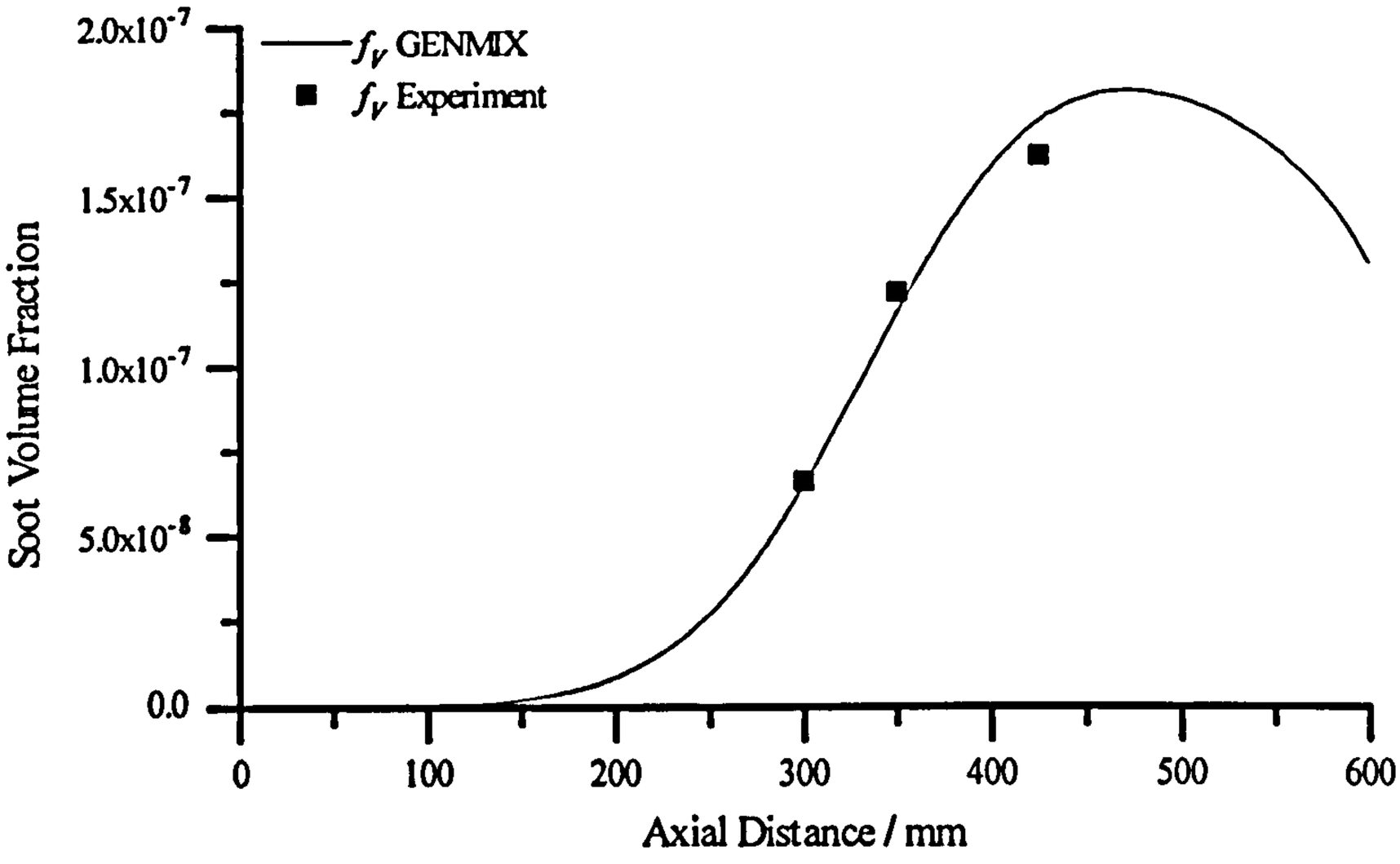

Figure 5.12. Centreline GENMIX data for the 1 atm flame. The soot model uses the uncorrelated form for the surface growth term and the conditional oxidation term suggested by Syed (1990).

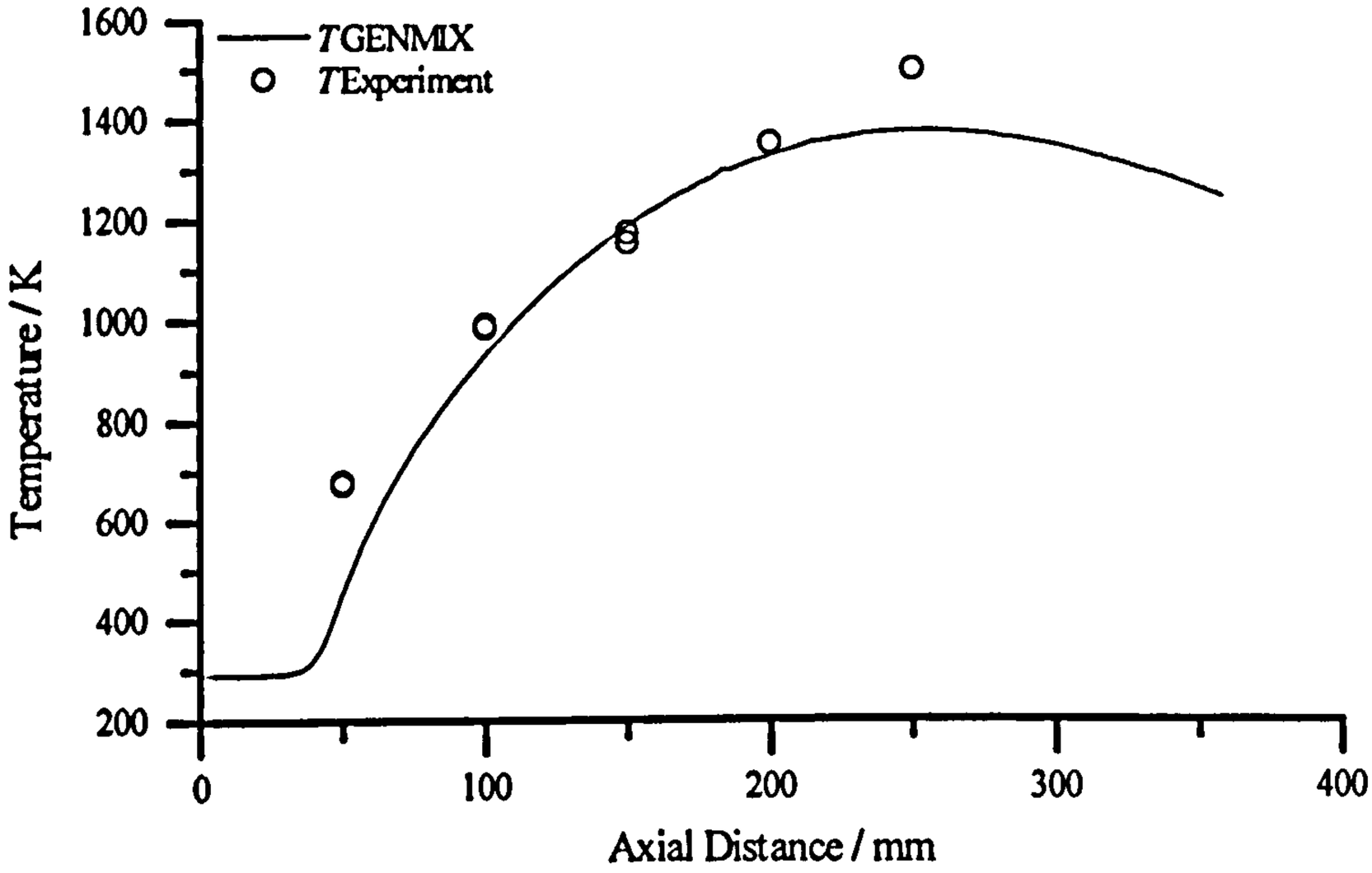

Figure 5.13a. Centreline temperature data for the 3 atm flame. Radiative loss is included. The soot model uses constant set 7 with the uncorrelated form for the surface growth term. Soot oxidation is omitted.

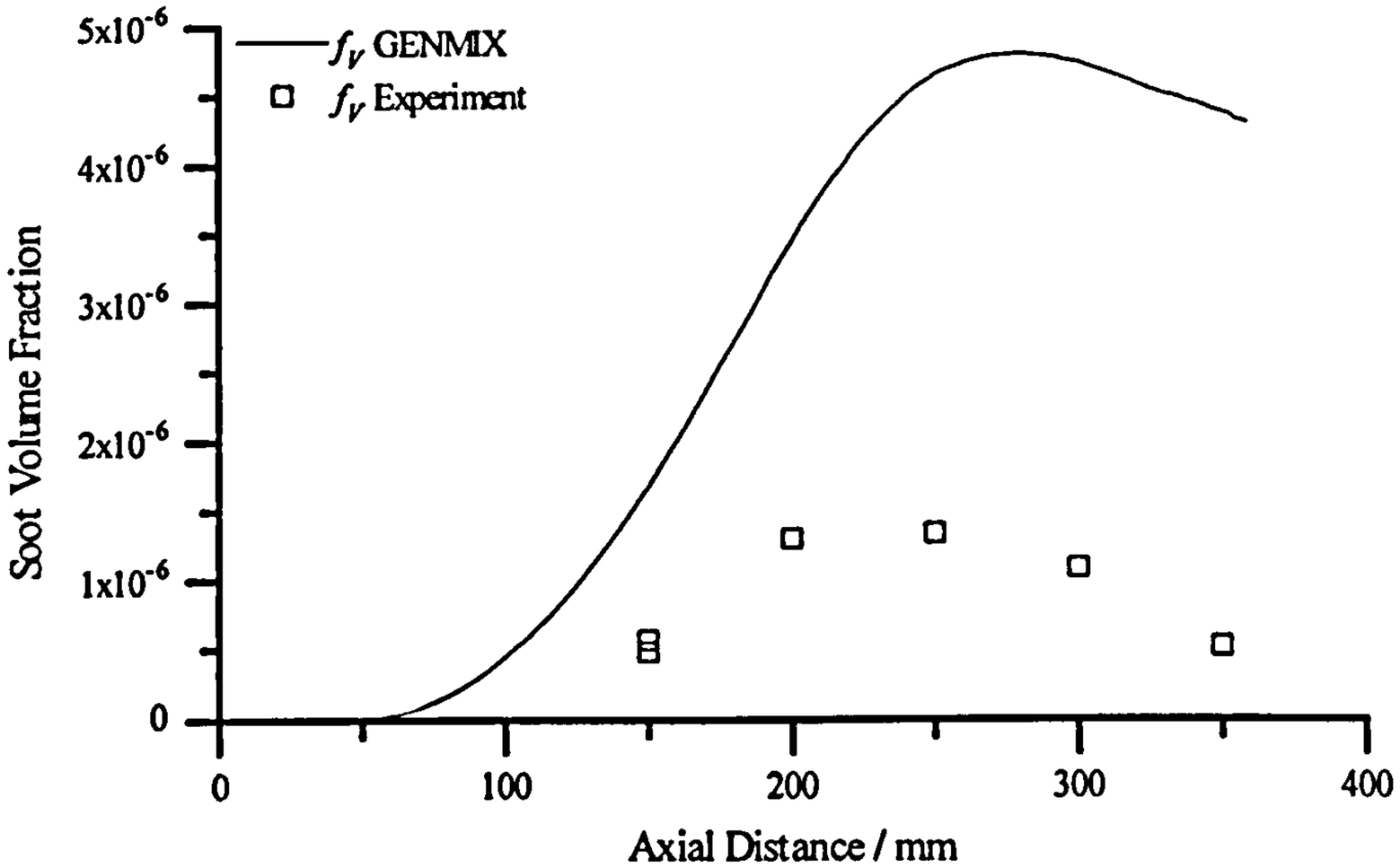

Figure 5.13b. Axial evolution of the soot volume fraction for the 3 atm flame. Calculation details as above.

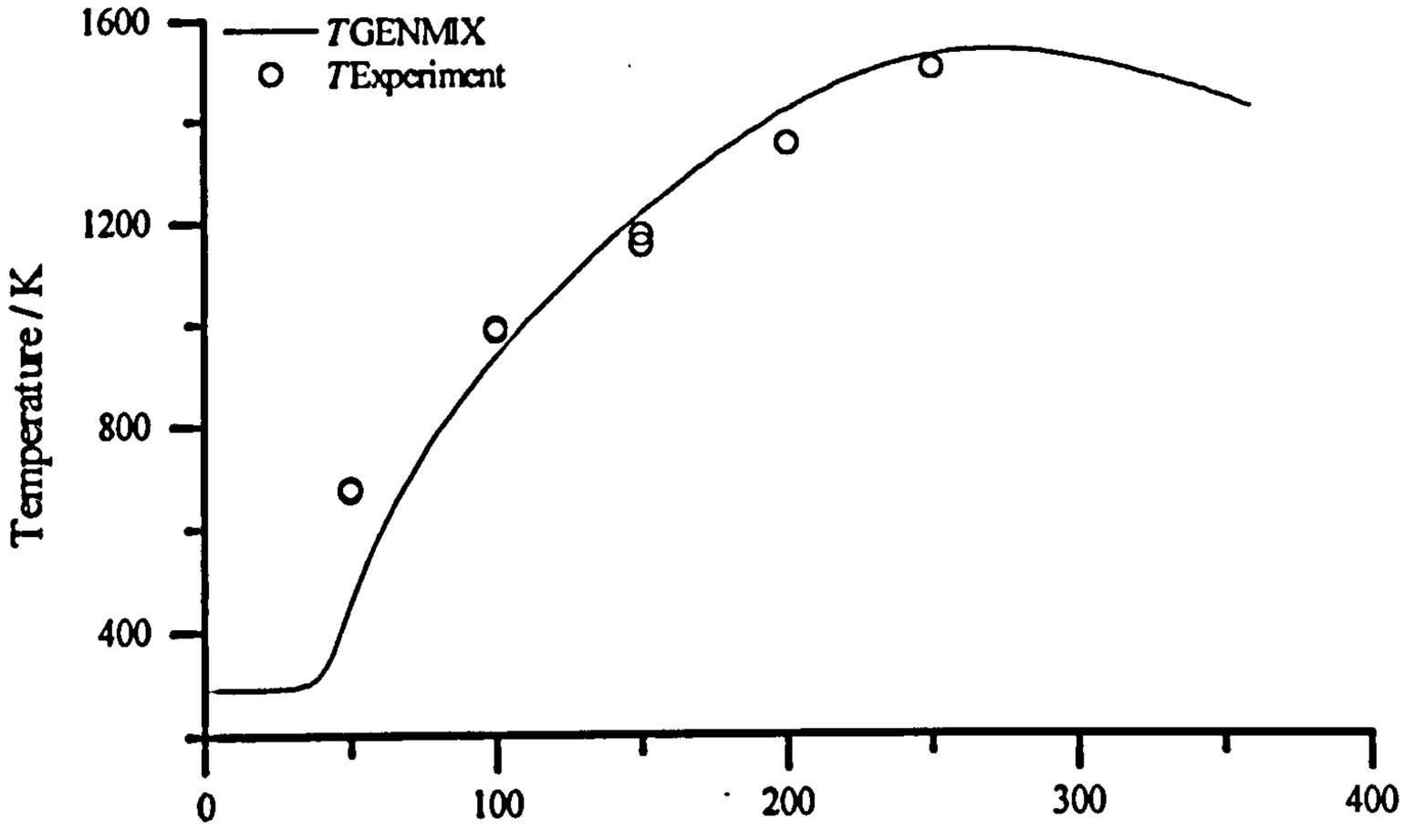

Figure 5.14a. Centreline GENMIX data for the 3 atm flame compared with experiment. Radiative loss is included in this calculation. The uncorrelated form of the soot model is used, with constant set 2. Uncorrelated soot oxidation is also included with a multiplying factor of 0.015.

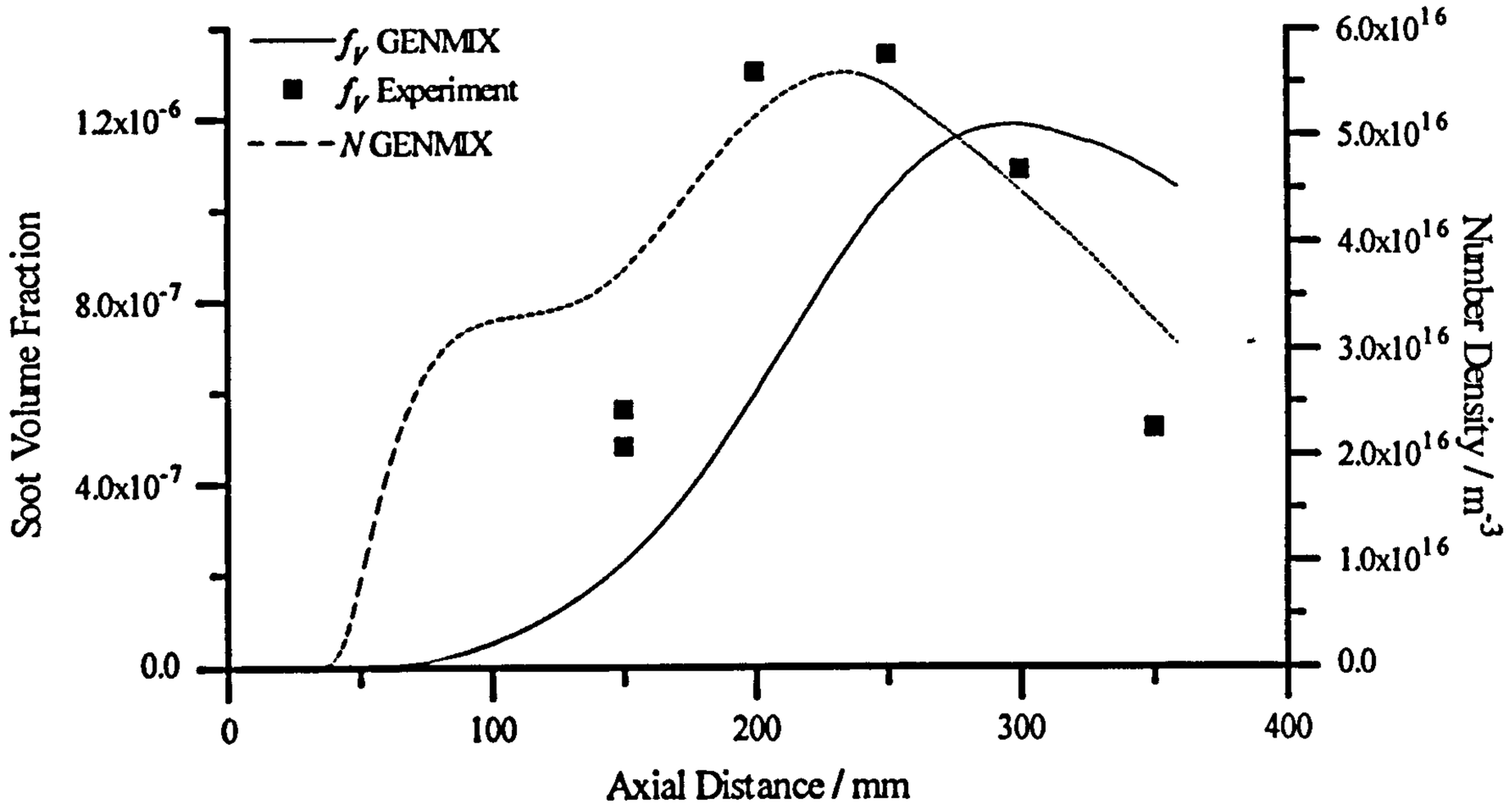

Figure 5.14b. Centreline GENMIX data for the 3 atm flame compared with experiment. Calculation details as above.

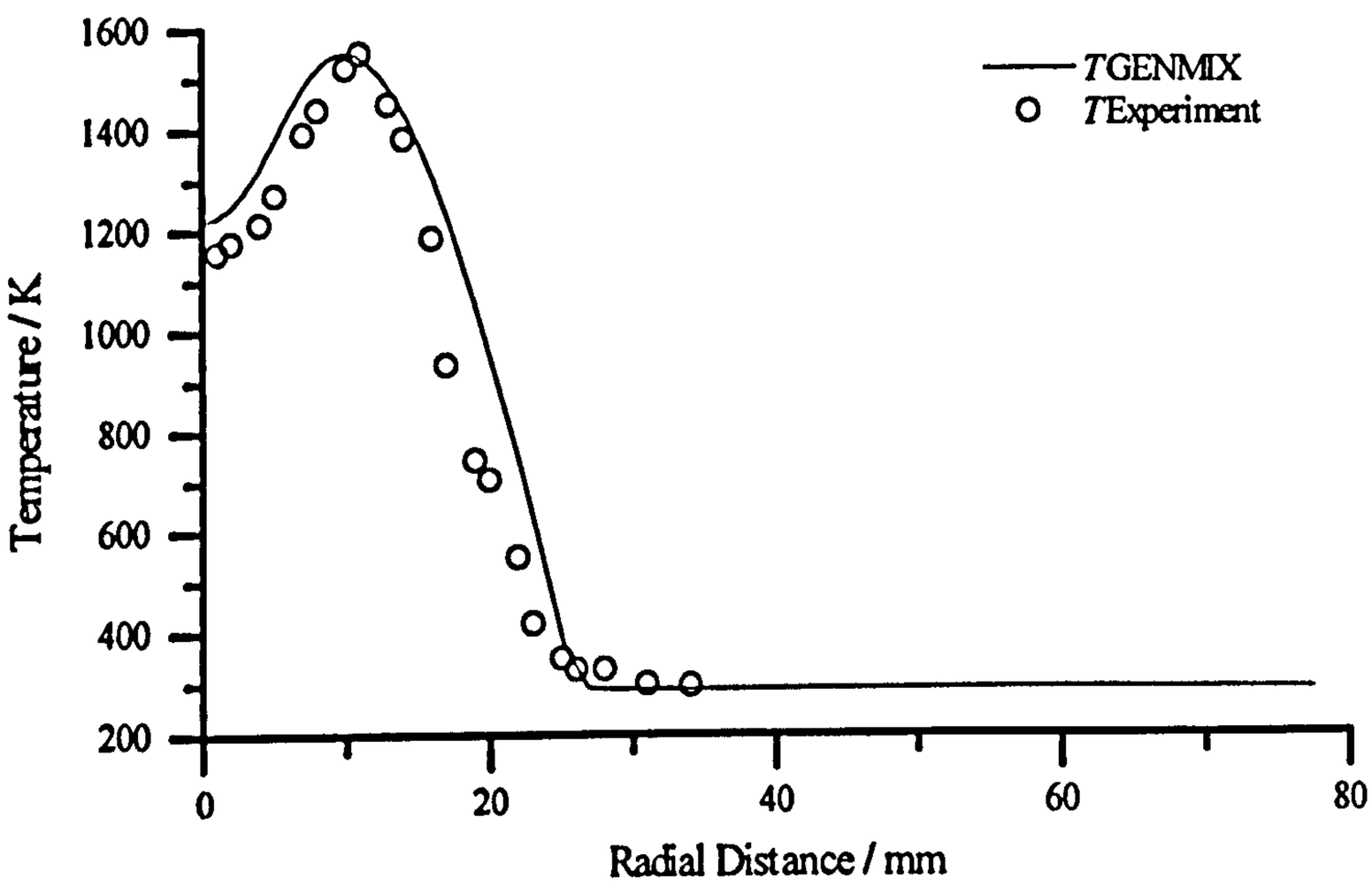

Figure 5.14c. Radial GENMIX data for the 3 atm flame compared with experiment 150 mm above the burner exit. Calculation details as above.

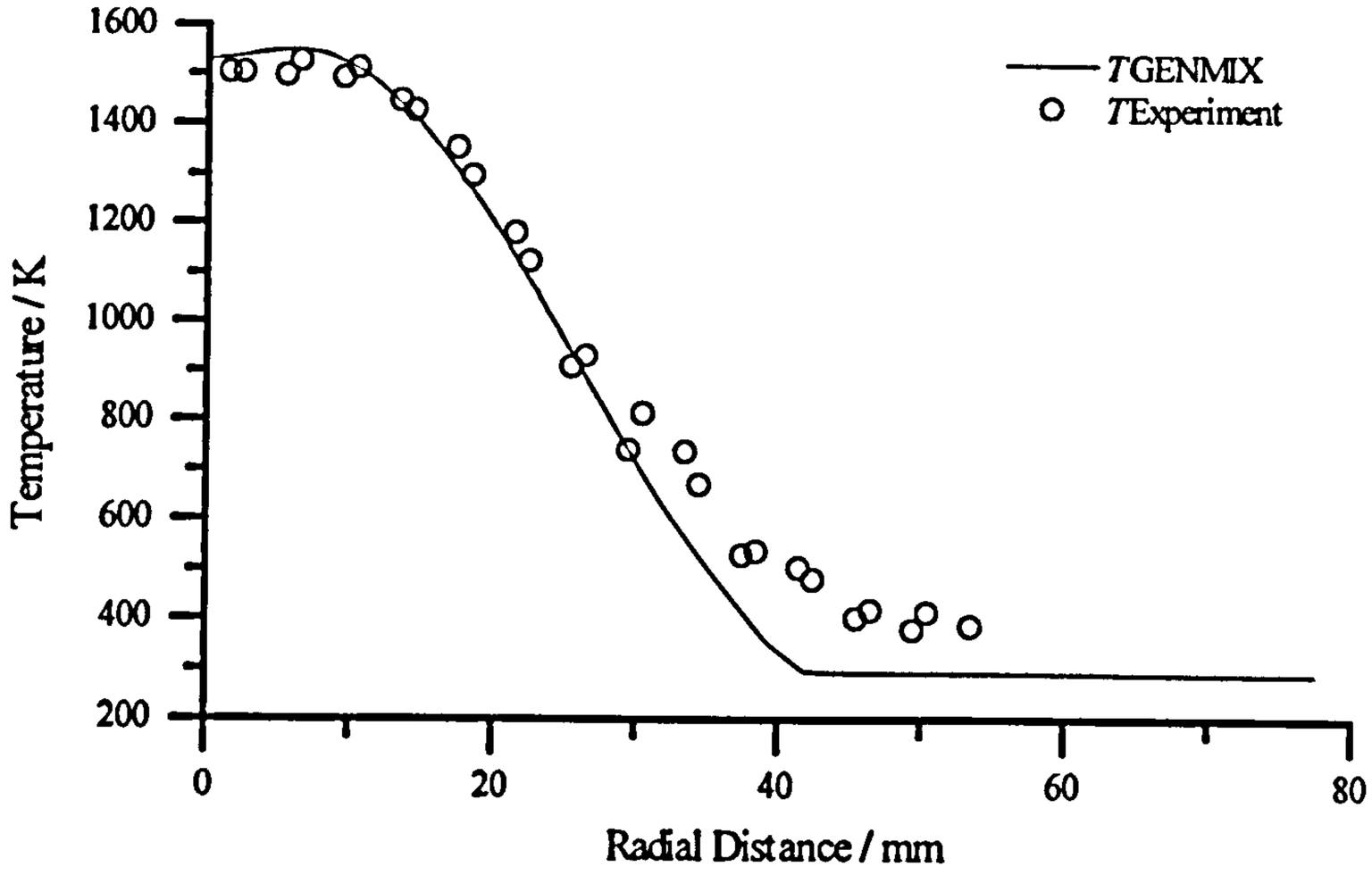

Figure 5.14d. Radial GENMIX data for the 3 atm flame compared with experiment 250 mm above the burner exit. Calculation details as above.

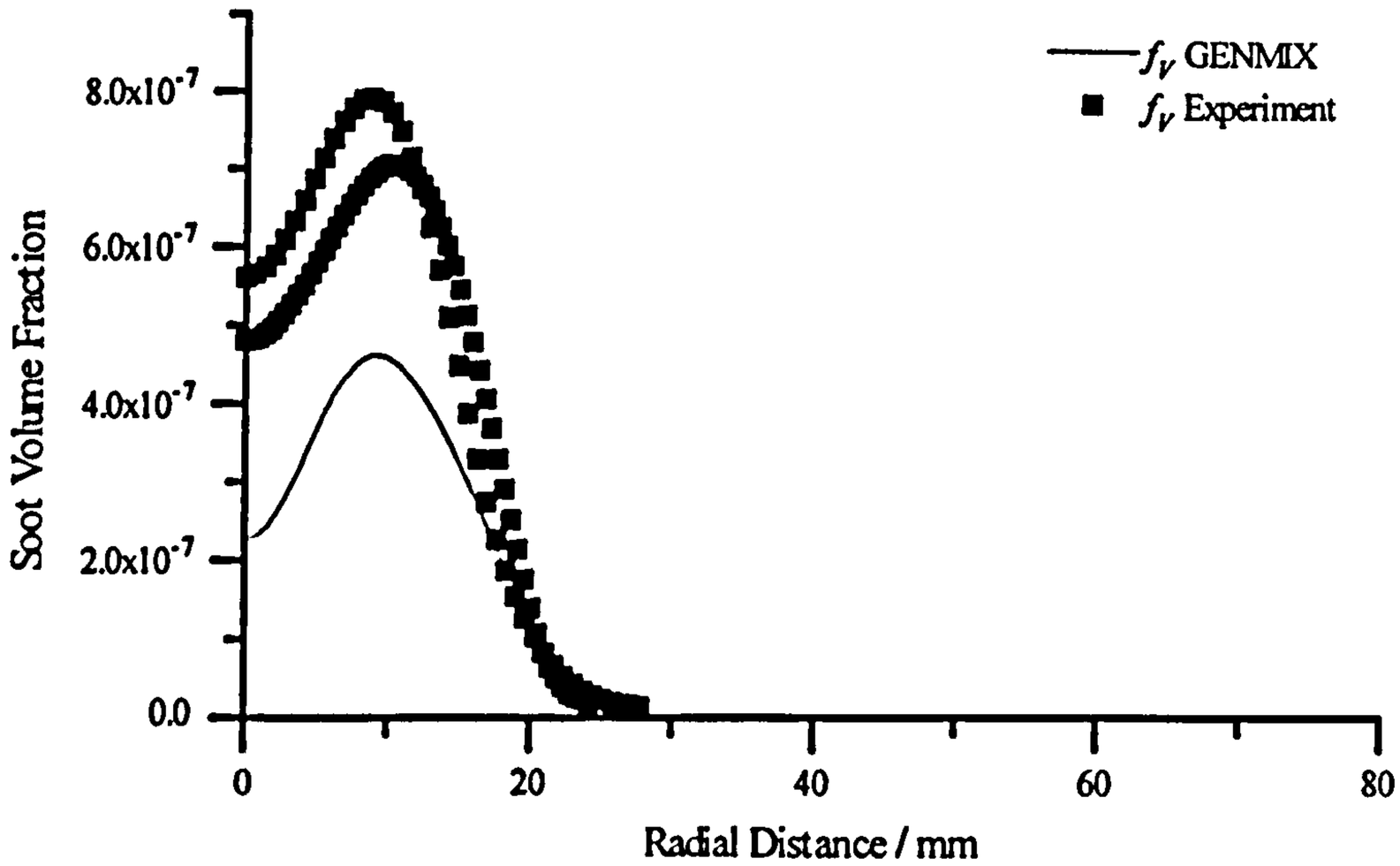

Figure 5.14e. Radial GENMIX data for the 3 atm flame compared with experiment 150 mm above the burner exit. Calculation details as above.

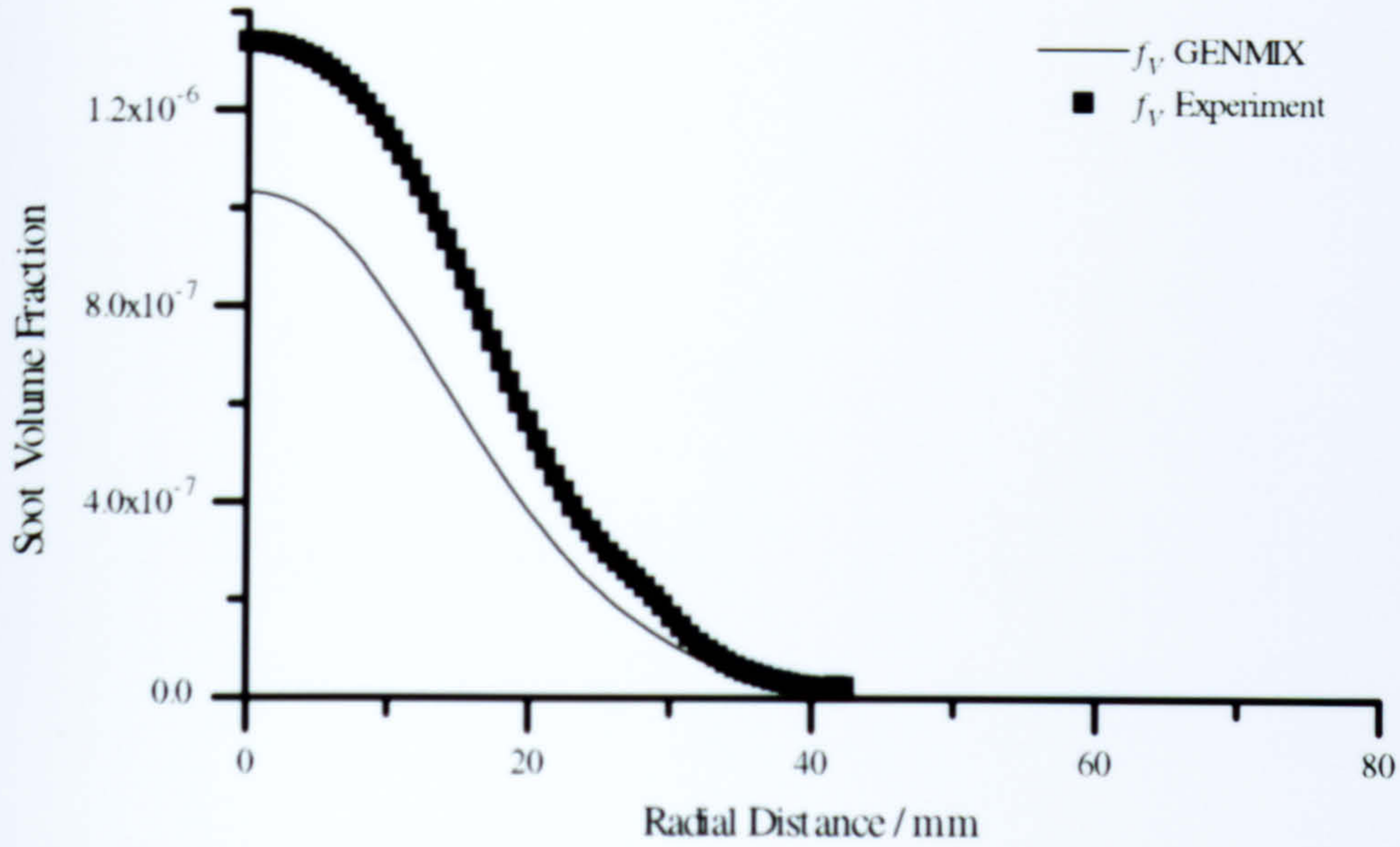

Figure 5.14f. Radial GENMIX data for the 3 atm flame compared with experiment 250 mm above the burner exit. Calculation details as above.

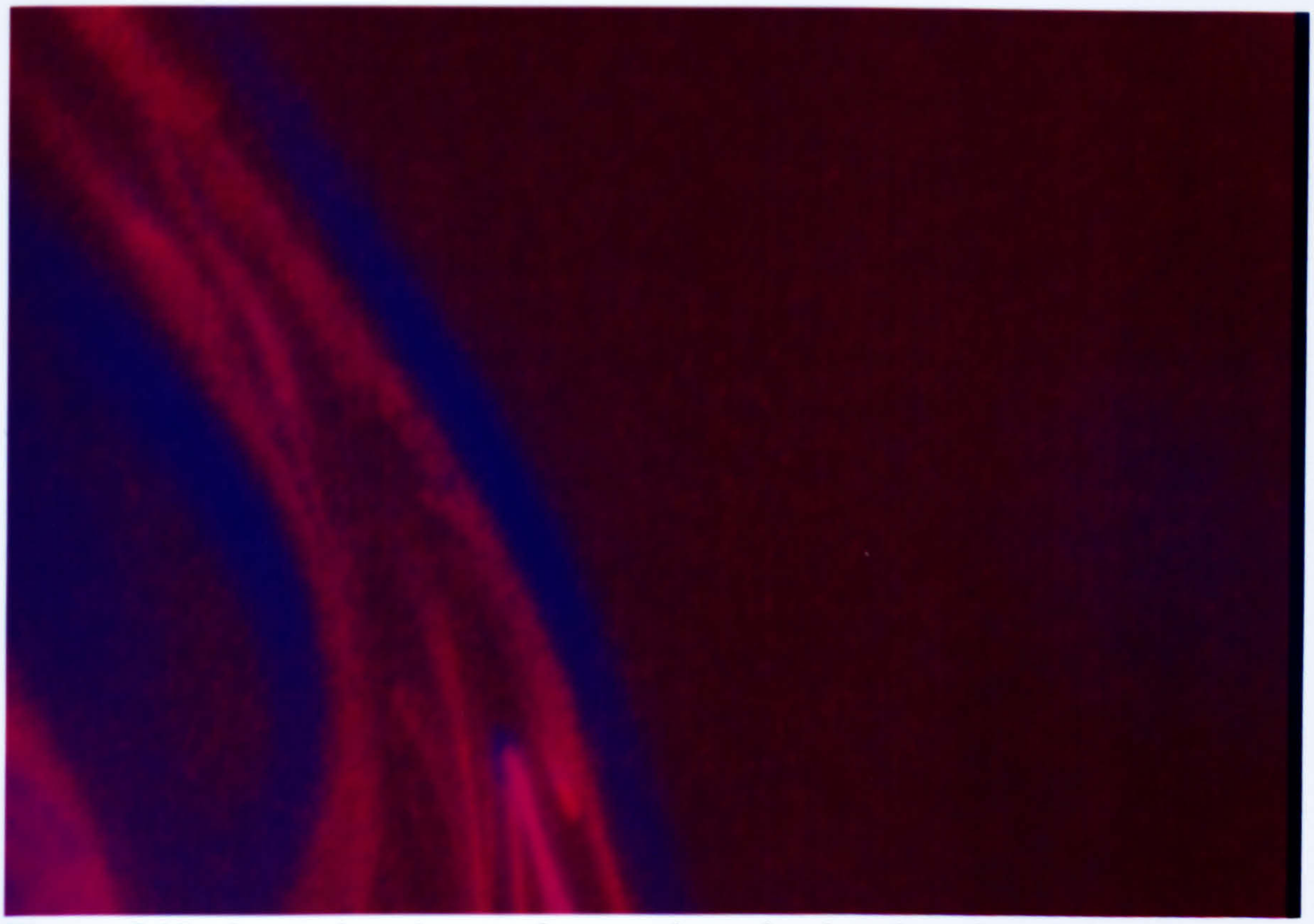

Figure 5.15. Laser sheet image of soot volume fraction (in red) and the OH radical concentration (in blue). Recorded using simultaneous LII and LIF. The image represents a physical area measuring 47.3 by 32.3 mm.

Chapter 6 - Modelling Flame Radiation

6.1 Introduction

The flames studied in this work lose a significant amount of their energy by thermal radiation (approximately 20 % for the 1 atm flame and 40 % for the 3 atm flame) and this is typical of most hydrocarbon fuelled flames. Clearly, an accurate predictive capability for flame radiation is desirable for many applications, ranging from hazard assessment to design of practical devices. The work embodied in this chapter, therefore, seeks to demonstrate a predictive capability for the detailed spectral emission from such hydrocarbon fuelled flames.

Flame radiation is a complex phenomena encompassing several issues. Thermal radiation is emitted by some of the gaseous products of combustion as well as soot, if present, and the hydrocarbon fuel. Gaseous radiation is limited to discrete wavelength bands corresponding to changes in the internal energy levels of the gas molecules. Joint transitions in the vibrational / rotational energy levels of these molecules at typical flame temperatures give rise to the banded emission structure. Soot particles radiate continuously across the spectrum. Hence, soot may be considered as a 'grey body' radiator. Therefore, to predict flame radiation with any accuracy the concentrations of these radiating species must be known in addition to their radiative properties. The prediction of thermal radiation is complicated in most practical situations by the presence of turbulence. Interactions between the flame radiation and the turbulence may become important. This becomes apparent by considering the basic equation of radiative emission

$$\bar{E} = \sigma \overline{\epsilon T^4} \tag{6.1}$$

where $\bar{E}$ is the mean total emissive power. The formulation of $\overline{\epsilon T^4}$ requires that the joint statistics of the radiating species and the temperature are known. This issue has already

been discussed in chapter 5, and is certainly feasible for the gaseous species and the temperature through the conserved scalar / presumed PDF combustion model, but is less practical when considering the soot. Arguably, the effect of such turbulent correlations will be more manifest in the radiation from the soot because the emission from soot particles is greatest at short wavelengths, where the sensitivity of the emissive power to temperature is also at its greatest - see figure 6.1.

Therefore, there are three principal issues to be addressed in this chapter. These are the origin of the detailed species and temperature information required, the accommodation of the radiation / turbulence interactions, and the derivation of the detailed radiative properties for the radiating flame species considered. These issues will be discussed in turn.

The flame calculations detailed in chapter 5 included radiative emission in a simple (optically thin) manner. The scalar fields obtained from these calculations show generally good agreement with the experimental data. This allows the information from these calculations to be confidently passed to a more detailed, 'post-processed', calculation for the spectrally resolved radiative properties.

Under the assumption of a grey gas, Cox (1977) showed that fluctuating temperature intensities greater than 40 % yield mean radiance values that are more than double those predicted using mean temperatures. This would lead to the conclusion that some method of addressing the radiation / turbulence interaction is vitally important for prediction of flame radiation. However, work conducted predicting the non-luminous spectral radiance of similar methane jet flames to those studied here, Jeng et al. (1984), lead the authors to conclude that the best strategy for predicting the radiation from such flames is to use mean flame properties. The stochastic method was used by Jeng et al. (1984) for modelling the interaction between the radiation and the turbulence. The assumption underlying this approach is that the flowfield consists of many statistically independent turbulent eddies. The properties within each of these eddies are considered to be uniform. The size of each eddy is equated to the dissipation length scale (L_e), determined from

$$L_e = C_\mu^{3/4} k^{3/2} / \epsilon \qquad (6.2)$$

The properties of each eddy are obtained stochastically, under the further assumption that all the scalar properties are functions of a conserved scalar and that the statistics of this conserved scalar are known. The cumulative distribution function of this conserved scalar is constructed for each eddy. The distribution function is then sampled by selecting a random number lying in the range from zero and unity and determining the value of the conserved scalar which gives this value of the distribution function. The process is repeated for each eddy along the path, until a single instantaneous realisation of the path is constructed. The spectral radiance for this realisation is computed and the whole process repeated until a stationary mean is achieved. Jeng et al. (1984) found that this stochastic technique over-predicted the intensity of the 4.3 μm carbon dioxide band by approximately 10 to 30 % whereas using mean properties gave very good agreement with experiment. Syed (1990) also compared the stochastic approach with that of using mean properties for calculating the spectrally resolved emission from a buoyant methane fire - Crauford (1984) and Charnley (1986). Syed (1990) also found that the stochastic method tends to over estimate the radiative flame emission. This is attributed to the over estimation of the path lengths through the high temperature reaction zones, with the resultant over estimation of their emission. However, in contrast to the Jeng et al. (1984) study, Syed (1990) found that the use of mean properties alone tended to under-estimate the flame emission. Gore and Faeth (1986) extended the use of the stochastic method for calculating flame emission, by modelling highly luminous ethene / air jet diffusion flames. Again the stochastic method was compared with that of using mean properties alone. The mean properties prediction tended to under-estimate the radiative emission, particularly at shorter wavelengths where the luminous contribution is at its greatest. However, the stochastic method tended to over-predict the flame emission at all points in the spectrum. Gore and Faeth (1986) attributed the success of the mean properties method to internal redistribution of energy by radiative emission and re-absorption within the flame.

The findings of these studies indicate that radiative / turbulence interaction is an important component for the accurate prediction of flame radiation. However, it is evident that in high Reynolds number jet flames, where the intensity of the scalar fluctuations is small, such interactions may be neglected whilst retaining an acceptable degree of accuracy. This is particularly true of flames which are relatively non-luminous. It is also noted that the mean properties method requires considerably less computing time. Hence, the predictions

of radiative emission presented in this chapter employ the mean property method exclusively.

The ability to post-process the predictions of radiative emission using existing flame data allows the use of detailed models for generating the radiative properties of the contributing species. The aim of this work is to reproduce the experimental profiles of mean spectrally resolved radiative emission for the methane flames studied. The emission from these flames is due mainly to the gaseous components. Gaseous emission occurs only at discrete positions in the spectrum. There are two type of models that are commonly used to generate the spectrally resolved radiative properties of gases.

The first, and simplest, of these is the 'wide-band' model. The radiation absorption characteristics of any gas may be studied experimentally and empirical relations fitted to the experimentally derived data. The band profile may be crudely fitted by a triangular or 'top-hat' profile, or may be represented by a more complex exponentially decaying function.

A more complex model which gives a better representation of the spectrally resolved absorption / emission properties of the gas is the 'narrow-band' model. The absorption / emission bands of gases actually consist of a large number of closely spaced absorption / emission lines, each line corresponding to a transition between quantised energy levels of the gas molecules. Narrow-band models divide the gas bands into smaller spectral regions and also simplify the actual process by assuming a line shape and arrangement of lines for each narrow band.

As each spectral line corresponds to a transition between quantised energy states it might be expected that the line would be monochromatic. The emission frequency being given by

$$E = h\nu \tag{6.3}$$

where E is the energy difference between the quantised energy states, h is Planck's constant, and ν is the emission frequency. However, several effects tend to broaden the actual frequency of emission. These line broadening effects are discussed in detail by Siegel and Howell (1971), but four of these effects will also be outlined here. The first phenomenon

is termed natural broadening. A completely stationary emitter unperturbed by any external effect emits energy over a finite spectral interval centred about a single transition frequency. This line broadening results from uncertainties in the energy levels, corresponding to the energy level transition, which are related to the Heisenberg uncertainty principle. The line half-width exhibited by natural broadening is small compared with other mechanisms, and is normally neglected. The second mechanism is due to the motion of the emitting molecules. The molecules of the emitting gas will have a distribution of velocities associated with their thermal energy. The motion of these molecules, relative to the observer, will cause a shift in the frequency (termed a Doppler shift) registered by the observer. However, this Doppler broadening mechanism is most important at very high temperatures. The third broadening mechanism, and probably the most important in combustion processes, is termed 'collision' broadening and results from the collisions between the radiating molecules. The spectral line takes on a Lorentz profile as a consequence of these collisions. As the pressure of the gaseous system is increased the frequency of the collisions between the molecules also increases. Hence, the half-width of the collision broadened spectral line is proportional to the pressure. The final broadening mechanism is not relevant to general combustion applications, and is caused by the effect of an external electrical field on the energy levels of the radiating gas molecules. This is called the Stark effect, and can lead to very pronounced line broadening. The profile assumed for each line, in the narrow band model, determines the effect of pressure, temperature, optical path length, and intrinsic gas properties on the radiation characteristics. From the above descriptions of the differing phenomena leading to line broadening it is apparent that the most appropriate line shape for combusting gases is that of the collision broadened line.

Two arrangements for the lines within each spectral region are commonly cited. In certain vibrational-rotational bands the lines are approximately equally spaced and the line intensity varies little across the band. Hence, the Elsasser model assumes that the spectral lines are equally spaced and that they all have identical profiles. In contrast, the statistical (or Mayer-Goody) model assumes that the lines have a random distribution of intensities and position.

The 'narrow-band' model is used in this work. A version of the RADCAL code,

Grosshandler (1979), is used to generate the spectrally resolved emission from various optical paths through the flames. The code RADCAL has been well validated against experimental emission data for non-homogeneous paths through water vapour and carbon dioxide - Grosshandler (1980). Of the remainder of this chapter, section 6.2 details the models used in the RADCAL code, section 6.3 discusses the results from RADCAL and compares them with the experimental spectra, and section 6.4 makes some conclusions.

6.2 RADCAL

The program RADCAL, Grosshandler (1979), solves for the radiation intensity along optical paths in a non-homogeneous absorbing / emitting medium. This section supplies a description of the RADCAL code as provided by Grosshandler (1979) and Grosshandler (1980). The spectral radiation intensity (I) received at the origin along a line of sight (of pathlength L) through a non-homogeneous (in temperature and concentration) absorbing / emitting gas, in local thermodynamic equilibrium, may be derived from

$$I_\omega = \int_0^U \kappa_\omega I_{\omega,b} \exp\left(-\int_0^u \kappa_\omega du' \right) du \tag{6.4}$$

where κ_ω is the spectral absorption coefficient for the gas, $I_{\omega,b}$ is the Planck blackbody distribution function, and U is the density pathlength defined by

$$du = \frac{\rho}{\rho_0} dl = \frac{P}{P_0} \frac{T_0}{T} dl \qquad U = \int_0^L \frac{\rho(l)}{\rho_0} dl \tag{6.5}$$

The major barrier to solution of equation 6.4 is the form of the function κ_ω, for the gases this is provided by the narrow band model discussed in the introduction. The absorption coefficient for the soot varies continuously across the entire spectrum and is more easily defined.

The principal bands present in the spectra from combustion products are those due to water vapour at 1.38, 1.88, 2.7, and 6.3 μm and carbon dioxide at 2.7 and 4.3 μm. Soot may contribute a significant amount of continuum radiation depending on the fuel and the conditions. Also, there will be a small amount of radiation from carbon monoxide at 5 μm and in the cases considered here methane at 2.4 and 3.3 μm. The statistical model with equal line strengths is used to model the emission from these molecules. As already stated in the introduction, individual line broadening is primarily due to collisions between the radiating molecules. Therefore a Lorentz line shape is assumed, with the small contribution from Doppler broadening taken as additive. The statistical model considers that all spectral lines comprising the band are randomly distributed. The two important parameters

describing this band are the mean line strength to spacing parameter ($\overline{S/d}$) and the mean inverse line spacing ($\overline{1/d}$). For carbon dioxide these parameters are determined from the modified anharmonic oscillator / rotator model - Malkmus (1963a) and Malkmus (1963b). For water vapour the parameters are experimentally derived and are given by Ludwig et al. (1973) as a function of temperature and wavenumber. For the 5 μm band of carbon dioxide the parameters were taken from Malkmus and Thomson (1961). The 3.3 μm band of methane is described using the wide band parameters of Edwards and Menard (1964), whereas for the 2.4 μm band the expressions of Gray and Penner (1965) are used.

The statistical model gives the following expression for the spectral absorption coefficient in a homogeneous gas of pathlength l

$$\kappa_{\omega,H} = \overline{S/d}\left[1 + \frac{\overline{S/d}\, l\, \rho/\rho_0}{4\gamma_L \overline{1/d}}\right]^{-1/2} \tag{6.6}$$

where γ_L is the half-width of the broadened line. However, this expression is only valid along a homogeneous path. The Curtis-Godson approximation, Goody (1964), replaces $\overline{S/d}$ and $\overline{1/d}$ with suitable averages for a non-homogeneous path. Using the Curtis-Godson approximation, the absorption coefficient at a location l, for radiation directed towards the origin, can be written as

$$\kappa_{\omega,CG}(l) = \overline{S/d}_{CG}\left[1 + \frac{\left(\int_0^l \frac{\rho(l')}{\rho_0}\, dl'\right)^2 (\overline{S/d}_{CG})^2}{4\int_0^l \gamma_L \overline{1/d}(l')\, \overline{S/d}(l')\, \rho(l')/\rho_0\, dl'}\right]^{-1/2} \tag{6.7}$$

where the Curtis-Godson average of the line strength to spacing parameter ($\overline{S/d}_{CG}$) is defined as

$$\overline{S/d}_{CG} = \frac{\int_0^l \overline{S/d}(l')\, \rho(l')/\rho_0\, dl'}{\int_0^l \rho(l')/\rho_0\, dl'} \tag{6.8}$$

The absorption coefficient for the soot may be obtained from the Lorentz-Mie theory - Kerker (1969) - as

$$\kappa_\lambda = \frac{36\,\pi\,n\,k}{4n^2k^2 + (n^2 - k^2 + 2)^2}\,\frac{f_V}{\lambda} \tag{6.9}$$

where n and k are the real and imaginary parts of the complex refractive index (defined as $m = n - ik$). In this work the value of the complex refractive index given by Mullins and Williams (1987) is employed. This has a value of $m = 1.92 - 0.45i$.

The optical depth along a non-homogeneous path may be written as

$$X_\omega(l) = \int_0^l \kappa_\omega(l')\,\frac{\rho(l')}{\rho_0}\,dl' \tag{6.10}$$

For a mixture of gases the total optical depth is determined by summing the individual optical depths of the various species. Hence, this mixture optical depth is given by

$$X_{\omega,Mix.}(l) = \int_0^l \left[\sum_i \kappa_{\omega,i}(l')\,P_i(l')\right]\frac{T_0}{P_0\,T(l')}\,dl' \tag{6.11}$$

The spectral transmittance may be defined from the optical depth

$$\tau_\omega(l) = e^{-X_\omega(l)} \tag{6.12}$$

Equation 6.4 may be written in terms of this transmittance

$$I_\omega = -\int_1^{\tau_\omega(L)} I_{\omega,b}(T)\,d\tau_\omega \tag{6.13}$$

This is the form of the radiative transfer equation solved numerically by RADCAL. The integration in equation 6.13 is replaced by a summation over *N* homogeneous elements

$$I_\omega = -\sum_{j=1}^{N} I_{\omega,b}(T_j)\,(\tau_{\omega,j} - \tau_{\omega,j-1}) \tag{6.14}$$

where $\tau_{\omega,j}$ is the narrow band average transmissivity for the gas mixture over cell j.

6.3 Results

The first set of results presented are for the relatively non-luminous 1 atm flame. Radiation spectra at eight flame heights are presented and compared with experiment in figures 6.2a - h. The flame structure used for these predictions of the flame emission was obtained from a GENMIX calculation - see chapter 5. This GENMIX calculation included radiative loss from the gas and the soot. The soot growth model applied constant set 7 and the uncorrelated form for the soot source terms. Soot oxidation was not included. The results from this GENMIX calculation are shown in figures 5.5a - j. The agreement between GENMIX and the experimental data is very good. Hence, any deficiencies, in the agreement of the predictions of radiative emission with the experimental data, are likely to lie with the method of using mean properties profiles as an input to RADCAL. The optical path considered for these predictions spans the internal diameter of the Pyrex flame tube used in the rig, a distance of 155 mm.

The first, readily apparent, feature of these spectra is the lack of continuum radiation due to soot. Soot radiation begins to show at about the 250 mm axial station and its relative contribution continues to grow up to 425 mm. The intensity in general increases with increasing axial distance. The only exception to this is the contribution from the 3.3 μm band of methane, which decreases with height in the flame. The agreement of the RADCAL predictions with experiment is only modest and improves with increasing axial distance. The 2.7 μm band of water and carbon dioxide is generally well predicted at all flame positions. However, the intensities of the 3.3 μm band of methane and the 4.3 μm band of carbon dioxide are initially over-predicted, with the over-prediction decreasing with height in the flame. The over-prediction of the methane emission is to be expected. The mean levels of methane concentration at low flame positions will be high. However, the temperature of the bulk of this methane will be low. Using mean temperature and species profiles to generate the emission spectra will place the local mean methane concentration at the local mean temperature, and this will be higher than the actual temperature of the majority of the methane. The over-prediction of the emission from the 4.3 μm band of carbon dioxide is disappointing. However, Jeng et al. (1984) similarly over-predicted in this band using predicted mean properties. The temperature dependence of the Planck distribution in this wavelength region is low - see figure 6.1 - therefore, it is unlikely that

it is a problem with the temperature profile causing the over-emission of this band. Also, the use of a mean temperature profile, as opposed to taking account of the turbulent fluctuations in temperature, would be expected to yield an under-prediction in the radiative emission rather than an over-prediction. The same may be said about the effect of the correlation between temperature and the concentration of carbon dioxide. However, the use of mean properties may over-estimate the pathlength of carbon dioxide. The carbon dioxide in the flame would be confined to spatially narrow regions positioned about the reaction zones. The flame, at low positions, may be laminar-like due to possible relaminarization, resulting from the increase in the molecular viscosity due to the heat release. The GENMIX prediction of the flame structure does not include this effect. It may be seen from the predictions of flame structure shown in chapter 5 that at low flame heights (150 mm and below) the predicted temperature profiles are broader and lower than those obtained experimentally. A similar effect would also be expected for the profiles of carbon dioxide. Therefore, initially the pathlength would be the critical factor in determining the intensity of the emission from the 4.3 μm band. However, as the flame dimensions increase with axial distance the flame becomes optically black in this region of the spectrum - Jeng et al. (1984). The emission from the flame is then independent of the pathlength and concentration of the carbon dioxide and depends only on the temperature. It has already been shown that the sensitivity of the Planck distribution function to temperature is low in this wavelength region.

Two reasons are suggested for the under-prediction of the continuum radiation from the soot. The axial soot volume fraction profile generated by GENMIX agrees very well with the experimental data. However, figure 5.5j shows that the total integrated soot volume fraction across the width of the flame is under-predicted by approximately 10 % at the 350 mm height. Absorption measurements (chapter 3) indicate that the flame is optically thin in this region of the spectrum. Therefore, the flame emission from the soot will be linearly related to the soot volume fraction (cf. equation 6.4 and 6.9). The second cause for the disparity between the predicted and experimental spectra, is due to the interaction between the turbulence and the radiation. There are two main issues to be considered. The first is the effect of the turbulent fluctuations on the Planck function, which is very sensitive to temperature at short wavelengths. The second issue relates to the actual temperature of the soot. These issues will be further explored after the introduction of the 3 atm flame data,

the spectra of which include a much greater contribution from continuum radiation.

Figures 6.3a - e show the comparisons between the RADCAL results for the 3 atm flame and experiment. The flame structure for these predictions of the emission spectra was also derived from GENMIX. Radiative heat loss from the gases and the soot was included in this GENMIX calculation. The soot model employed constant set 2 and the uncorrelated form of the soot source terms. Soot oxidation was also included in this calculation, the oxidation term being factored by 0.015. The striking feature of the spectra for the 3 atm flame is that the spectral 'hole', present in the experimental data, is absent from the RADCAL predictions. Before discussing the general agreement between RADCAL and the experimental spectra, this feature will be investigated. In chapter 3 the location of a nearly stagnant region of gas inside the pressure rig was identified. It is likely that this region would fill with combustion products. The overall equivalence ratio inside the rig is 0.25. If it is assumed that the combustion products entering the stagnant region are at this equivalence ratio then the composition of this product gas may be easily found. An equivalence ratio of 0.25 corresponds to a mixture fraction of 0.01434. The flamelets illustrated in chapter 5 yield the values of mole fraction for carbon dioxide, carbon monoxide, water, and methane corresponding to this mixture fraction. The adiabatic temperature flamelet gives a value of 1011 K for the temperature of a mixture with this composition, but due to the effects of radiative loss in the flame and conduction to the rig casing a more realistic temperature would probably be approximately 500 K. The optical pathlength through the stagnant region is approximately 85 mm. With these parameters known it is an easy matter to add this path on to the optical path through the flame used for predicting the flame emission. Figure 6.4 shows the effect of doing this on the spectra at the 250 mm axial station. The spectral 'hole' would indeed seem to be caused by the presence of cool combustion products in the rig. The location of the spectral 'hole' matches that in the experimental spectra. However, the predicted depth of the 'hole' is not great enough. This is probably due to the temperature assumed for the products being too high. Figure 6.4 also indicates that the magnitude of the peak in the 4.3 μm band is relatively unaffected by the absorption caused by these products.

The comparisons shown in figures 6.3a - e indicate reasonable agreement for the banded gas radiation, with the exception of the 50 mm axial station where the earlier argument

concerning relaminarization applies. Also, in this elevated pressure flame the reaction zones are likely to be thinner in physical space. This will tend to exacerbate the problem created by GENMIX over-estimating the turbulence intensities at low flame positions. At higher flame positions the experimental spectra are dominated by continuum radiation from the soot. The RADCAL predictions under-estimate the contribution of this continuum radiation at all axial stations. However, the soot volume fractions provided by GENMIX are generally lower than those measured. The best agreement between the GENMIX soot volume fraction profile and experiment is obtained at the 250 mm axial position. At this height in the flame the experimental profile is approximately 30 % higher than the GENMIX profile. However, the emission from the soot measured by experiment is approximately 100 % greater than the RADCAL prediction.

This level of disagreement is similar in the 1 atm flame, where at the 425 mm axial station the experimental soot radiation is approximately double that predicted by RADCAL. However, although the contribution from soot radiation at lower flame positions is lower the agreement is much better. There are two factors to be considered. The first is the level of correlation between the soot volume fraction and the temperature, which may be linked to the mixture fraction. The second factor is the effect of the turbulent fluctuations on the Planck distribution function. Syed (1990) considered the effect of the turbulence on the Planck distribution function and the correlation between species and temperature in the modelling of the emission from a buoyant methane fire. Syed (1990) concluded that the dominant effect was that of the temperature fluctuations on the highly non-linear Planck distribution function. Unfortunately, the effect of such fluctuations in temperature has not been investigated in this study, so no further conclusions may be drawn. However, an approximation for the correlation between the soot volume fraction and the temperature may made. It is known that the soot forms in the high temperature, fuel rich regions of the flame. It is suggested in chapter 5 that the normalised soot properties are nearly constant functions of mixture fraction. It may be ventured, therefore, that if radiative heat loss is ignored the soot will only be radiating over a very narrow range of temperatures. Radiative heat loss would be expected to lower this temperature range with increasing axial distance. If the soot only exists within a limited temperature range then using the mean temperature profile to generate the continuum emission will clearly be in error.

An estimate of the soot temperature may be made and this may be compared with the mean flame temperatures. Two colour pyrometry may be used to estimate the temperature of the soot particles. This technique derives the temperature of an emitting body from the ratio between the emission intensities at two wavelengths. For identical concentration pathlengths and optically thin conditions, the emission intensity from the soot is proportional to the product of the absorption coefficient and the Planck distribution function. If it is assumed that equation 6.9 adequately represents the absorption coefficient of the soot (ie. that the refractive index is not a function of wavelength and temperature) then the emission intensity is proportional to (cf. equations 3.20 and 6.9)

$$I_\lambda \propto \frac{1}{\lambda} \frac{1}{\lambda^5(\exp(hc_0/\lambda kT) - 1)} \tag{6.15}$$

The ratio of the emission intensities at different wavelengths is, therefore, a function of temperature only. This ratio is given by

$$\frac{I_{\lambda_1}}{I_{\lambda_2}} = \frac{\lambda_2{}^6(\exp(hc_0/\lambda_2 kT) - 1)}{\lambda_1{}^6(\exp(hc_0/\lambda_1 kT) - 1)} \tag{6.16}$$

Figure 6.5 plots temperature against the ratio of the intensities at 1.6 and 1.2 μm. Hence, from this graph, the ratio of the experimental intensities at 1.6 and 1.2 μm may be used to derive the soot temperatures found in the flames. The following table shows the result of doing this at three flame positions in each flame.

Table 6.1					
Flame Pressure	Height / mm	Intensity @ 1.6 μm	Intensity @ 1.2 μm	Ratio $I_{1.6} / I_{1.2}$	Soot Temp. / K
1	300	3.6588×10^{-2}	3.4944×10^{-2}	1.047	1696
1	350	5.2924×10^{-2}	5.0558×10^{-2}	1.047	1696
1	425	7.5142×10^{-2}	7.2483×10^{-2}	1.037	1705
3	150	1.3688×10^{-1}	1.2405×10^{-1}	1.103	1647
3	200	2.5488×10^{-1}	2.2460×10^{-1}	1.135	1621
3	250	3.4754×10^{-1}	3.0979×10^{-1}	1.122	1631

Two features of these soot temperatures are apparent. First, they are all higher than the peak mean flame temperature at their respective heights. Second, despite the total radiative energy loss from the flame increasing with axial distance, the soot temperature appears to be constant. This may be explained by the soot moving into leaner, oxidising regions at higher flame positions, these regions having a higher temperature than the regions where the soot formed. This would tend to offset the effect of the temperature reduction due to the radiative heat loss.

If it is assumed that all the soot at a given flame position exists at the characteristic temperature given in the table above then a good prediction of the flame emission should be possible, even if the turbulence / radiation interaction is ignored entirely. This is partially because the turbulent fluctuations will obviously have no effect on the temperature of the soot. Also, because the flames in this study are optically thin in this region of the spectrum and the continuum radiation is linearly related to the soot volume fraction, the mean radiative emission from the soot will be proportional to the mean integral soot volume fraction over the pathlength. Coppalle and Joyeux (1993) also report measurements of flame (soot) temperature using two colour pyrometry. The radial mean temperature profile from an ethene / air turbulent jet flame is reported at an axial distance of $x / d = 65$. The mean temperature profile reported is very flat, with an almost constant temperature of 1500 K. The 250 mm axial station in the 3 atm flame corresponds to a value for x / d of 62.5. Figure 6.6 compares the experimental spectrum from the 3 atm flame at a height of

250 mm with a soot emission spectrum generated by RADCAL. The mean gas radiation is not considered in this RADCAL calculation, but would be essentially additive to the mean soot emission. The mean soot volume fraction profile from the GENMIX calculation is employed, but the mean temperature profile is replaced by the single soot temperature value from table 6.1. This single value for the soot temperature (of 1631 K) is used across the entire width of the flame. The agreement of the RADCAL soot emission with experiment appears to be very good although there is still a slight under-prediction. However, it should be recognised that the GENMIX soot volume fraction profile also slightly under-predicts the experimental measurement.

6.4 Conclusion

The use of mean scalar properties for the prediction of flame radiative emission only allows limited success. The error in the predicted gas band radiation varies from 0 % in the 2.7 μm carbon dioxide and water band, up to 50 % in the 4.3 μm carbon dioxide band, and over 100 % in the 3.3 μm methane band. The error in the predicted gas band radiation decreases with increasing flame height. For the 4.3 μm carbon dioxide band this is probably due to the increasing optical depth of the flame, which decreases the role of the concentration pathlength in predicting the emission. Continuum radiation from the soot is consistently under-predicted at all flame positions. The results seem to indicate that the dominant effect for this decrease in the predicted soot emission is the omission of the correlations between the soot and temperature. It has been suggested earlier in this chapter that the soot only radiates over a very limited range of temperatures. Prescribing a representative temperature for this soot allows the soot emission to be realistically reproduced, while retaining the computationally desirable form of a mean properties solution. The soot temperature prescribed in this work was obtained from the experimental dataset. Clearly, this temperature will not be universal. Also, the prescription of a soot temperature from an experimental measurement does not represent a predictive capability. However, the normalised soot mass concentration function presented in chapter 5 (figure 5.4) shows a fairly well defined peak at a mixture fraction value of approximately 0.1. It is suggested that during a flame calculation this temperature, taken from the appropriate flamelet which includes the requisite degree of radiative heat loss, is stored for each flame position to be subsequently applied as the representative soot temperature at that position.

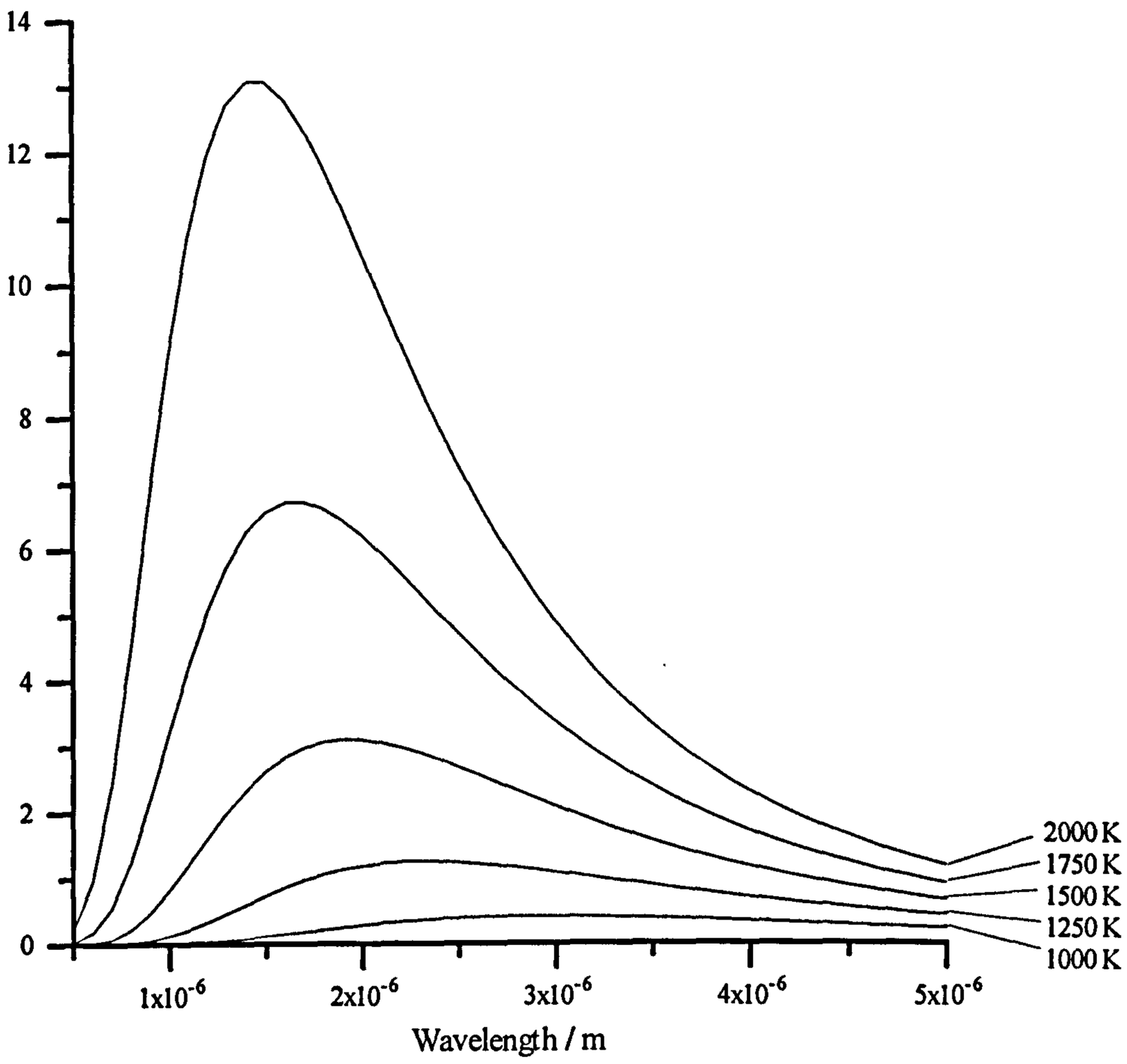

Figure 6.1. Planck distribution function of blackbody intensity.

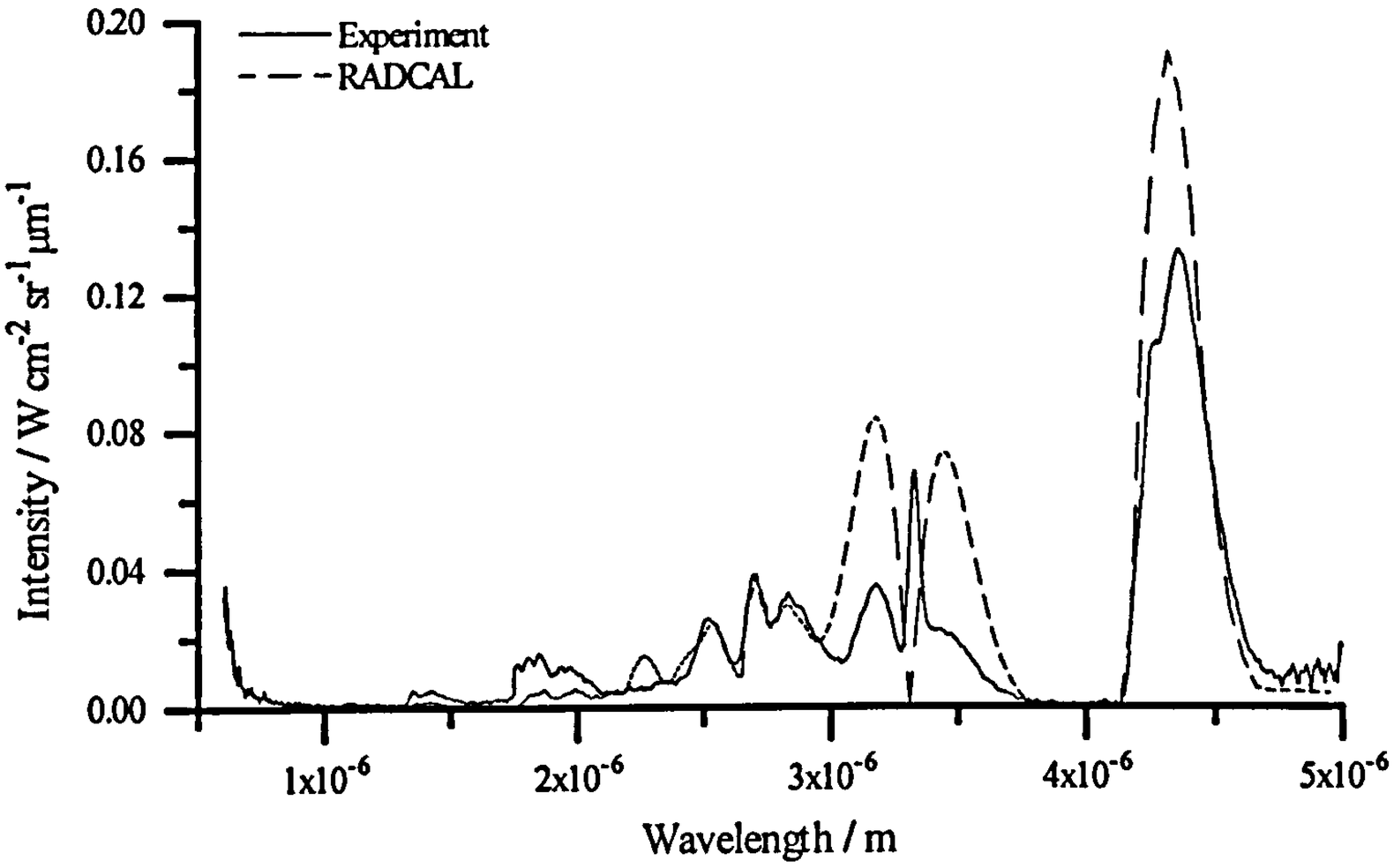

Figure 6.2a. RADCAL and experimental radiation intensity spectra for the 1 atm flame, along a horizontal optical path through the flame's axis 50 mm above the burner exit.

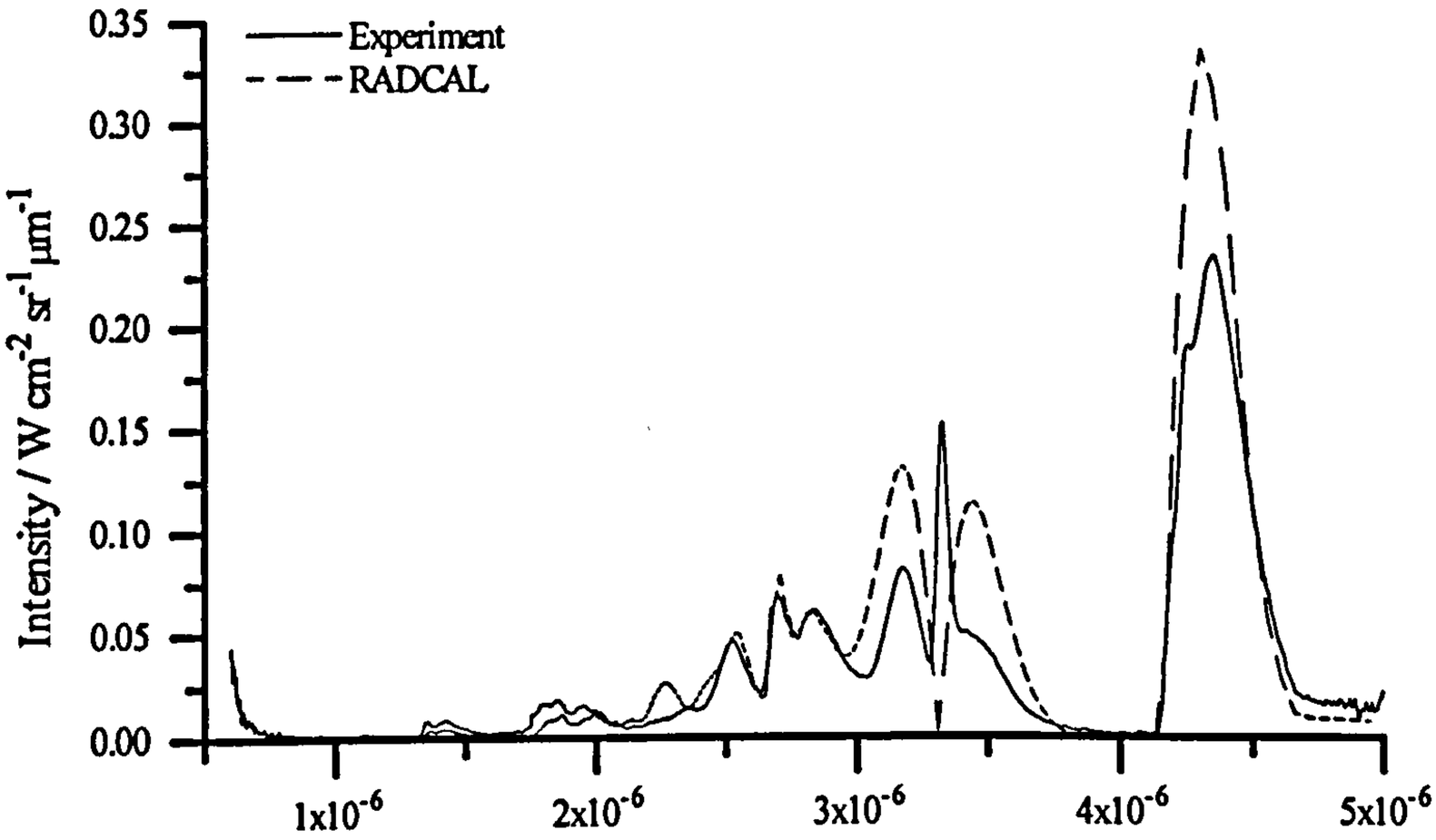

Figure 6.2b. RADCAL and experimental radiation intensity spectra for the 1 atm flame, along a horizontal optical path through the flame's axis 100 mm above the burner exit.

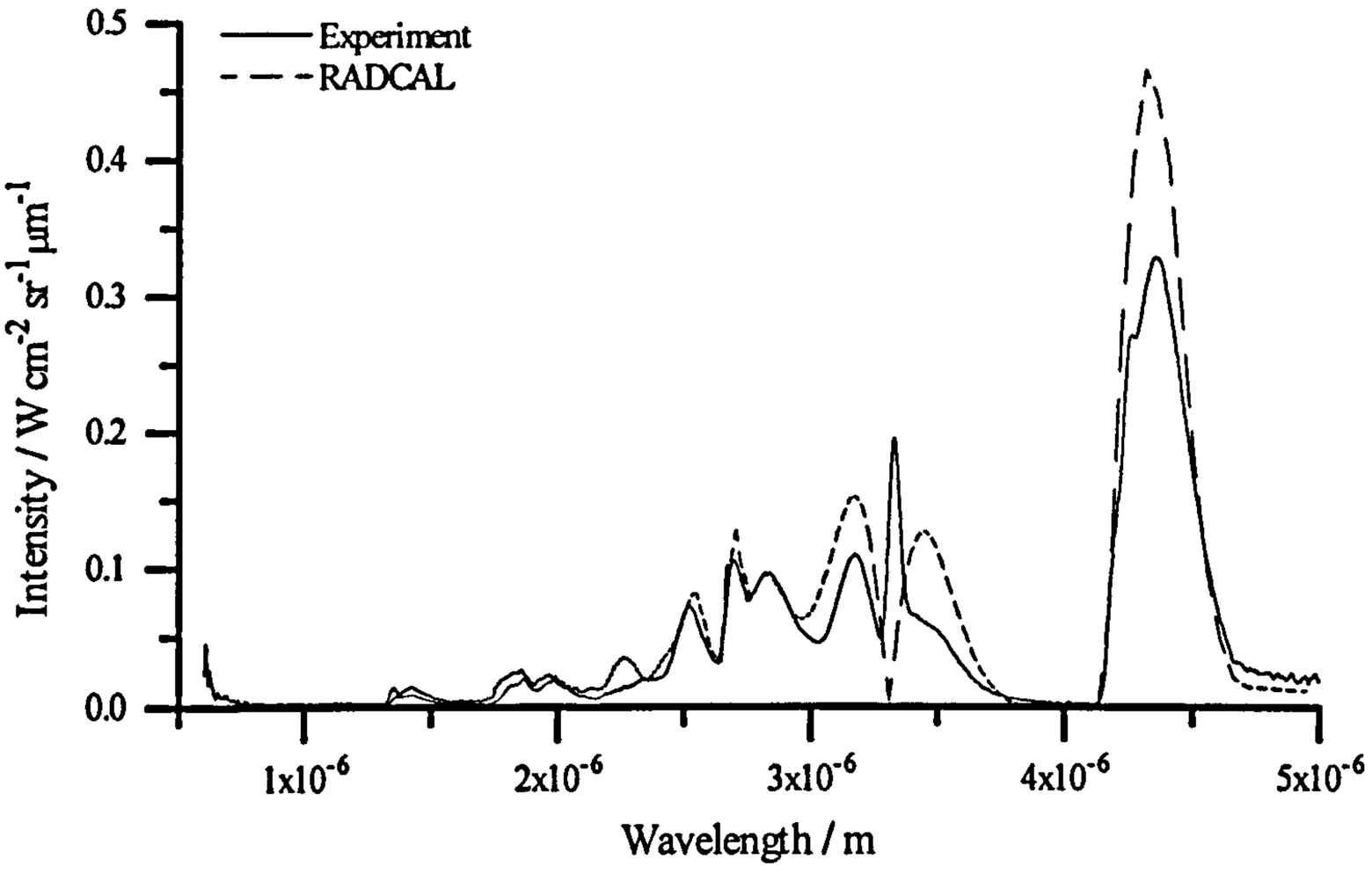

Figure 6.2c. RADCAL and experimental radiation intensity spectra for the 1 atm flame, along a horizontal optical path through the flame's axis 150 mm above the burner exit.

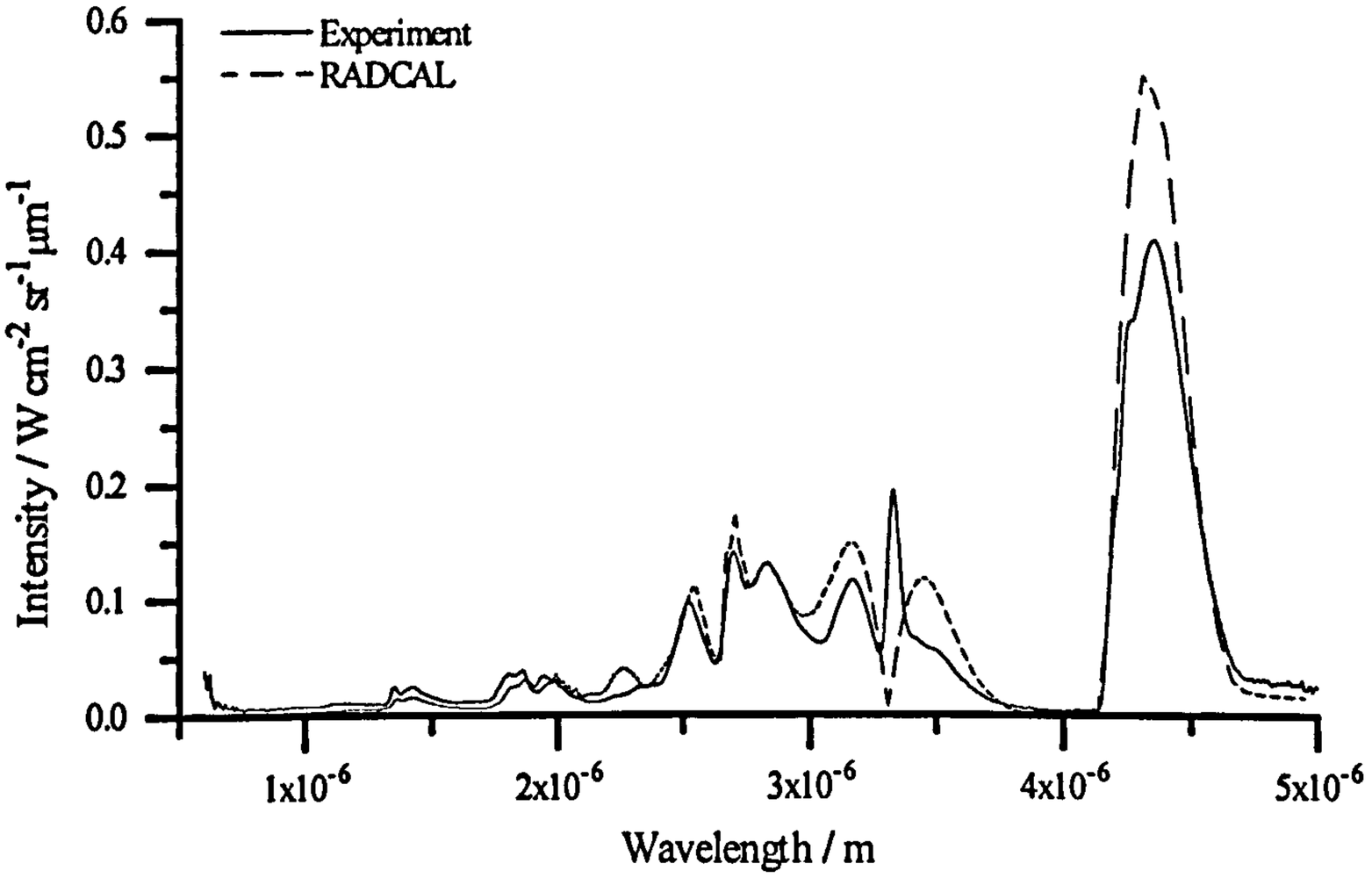

Figure 6.2d. RADCAL and experimental radiation intensity spectra for the 1 atm flame, along a horizontal optical path through the flame's axis 200 mm above the burner exit.

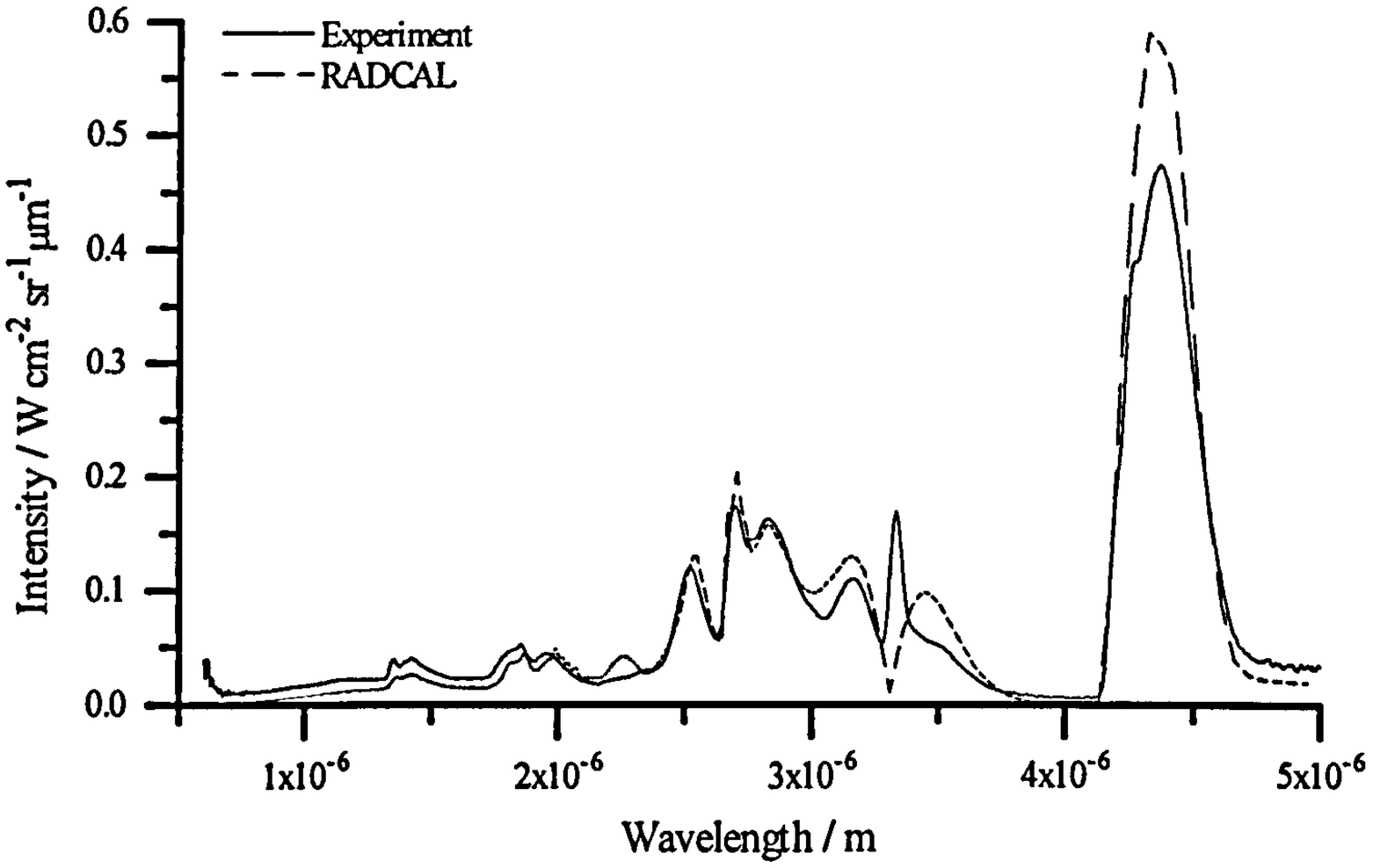

Figure 6.2e. RADCAL and experimental radiation intensity spectra for the 1 atm flame, along a horizontal optical path through the flame's axis 250 mm above the burner exit.

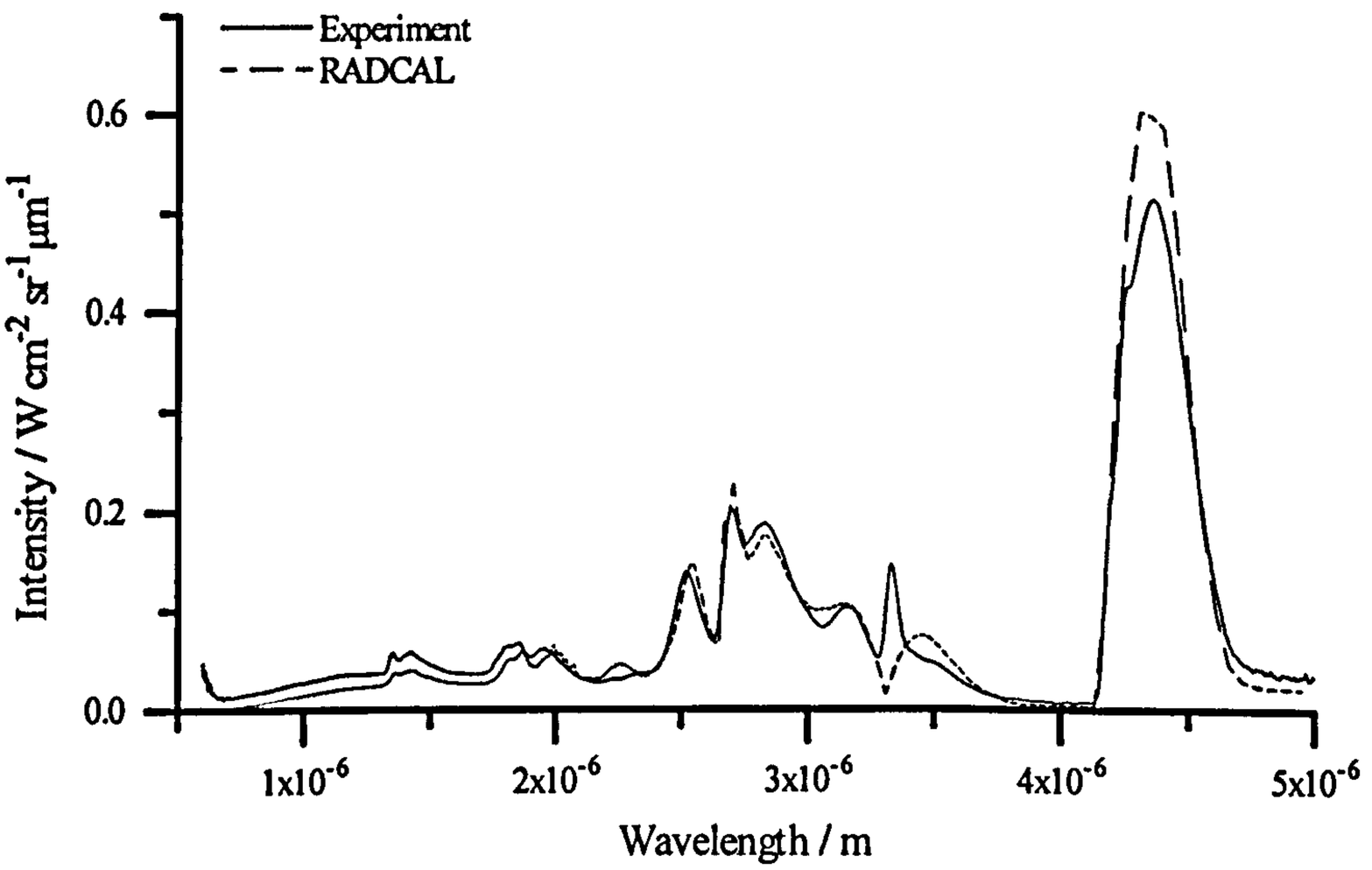

Figure 6.2f. RADCAL and experimental radiation intensity spectra for the 1 atm flame, along a horizontal optical path through the flame's axis 300 mm above the burner exit.

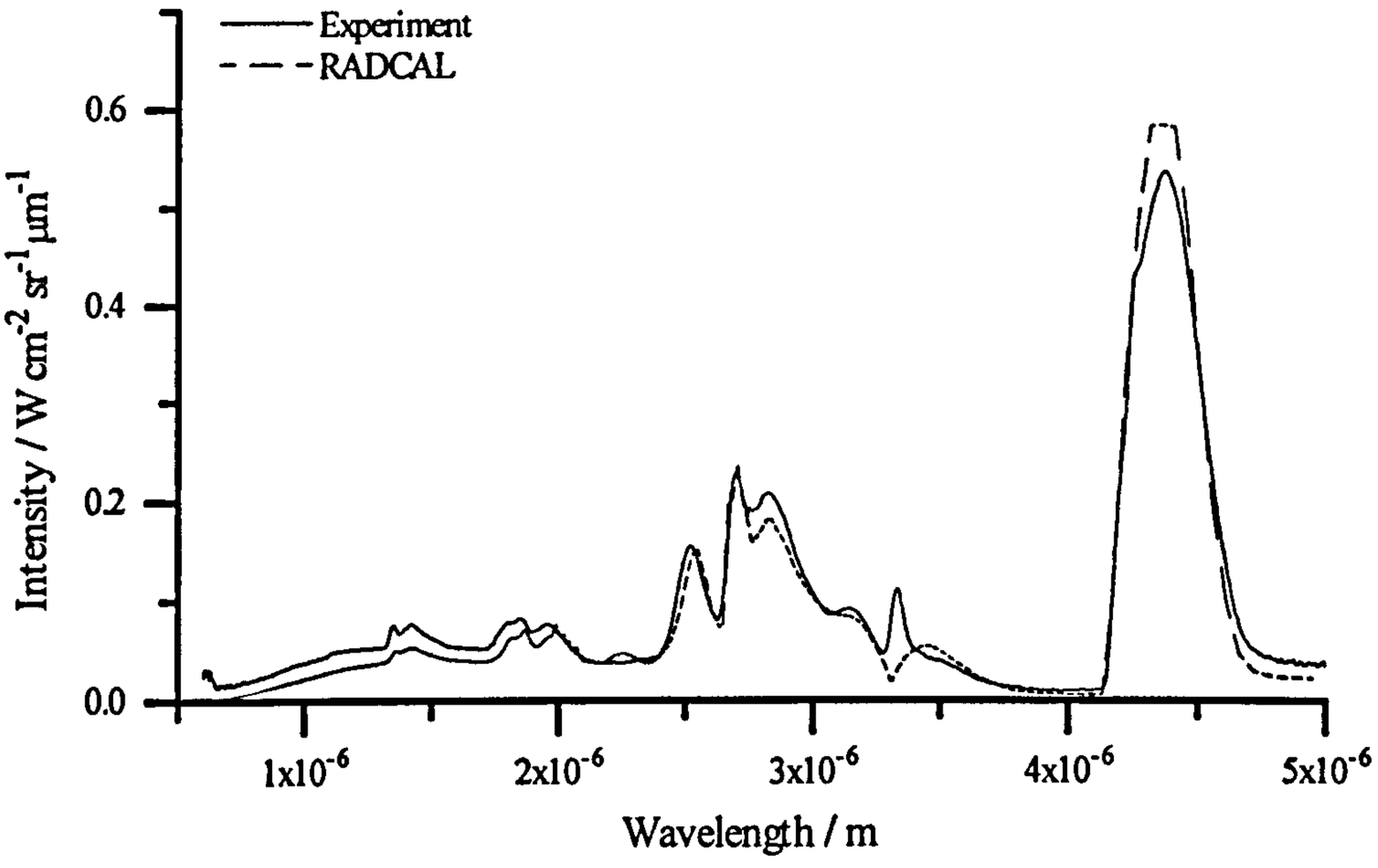

Figure 6.2g. RADCAL and experimental radiation intensity spectra for the 1 atm flame, along a horizontal optical path through the flame's axis 350 mm above the burner exit.

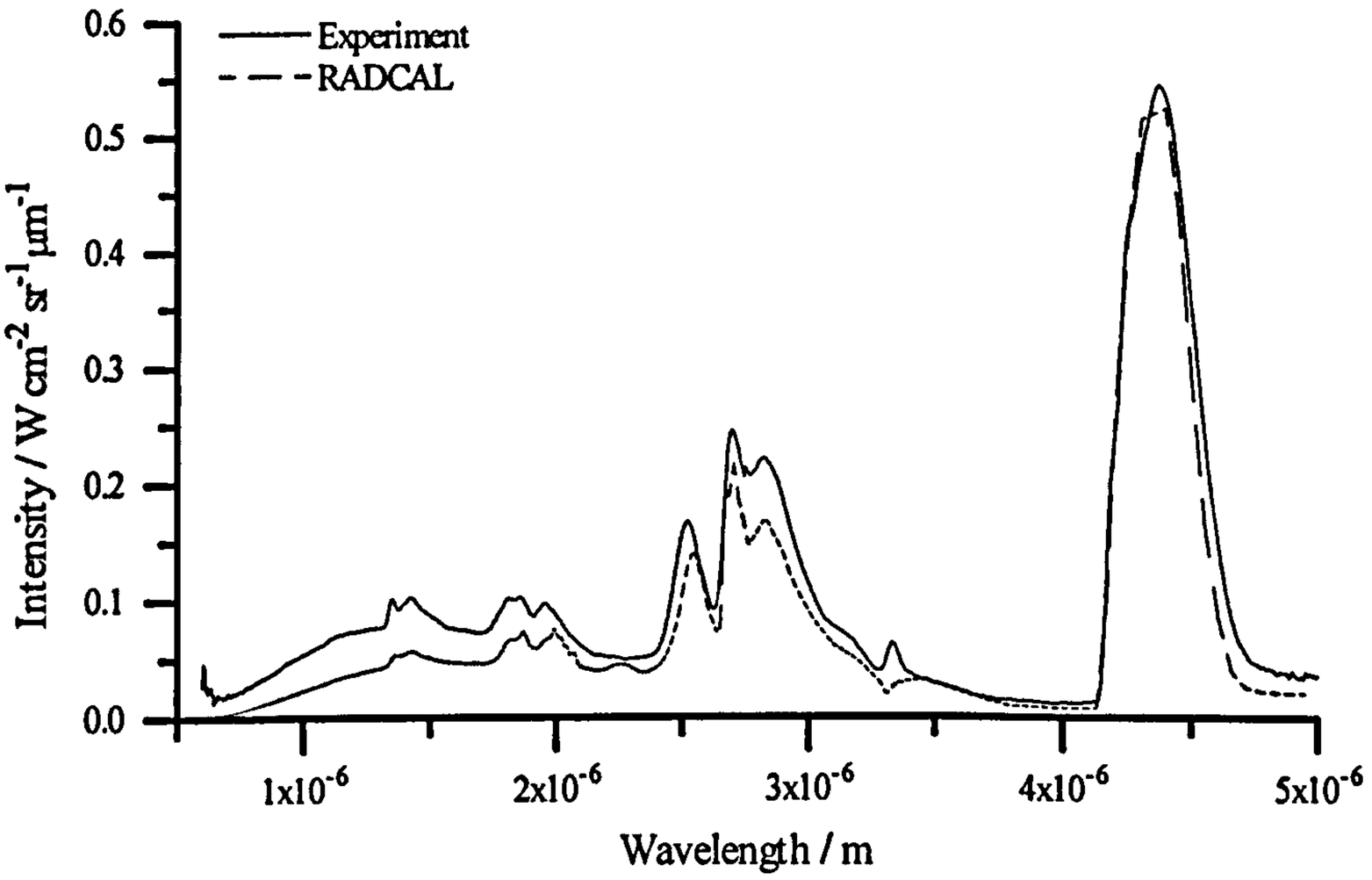

Figure 6.2h. RADCAL and experimental radiation intensity spectra for the 1 atm flame, along a horizontal optical path through the flame's axis 425 mm above the burner exit.

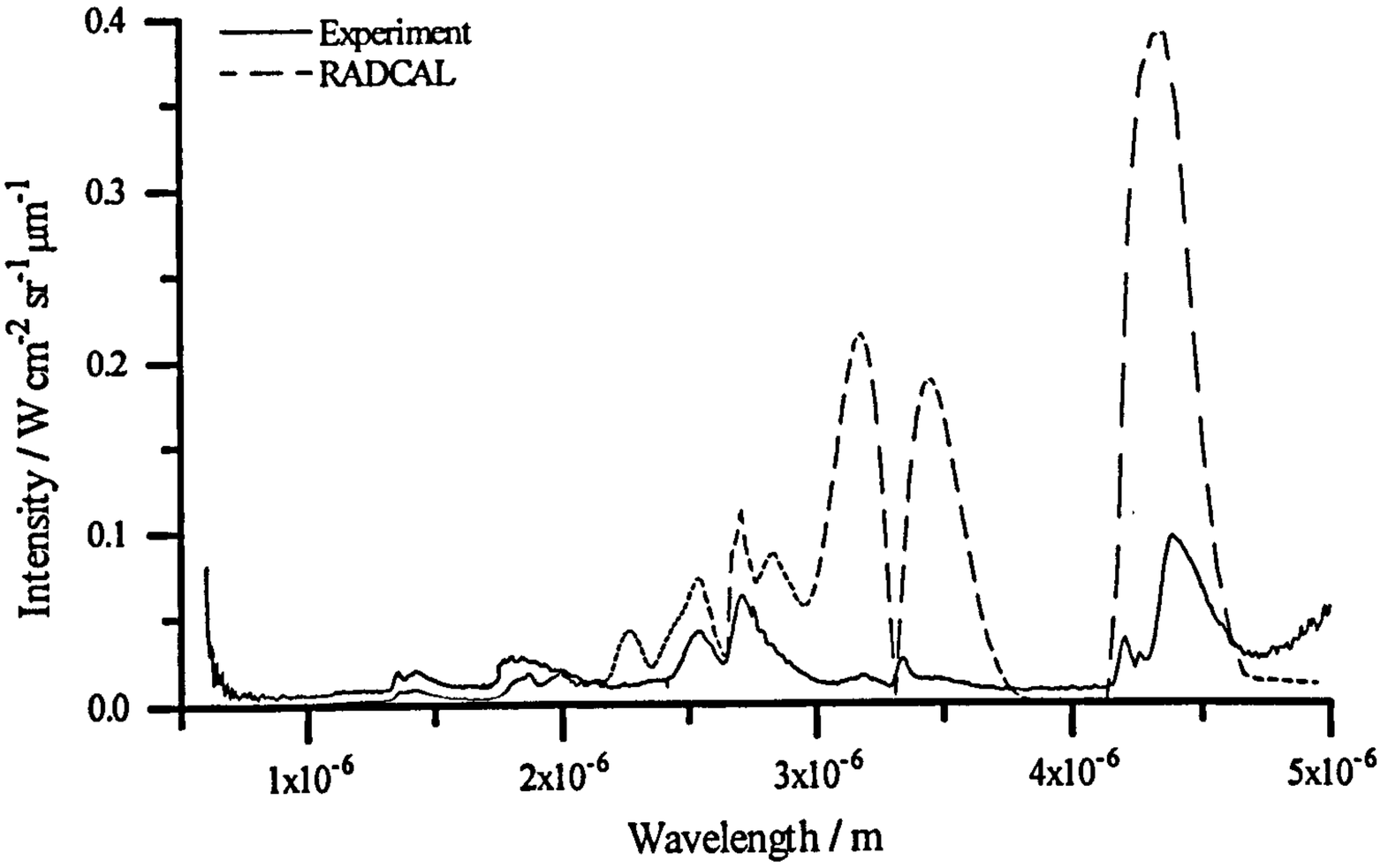

Figure 6.3a. RADCAL and experimental intensity spectra for the 3 atm flame along a horizontal optical path through the flame's axis 50 mm above the burner exit.

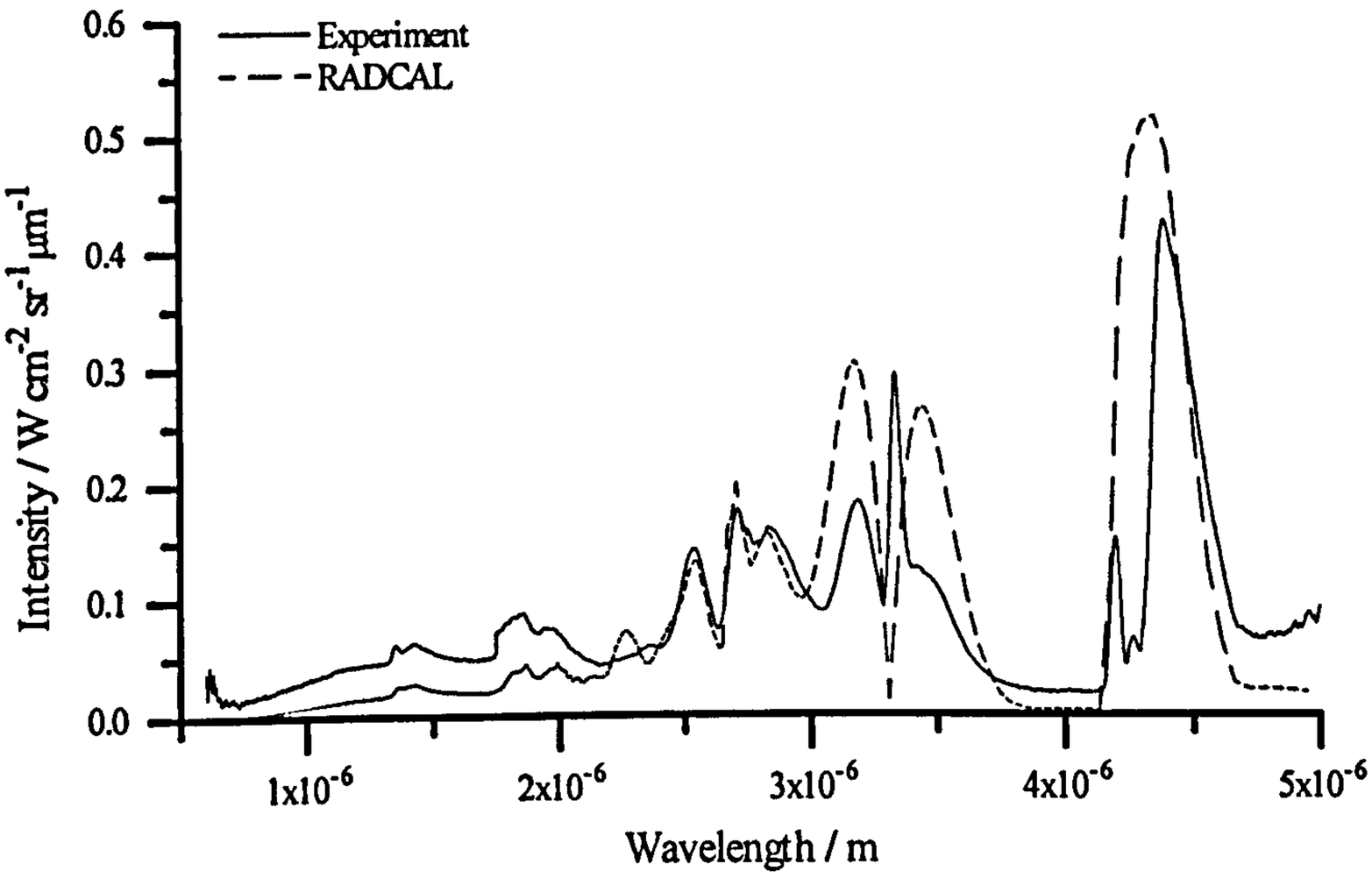

Figure 6.3b. RADCAL and experimental intensity spectra for the 3 atm flame along a horizontal optical path through the flame's axis 100 mm above the burner exit.

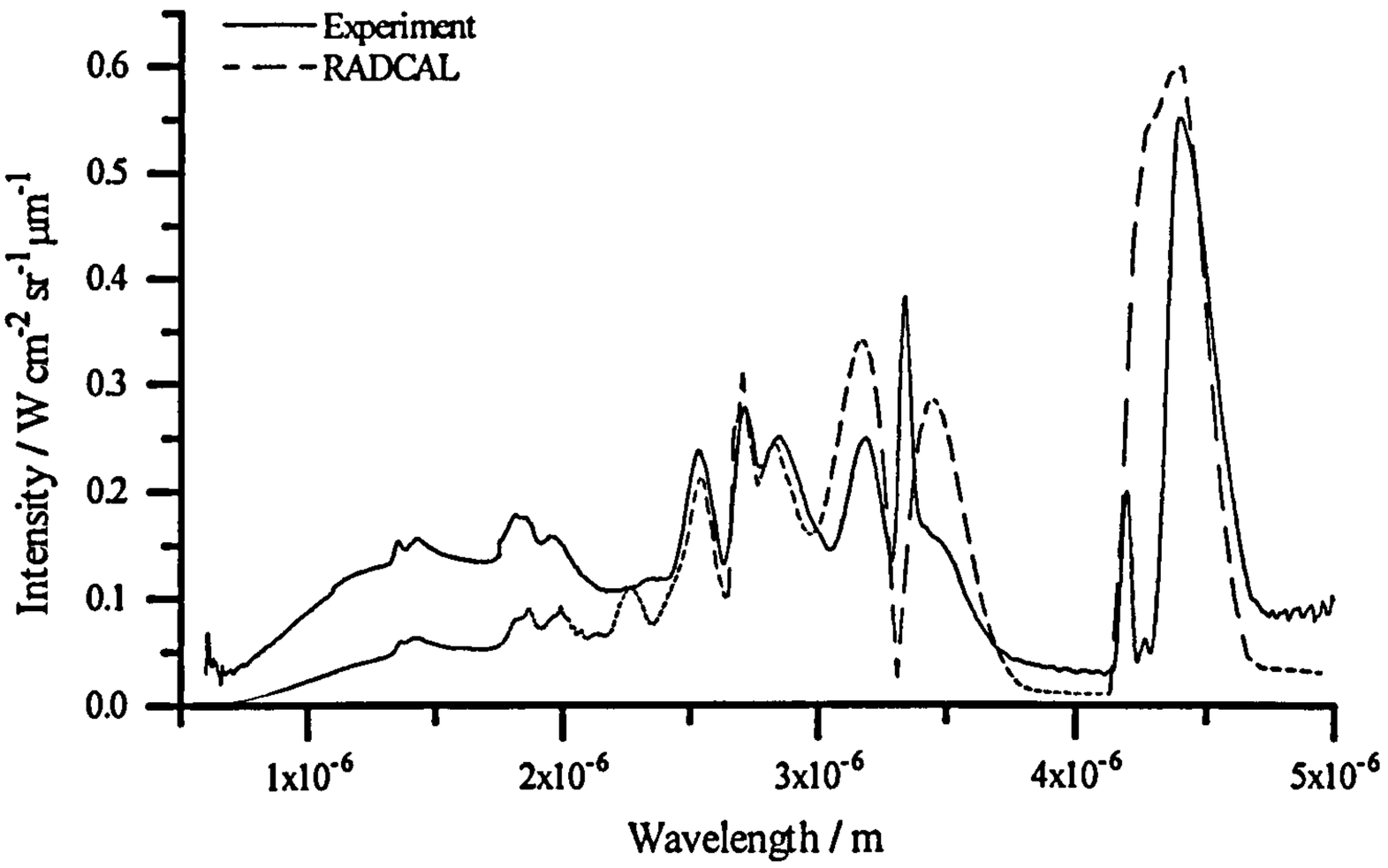

Figure 6.3c. RADCAL and experimental intensity spectra for the 3 atm flame along a horizontal optical path through the flame's axis 150 mm above the burner exit.

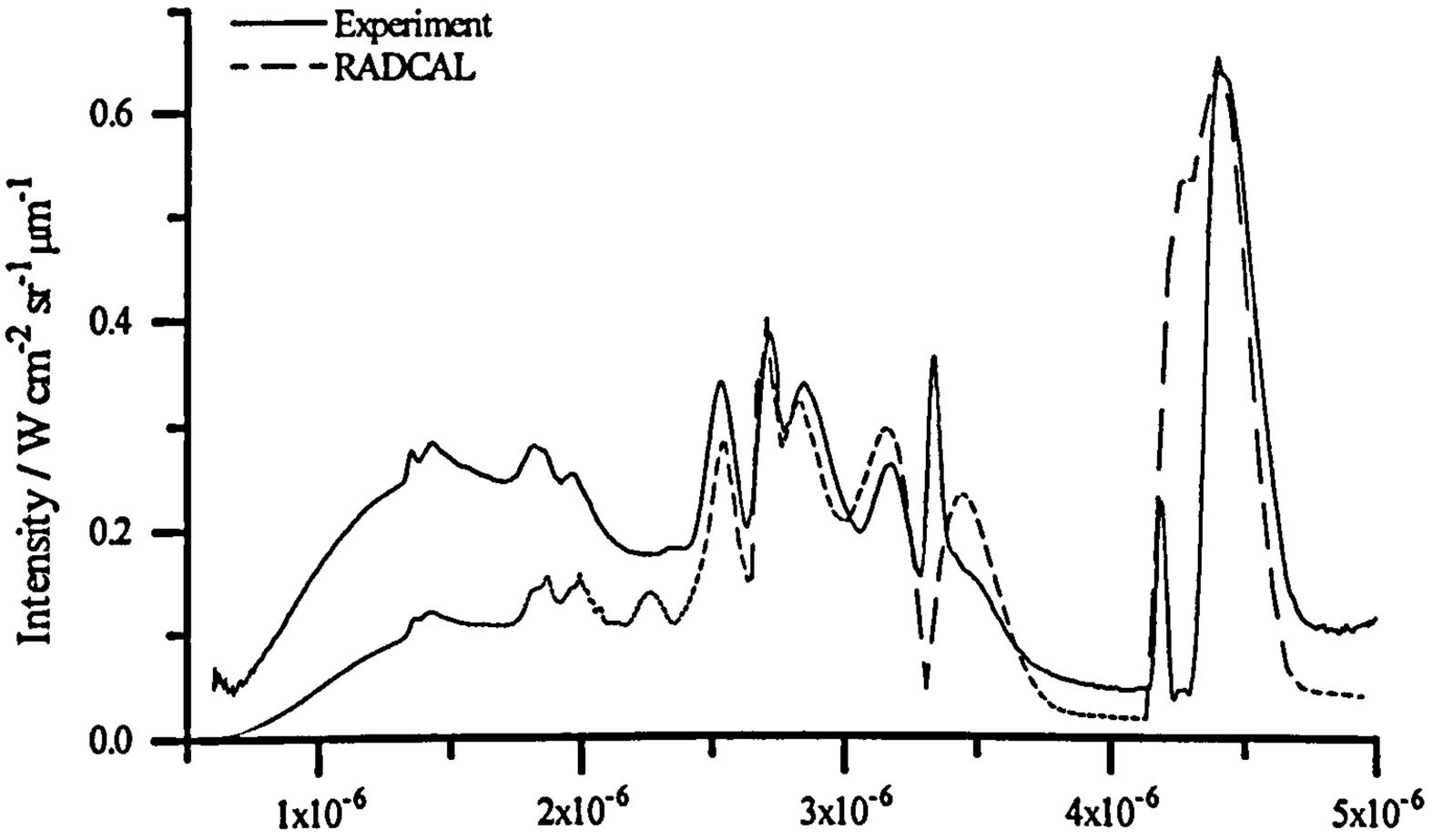

Figure 6.3d. RADCAL and experimental intensity spectra for the 3 atm flame along a horizontal optical path through the flame's axis 200 mm above the burner exit.

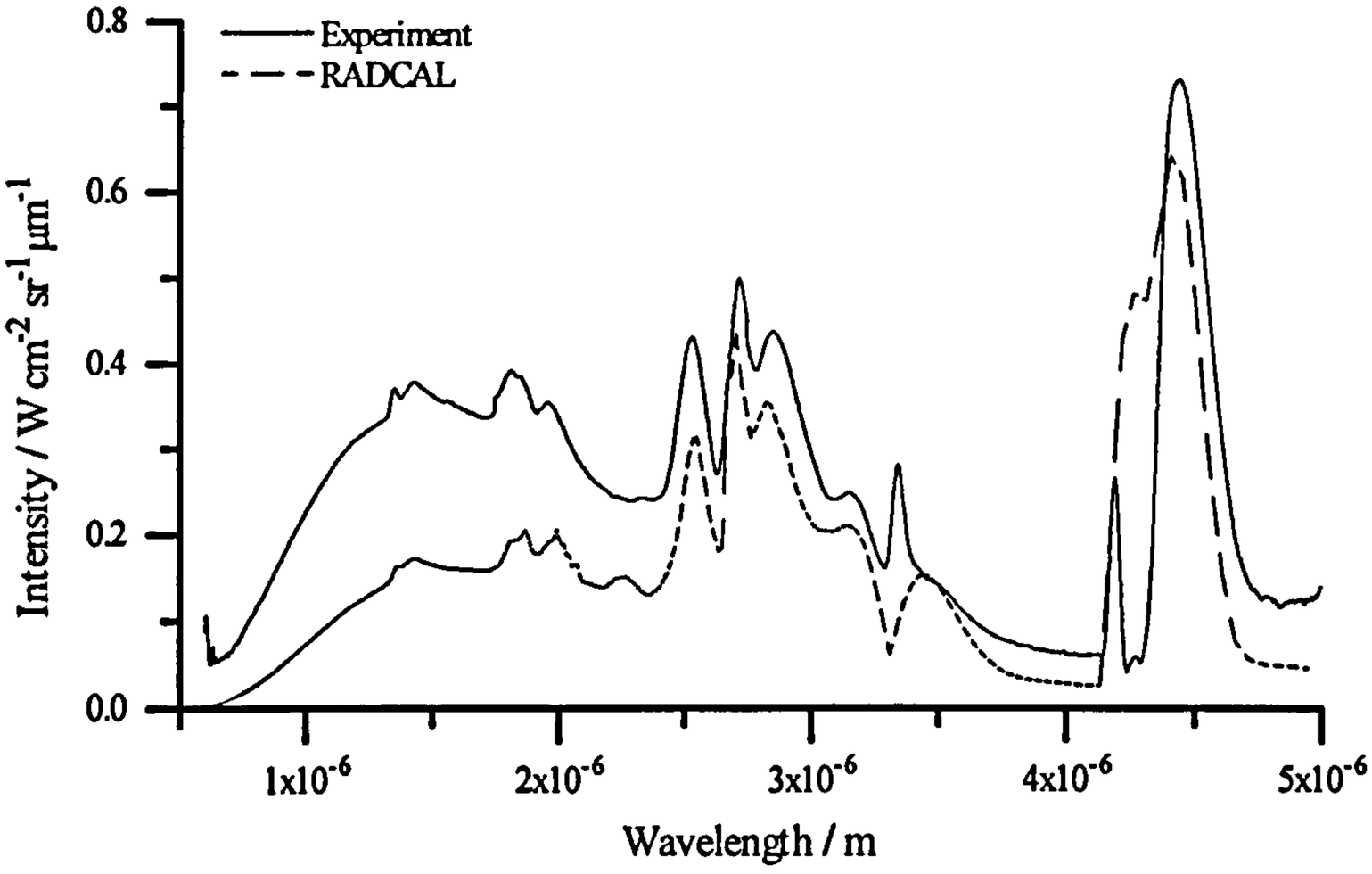

Figure 6.3e. RADCAL and experimental intensity spectra for the 3 atm flame along a horizontal optical path through the flame's axis 250 mm above the burner exit.

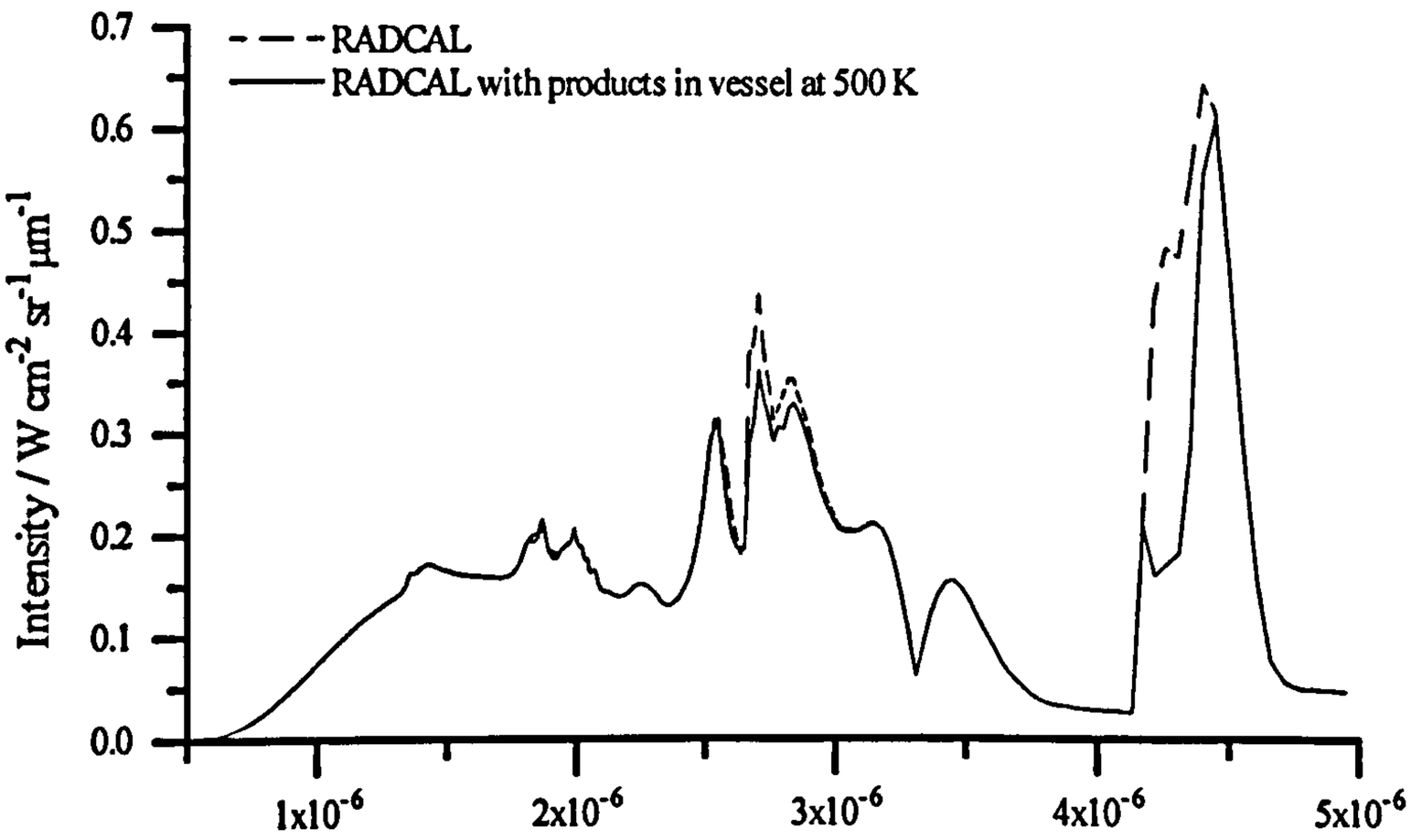

Figure 6.4. RADCAL intensity spectra for the 3 atm flame along a horizontal optical path through the flame's axis 250 mm above the burner exit. Figure shows the effect of including the stagnant gas region, contained within the pressure rig, in the RADCAL calculation.

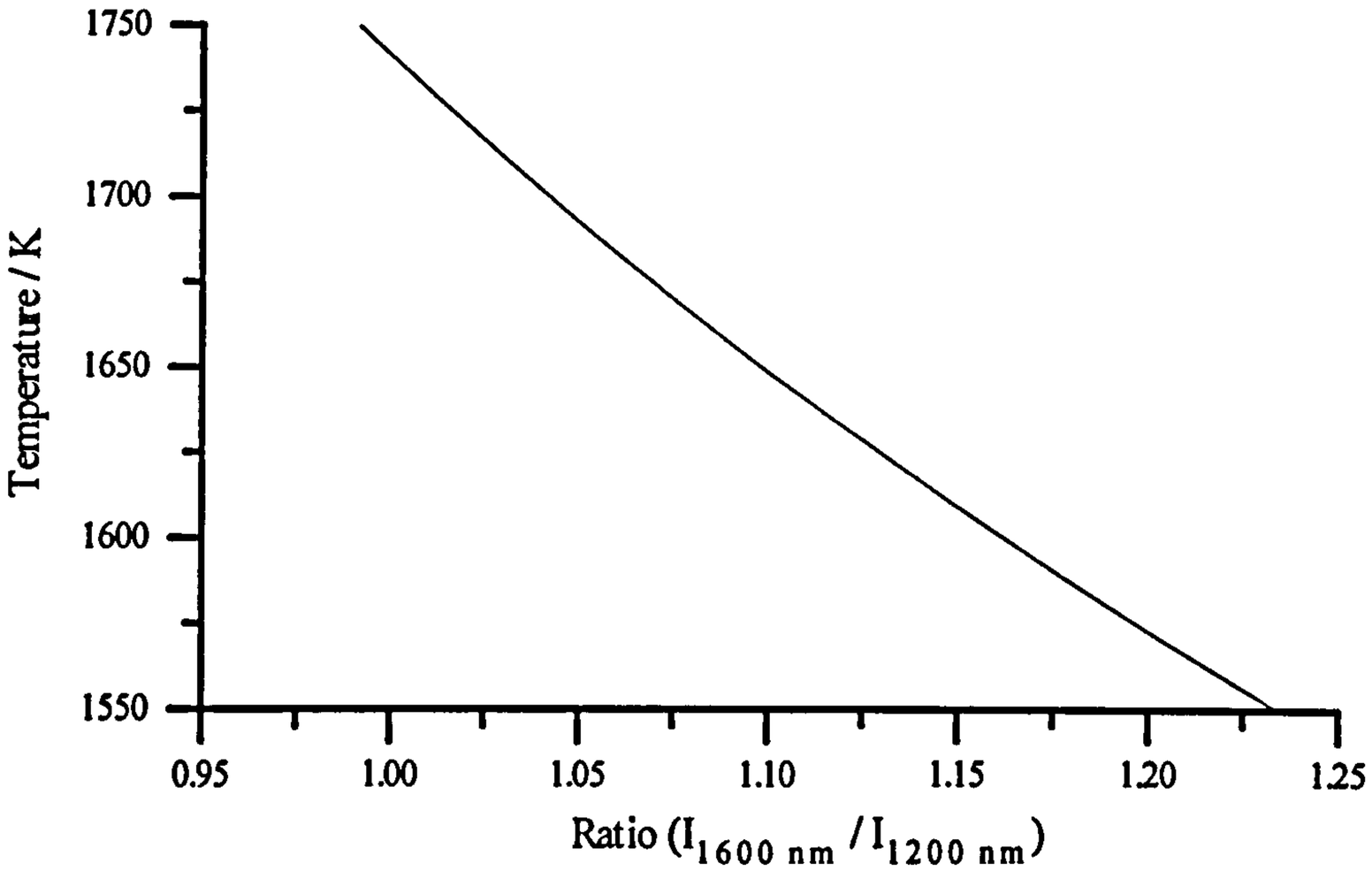

Figure 6.5. Temperature versus the ratio of intensities at 1600 nm and 1200 nm.

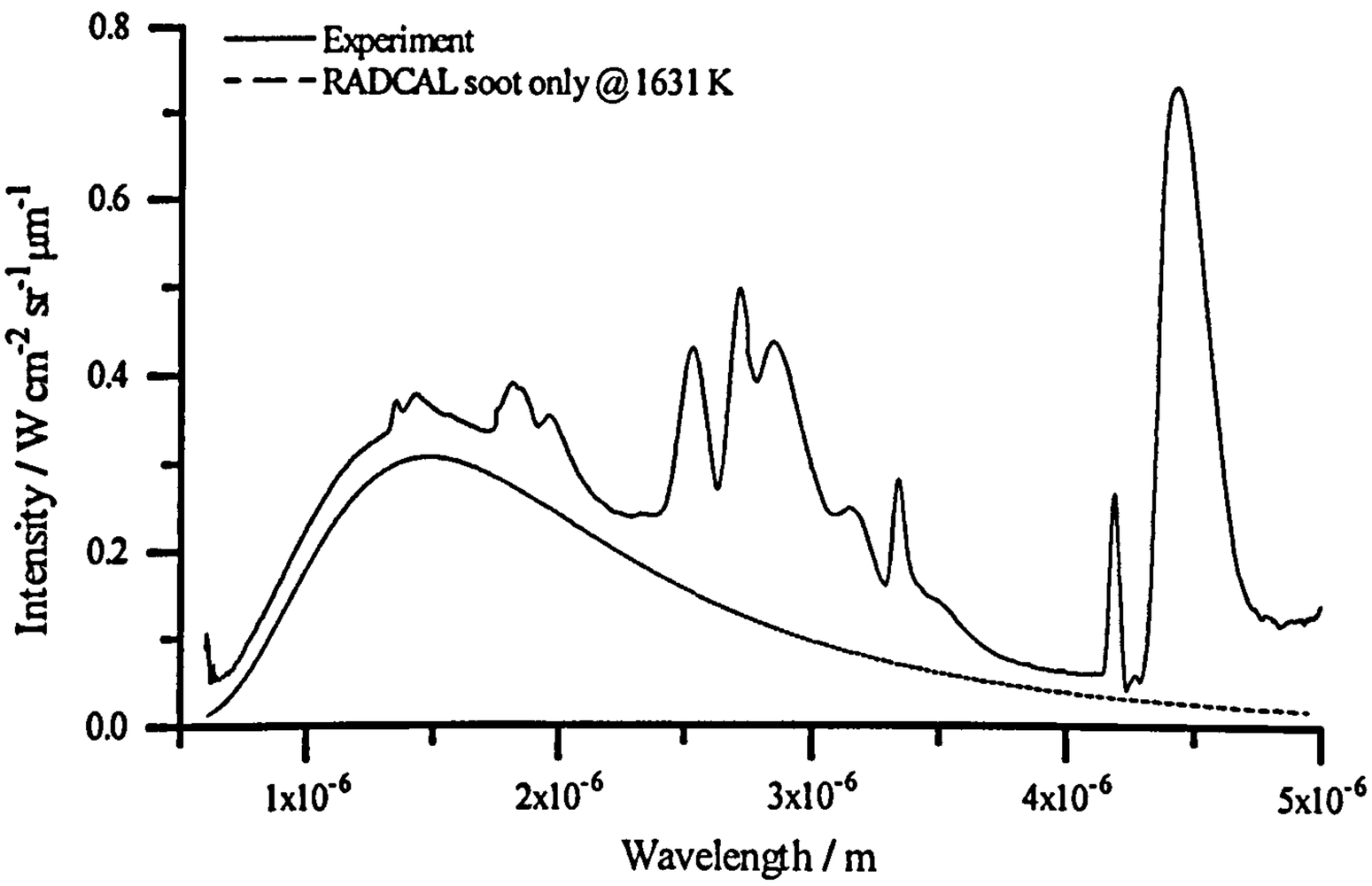

Figure 6.6. Comparison of the RADCAL generated continuum radiation, under the assumption of constant soot temperature, with experiment. Spectra shown are from the 3 atm flame, at 250 mm above the burner.

Chapter 7 - Conclusion

This chapter concludes the thesis. Firstly, by summarising the work detailed in the preceding chapters and making some overall conclusions regarding the work. Some recommendations for future work subjects are then suggested, that may answer some of the questions posed by this study.

An experimental study of turbulent methane / air jet diffusion flames has been carried out at atmospheric and elevated pressure. In particular two flames have been investigated at 1 and 3 atm. The aim of the experimental study was to create a database of flame measurements that would allow development of physical models, suitable for inclusion in CFD calculations of turbulent flame structure. This aim was mostly achieved and a database comprising measurements of mean mixture fraction, mean temperature, mean soot volume fraction, and mean and instantaneous spectrally resolved radiation intensity has been compiled. The soot measurements in particular represent a step forward, as measurements of the soot properties in turbulent methane / air flames have not been included in previous studies. The soot yield of methane was found to increase enormously with pressure, with the peak soot volume fraction found to be proportional to approximately the absolute pressure squared. This allowed the creation of a highly radiating, optically thick flame at a laboratory scale. Generally, large scale methane jet flames and LNG pool flames are still being studied. However, the range of experimental measurements that may be performed in such large scale flames is limited. Also the costs of running large scale flame / fire experiments are extremely high. It is clear that some large scale experiments may be replaced by the type of experiments performed in this study.

A new soot model has been developed with the aim of improving upon the deficiencies found in previous models. This soot model is based on the work of Moss et al. (1988) and is a two parameter model. The soot is described by its particle number density and its volume fraction. The key processes of soot formation, nucleation, coagulation, surface growth, and oxidation, are included in an approximate fashion. The model has been

calibrated by the detailed simulation of laminar methane diffusion flames and comparison with experimental measurements. The model is found to reproduce accurately the sooting trends found in these laminar flames. The source terms for the model may be expressed as functions of the two soot parameters and the mixture fraction only, which allows the use of the model to be extended to turbulent flame calculations.

The 1 and 3 atm flames studied experimentally have been modelled using the parabolic CFD code GENMIX. The conserved scalar / laminar flamelet approach is used to model the interaction between the turbulence and the chemical reactions. The flamelets are derived from the laminar flame code of Warnatz (1981). This laminar flame code incorporates a detailed model of the combustion chemistry for methane / air. The non-adiabatic nature of the flames is accommodated by using a flamelet library for each scalar. The flamelets in each library are differentiated by the amount of radiative energy loss they include. Flamelets are selected from the library by comparing the integrated flamelet enthalpy with the enthalpy obtained from a balance equation, which includes a source term for the radiative heat loss. The radiative heat loss source term includes contributions from the gaseous radiators and the soot. This multiple flamelet combustion model is found to provide excellent agreement between the predicted temperature field and experiment. Balance equations are also solved for the two soot parameters. The source terms for these soot parameters are functions of the mixture fraction as well as the soot parameters themselves. The correlation that is assumed between these three variables is found to be critical in accurately predicting the sooting behaviour of the flame. This particularly applies to the oxidation rate. Four strategies for modelling the correlation between these variables are investigated. The results indicate that some method of modelling the turbulence / chemistry interaction for the soot particles is essential for accurate prediction of the soot burnout. Within the soot growth region of the turbulent flame the assumed correlation is not found to be as critical. However, the coupling of the soot production rate with the radiative heat loss is found to be very important within this growth region. The pressure dependency of the soot surface growth and nucleation rate has not been fully determined. Further measurements of soot volume fraction and particle number density in laminar flames are needed at atmospheric and elevated pressures.

The spectral radiative emission from each of the flames has been modelled using the

RADCAL code. Mean flame properties, obtained from the GENMIX code, are used as an input to RADCAL. The prediction of the banded gaseous radiation is found to be in reasonable agreement with the experimental data. However, the continuum emission from the soot is consistently under-predicted. This is thought to be as a result of using the mean temperature profile. It is suggested that the soot in the flame only exists over a very limited range of temperatures. Two-colour pyrometry has been used to obtain a representative temperature for the soot from the experimental measurements of the radiative emission. Using this temperature for the soot in the RADCAL code, in place of the GENMIX mean temperature profile, has been found to give good agreement with experiment.

The recurring problem, which has afflicted both the modelling of the turbulent flame structure and the prediction of its emission, has been how to model the correlation between the soot properties and the gaseous species / temperature. Work still needs to be carried out in order to elucidate the instantaneous structure of sooting turbulent flames. Two dimensional, spectroscopic laser based techniques offer the most hope of providing the experimental information required. Laser induced fluorescence may be used to provide quantitative information about instantaneous species concentrations. This may be coupled with simultaneous laser induced incandescence to give quantitative information about local soot properties.

It is clear that the main barrier to satisfactorily modelling the sooting properties of turbulent diffusion flames lies not with the soot formation model but with the assumptions used for modelling the burnout of the soot. The current trend in soot model development seems to be to increase the complexity of the growth model. However, within the context of a turbulent flame calculation, this increased complexity in the soot growth term seems to amount to wasted effort. Models that ignore the highly intermittent nature of the soot and the correlation between the soot and its oxidant are totally inadequate. It is hoped that information from experiments, of the type proposed above, may allow this process to be modelled without needing to resort to the complexities of PDF transport modelling or direct numerical simulation. The fully correlated model presented in chapter 5, although clearly not a solution in itself, may represent the direction such models need to take. However, the generality of this type of model has not been tested.

7 - Conclusion

The success achieved in modelling the continuum emission from the 3 atm flame under the assumption of a constant soot temperature allows some hope that predicting the emission from such flames is actually simpler than might have been thought. However, this success lies with two factors that will not be universally applicable. The first of these is that at any particular flame location it is suggested that the soot exists over a very limited range of temperatures, this hypothesis has not been tested for its generality at all. The second factor is that the flames modelled in this work, even the 3 atm flame, are relatively optically thin. In the optically thin limit the mean emission along a ray is equal to the mean contribution from any region along the ray, as all regions are totally radiatively independent. As the optical depth of the flame increases self absorption along the ray will also increase. Hence, multi-point correlations in the radiative properties will become important. The stochastic approach discussed in chapter 6 provides a starting point for addressing such interactions between turbulence and radiative emission. However, this model has a tendency to over-estimate flame emission. Syed (1990) attributed this to the over-estimation of the widths of the high temperature reaction zones. Again, model development could be aided by experiment.

To summarise these conclusions:

i) Soot growth models are now adequate for predicting the sooting behaviour of laminar and turbulent flames, in the soot growth regions of such flames, at atmospheric pressure.

ii) The critical issue in modelling the soot yield from turbulent flames is the form of the soot burnout term. The results from this study indicate that the interaction between the turbulence and the soot burnout must be accommodated.

iii) The radiation / turbulence interaction in flames of a moderate optical depth may be ignored without compromising the accuracy of the predicted radiative emission.

References

Bilger R W (1976); The Structure of Diffusion Flames; Combustion Science and Technology; Vol. 13; pp. 155 - 170

Bilger R W (1977); Reaction Rates in Diffusion Flames; Combustion and Flame **30**: 277 - 284

Bilger R W (1988); The Structure of Turbulent Nonpremixed Flames; Twenty-Second Symposium (International) on Combustion / The Combustion Institute / pp. 475 - 488

Brookes S J, Hargrave G K, and Sherwood G (in preparation); Simultaneous Imaging of Soot Volume Fraction and OH Concentration in a Turbulent Diffusion Flame

Burke S P and Schumann T E W (1928); Diffusion Flames; Ind. Eng. Chem. **20**, 998

Charnley D (1986); Radiating Flamelet Models of Turbulent Buoyant Diffusion Flames; PhD Thesis; Southampton University

Chen J-Y, Kollmann W, and Dibble R W (1989); PDF Modelling of Turbulent Nonpremixed Methane Jet Flames; Combustion Science and Technology; Vol. 64; pp. 315 - 346

Chippet S and Gray W A (1978); The Size and Optical Properties of Soot Particles; Combustion and Flame **31**: 149 - 159

References

Coppalle A and Joyeux D (1993); Experimental and Theoretical Studies on Soot Formation in an Ethylene Jet Flame; Combustion Science and Technology; Vol. 93; pp. 375 - 386

Cox G (1977); On Radiant Heat Transfer from Turbulent Flames; Combustion Science and Technology; Vol. 17; pp. 75 - 78

Crauford N L (1984); The Structure of an Unconfined Buoyant Turbulent Diffusion Flame; PhD Thesis; Southampton University

Dalzell W H and Sarofim A F (1969); Optical Constants of Soot and their Application to Heat Flux Calculations; J. Heat Transfer; **91**; pp. 100 - 104

Delichatsios M A (1994); A Phenomenological Model for Smoke-Point and Soot Formation in Laminar Flames; Combustion Science and Technology; Vol. 100; pp. 283 - 298

Edwards D K and Menard W A (1964); Correlations for Absorption by Methane and Carbon Dioxide; Applied Optics; Vol. 3; pp. 847 - 852

El-Banhawy Y, Hassan M A, Lockwood F C, and Moneib H A (1983); Velocity and Unburned Hydrocarbon Measurements in a Vertical Turbulent Free Jet Diffusion Flame; Combustion and Flame; **53**: 145 - 148

Fairweather M, Jones W P, and Lindstedt R P (1992a); Predictions of Radiative Transfer from a Turbulent Reacting Jet in a Cross-Wind; Combustion and Flame **89**: pp 45 - 63

Fairweather M, Jones W P, Ledin H S, and Lindstedt R P (1992b); Predictions of Soot Formation in Turbulent Non-Premixed Propane Flames; Twenty-Fourth Symposium (International) on Combustion / The Combustion Institute, 1992 / pp 1067 - 1074

References

Favre A (1969); Statistical Equations of Turbulent Gases; Problems of Hydrodynamics and Continuum Mechanics; Society for Industrial and Applied Mathematics

Frenklach M (1989); J. Appl. Phys. **65**, 5142

Frenklach M, Clary D W, Gardiner W C, and Stein S E (1984); Detailed Kinetic Modelling of Soot Formation in Shock-tube Pyrolysis of Acetylene; Twentieth Symposium (International) on Combustion / The Combustion Institute / pp. 887 - 901

Frenklach M, Taki S, Durgaprasad M B, and Matula R A (1983); Soot Formation in Shock-Tube Pyrolysis of Acetylene, Allene, and 1,3-Butadiene; Combustion and Flame **54**: 81 - 101

Frenklach M and Wang H (1990); Detailed Modelling of Soot Particle Nucleation and Growth; Twenty-Third Symposium (International) on Combustion / The Combustion Institute / pp. 1559 - 1566

Fristrom R M and Westernberg A A (1965); Flame Structure; McGraw - Hill Series in Advanced Chemistry; USA

Fuchs N A (1964); The Mechanics of Aerosols; Pergamon Press

Garo A (1984); PhD Thesis; Université de haute-Alsace

Garo A, Lahaye J, and Prado G (1986); Mechanisms of Formation and Destruction of Soot Particles in a Laminar Methane-Air Diffusion Flame; Twenty-First Symposium (International) on Combustion / The Combustion Institute, 1986 / pp. 1023 - 1031

Garo A, Prado G, and Lahaye J (1990); Chemical Aspects of Soot Particles Oxidation in a Laminar Methane-Air Diffusion Flame; Combustion and Flame **79**: 226 - 233

References

Gilyazetdinov L P (1972); The Kinetics and Formation Mechanism of Carbon Black During the Thermal Decomposition of Hydrocarbons in the Gas Phase; Khim. Tverd. Topl.; 3; pp 103 - 111

Goody R M (1964); Atmospheric Radiation; Clarendon Press

Gore J P and Faeth G M (1986); Structure and Spectral Radiation Properties of Turbulent Ethylene / Air Diffusion Flames; Twenty-first Symposium (International) on Combustion / The Combustion Institute / pp. 1521 - 1531

Gore J P, Ip U-S, and Sivathanu Y R (1992); Coupled Structure and Radiation Analysis of Acetylene / Air Flames; Journal of Heat Transfer; Vol. 114; p. 487

Gray L P and Penner S S (1965); Approximate Band Absorption Calculations for Methane; J. Quant. Spec. Rad. Transfer; Vol. 5; pp. 611 - 620

Grosshandler W L (1979); Radiation from Non-homogeneous Fires; Factory Mutual Research Corp.; RC79-BT-9

Grosshandler W L (1980); Radiative Heat Transfer in Nonhomogeneous Gases: A Simplified Approach; International Journal of Heat and Mass Transfer; Vol. 23; pp. 1447 - 1459

Habib Z G and Vervisch P (1988); On the Refractive Index of Soot at Flame Temperature; Combustion Science and Technology; Vol. 59; pp. 261 - 274

Hall R J (1988); Computation of the Radiative Power Loss in a Sooting Diffusion Flame; Applied Optics; Vol 27, No 5; pp 809 - 811

Harris S J, Weiner A M, and Blint R J (1988); Formation of Small Aromatic Molecules in a Sooting Ethylene Flame; Combustion and Flame **72**: 91 - 109

References

Hassan M A, Lockwood F C, and Moneib H A (1980); Fluctuating Temperature and Mean Concentration Measurements in a Vertical Turbulent Free Jet Diffusion Flame; Italian Flame Days; IFRF

Hawthorne W R, Weddell D S, and Hottel H C (1949); Mixing and Combustion in Turbulent Gas Jets; Third Symposium on Combustion, Flame and Explosion Phenomena

Hottel H C and Sarofim A F (1967); Radiative Transfer; McGraw - Hill

Hubbard G L and Tien C L (1978); Infrared Mean Absorption Coefficients of Luminous Flames and Smoke; Journal of Heat Transfer; Vol 100; pp 235 - 239

Hughey B J and Santavicca D A (1982); A Comparison of Techniques for Reconstructing Axisymmetric Reacting Flow Fields from Absorption Measurements; Combustion Science and Technology; Vol. 29; pp. 167 - 190

Jeng S-M, Chen L-D, and Faeth G M (1982); The Structure of Buoyant Methane and Propane Diffusion Flames; Nineteenth Symposium (International) on Combustion / The Combustion Institute / pp. 349 - 358

Jeng S-M and Faeth G M (1984); Species Concentrations and Turbulence Properties in Buoyant Methane Diffusion Flames; Journal of Heat Transfer; Vol. 106; p. 721

Jeng S-M, Lai M-C, and Faeth G M (1984); Nonluminous Radiation in Turbulent Buoyant Axisymmetric Flames; Combustion Science and Technology; Vol. 40; pp. 41 - 53

Jones W P and Launder B E (1972); The Prediction of Laminarization with a Two-Equation Model of Turbulence; International Journal of Heat and Mass Transfer; Vol. 15; pp 301 - 314

Jones W P and Lindstedt R P (1988); Global Reaction Schemes for Hydrocarbon Combustion; Combustion and Flame **73**: 233 - 249

References

Kaplan C R, Baek S W, Oran E S, and Ellzey J L (1994); Dynamics of a Strongly Radiating Unsteady Ethylene Jet Diffusion Flame; Combustion and Flame **96**: 1 - 21

Kennedy I, Kollmann W, and Chen Y (1990a); Predictions of Soot in Laminar Diffusion Flames; AIAA 90-0459

Kennedy I M, Kollmann W, and Chen J-Y (1990b); A Model for Soot Formation in a Laminar Diffusion Flame; Combustion and Flame **81**: 73 - 85

Kerker M (1969); The Scattering of Light; Academic Press, London

Khan I M, Greeves G, and Probert D M (1971); Air Pollution Control in Transport Engines; Inst. Mech. Eng., 205

Kumar S and Tien C L (1989); Effective Diameter of Agglomerates for Radiative Extinction and Scattering; Combustion Science and Technology; Vol. 66; pp. 199 - 216

Lee S C and Tien C L (1981); Optical Constants of Soot in Hydrocarbon Flames; Eighteenth Symposium (International) on Combustion / The Combustion Institute / pp. 1159 - 1166

Leung K M, Lindstedt R P, and Jones W P (1991); A Simplified Reaction Mechanism for Soot Formation in Nonpremixed Flames; Combustion and Flame **87**: 289 - 305

Liew S K, Bray K N C, and Moss J B (1981); A Flamelet Model of Turbulent Non-Premixed Combustion; Combustion Science and Technology; Vol. 27; pp. 69 - 73

Liew S K, Bray K N C, and Moss J B (1984); A Stretched Laminar Flamelet Model of Turbulent Nonpremixed Combustion; Combustion and Flame **56**: 199

Lindstedt R P (1991); A Simple Reaction Mechanism for Soot Formation in Non-Premixed Flames; IUTAM Conference on Aerothermochemistry in Combustors, Taipei, Taiwan

References

Ludwig C B, Malkmus W, Reardon J E, and Thompson J A L (1973); Handbook of Infrared Radiation from Combustion Gases; NASA SP - 3080

Magnussen B F and Hjertager B H (1976); On Mathematical Modelling of Turbulent Combustion with Special Emphasis on Soot Formation and Combustion; Sixteenth Symposium (International) on Combustion / The Combustion Institute / pp. 719 - 729

Malkmus W (1963a); Infrared Emissivity of Carbon Dioxide (2.7 μm band); General Dynamics / Astronautics AE63 - 0047

Malkmus W (1963b); Infrared Emissivity of Carbon Dioxide (4.3 μm band); Journal of the Optical Society of America; Vol. 53; p. 951

Malkmus W and Thomson A (1961); Infrared Emissivity of Diatomic Gases for the Anharmonic Vibrating-Rotator Model; J. Quant. Spec. Rad. Trans.; Vol. 2; pp. 17 - 39

McBride B J, Gordon S, and Reno M A (1993); Coefficients for Calculating Thermodynamic and Transport Properties of Individual Species; NASA TM - 4513

Megaridis C M and Dobbins R A (1988); Soot Aerosol Dynamics in a Laminar Ethylene Diffusion Flame; Twenty Second Symposium (International) on Combustion / The Combustion Institute / pp. 353 - 362

Metternich M, Kollmann W, and Kennedy I M (1991); PDF Prediction of Sooting Turbulent Flames; AIAA 91-0481

Miake-Lye R C and Toner S J (1987); Laser Soot-Scattering Imaging of a Large Buoyant Diffusion Flame; Combustion and Flame **67**: 9 - 26

Mitchell R E, Sarofim A F, and Clomburg L A (1980a); Experimental and Numerical Investigation of Confined Laminar Diffusion Flames; Combustion and Flame **37**: 227 - 244

Mitchell R E, Sarofim A F, and Yu R (1980b); Nitric Oxide and Hydrogen Cyanide Formation in Laminar Methane / Air Diffusion Flames; Combustion Science and Technology; Vol. 21; pp. 157 - 167

Moneib H A (1980); PhD Thesis; University of London

Moss J B (1995); Turbulent Diffusion Flames; Combustion Fundamentals of Fire; ISBN 0-12-194230-9

Moss J B, Stewart C D, and Syed K J (1988); Flowfield Modelling of Soot Formation at Elevated Pressure; Twenty Second Symposium (International) on Combustion / The Combustion Institute / p. 413

Mullins J and Williams A (1987); The Optical Properties of Soot: A Comparison between Experimental and Theoretical Values; Fuel; Vol. 66; pp. 277 - 280

Nagle J and Strickland-Constable R F (1962); Oxidation of Carbon Between 1000 and 2000 °C; Proc. 5th Carbon Conf.; Vol. 1; pp. 154 - 164

Norton T S, Smyth K C, Housten Miller J, and Smooke M D (1993); Comparison of Experimental and Computed Species Concentration and Temperature Profiles in Laminar, Two-Dimensional Methane / Air Diffusion Flames; Combustion Science and Technology; Vol. 90; pp. 1 - 34

Planck M (1959); The Theory of Heat Radiation; Dover Publications; New York

Prado G, Garo A, Ko A, and Sarofim A (1984); Polycyclic Aromatic Hydrocarbons Formation and Destruction in a Laminar Diffusion Flame; Twentieth Symposium (International) on Combustion / The Combustion Institute, 1984 / pp. 989 - 996

Prandtl L (1925); Bericht uber Untersuchungen zur aus-gebildeten Turbulenz; ZAMM 5; 136

References

Puri R, Richardson T F, and Santoro R J (1993); Aerosol Dynamic Processes of Soot Aggregates in a Laminar Ethene Diffusion Flame; Combustion and Flame **92**: 320 - 333

Puri R, Santoro R J, and Smyth K C (1994); The Oxidation of Soot and Carbon Monoxide in Hydrocarbon Diffusion Flames; Combustion and Flame **97**: 125 - 144

Reid R C, Prausnitz J M, and Sherwood T K (1977); The Properties of Gases and Liquids; McGraw - Hill Book Company

Richardson T F (1993); PhD Dissertation; Pennsylvania State University

Rodi W (1972); The Prediction of Free Turbulent Boundary Layers by Use of a Two-Equation Model of Turbulence; PhD Thesis; London University; England

Selamet A and Arpaci V S (1991); Monochromatic Absorption of Luminous Flames; Combustion Science and Technology; Vol.78; pp. 165 - 175

Shepp L A and Logan B F (1974); The Fourier Reconstruction of a Head Section; IEEE Transactions on Nuclear Science; Vol. NS - 21; Page 21

Siegel R and Howell J P (1971); Thermal Radiation Heat Transfer; NASA SP - 164 Vol. 3

Sivathanu Y R and Faeth G M (1990); Temperature / Soot Volume Fraction Correlations in the Fuel-Rich Region of Buoyant Turbulent Diffusion Flames; Combustion and Flame **81**: 150 - 165

Smooke M D, Mitchell R E, and Keyes D E (1989); Numerical Solution of Two-Dimensional Axisymmetric Laminar Diffusion Flames; Combustion Science and Technology; Vol. 67; pp. 85 - 122

Smyth K C, Miller J H, Dorfman R C, Mallard W G, and Santoro R J (1985); Soot Inception in a Methane / Air Diffusion Flame as Characterized by Detailed Species Profiles; Combustion and Flame **62**: 157 - 181

Spalding D B (1971); Concentration Fluctuations in a Round Turbulent Free Jet; Chem. Eng. Sci. **26**, 95

Spalding D B (1977); GENMIX - A General Program for Two-Dimensional Parabolic Phenomena; Pergamon Press

Stårner S H and Bilger R W (1985); Characteristics of a Piloted Diffusion Flame Designed for Study of Combustion Turbulence Interactions; Combustion and Flame **61**: 29 - 38

Syed K J (1990); Soot and Radiation Modelling in Buoyant Fires; PhD Thesis; Cranfield Institute of Technology

Tait N P and Greenhalgh D A (1993); PLIF Imaging of Fuel Fraction in Practical Devices and LII Imaging of Soot; Ber. Bunsenges. Phys. Chem. 97, 1619 - 1625 (1993) No. 12

Tesner P A, Snegirova T D, and Knorre V G (1971); Kinetics of Dispersed Carbon Formation; Combustion and Flame **17**: 253

Tien C L and Lee S C (1982); Flame Radiation; Prog. Energy Combust. Sci.; Vol. 8; pp. 41 - 59

Tsuji H and Yamaoka I (1969); The Counterflow Diffusion Flame in the Forward Stagnation Region of a Porous Cylinder; Twelfth Symposium (International) on Combustion / The Combustion Institute / pp 997 - 1005

Viskanta R and Mengüç M P (1987); Radiation Heat Transfer in Combustion Systems; Prog. Energy Combust. Sci.; Vol. 13; pp. 97 - 160

References

Warnatz J (1981); The Structure of Laminar Alkane-, Alkene- and Acetylene Flames; Eighteenth Symposium (International) on Combustion / The Combustion Institute / pp 369 - 384

Whitaker S (1972); AIChE J.; 18; 361

Young K J (1993); Soot Formation in Turbulent Vaporised Kerosine - Air Jet Flames at Elevated Pressure; PhD Thesis; Cranfield Institute of Technology

Young K J and Moss J B (1995); Modelling Sooting Turbulent Jet Flames Using an Extended Flamelet Technique; Combustion Science and Technology; Vol. 105; pp 33 - 53

Appendix - Experimental Data

The experimental data for the two flames are presented in this section. Tables are given for the mixture fraction and temperature data. The soot volume fraction and radiation intensity data are presented graphically. The two flames are referred to by their operating pressure.

Radial Mixture Fraction Profile - 1 atm Flame - Height = 150 mm	
Radial Position from Axis / mm	Mixture Fraction
29.48	0.0207
26.48	0.029
23.48	0.034
20.48	0.050
17.48	0.074
14.48	0.124
11.48	0.150
8.48	0.191
5.48	0.233
2.48	0.257
0.52	0.262
3.52	0.255
6.52	0.226

Radial Mixture Fraction Profile - 1 atm Flame - Height = 200 mm	
Radial Position from Axis / mm	Mixture Fraction
29.48	0.022
26.48	0.029
23.48	0.044

20.48	0.064
17.48	0.085
14.48	0.111
11.48	0.142
8.48	0.164
5.48	0.187
2.48	0.202
0.52	0.213

Radial Mixture Fraction Profile - 1 atm Flame - Height = 200 mm	
Radial Position from Axis / mm	Mixture Fraction
29.48	0.019
26.48	0.030
23.48	0.051
20.48	0.081
17.48	0.100
14.48	0.142
11.48	0.177
8.48	0.204
5.48	0.224
2.48	0.237
0.52	0.233
3.52	0.235
6.52	0.216
9.52	0.192

Radial Mixture Fraction Profile - 1 atm Flame - Height = 250 mm	
Radial Position from Axis / mm	Mixture Fraction
34.48	0.017
30.48	0.025
26.48	0.036
22.48	0.056
18.48	0.088
14.48	0.118
10.48	0.146
6.48	0.170
2.48	0.173
1.52	0.186
5.52	0.180

Radial Mixture Fraction Profile - 1 atm Flame - Height = 300 mm	
Radial Position from Axis / mm	Mixture Fraction
43.1	0.023
38.1	0.025
33.1	0.032
28.1	0.041
23.1	0.060
18.1	0.081
13.1	0.107
8.1	0.130
3.1	0.141
1.9	0.144

6.9	0.135
11.9	0.116
16.9	0.090
21.9	0.066

Radial Mixture Fraction Profile - 1 atm Flame - Height = 350 mm	
Radial Position from Axis / mm	Mixture Fraction
44.74	0.020
39.74	0.023
34.74	0.028
29.74	0.034
24.74	0.046
19.74	0.055
14.74	0.071
9.74	0.085
4.74	0.093
0.26	0.094
5.26	0.092
10.26	0.081
15.26	0.069
20.26	0.055
25.26	0.042

Radial Mixture Fraction Profile - 1 atm Flame - Height = 425 mm	
Radial Position from Axis / mm	Mixture Fraction
45	0.018

40	0.021
35	0.027
30	0.031
25	0.037
20	0.045
15	0.051
10	0.059
5	0.063
0	0.066
5	0.065

Axial Mixture Fraction Profile - 1 atm Flame - Centreline	
Height Above Burner / mm	Mixture Fraction
50	0.737
100	0.473
150	0.359

Radial Temperature Profile - 1 atm Flame - Height = 150 mm	
Radial Position from Axis / mm	Temperature / K
34	288
31	288
28	302
25	402
22	915
19	1474
16	1719

13	1612
10	1439
7	1312
4	1245
1	1206
2	1220
5	1270
8	1330
11	1513
14	1682
17	1677
20	1245
23	736
26	366
29	290
32	288

Radial Temperature Profile - 1 atm Flame - Height = 150 mm	
Radial Distance from Axis / mm	Temperature / K
33.8	288
30.8	288
27.8	293
24.8	397
21.8	879
18.8	1506
15.8	1741

12.8	1594
9.8	1410
6.8	1306
3.8	1243
0.8	1215
2.2	1229
5.2	1274
8.2	1357
11.2	1524
14.2	1727
17.2	1688
20.2	1228
23.2	560
26.2	342
29.2	288
32.2	288

Radial Temperature Profile - 1 atm Flame - Height = 200 mm	
Radial Distance from Axis / mm	Temperature / K
44.5	288
41.5	288
38.5	292
35.5	355
32.5	419
29.5	658
26.5	927

23.5	1330
20.5	1635
17.5	1685
14.5	1604
11.5	1506
8.5	1412
5.5	1361
2.5	1332
0.5	1300
3.5	1313
6.5	1345
9.5	1436
12.5	1592
15.5	1679
18.5	1669
21.5	1488
24.5	1163
27.5	816
30.5	589
33.5	359
36.5	298
39.5	291
42.5	288

Radial Temperature Profile - 1 atm Flame - Height = 200 mm	
Radial Distance from Axis / mm	Temperature / K

44.3	288
41.3	288
38.3	297
35.3	327
32.3	412
29.3	670
26.3	956
23.3	1373
20.3	1587
17.3	1695
14.3	1609
11.3	1496
8.3	1424
5.3	1359
2.3	1315
0.7	1304
3.7	1316
6.7	1355
9.7	1441
12.7	1615
15.7	1721
18.7	1690
21.7	1510
24.7	1167
27.7	878
30.7	510

33.7	360
36.7	296
39.7	288
42.7	288

Radial Temperature Profile - 1 atm flame - Height = 250 mm	
Radial Distance from Axis / mm	Temperature / K
54.8	288
50.8	288
46.8	314
42.8	331
38.8	492
34.8	746
30.8	1005
26.8	1275
22.8	1541
18.8	1659
14.8	1635
10.8	1539
6.8	1466
2.8	1421
1.2	1408
5.2	1434
9.2	1533
13.2	1626
17.2	1688

21.2	1599
25.2	1448
29.2	1172
33.2	763
37.2	542
41.2	384
45.2	334
49.2	290
53.2	289

Radial Temperature Profile - 1 atm Flame - Height = 250 mm	
Radial Distance from Axis / mm	Temperature / K
54.6	288
50.6	288
46.6	305
42.6	330
38.6	521
34.6	725
30.6	983
26.6	1320
22.6	1510
18.6	1661
14.6	1630
10.6	1534
6.6	1465
2.6	1426

1.4	1391
5.4	1402
9.4	1508
13.4	1637
17.4	1709
21.4	1629
25.4	1403
29.4	1090
33.4	791
37.4	564
41.4	414
45.4	297
49.4	290
53.4	288

Radial Temperature Profile - 1 atm Flame - Height = 250 mm	
Radial Distance from Axis / mm	Temperature / K
53.7	291
49.7	298
45.7	346
41.7	387
37.7	563
33.7	806
29.7	1112
25.7	1388
21.7	1611

17.7	1656
13.7	1621
9.7	1546
5.7	1481
1.7	1452
2.3	1451
6.3	1507
10.3	1578
14.3	1652
18.3	1670
22.3	1559
26.3	1295
30.3	1058
34.3	754
38.3	518
42.3	396
46.3	335

Radial Temperature Profile - 1 atm Flame - Height = 300 mm	
Radial Distance from Axis / mm	Temperature / K
57.5	311
52.5	342
47.5	491
42.5	531
37.5	816
32.5	1037

27.5	1359
22.5	1560
17.5	1654
12.5	1638
7.5	1577
2.5	1520
2.5	1522
7.5	1569
12.5	1643
17.5	1647
22.5	1555
27.5	1334
32.5	1064
37.5	849
42.5	608
47.5	451
52.5	332

Radial Temperature Profile - 1 atm Flame - Height = 350 mm	
Radial Distance from Axis / mm	Temperature / K
62.7	365
57.7	367
52.7	439
47.7	641
42.7	807
37.7	952

32.7	1170
27.7	1410
22.7	1490
17.7	1642
12.7	1630
7.7	1618
2.7	1604
2.3	1596
7.3	1601
12.3	1654
17.3	1631
22.3	1552
27.3	1424
32.3	1184
37.3	963
42.3	808
47.3	664
52.3	437

Radial Temperature Profile - 1 atm Flame - Height = 425 mm	
Radial Distance from Axis / mm	Temperature / K
63.9	451
58.9	489
53.9	665
48.9	751
43.9	872

38.9	1050
33.9	1224
28.9	1348
23.9	1458
18.9	1563
13.9	1630
8.9	1664
3.9	1658
1.1	1667
6.1	1653
11.1	1645
16.1	1573
21.1	1501
26.1	1414
31.1	1230
36.1	1130
41.1	990
46.1	802
51.1	640

Axial Temperature Profile - 1 atm Flame - Centreline	
Height Above Burner / mm	Temperature / K
50	677
100	1024
150	1197
200	1290

250	1354

Axial Temperature Profile - 1 atm Flame - Centreline	
Height Above Burner / mm	Temperature / K
50	672
100	1021
150	1198
200	1291
250	1348

Radial Temperature Profile - 3 atm Flame - Height = 50 mm	
Radial Distance from Axis / mm	Temperature / K
19.5	293
18.5	294
17.5	294
16.5	295
15.5	294
14.5	294
13.5	295
12.5	296
11.5	295
10.5	301
9.5	320
8.5	586
7.5	1255
6.5	1848

5.5	1616
4.5	1344
3.5	1065
2.5	890
1.5	755
0.5	680
0.5	674
1.5	731
2.5	824
3.5	944
4.5	1122
5.5	1305
6.5	1690
7.5	1618
8.5	905
9.5	347

Radial Temperature Profile - 3 atm Flame - Height = 100 mm	
Radial Distance from Axis / mm	Temperature / K
19.2	294
16.2	345
13.2	769
10.2	1527
7.2	1507
4.2	1138
1.2	993

1.8	987
4.8	1117
7.8	1386
10.8	1596
13.8	856
16.8	322

Radial Temperature Profile - 3 atm - Height = 150 mm	
Radial Distance from Axis / mm	Temperature / K
34	297
31	301
28	331
25	351
22	551
19	745
16	1187
13	1452
10	1524
7	1394
4	1213
1	1158
2	1177
5	1273
8	1440
11	1553
14	1385

17	936
20	706
23	420
26	330

Radial Temperature Profile - 3 atm Flame - Height = 200 mm	
Radial Distance from Axis / mm	Temperature / K
43.2	298
39.2	321
35.2	375
31.2	425
27.2	575
23.2	911
19.2	1088
15.2	1381
11.2	1495
7.2	1467
3.2	1377
0.8	1356
4.8	1427
8.8	1493
12.8	1468
16.8	1246
20.8	1026
24.8	788
28.8	564

32.8	436
36.8	344

Radial Temperature Profile - 3 atm Flame - Height = 250 mm	
Radial Distance from Axis / mm	Temperature / K
53.5	387
49.5	378
45.5	402
41.5	503
37.5	529
33.5	735
29.5	740
25.5	908
21.5	1181
17.5	1354
13.5	1449
9.5	1496
5.5	1500
1.5	1505
2.5	1504
6.5	1528
10.5	1514
14.5	1430
18.5	1298
22.5	1125
26.5	930

30.5	814
34.5	670
38.5	535
42.5	480
46.5	418
50.5	413

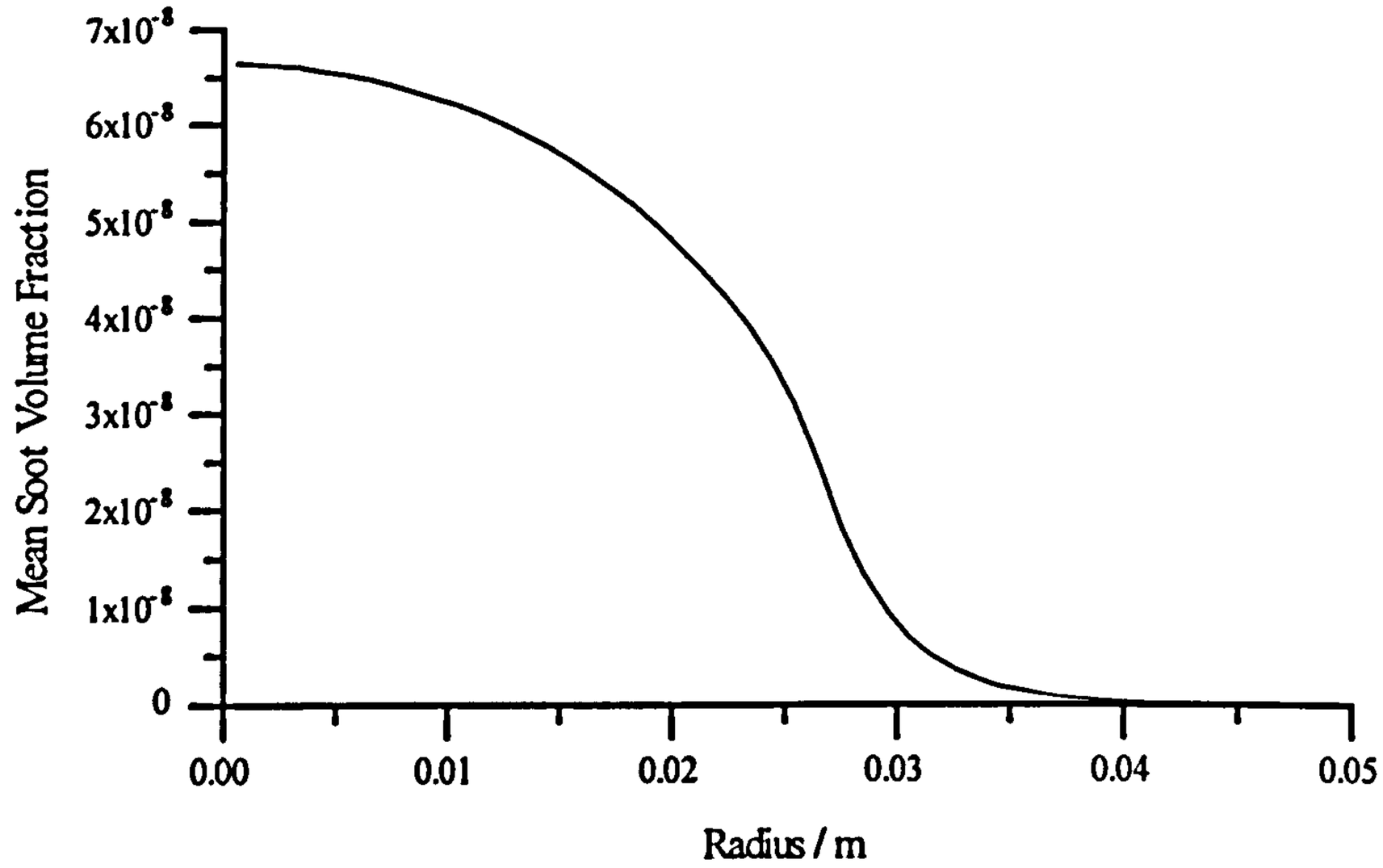

Radial soot volume fraction profile. Profile measured in the 1 atm flame at a height of 300 mm above the burner exit plane.

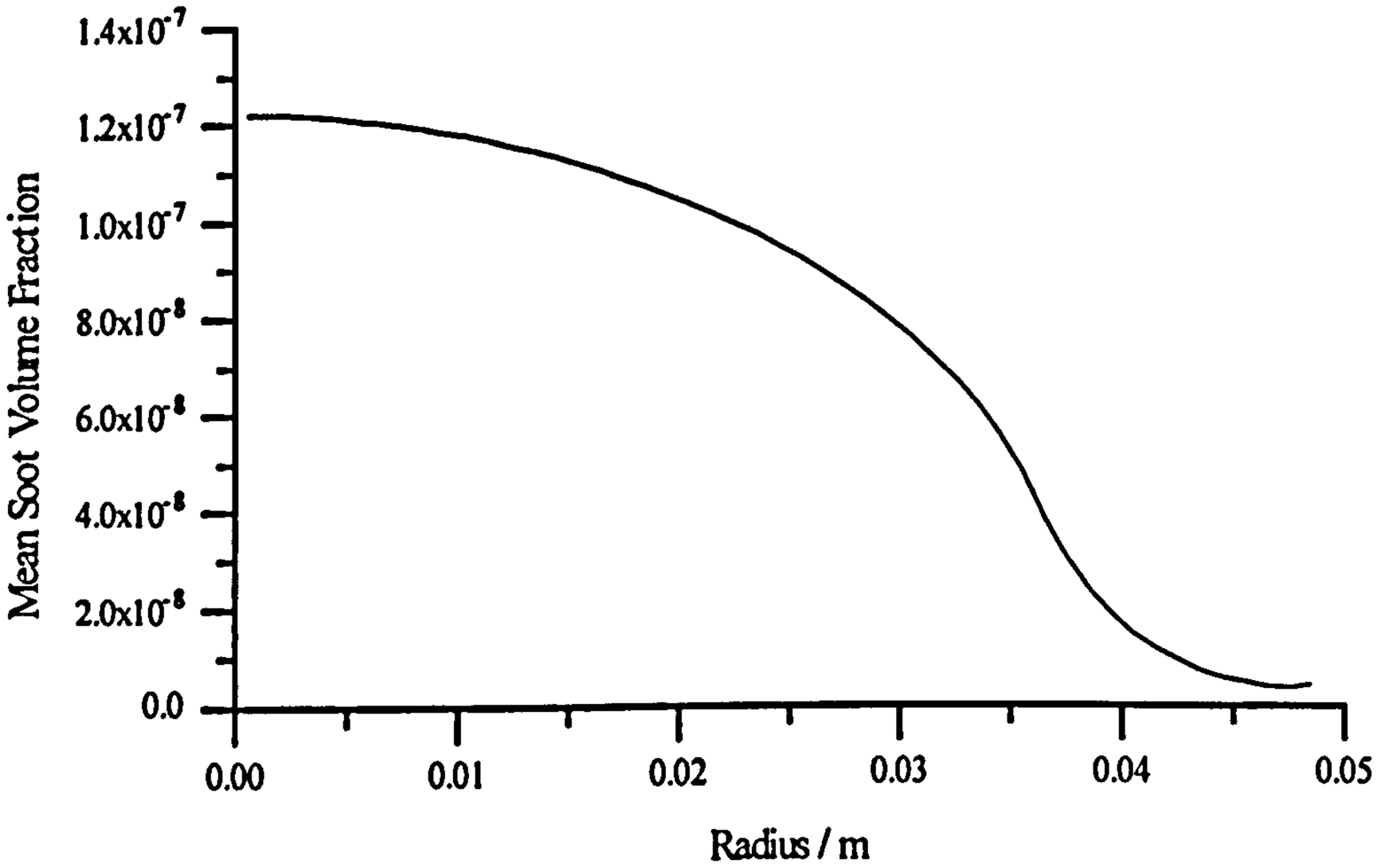

Radial soot volume fraction profile. Profile measured in the 1 atm flame at a height of 350 mm above the burner exit plane.

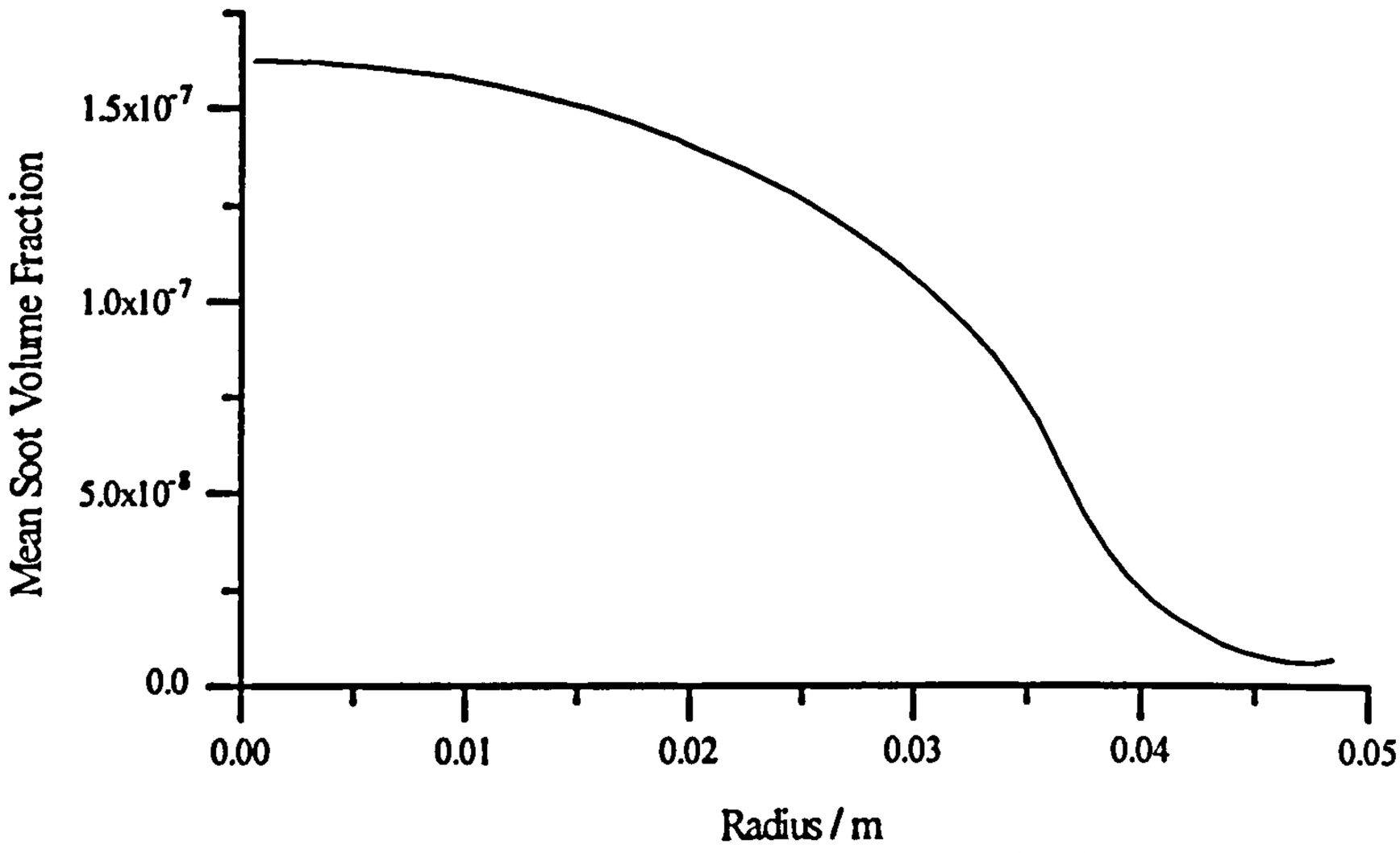

Radial soot volume fraction profile. Profile measured in the 1 atm flame at a height of 425 mm above the exit plane of the burner.

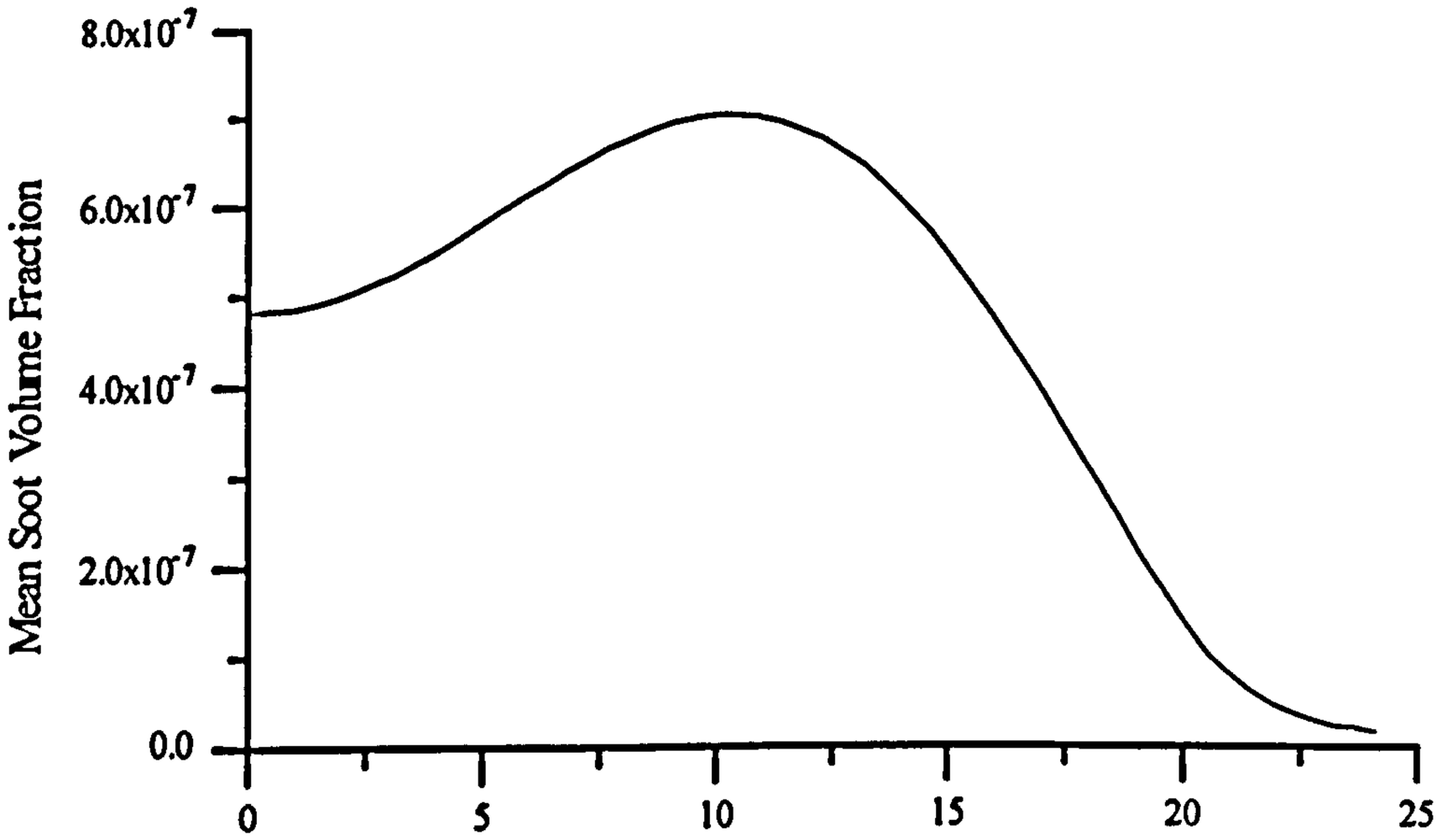

Radial soot volume fraction profile. Profile measured in the 3 atm flame at a height of 150 mm above the exit plane of the burner.

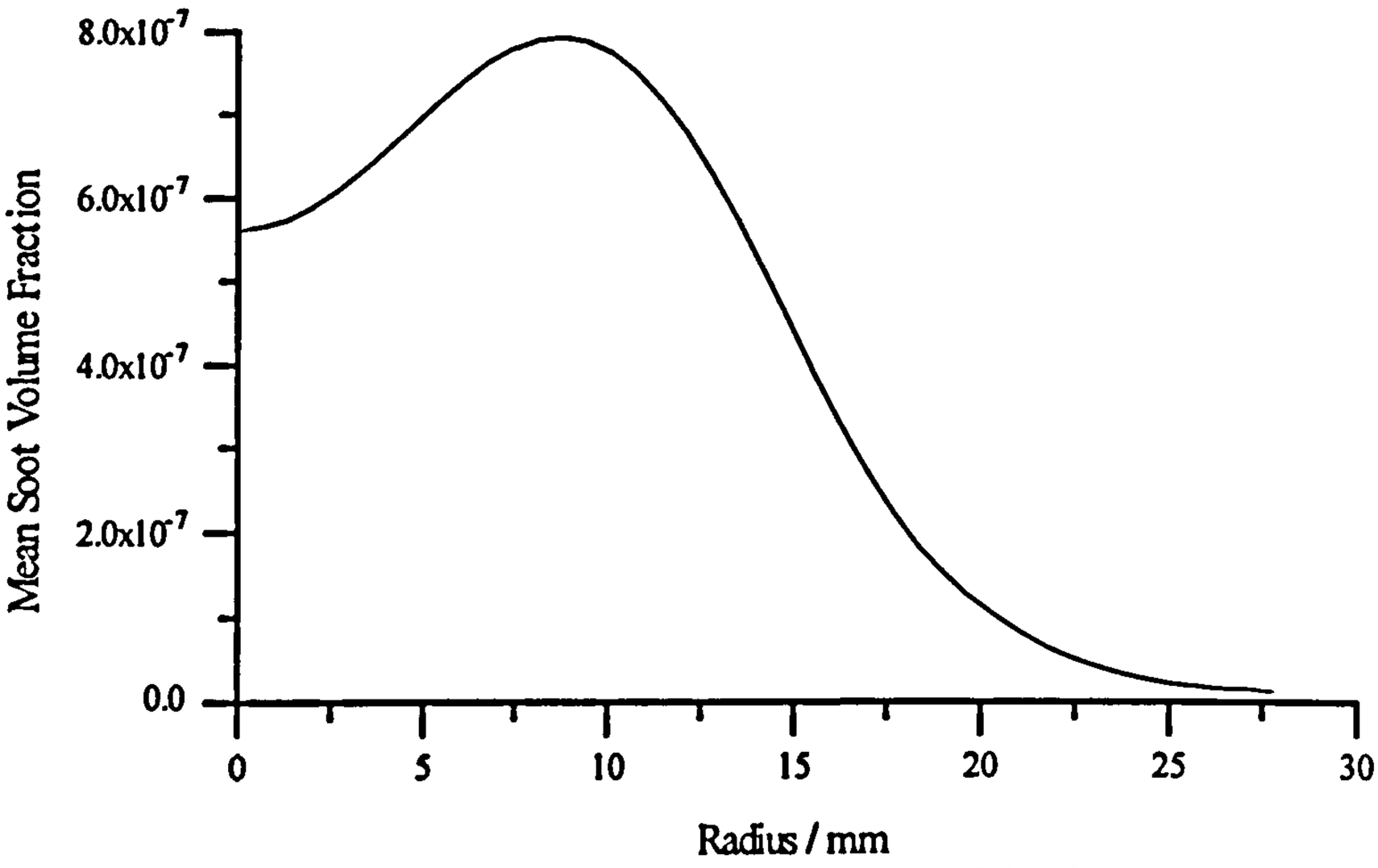

Radial soot volume fraction profile. Profile measured in the 3 atm flame at a height of 150 mm above the exit plane of the burner.

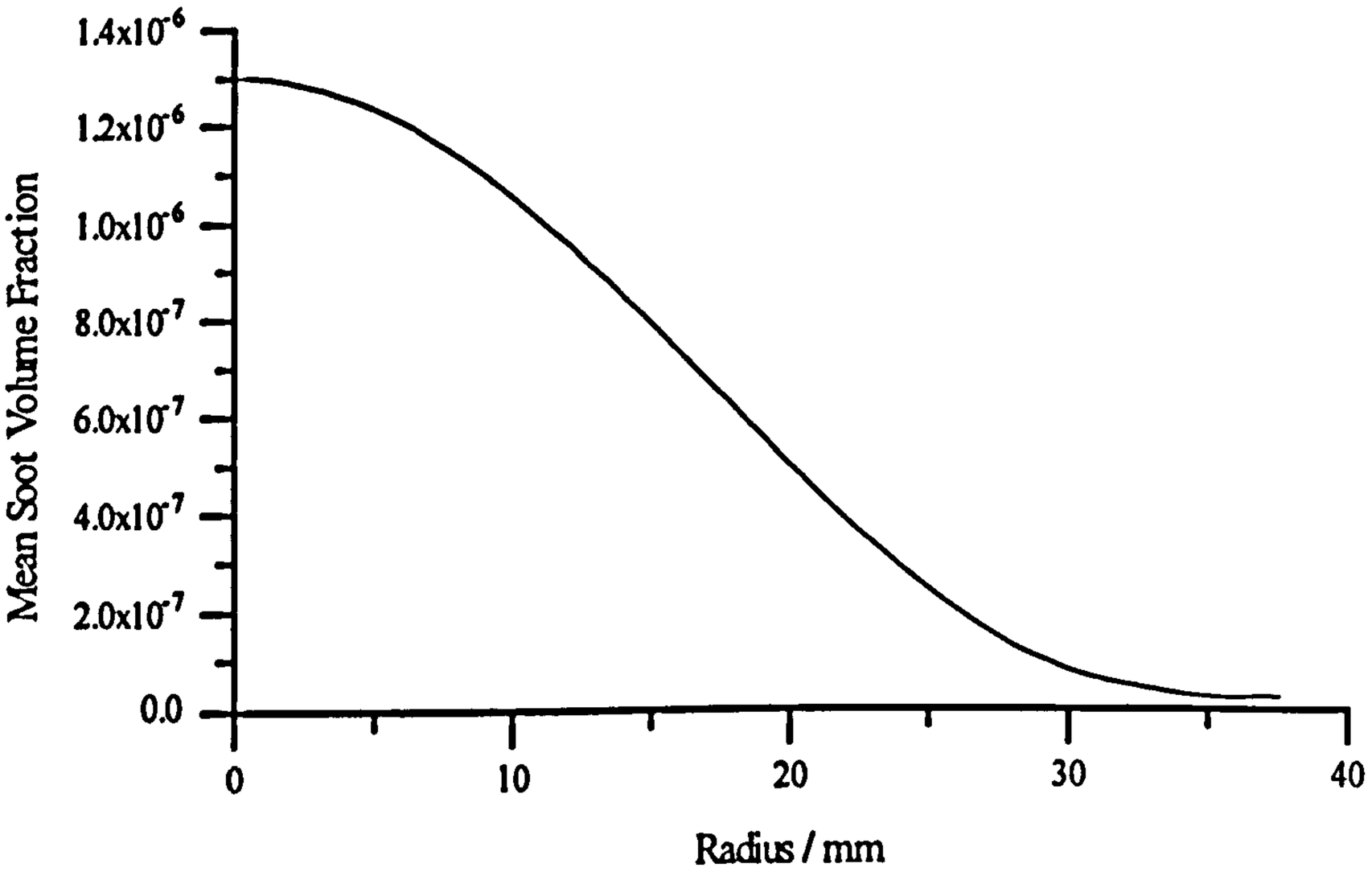

Radial soot volume fraction profile. Profile measured in the 3 atm flame at a height of 200 mm above the exit plane of the burner.

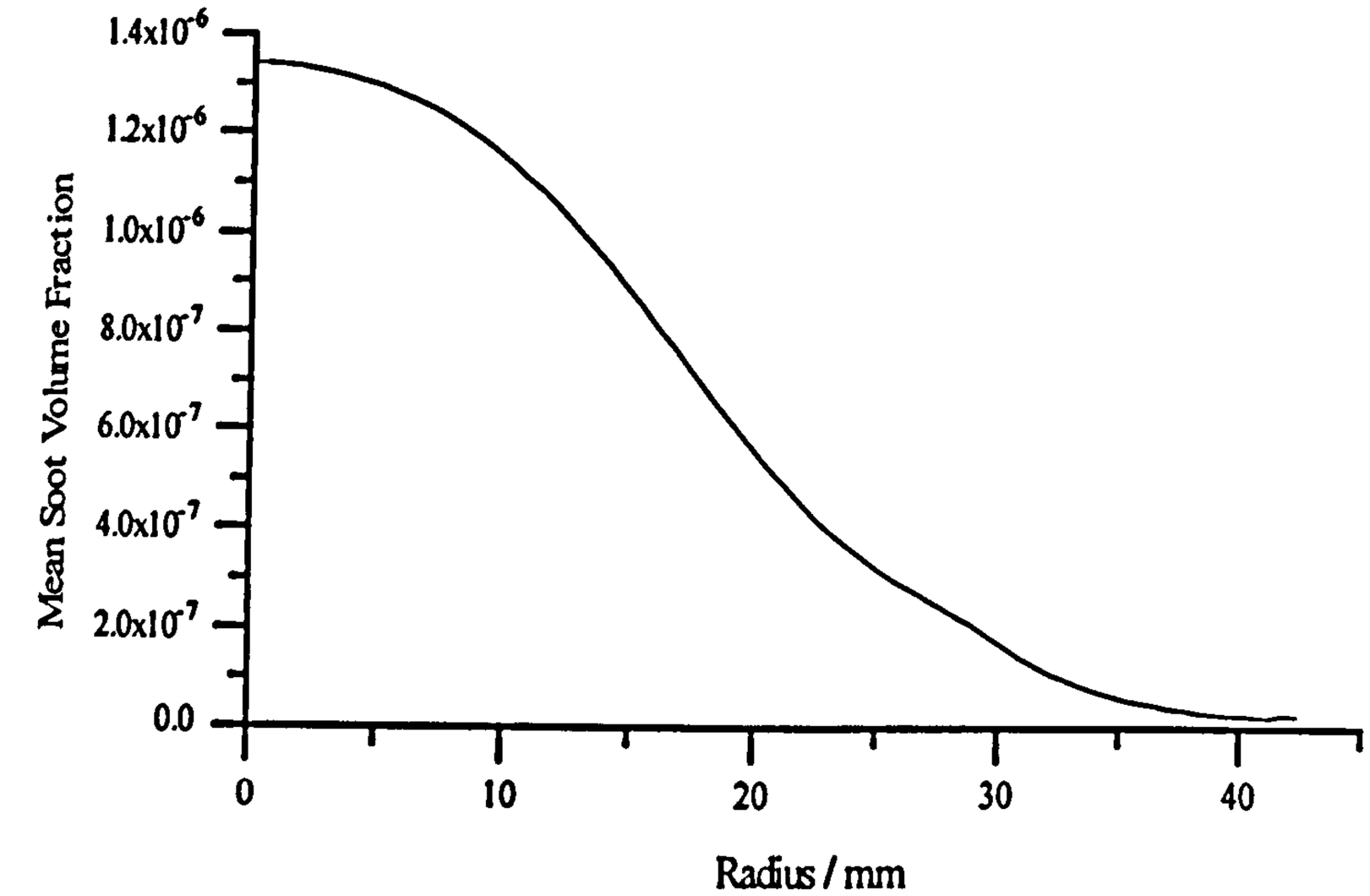

Radial soot volume fraction profile. Profile measured in the 3 atm flame at a height of 250 mm above the exit plane of the burner.

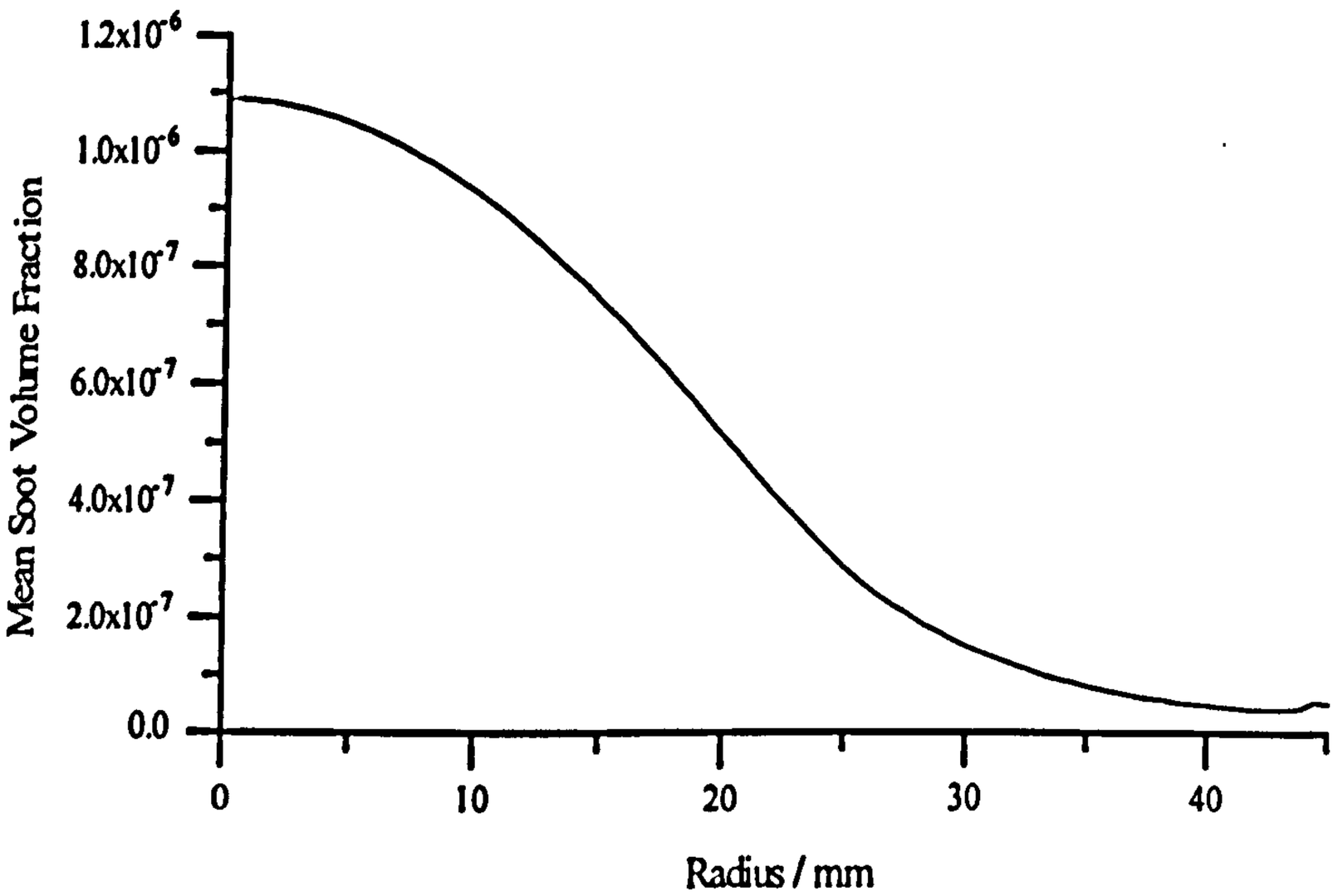

Radial soot volume fraction profile. Profile measured in the 3 atm flame at a height of 300 mm above the exit plane of the burner.

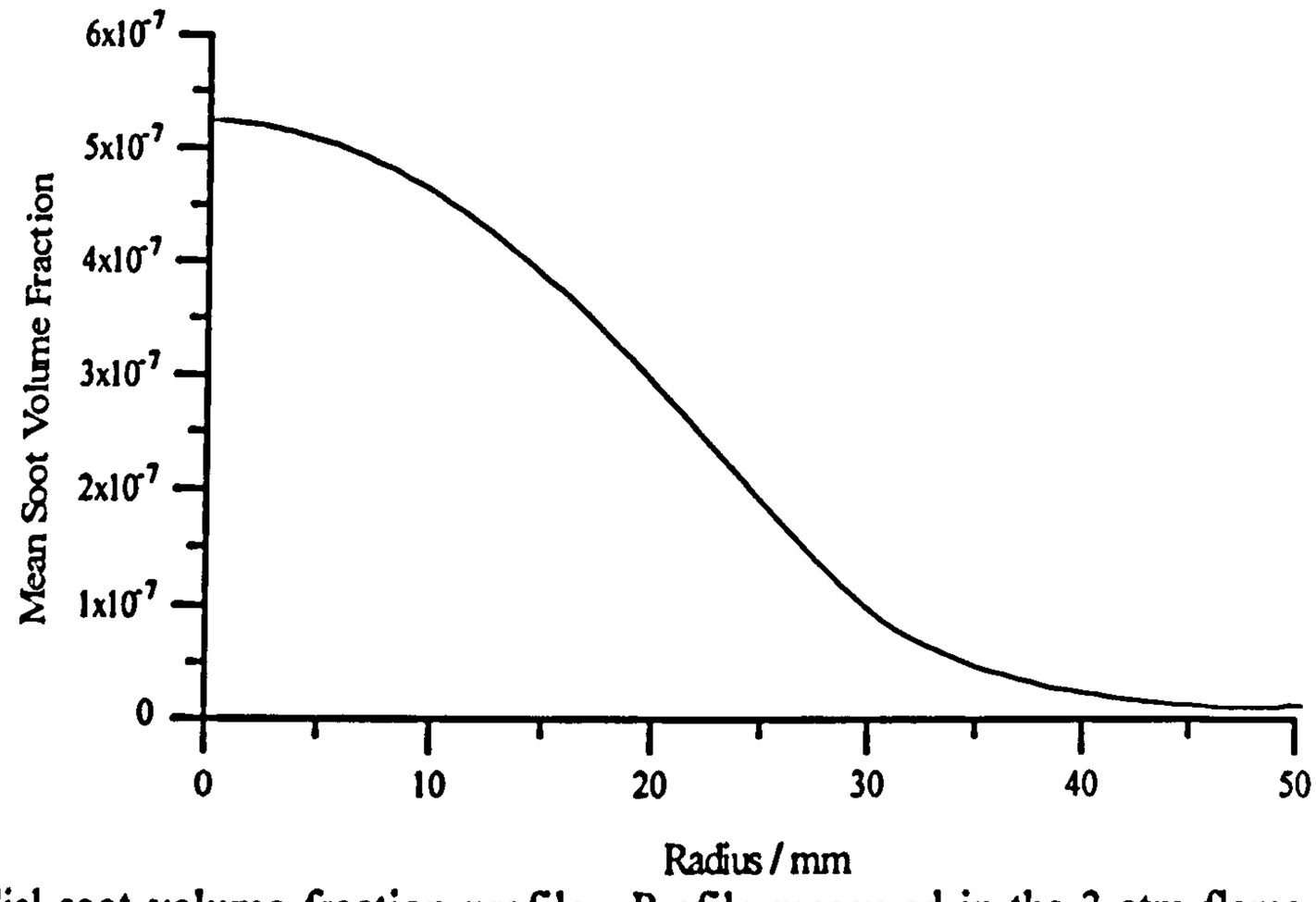

Radial soot volume fraction profile. Profile measured in the 3 atm flame at a height of 350 mm above the exit plane of the burner.

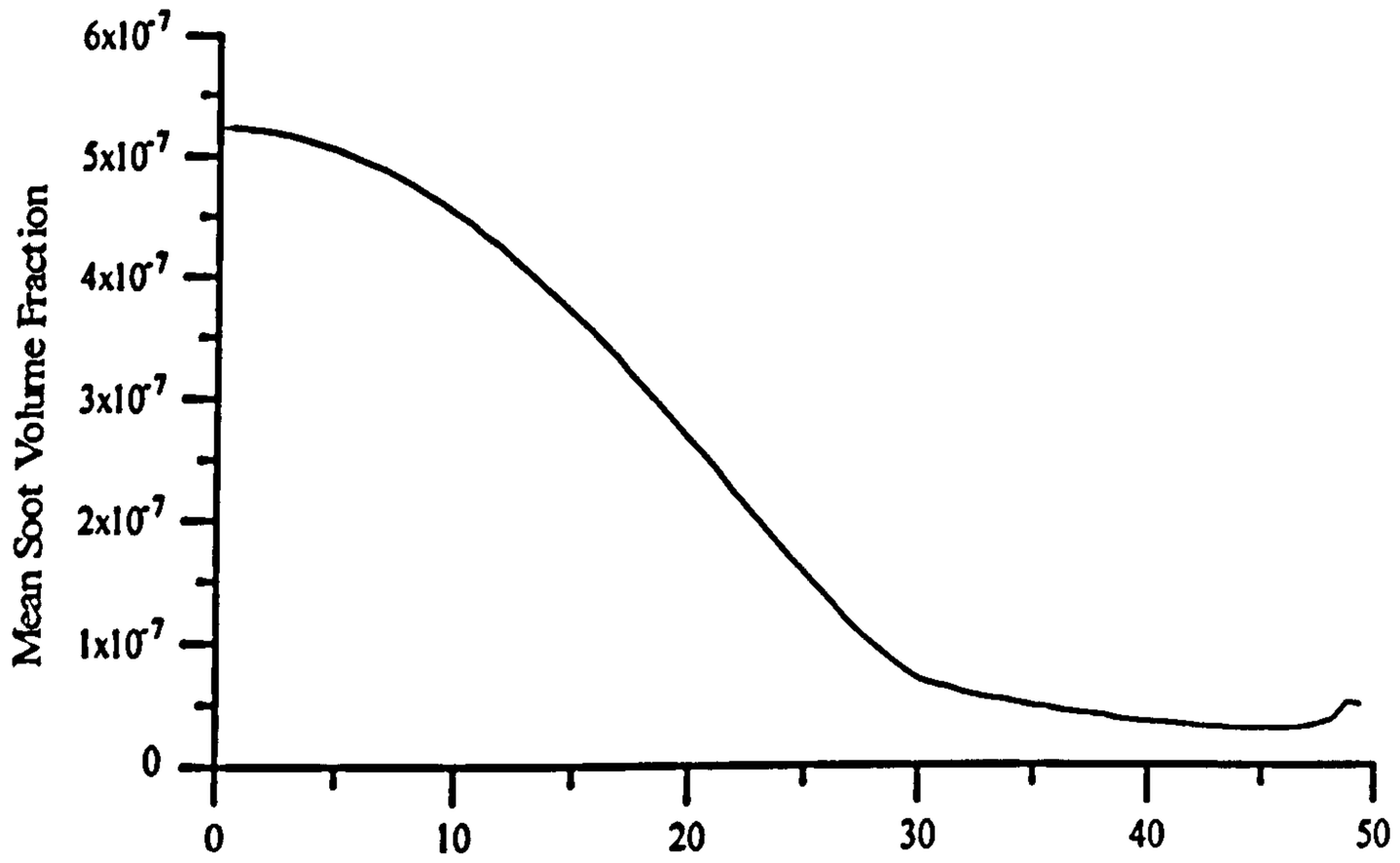

Radial soot volume fraction profile. Profile measured in the 3 atm flame at a height of 350 mm above the exit plane of the burner.

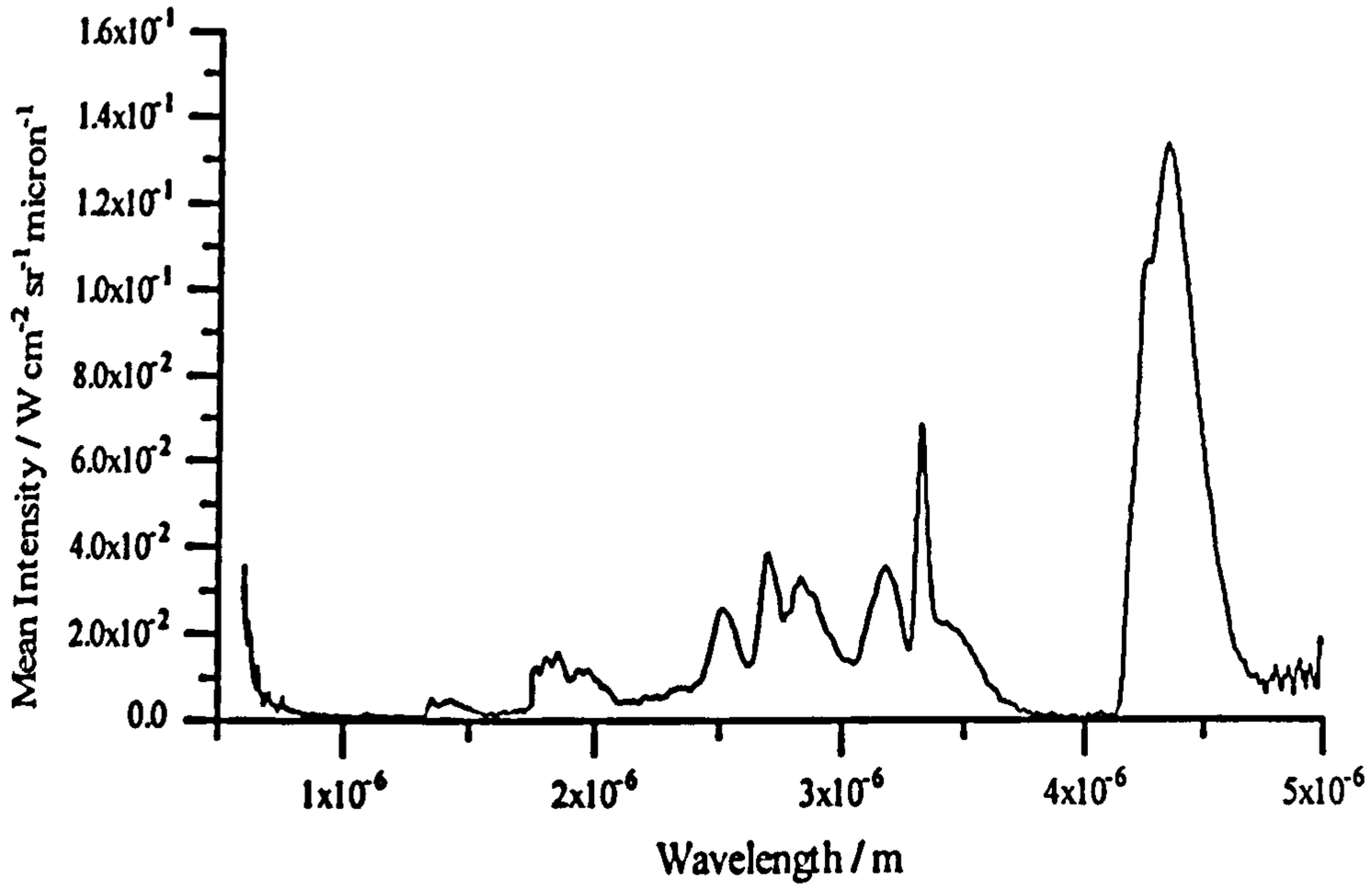

Radiation intensity along a ray perpendicular to, and passing through, the axis of the flame. This spectrum was recorded in the 1 atm flame at a height of 50 mm above the burner exit plane.

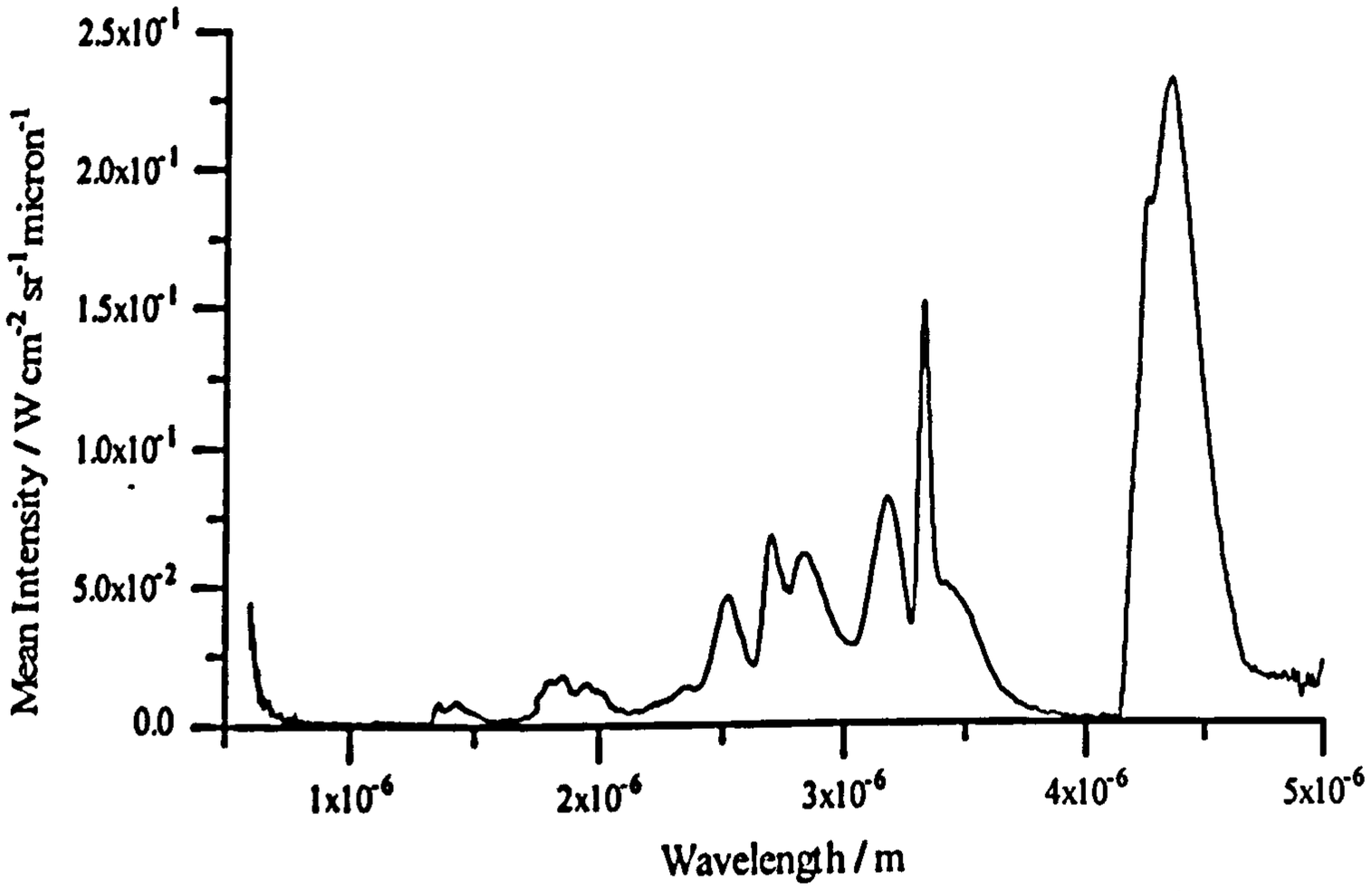

Radiation intensity. This spectrum was recorded in the 1 atm flame at a height of 100 mm above the exit plane of the burner.

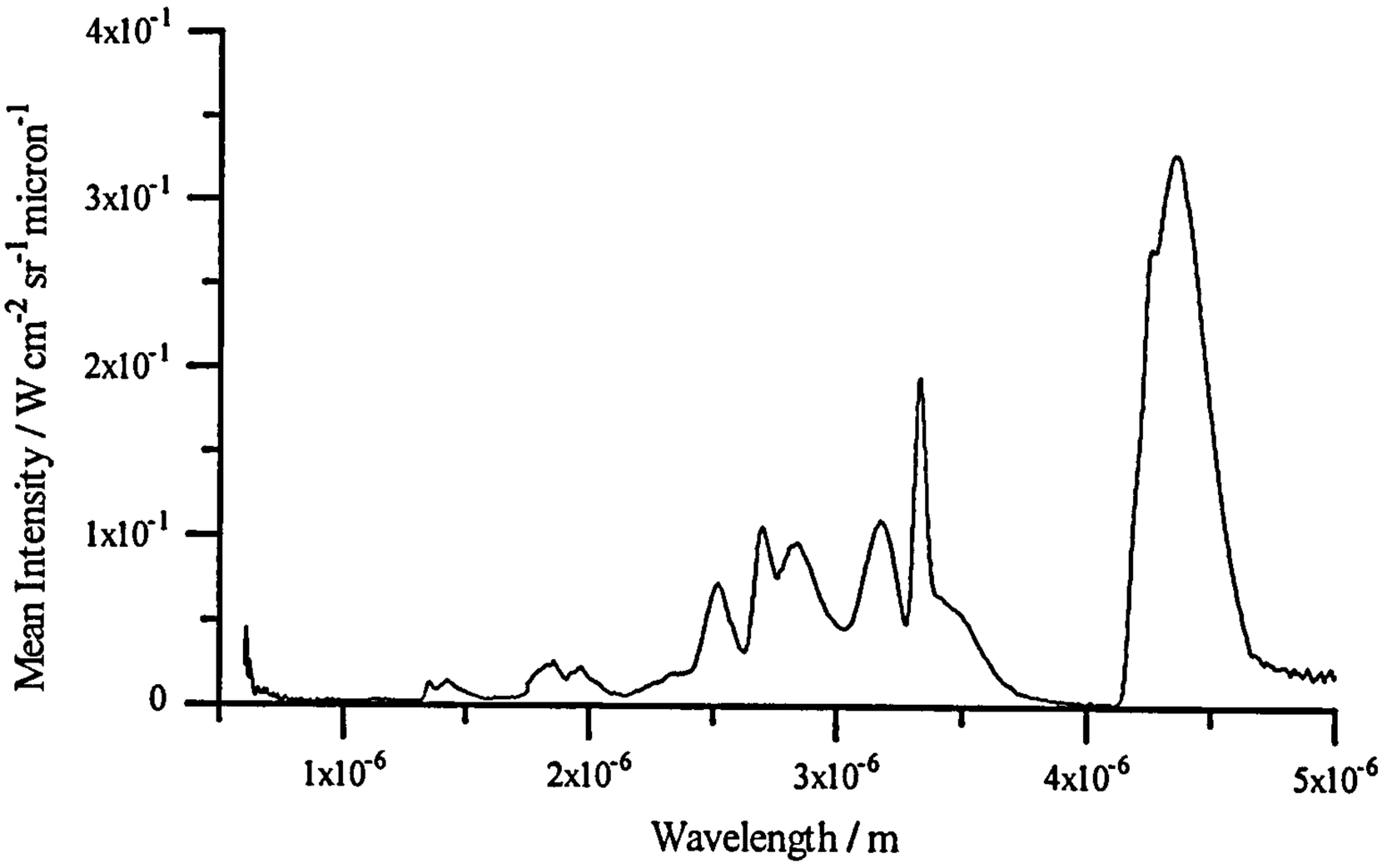

Radiation intensity. This spectrum was recorded in the 1 atm flame at a height of 150 mm above the burner exit plane.

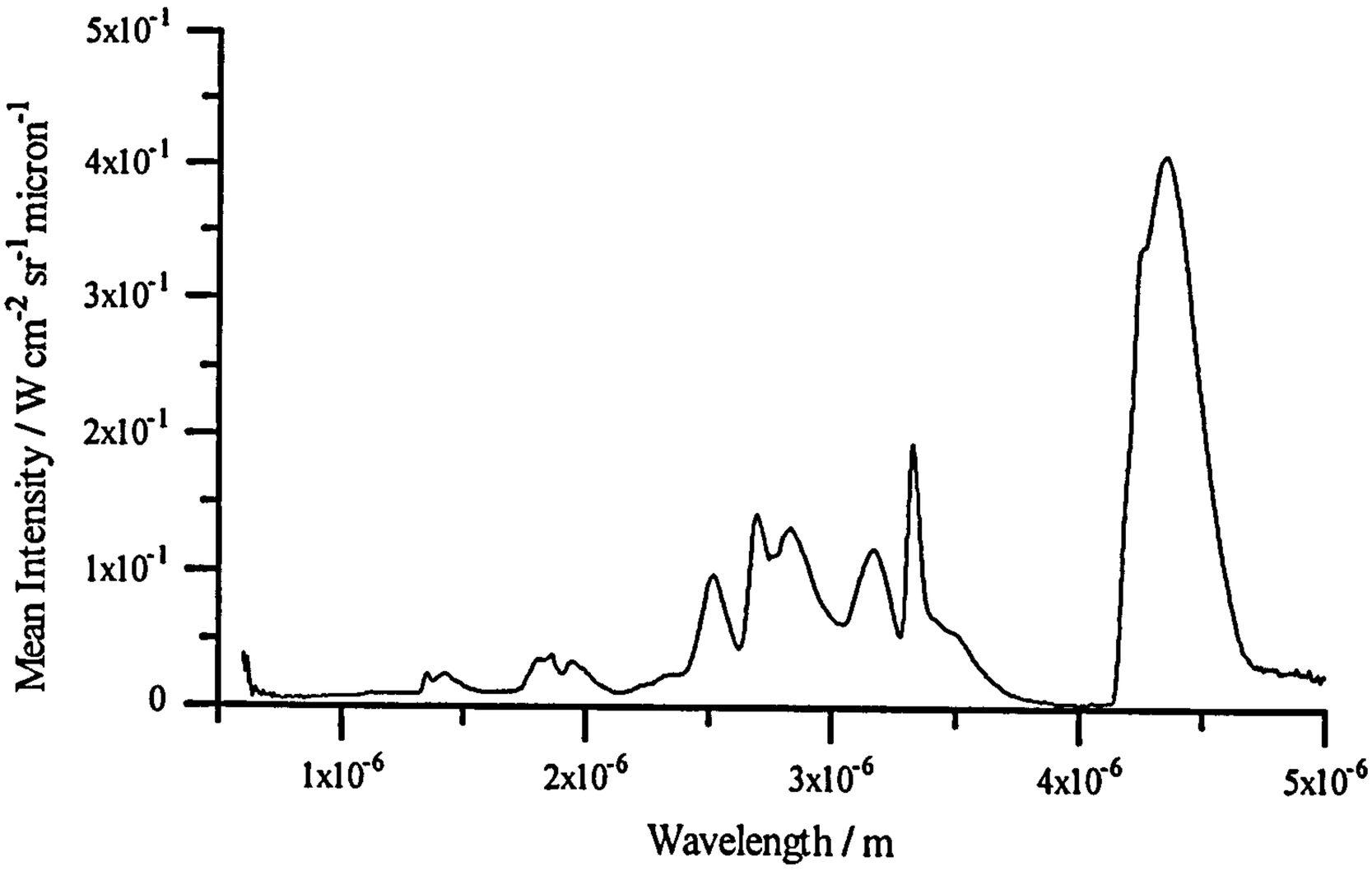

Radiation intensity. This spectrum was recorded in the 1 atm flame at a height of 200 mm above the burner exit plane.

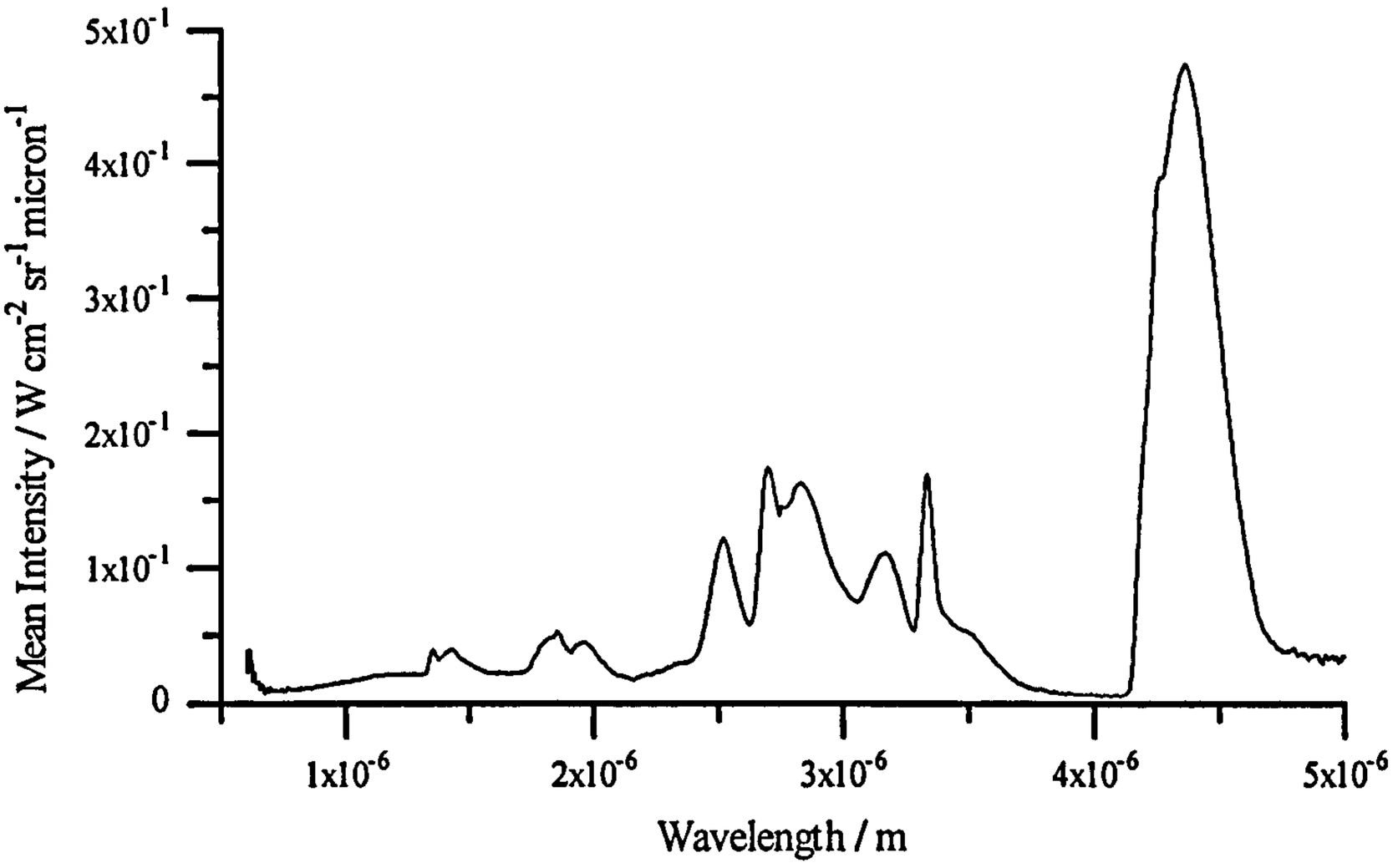

Radiation intensity. This spectrum was recorded from the 1 atm flame at a height of 250 mm above the exit plane of the burner.

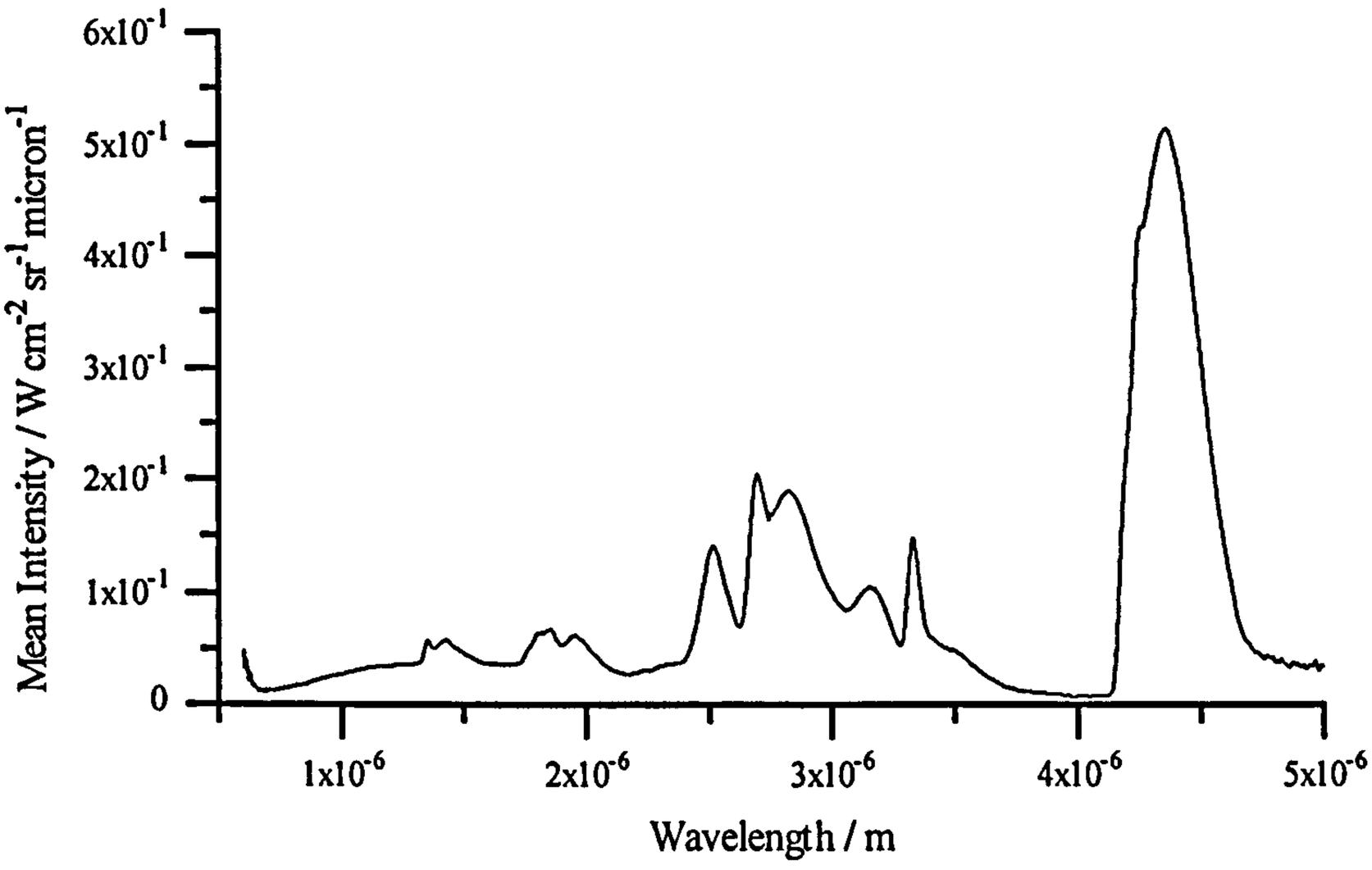

Radiation intensity. This spectrum was recorded from the 1 atm flame at a height of 300 mm above the exit plane of the burner.

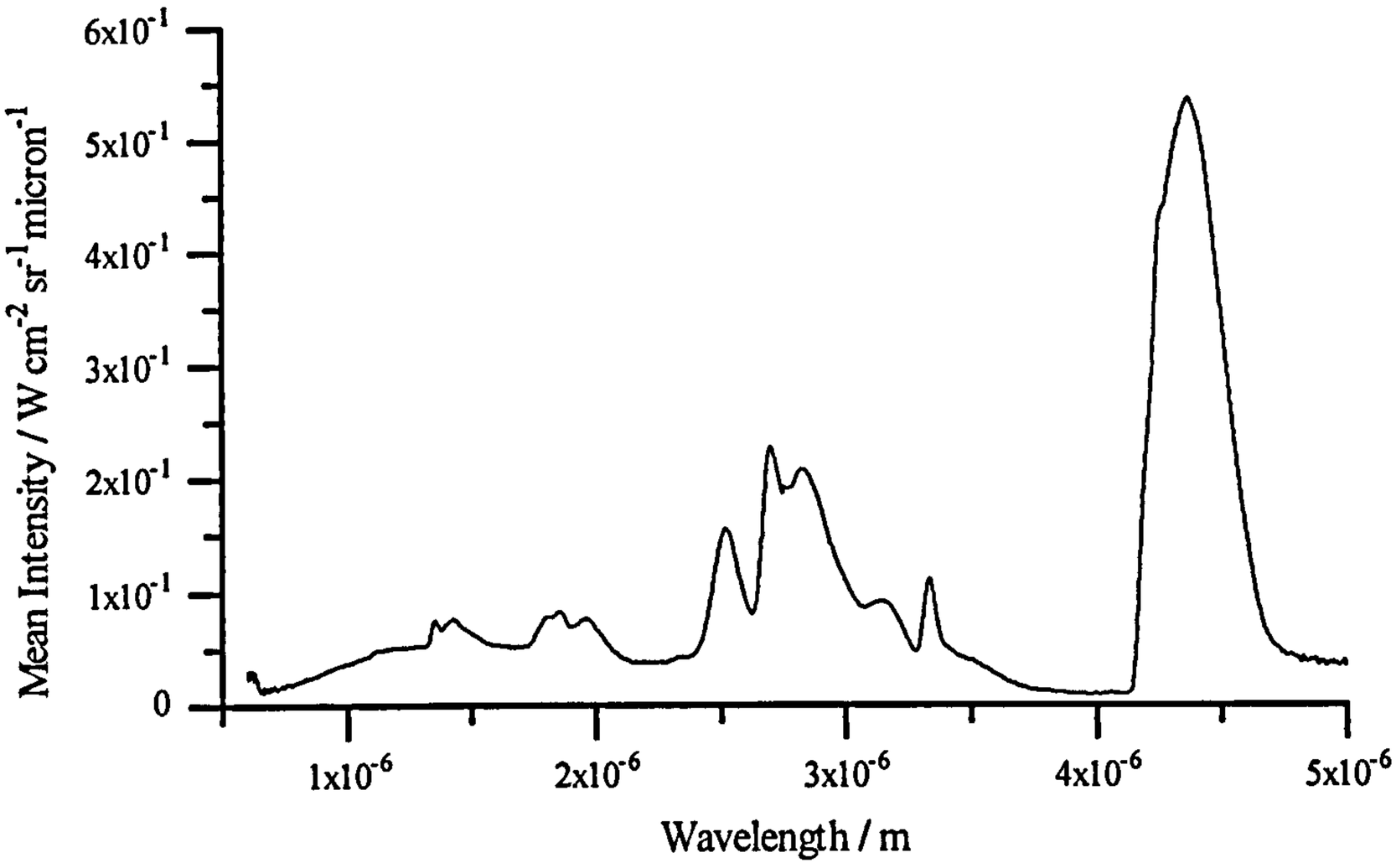

Radiation intensity. This spectrum was recorded from the 1 atm flame at a height of 350 mm above the exit plane of the burner.

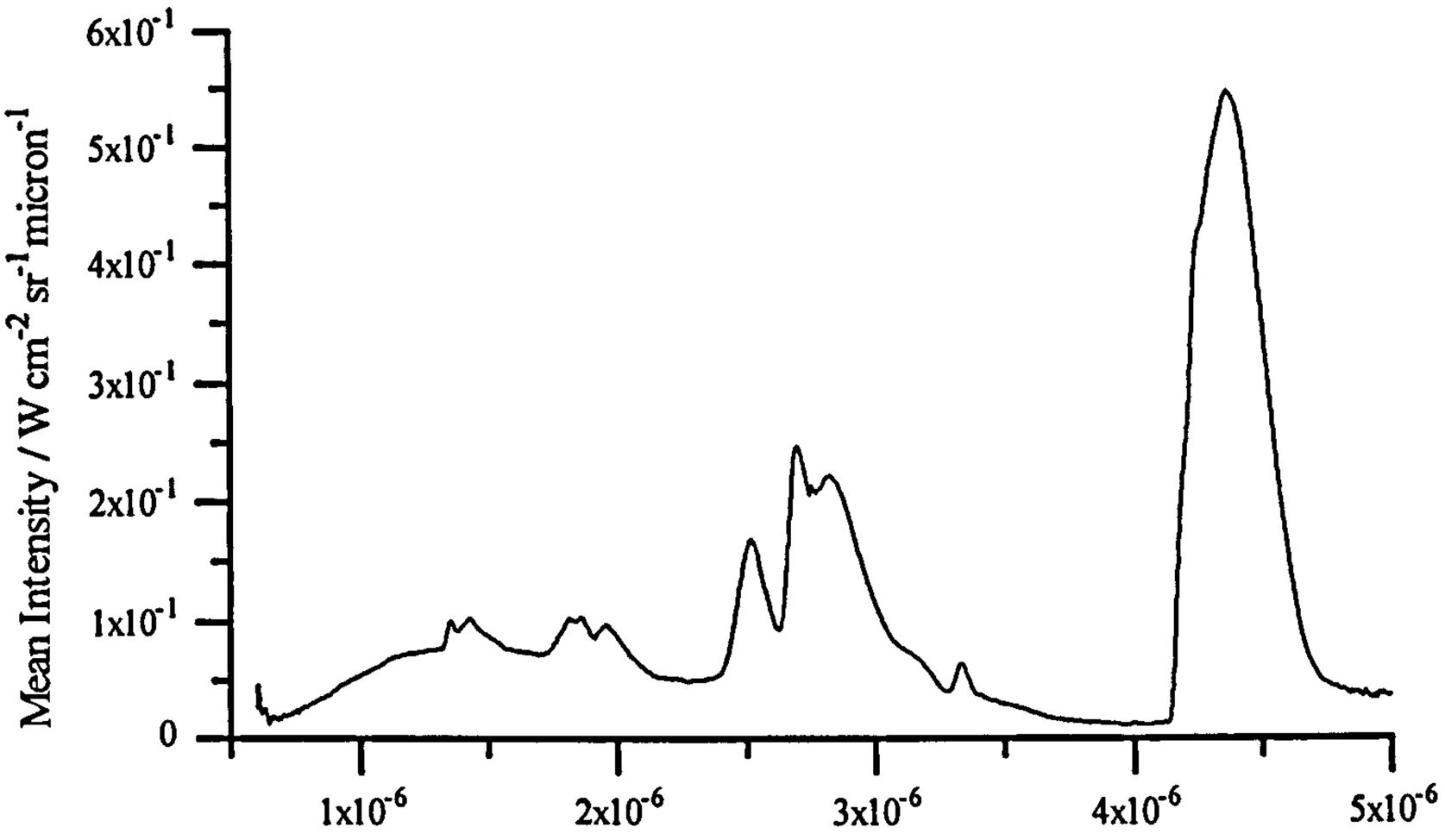

Radiation intensity. This spectrum was recorded from the 1 atm flame at a height of 425 mm above the exit plane of the burner.

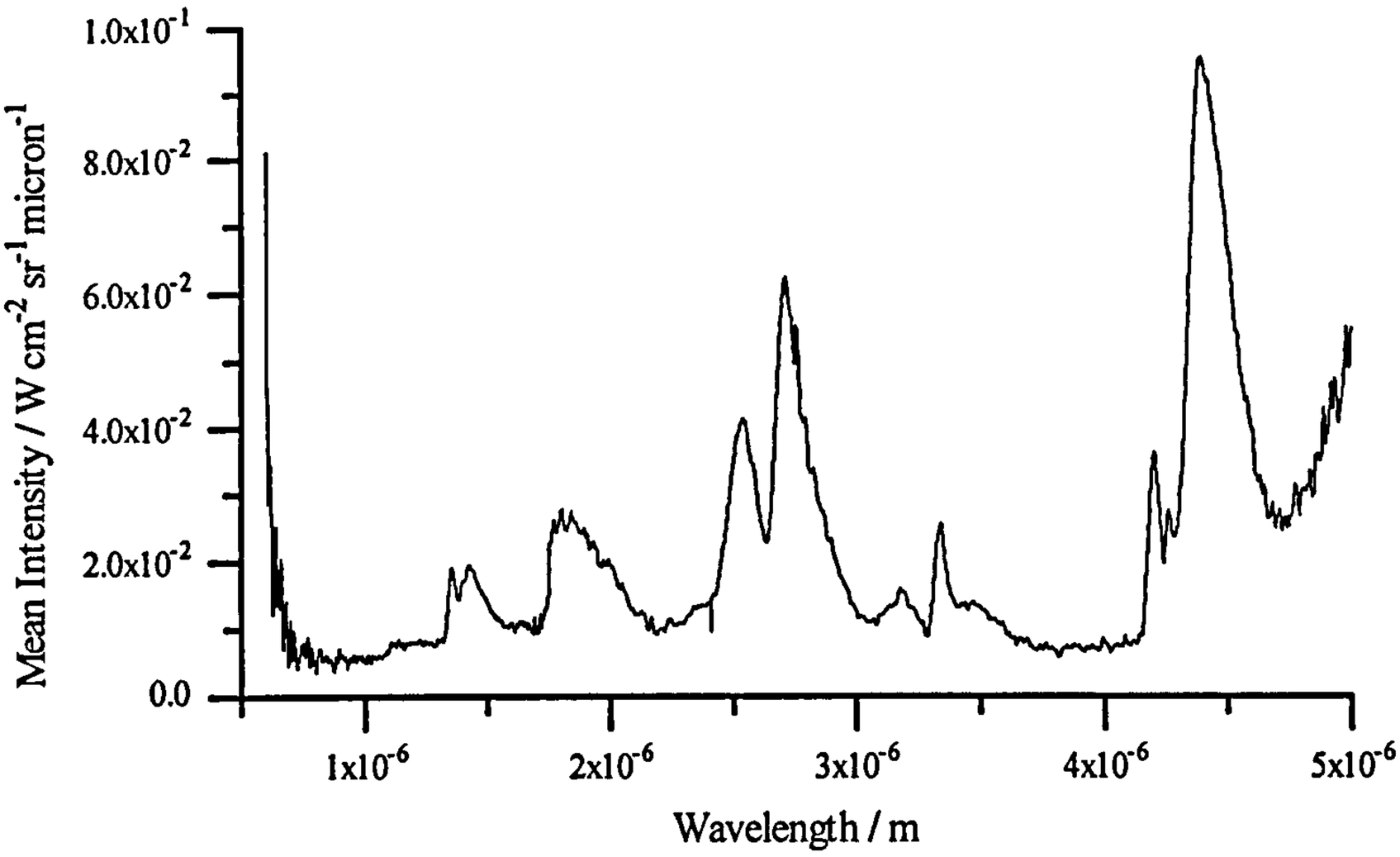

Radiation intensity. Spectrum recorded from 3 atm flame at a height of 50 mm above the exit plane of the burner.

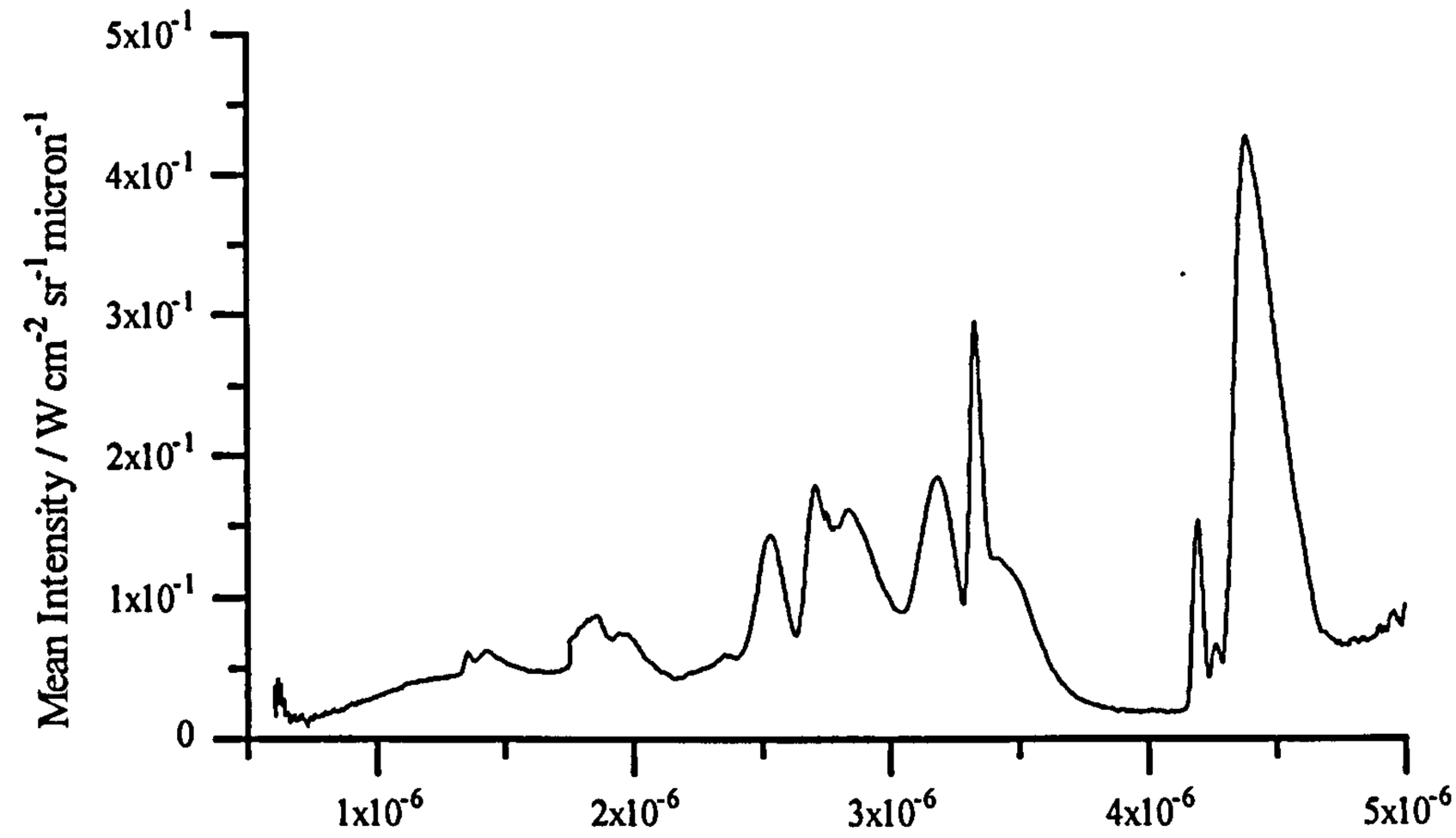

Radiation intensity. Spectrum recorded from 3 atm flame at a height of 100 mm above the exit plane of the burner.

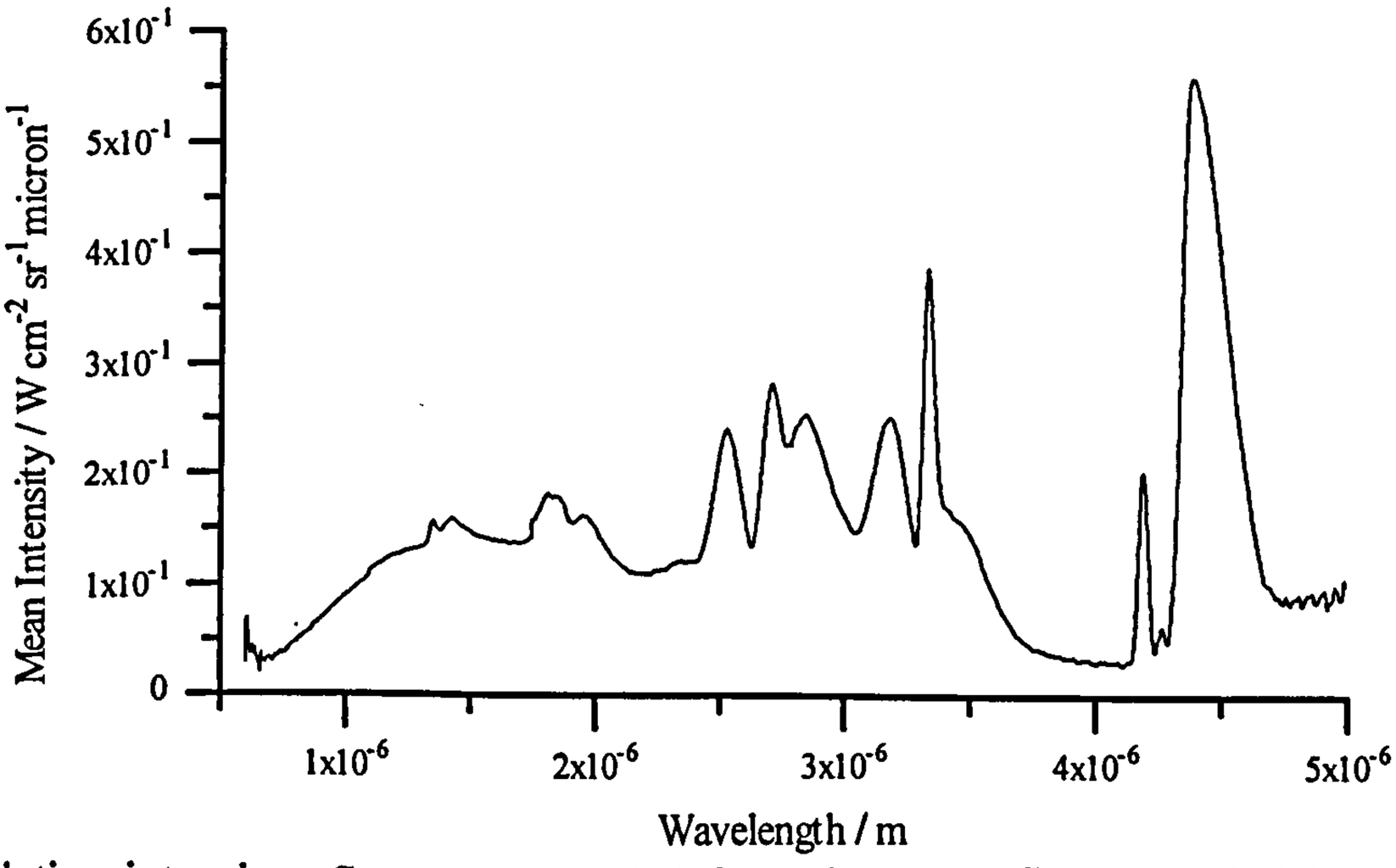

Radiation intensity. Spectrum recorded from the 3 atm flame at a height of 150 mm above the exit plane of the burner.

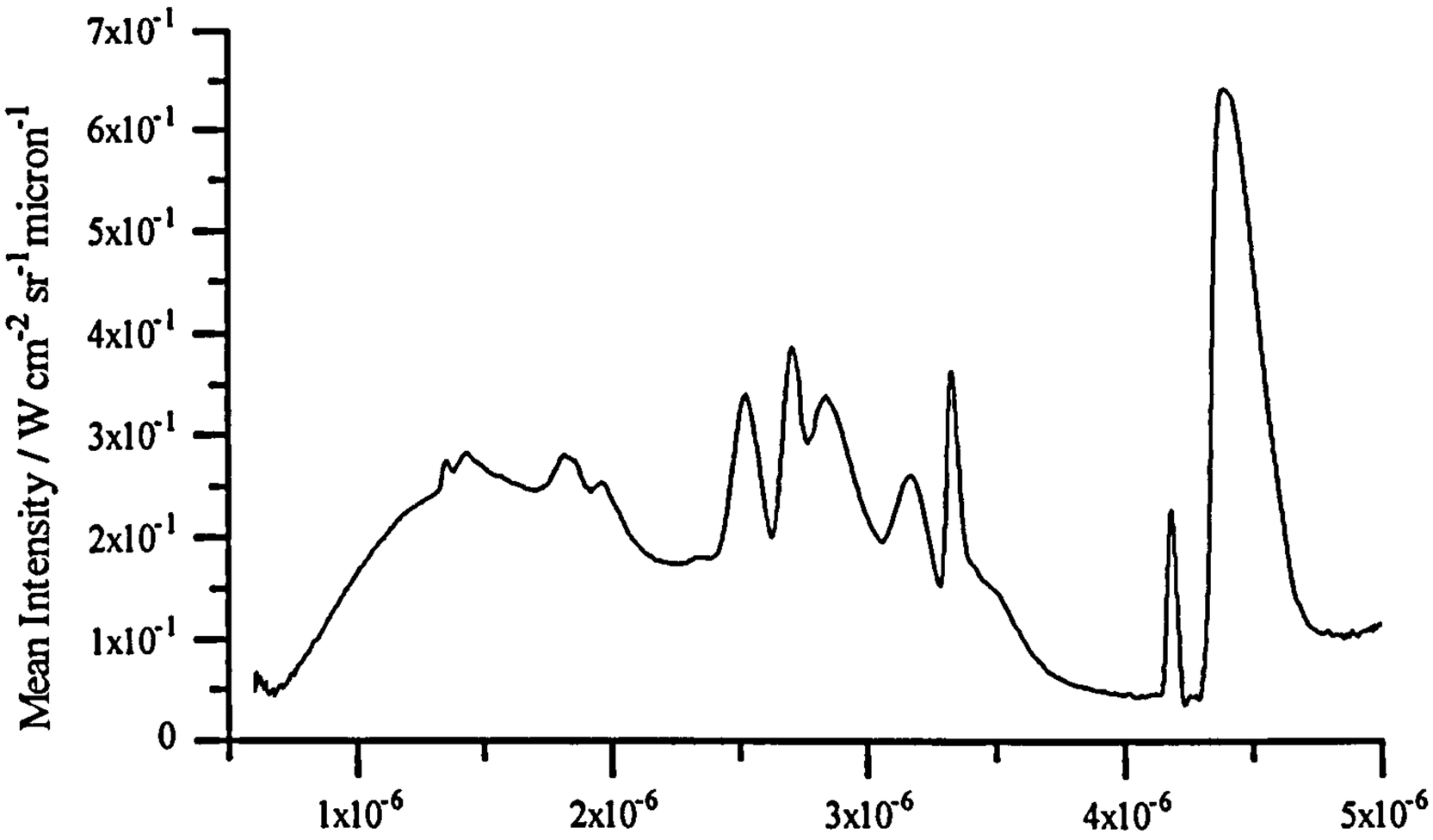

Radiation intensity. Spectrum recorded from the 3 atm flame at a height of 200 mm above the burner exit plane.

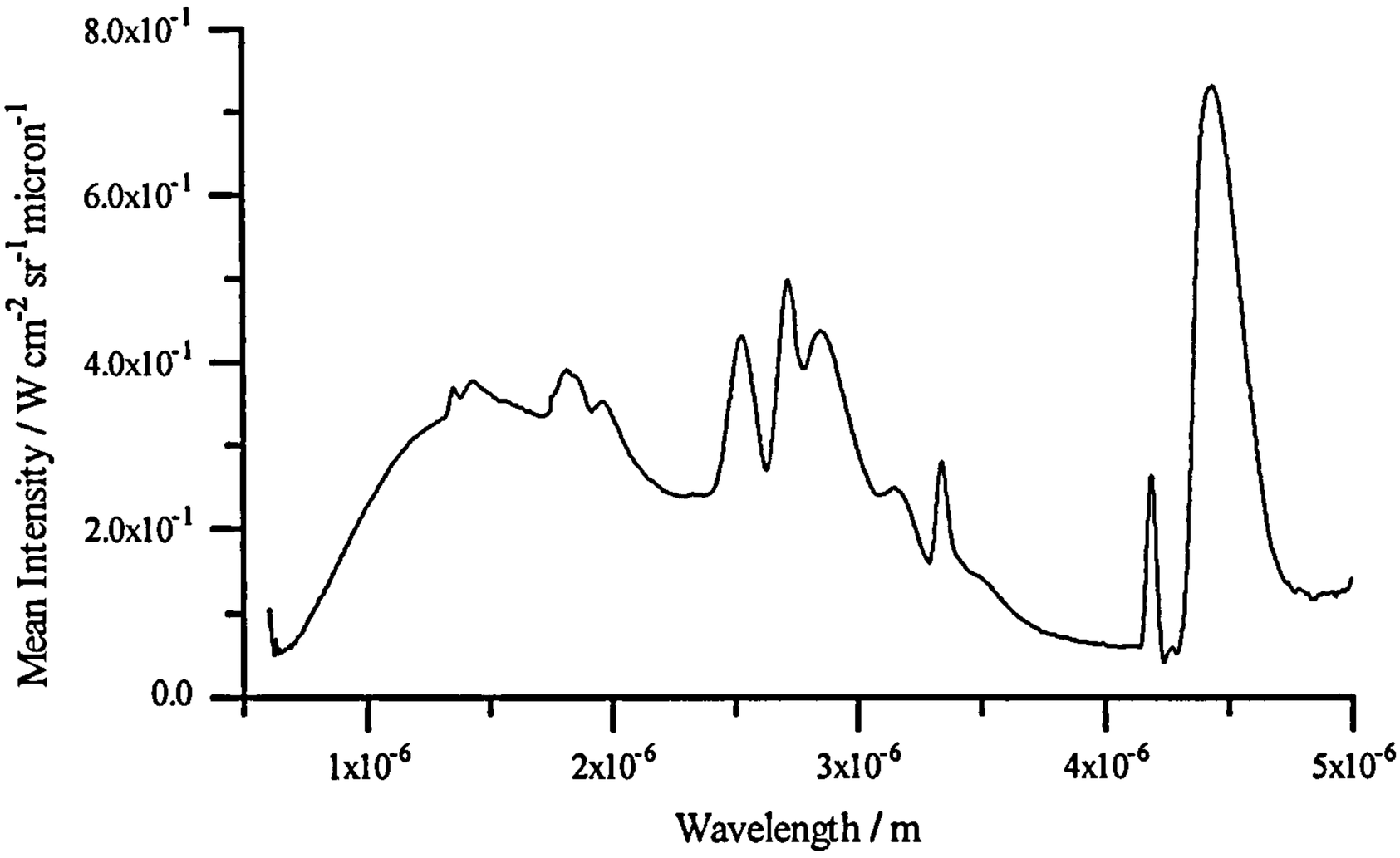

Radiation intensity. Spectrum recorded from the 3 atm flame at a height of 250 mm above the burner exit plane.

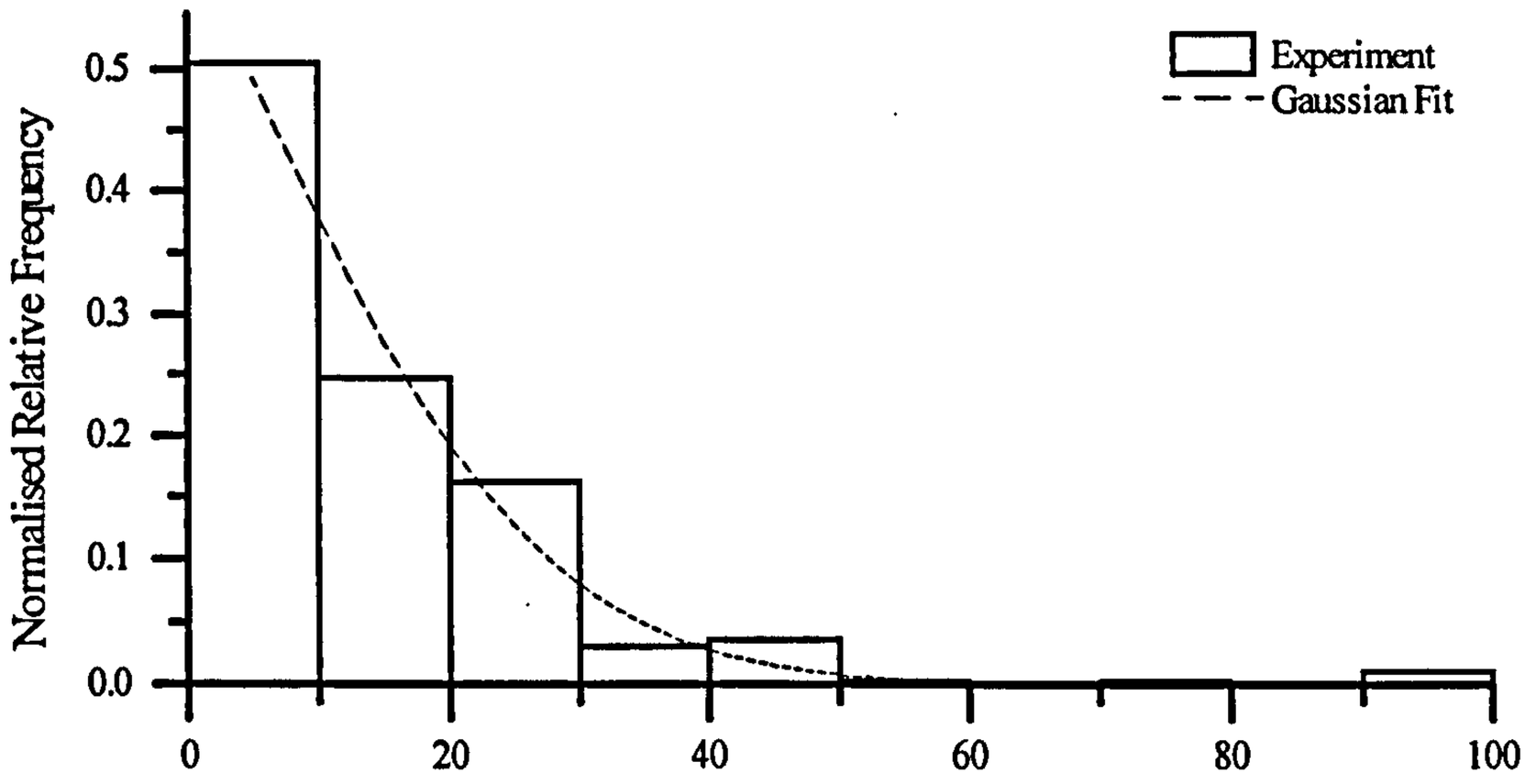

Experimental discrete PDF of radiation intensity. 1 atm flame. Height = 250 mm. Wavelength = 1650 nm. Maximum intensity = 0.153 W cm^{-2} sr^{-1} micron^{-1}. Mean = 14.5 % of the maximum.

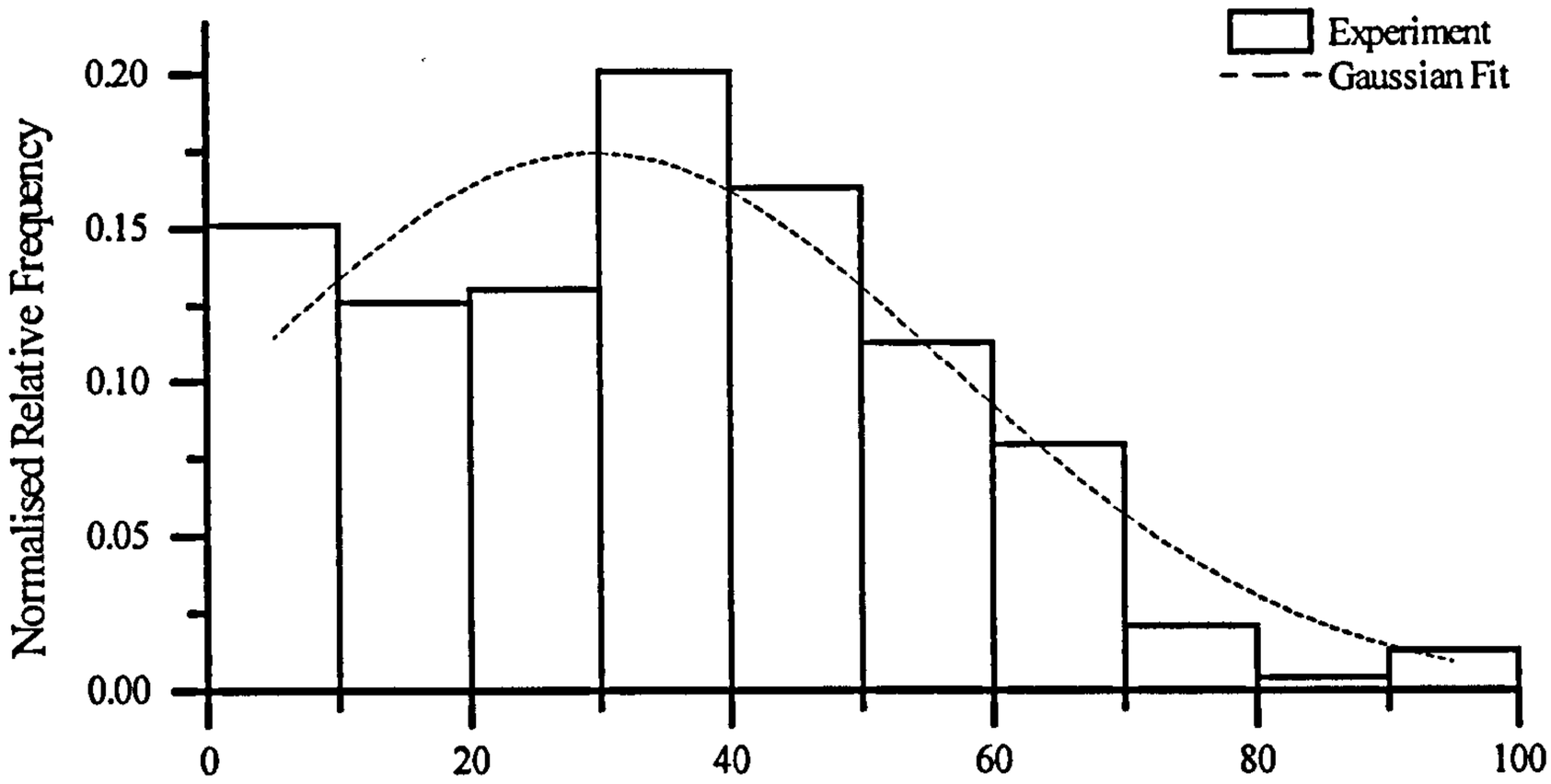

Experimental discrete PDF of radiation intensity. 1 atm flame. Height = 250 mm. Wavelength = 2834 nm. Maximum intensity = 0.468 W cm^{-2} sr^{-1} $micron^{-1}$. Mean = 34.7 % of the maximum.

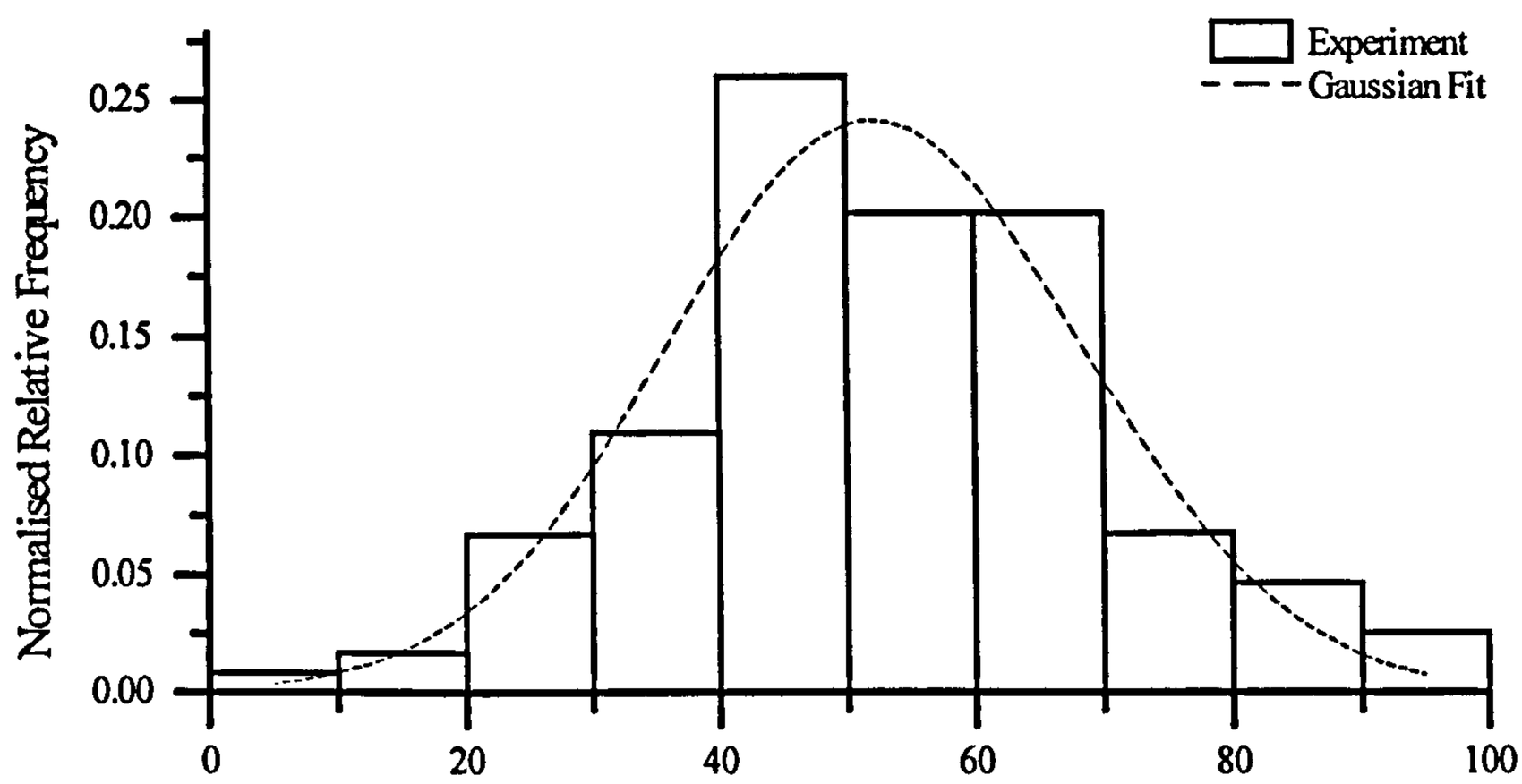

Experimental discrete PDF of radiation intensity. 1 atm flame. Height = 250 mm. Wavelength = 3332 nm. Maximum intensity = 0.320 W cm^{-2} sr^{-1} $micron^{-1}$. Mean = 52.9 % of the maximum.

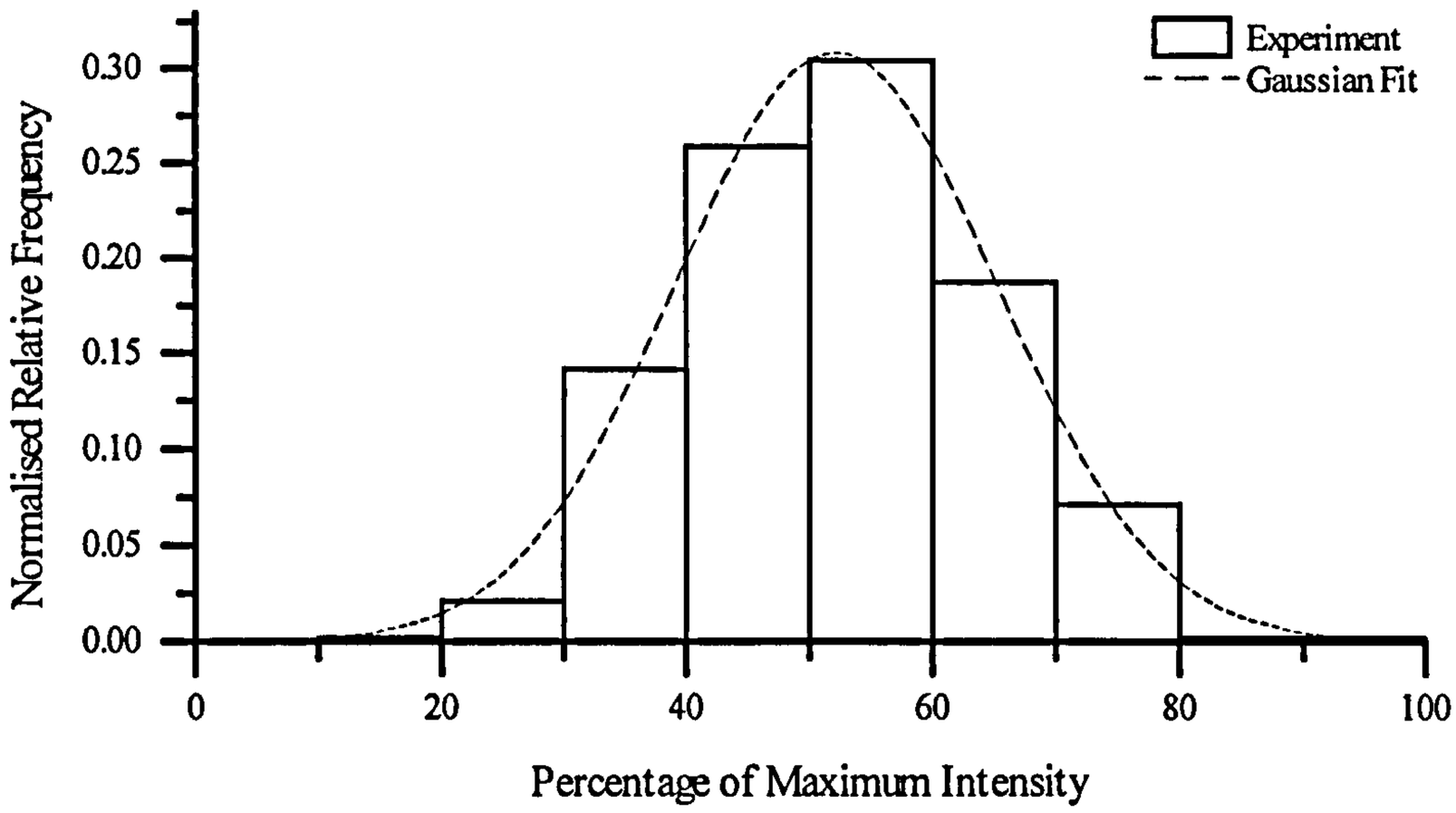

Experimental discrete PDF of radiation intensity. 1 atm flame. Height = 250 mm. Wavelength = 4359 nm. Maximum intensity = 0.907 W cm^{-2} sr^{-1} $micron^{-1}$. Mean = 52.4 % of the maximum.

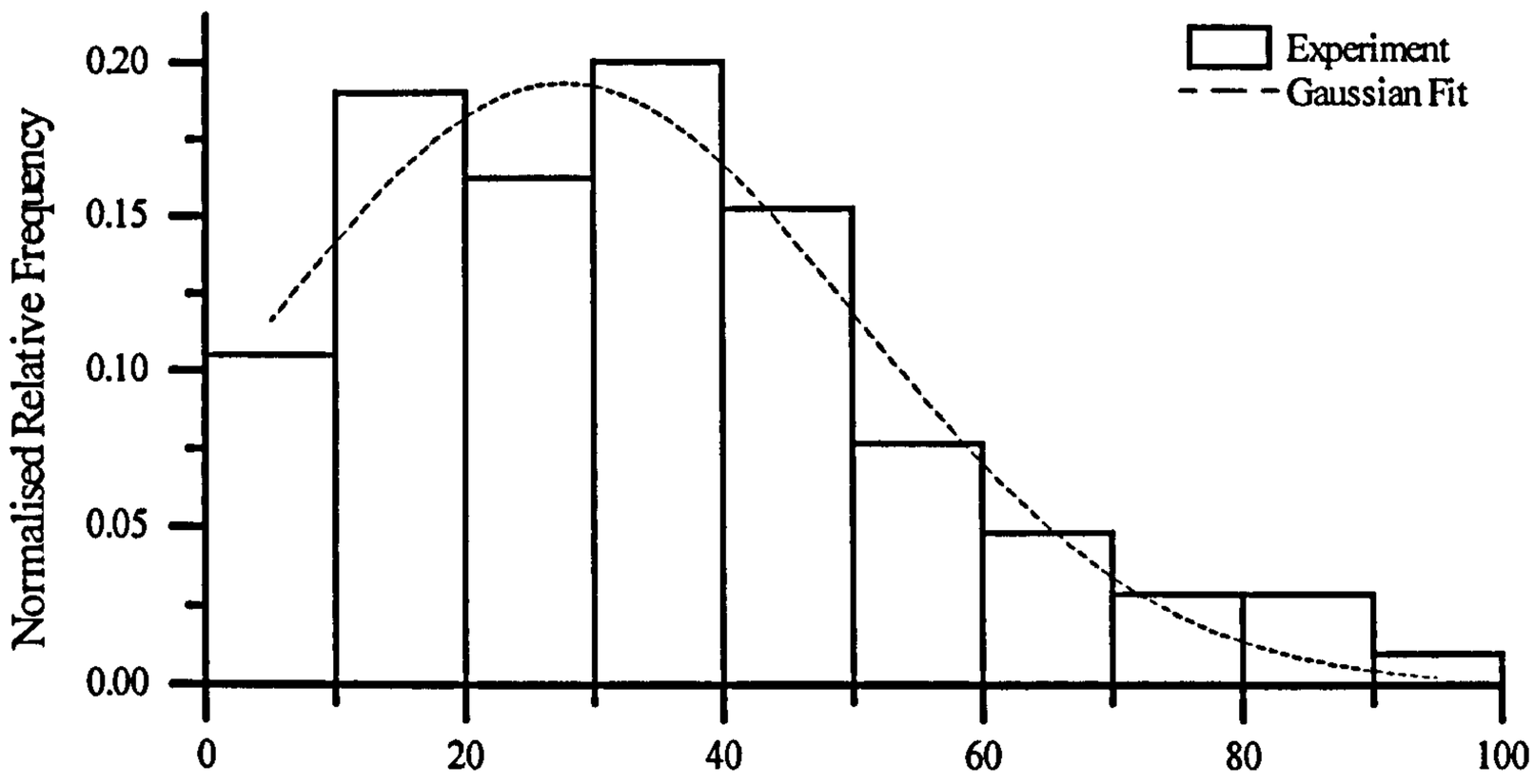

Experimental discrete PDF of radiation intensity. 3 atm flame. Height = 250 mm. Wavelength = 1700 nm. Maximum intensity = 0.985 W cm^{-2} sr^{-1} $micron^{-1}$. Mean = 34.0 % of the maximum.

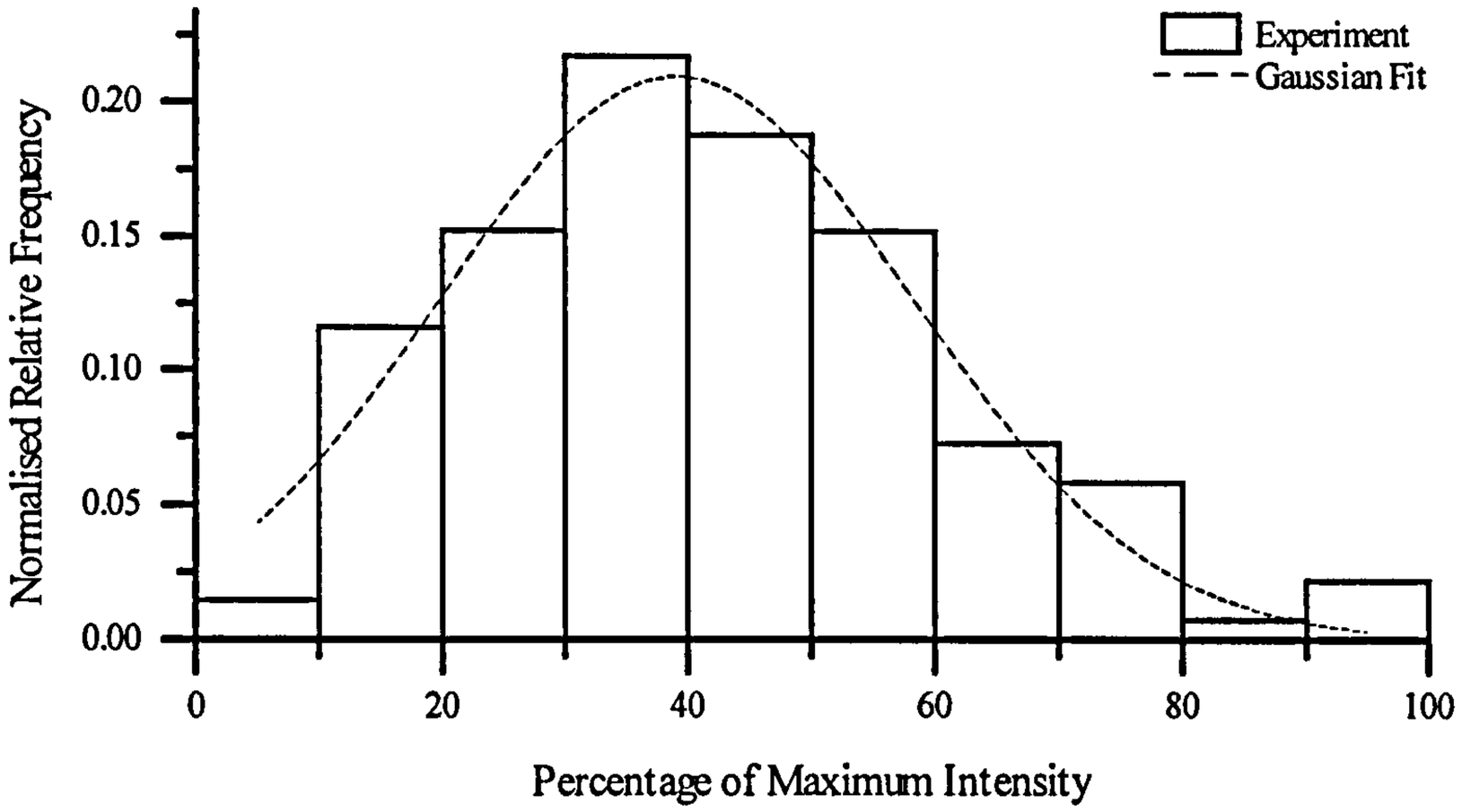

Experimental discrete PDF of radiation intensity. 3 atm flame. Height = 250 mm. Wavelength = 2846 nm. Maximum intensity = 1.045 W cm^{-2} sr^{-1} $micron^{-1}$. Mean = 41.8 % of the maximum.

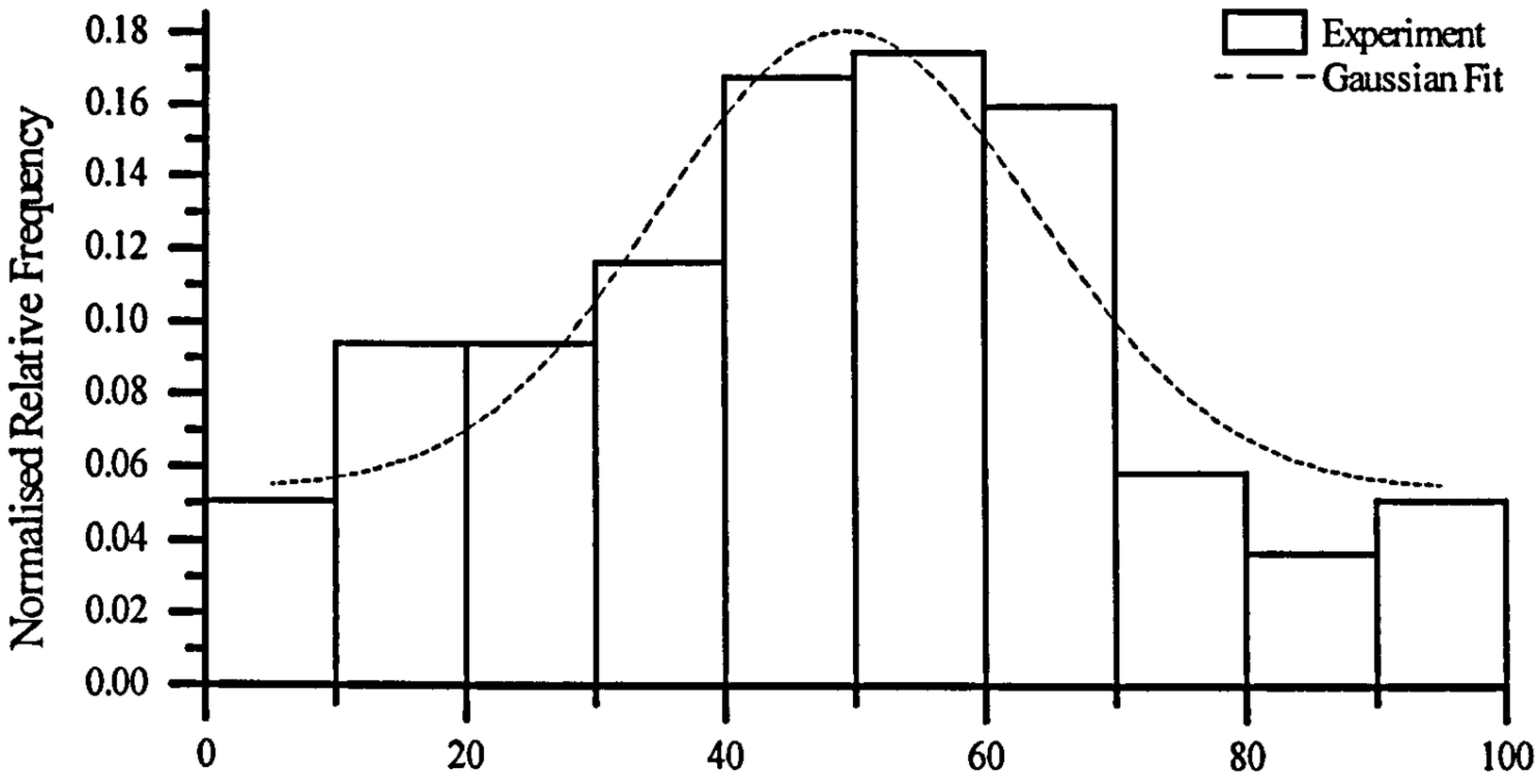

Experimental discrete PDF of radiation intensity. 3 atm flame. Height = 250 mm. Wavelength = 3342 nm. Maximum intensity = 0.587 W cm^{-2} sr^{-1} $micron^{-1}$. Mean = 47.8 % of the maximum.

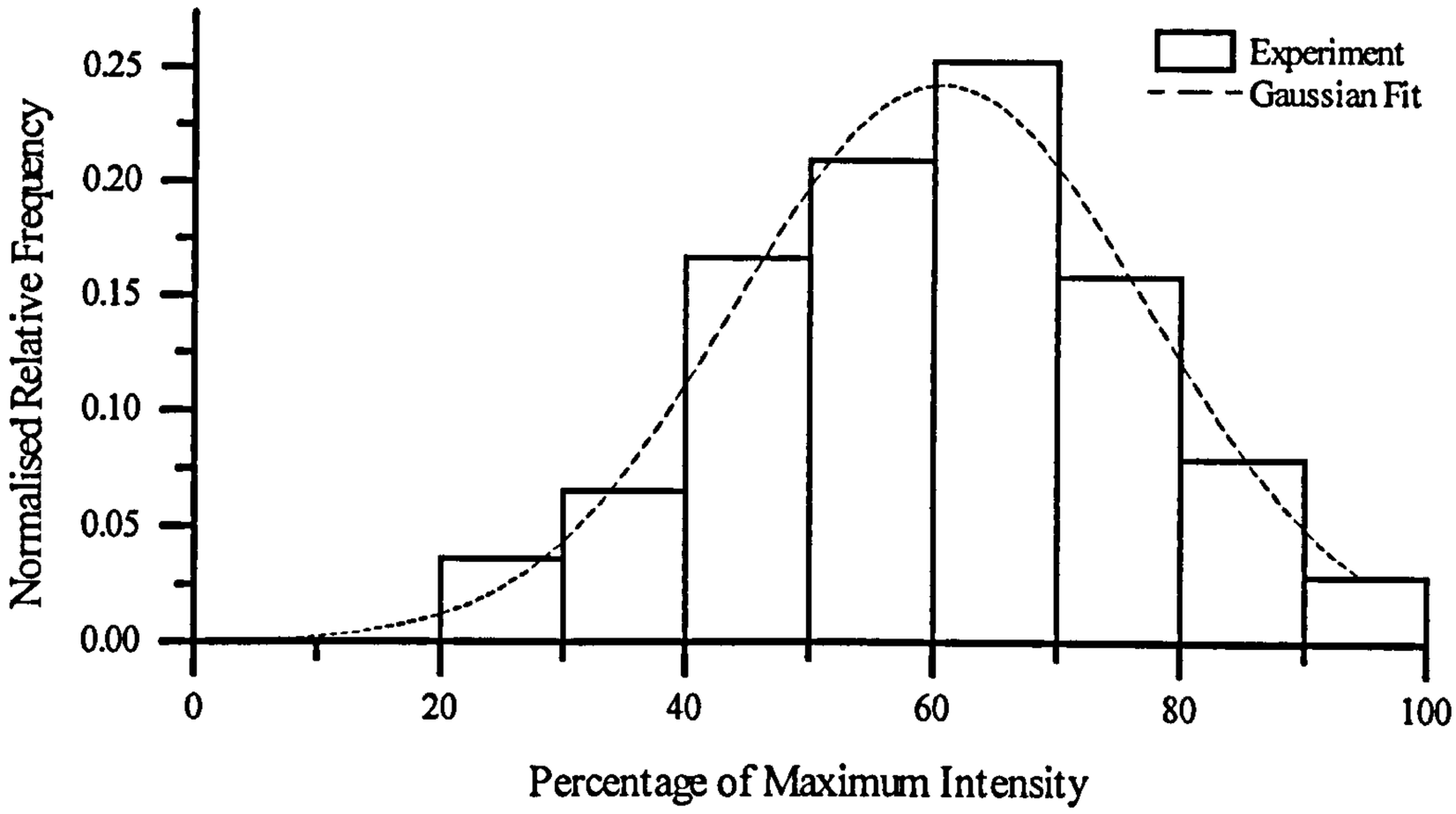

Experimental discrete PDF of radiation intensity. 3 atm flame. Height = 250 mm. Wavelength = 4435 nm. Maximum intensity = 1.22 W cm^{-2} sr^{-1} $micron^{-1}$. Mean = 60.2 % of maximum.